Absolute Absorption and Dispersion in a Thermal Rb Vapour at High Densities and High Magnetic Fields.

Lee Weller

Abstract

This thesis presents a comparative study of the measured and calculated absolute absorption and dispersion properties of the Rb D lines through a dense thermal vapour in the absence and presence of an applied magnetic field. A detailed theoretical model valid in the weak-probe regime is calculated. The model uses a matrix representation of the atomic Hamiltonian including the magnetic field interaction for Rb in the completely uncoupled basis. Numerical diagonalisation allows the frequency detunings and transition strengths to be calculated. The lineshape of each transition is modelled as a Voigt profile, a convolution of the inhomogeneous and homogeneous profiles. The medium's susceptibility is found by summing over all the electric-dipole-allowed transitions. For dense thermal vapours a modification to the homogeneous linewidth of each transition, which grows linearly with the number density of atoms, arises due to resonant dipole-dipole interactions between identical atoms in superpositions of the ground and excited terms. In the presence of an applied magnetic field we investigate the Stokes parameters of light propagating through a dense thermal vapour. For fields larger than 0.33 T we enter the hyperfine Paschen-Back regime on the Rb D lines. We present a compact optical isolator based on an atomic vapour, exploiting the spectral region of high transmission and large dispersion where we would normally expect absorption on the Rb D lines. Frequency up-conversion is shown in the fluorescence measurements over the visible and near infra-red regions for strong excitation. Low density transfer arises due to the energy-pooling effect between two identical atoms in their first excited terms. At high densities resonant dipole-dipole interactions give rise to a threshold for the energy transfer. We characterise the threshold behaviour with increasing number density.

Absolute Absorption and Dispersion in a Thermal Rb Vapour at High Densities and High Magnetic Fields.

Lee Weller

A thesis submitted in partial fulfilment
of the requirements for the degree of
Doctor of Philosophy

Department of Physics
Durham University

August 9, 2013

Contents

List of Figures

List of Tables

Declaration

I confirm that no part of the material offered has previously been submitted by myself for a degree in this or any other University. Where material has been generated through joint work, the work of others has been indicated.

Lee Weller
Durham, August 9, 2013

To Mum and Dad,

Acknowledgements

A great number of people have donated time and effort to the creation of this thesis, and whether it was a small or large contribution, I wholeheartedly thank them all. First and foremost I would like to thank my supervisors Ifan and Charles, for taking me on as PhD student and providing encouragement, confidence and a good kick up the arse when I needed it. To Ifan, whom none of this would have been possible, I thank not only as a supervisor but as a friend. Without his love and enthusiasm for physics, and all things Welsh, I would not be here today writing an acknowledgements section to a thesis that I had completed, "Diolch yn fawr". Furthermore he was the only person in the physics department that understood me when I wanted to have a rant about the Swans. Lets hope they stay in the premiership for many years to come! To Charles for his valuable insights into the project and for improving my figure creation no end. I will also miss our random chats on the state of the English and Welsh cricket team.

The present stage of the project would not exist without the past proprietor, so I would like to give a huge thanks to Paul, for sticking by me when I am sure it appeared like I did not know my right from my left (circular polarisations). The future of the project is now in the capable hands of Mark, who is discovering that (when he is not brewing beer, which to be fair does brighten up our meetings) the unexpected observations are usually the most interesting. I would also like to acknowledge some physicists outside AtMol. Firstly, Dr Svenja Knappe for her kindness with the 1 mm vapour cell, without which several chapters in this thesis would not be possible - it has been a pleasure to collaborate with her. Secondly, I would like to thank Dr Aidan Arnold and Dr Sonja Franke-Arnold for stimulating discussions and the first observation that the blue light might not necessarily be blue light.

The day-by-day supervision of five students has led to the majority of this work being completed. First of all I would like to thank Robert J. Bettles whom helped with the fitting algorithms used in this thesis and most recently the theoretical calculations for the cooperative enhancement work. I thank Toryn Dalton for all the work he did for me in the summer of 2012. The level of agreement he was striving for has led to the named "Toryn syndrome". Also, I thank Lee Stothert for all the work he did for me in the summer of 2013. I am sure the development of the new lasers will contribute to some

valuable experiments in the future. Finally I thank the Erasmus students Kathrin Kleinbach and Tobias Bäuerle. Kathrin's work on the magnetic field interaction helped tremendously with the publication of two papers and I am sure Tobias's work on four-wave mixing will lead to another publication. I am grateful to the people with whom I shared an office and tea breaks; in particular James, Tim, Chris and Dan, whose friendship has made thesis writing all the more bearable. I thank James for general dipole-dipole discussions and theoretical assistance with Python. I thank Tim whom has been on the journey from the start when we met for the very first time in first year undergraduate labs. I thank Chris for his knowledge on all things collective or is that cooperative. Finally I thank Dan for endless times where I have needed a cup of tea and left all my money at home.
Outside the department I have been fortunate enough to make friends with a large number of people at Durham during my extended 8 year period. To all the times I have shared and the people with whom I have shared them with I would like to say thank you. In particular Matt and Alex, who I know I will miss when I venture South. I wish the best of luck to Alex who continues in his studies and to Matt who I am sure will make a brilliant head of department in his new school. I would also like to thank Pippa, my girlfriend who has kept me on the straight and narrow over the last two years and the smart ones amongst you would notice has been my most productive time during my PhD. I know she will make a wonderful teacher and I can not wait to move to Cambridge with her and continue our lives together.
Finally I give all my thanks to my parents Richard and Linda and my brother Robert for their love and support in all I do. I thank my brother for his honest approach on life which has made me realise there is more to life than just work. I thank my Mum and Dad without whom I would not be where I am today and hopefully if I could even get near to what they have done for me as parents with my own kids one day then I will be a happy person. I love you.

Chapter 1

Introduction

1.1 Motivation

The aim of this investigation is to study the atom-light interaction for low and high density atomic media in the absence and presence of an applied magnetic field. Comparing experimental measurements and a developed theoretical model incorporating the magnetic field interaction, one can investigate the Faraday effect and in particular the Stokes parameters for light. One can also investigate the Paschen-Back effect and realise an optical isolator based on an atomic vapour. For high density atomic media there is the possibility for investigating cooperative effects due to resonant dipole-dipole interactions. Of particular interest is the enhancement of energy transfer in such media.

1.2 Atom-light interactions

Understanding and controlling the propagation of light through a thermal vapour is a burgeoning area of research. Specific topics of interest include modifying the speed of light propagation in a medium ("slow light") [1, 2] or ("fast light") [3]; studying the quantum interface between light and atomic ensembles [4], for example in quantum memory [5]; all-optical switching [6, 7]; and measurements of transition amplitudes between low-lying states providing a valuable test of *ab initio* calculations [8].

The theory of quantum electrodynamics [9] provides a complete quantum mechanical description of the interaction between light and atoms. Light can be thought of as containing an integer number of quanta, known as photons, whereas atoms exist as quantised energy states where charge carriers reside. The interaction describes the exchange of quanta between the light and atom. The problem with this description is that from an experimental perspective we deal with a large number of photons (typically for a 1 mW beam with intensity over the volume of a vapour 10^{17} photons enter the vapour every second) interacting with a large collection of atoms (for a room temperature vapour of rubidium (Rb) we have an atomic density of 10^{10} cm^{-3}, therefore inside an interaction volume of 1 cm^3 we have 10^{10} atoms) in various states of excitation. Following the trajectory of every single photon as it interacts with every single atom (which are themselves interacting) is computationally intractable. Therefore the atom-light interaction must be thought of in terms of the statistical behaviour. For this thesis we introduce two approximations, firstly instead of the concept of photons we shall only consider classical electromagnetic fields, and secondly we shall treat a collection of atoms as a statistical ensemble. Starting with the interaction of a classical light field with a two-level quantum system we are able to develop a model that will allow us to predict macroscopic properties of realistic systems.

A theoretical model for the electric susceptibility of a vapour of alkali-metal atoms finds utility in, for example, analysing electromagnetically induced transparency (EIT) spectra [10–12]; understanding Doppler-broadened absorption spectroscopy [13]; designing a broadband optical delay line [14, 15]; controlling ultrabroadband slow light [16]; enhancing the frequency upconversion of light [17]; investigating cooperative effects in an atomic nanolayer [18]; imaging microwave fields in vapour cells [19]; Hanle-type coherent population trapping [20]; and achieving quantitative spectroscopy for a primary standard [21].

For this thesis we shall consider the atom-light interaction in two parts. In part I the absorption and dispersion experienced by a weak beam as it propagates through a medium of Rb in the absence and presence of an external magnetic field is shown. In this case, the atoms remain unperturbed during the interaction so the approximation that the population remains in the

ground states is valid. In part II of the thesis we consider an atomic medium of Rb subject to strong excitation, where the state of the atoms is dramatically affected. In the high density regime where dipole-dipole interactions are significant [22] (see chapter 3), cooperative effects manifest themselves.

1.3 Magnetic-field interaction

The study of light propagation through thermal atomic vapours subject to external magnetic fields is a flourishing area of research especially with a view to applications in quantum information processing, such as the quantum internet [23] and quantum memories [5]. The addition of an external magnetic field for such an ensemble further increases the possibilities for these interfaces to be realised. As first observed by Zeeman in 1896 [24], the energy levels and transition probabilities of an atomic ensemble are extremely sensitive to an external magnetic field. Most experimental observations before the 21st century concentrated on the comparison between theoretical and measured line centres [25]. A full calculation of the electric susceptibility describing the absorptive and dispersive properties was not realised until comparisons between experiment and theory for the performance of devices in the FADOF (the Faraday anomalous dispersion optical filter) community became a necessity [26]. A theoretical model describing such properties in external magnetic fields now finds utility in many applications. For this thesis we shall compare experimental measurements and theoretical calculations for the absorption of a Rb vapour subject to an external magnetic field [27] (see chapter 6).

Faraday [28] discovered the magneto-optical phenomenon which bears his name where an axial magnetic field causes the rotation of the plane of polarisation of incident linearly polarised light. Much attention has been paid to resonant linear and nonlinear magneto-optical effects in multi-particle ensembles and has allowed for the observation of quantum teleportation between light and matter [29] and control of atomic Zeeman populations in long-lived quantum memories [30]. A comprehensive review of this field can be found in the article by Budker *et al.* [31]. The resonant atom-light interaction can be exploited to construct some of the most sensitive magnetometers [32] and

there are prospects for magnetometers with nanometric spatial resolution using nanothickness atomic vapour layers [33]. The off-resonant Faraday effect is also beneficial in, for example, achieving a narrow-bandwidth optical filter with ultrahigh background rejection with atoms [34, 35] and crystals [36]; realising a dichroic beam splitter for Raman light [37]; performing far-off resonance Faraday spectroscopy [38]; and producing suitable spectral features for laser stabilisation [39, 40]. For this thesis we shall compare experimental measurements and theoretical calculations of Stokes parameters for off-resonant light transmitted through a high-density Rb vapour [41] (see chapter 5).

1.4 Optical isolators

Optical isolators are fundamental components of many laser systems as they prevent unwanted feedback. Such devices consist of a magneto-optically active medium placed in a magnetic field such that the Faraday effect can be exploited to restrict the transmission of light to one direction. For an applied axial field B along a medium of length L, the Faraday effect induces a rotation θ for an initially linearly polarised light beam, where $\theta = VBL$, and V is the Verdet constant. An optical isolator is realised when such a medium is positioned between two polarisers set at $\pi/4$ to each other, with an induced rotation of $\theta = \pi/4$; this arrangement provides high transmission in one direction and isolation in the other.

The technologies of atomic Micro-Electro-Mechanical Systems (MEMS) (i.e. the technology of very small devices) will eventually be required to create lighter and more compact components [42] for use in free-space laser communications, ocean measurements and telecommunications. Currently there is much interest in small, reliable low-power laser systems [43], fabrication of chip-sized alkali-vapour cells [44] and gas atoms in hollow core fibers [45, 46] for atomic frequency references [47] and magnetometers [48]. Other applications include gyroscopes [49], laser frequency stabilisation [50] and atomic sensors [51] for cold-atom devices, accelerometers and gravimeters. For this thesis we show that using similar technologies one can envisage a light, compact, high-performance permanent-magnet isolator [52] (see chapter 6).

Material	V (rad T^{-1} m^{-1})	FOM (rad T^{-1})
TGG [54]	82	1×10^3
YIG [53]	3.8×10^2	2.5
Rb vapour	1.4×10^3	1×10^2

Table 1.1: Verdet constants and figure of merits (FOMs) for the three magneto-optic materials: TGG, YIG and Rb vapour (this work), at a wavelength of 780 nm.

Isolators require large Verdet constants whilst maintaining a small absorption coefficient α, hence the figure of merit (FOM) for an isolator is the ratio V/α. Commercial isolators often use terbium gallium garnet (TGG), with yttrium iron garnet (YIG) also used in the IR region. Table 1.1 shows the Verdet constants and FOM for TGG, YIG and Rb vapour at 780 nm. Note that although the Verdet constant of YIG is much larger than that for TGG, the latter is used at 780 nm, as the performance of the former is strongly compromised by the poor transparency of YIG below 1100 nm [53]. Note also that the Verdet constant and absorption coefficient of the atomic vapour are strongly frequency dependent, unlike the crystal media. The FOM for Rb vapour is less than TGG, the much higher Verdet constant however allows a more compact design, as the same rotation is achieved over a much shorter optical path.

The frequency dependence of the dichroic and birefringent properties of atomic vapours have also been exploited to realise narrowband atomic filters; see e.g. [35] and dichroic beam splitter [37].

1.5 Cooperative effects

Cooperative effects are fundamental in nature for the oxygenation of haemoglobin [55], light-harvesting components of photosynthetic organisms [56] and properties of water [57]. Alkali-metal atoms are an ideal tool for understanding the mechanisms for such complex systems. The magnitude of these cooperative processes is defined by the strength of the dipole-dipole interaction. Rydberg (state of high principal quantum number) ensembles exhibit large dipole-dipole interactions that display cooperative effects in,

for example, atom-light interactions in a blockaded ensemble [58], many-body interactions in an excited cold gas [59] and nonlinear optics with single photons [60]. These effects can also be realised for low-lying excited states, for example in the measurement of the cooperative Lamb shift in a nanothickness atomic vapour [18] and collisional redistribution of radiation for laser cooling [61].

Cooperative effects could be beneficial to many systems. Examples include spontaneous radiation processes [62]; blue-light generation in a two-photon rubidium vapour [17, 63, 64]; four-wave mixing [65, 66] including the possibility for generated correlated photon pairs [67]; intrinsic optical bistability in a warm cesium vapour [68]; a high-transmission FADOF edge filter with large magnetic fields [69]; enhanced light-assisted-collision rates for magneto-optical traps [70] and energy-pooling processes in laser-excited alkali-metal vapours [71].

The energy-pooling effect is an inelastic collision between two excited atoms in terms $\mathrm{A}(nL_J)$, where n is the principal quantum number, L is the total orbital angular momentum and J is the total electronic angular momentum. Both atoms transfer their terms such that

$$2\mathrm{A}(nL_J) + \Delta\mathrm{E} \rightarrow \mathrm{A}(n'L'_{J'}) + \mathrm{A}(n''L''_{J''}), \tag{1.1}$$

with the internal energy defect, ΔE, between the initial and final pair terms, which are compensated by the energy of the translational atomic motion. Energy-pooling collisions have been studied extensively for the alkali metals sodium [72, 73], potassium, [74, 75], rubidium [76–83] and cesium [84–90]. For this thesis we show field enhancement due to dipole-dipole interactions in a dense atomic vapour gives rise to a threshold for non-linear effects such as frequency up-conversion [91] (see chapter 7).

1.6 Thesis summary

A summary of the thesis is as follows:

Chapter 2 The theoretical model is developed and we show frequency detunings and relative line-strengths for the D lines. Using the

medium's susceptibility we calculate the refractive index and absorption coefficients, and compare the predictions to experimental measurements through a 75 mm vapour cell. This chapter is based on the article [92].

Chapter 3 At high number densities resonant dipole-dipole interactions between two identical alkali-metal atoms, in superpositions of the ground and excited terms, give rise to the phenomenon of self-broadening. Measurements of the susceptibility show a linear increase in the homogeneous linewidth with number density. Including the impact self-broadening parameter into the model described in chapter 2 gives excellent agreement with theory through a 2 mm vapour cell at increased densities. This chapter is based on the article [22].

Chapter 4 A matrix representation of the magnetic interaction Hamiltonian for the $5^2S_{1/2}$ and $5^2P_{1/2}$ terms is shown. Analytic diagonalisation leads to generalised eigenvalues and eigenfunctions given by the well-known Breit-Rabi formula. Calculated relative line-strengths and transition frequencies provide an insight into different magnetic regimes. We present the experimental details for the investigations of the Stokes parameters for light in chapter 5, and the Paschen-Back regime and optical isolation in chapter 6. This chapter is based on the article [27].

Chapter 5 Theory and experiment are compared for moderate magnetic fields as a function of number density and magnet separation. The Stokes parameters are derived for a circularly anisotropic medium. We compare experimental and theoretical Stokes parameters for off-resonant light transmitted through a high-density Rb vapour. The Poincaré representation is introduced and the evolution of the polarisation state of light as a function of detuning on the Poincaré sphere is shown. This chapter is based on the article [41].

Chapter 6 Absorption and dispersion in the hyperfine Paschen-Back regime is shown. We begin by measuring the evolution of the absolute optical depths as a function of field and detuning. We then compare

theory and experiment for the medium's absolute absorption and dispersive properties. The origin of the weak transitions is described in terms of the relative line-strength factors and transition frequencies. We finish by realising an optical isolator based on an atomic medium in the HPB regime. The theoretical and experimental rotation together with the characteristics for the isolator are shown in detail. This chapter is based on the articles [27] and [52].

Chapter 7 The methods of confocal microscopy and side imaging are outlined for investigating the cooperative enhancement of energy transfer in a high-density thermal vapour. The energy levels of Rb are shown and fluorescence spectra for both D lines is presented. We summarise the theoretical calculations for the potential energy curves, kinetic theory and enhancement in the electric field. Experimental measurements are shown for dependencies with number density. This chapter is based on the article [91].

Chapter 8 We draw our conclusions and give a brief outlook on the future of the work presented in this thesis.

1.7 Publications

During the preparation of work for this thesis the following papers have been published:

[22] L. Weller, R. J. Bettles, P. Siddons, C. S. Adams, and I. G. Hughes, *Absolute absorption on the rubidium D_1 line including resonant dipole-dipole interactions*, J. Phys. B: At. Mol. Opt. Phys. **44**, 195006 (2011), 10.1088/0953-4075/44/19/195006

[41] L. Weller, T. Dalton, P. Siddons, C. S. Adams, and I. G. Hughes, *Measuring the Stokes parameters for light transmitted by a high-density rubidium vapour in large magnetic fields*, J. Phys. B: At. Mol. Opt. Phys. **45**, 055001 (2012), 10.1088/0953-4075/45/5/055001

[52] L. Weller, K. S. Kleinbach, M. A. Zentile, S. Knappe, I. G. Hughes, and C. S. Adams, *Optical isolator using an atomic vapour in the hyperfine Paschen-Back regime*, Opt. Lett. **37**, 3405 (2012), 10.1364/OL.37.003405

[27] L. Weller, K. S. Kleinbach, M. A. Zentile, S. Knappe, C. S. Adams, and I. G. Hughes, *Absolute absorption and dispersion of a rubidium vapour in the hyperfine Paschen-Back regime*, J. Phys. B: At. Mol. Opt. Phys. **45**, 215005 (2012), 10.1088/0953-4075/45/21/215005

[91] L. Weller, R. J. Bettles, C. Vaillant, M. A. Zentile, R. M. Potvliege, C. S. Adams, and I. G. Hughes, *Cooperative enhancement of energy transfer in a high-density thermal vapour* in preparation.

1.8 Author contributions

L. Weller carried out most of the experiments, did most of the analysis and contributed to the writing of each paper. R. J. Bettles assisted with the experiment and numerical fitting for article one and did the theoretical calculations for article five. P. Siddons assisted with the experiment for article one and the theoretical calculations for article two. T. Dalton assisted with the experimental results of article two. K. S. Kleinbach assisted with the experiment and theoretical analysis for articles three and four. S. Knappe provided the microfabricated cell for articles three and four. M. A. Zentile assisted with the experiment and theoretical analysis for articles three, four and five. C. Vaillant did the theoretical calculations for article five. R. M. Potvliege contributed to the writing of article five. C. S. Adams contributed to the writing of each article and is the co-investigator for this project. I. G. Hughes contributed to the writing of each article and is the principal investigator for this project.

Part I

Absolute Absorption and Dispersion

Chapter 2

Model for the absolute susceptibility

This chapter closely relates to the following publication

P. Siddons, C. Ge, C. S. Adams, and I. G. Hughes, *Absolute absorption on rubidium D lines: comparison between theory and experiment*, J. Phys. B: At. Mol. Opt. Phys. **41**, 155004 (2008), 10.1088/0953-4075/41/15/155004

We study the Doppler-broadened absorption of a weak monochromatic probe beam in a thermal rubidium vapour cell on D lines. A detailed model of the susceptibility is developed which takes into account the absolute linestrengths of the allowed electric dipole transitions and the motion of the atoms parallel to the probe beam. All transitions from both hyperfine levels of the ground term of both isotopes are incorporated. The absorption and refractive index as a function of frequency are expressed in terms of the complementary error function. The absolute absorption profiles are compared with experiment, and are found to be in excellent agreement provided a sufficiently weak probe beam with an intensity under one-thousandth of the saturation intensity is used. The importance of hyperfine pumping for open transitions is discussed in the context of achieving the weak-probe limit. Theory and experiment show excellent agreement, with an rms error better than 0.2% for the D_2 line at 16.5 °C.

2.1 Introduction

In chapter 1 the motivation for the thesis was outlined. In chapter 2 we develop a model for the electric susceptibility, χ, that will allow us to make quantitative predictions for the absorptive and dispersive properties of a low-density Rb vapour probed in the vicinity of the D lines[1]. We start by calculating the susceptibility for an ensemble of two-level atoms. The lineshape is modeled as a Voigt profile, given by a convolution of the Lorentzian and Gaussian distributions. A matrix representation of the atomic Hamiltonian for Rb is then calculated in the completely uncoupled basis. A numerical diagonalisation of this representation allows one to calculate the frequency detunings and transition strengths of the D lines. The medium's susceptibility is calculated by summing over the electric-dipole-allowed transitions. From the total susceptibility, the refractive index and absorption coefficients are calculated. Measurements of the frequency dependence of the absolute Doppler-broadened transmission for the D_1 and D_2 lines are performed for temperatures up to 20.7°C and 20.9°C, showing excellent agreement with the theoretical model.

2.2 Susceptibility of a two-level atom

In section 2.2 we calculate the susceptibility for a two-level atom. We then show the optical-Bloch equations assuming the weak regime, before finally presenting the real and imaginary parts of the susceptibility.

2.2.1 Two-level atom

We start by considering a simple atom-light system. The atom is a closed two-level quantum system with ground state $|1\rangle$ and excited state $|2\rangle$ separated in energy by $\hbar\omega_0$, where ω_0 is the resonant frequency. The light has a classical electric field, $\hat{\mathcal{E}}$, with an angular frequency ω. The detuning of the light from the resonant frequency is given by $\Delta = \omega - \omega_0$. The strength of the

[1]For an alkali-metal atom the D_1 transition is $n^2S_{1/2} \rightarrow n^2P_{1/2}$, where n is the principal quantum number of the valence electron, and the D_2 transition is $n^2S_{1/2} \rightarrow n^2P_{3/2}$.

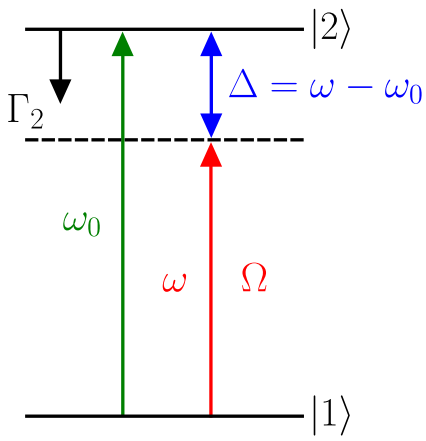

Figure 2.1: A two-level quantum system. The two levels are $|1\rangle$, the ground state, and $|2\rangle$, the excited state. The levels are separated by an energy $\hbar\omega_0$. The light field has angular frequency ω and Rabi frequency Ω (see equation 2.1). The detuning of the light from resonance is given by Δ. The excited state lifetime is Γ_2.

atom-light interaction is given by the Rabi frequency

$$\Omega = -\frac{\mu\mathcal{E}_0}{\hbar} \ , \tag{2.1}$$

where μ is the electric dipole operator and $\mathcal{E}_0$ is the total electric field. Dephasing from the excited state is given by the rate Γ_2 with all the population returning to the ground state. As this is a closed system no population is lost from the ground state, hence $\Gamma_1 = 0$. Figure 2.1 shows a schematic of the described two-level quantum system.

The density matrix formalism for a two-level atom is well known [93]. For the interaction Hamiltonian $-\mu\cdot\hat{\mathcal{E}}$ (this interaction will be discussed in depth in section 2.4.1) within the rotating wave approximation the optical-Bloch equations describing the evolution of both the coherence and populations of a two-level system are [94]

$$\dot{\tilde{\rho}}_{11} = \frac{\mathrm{i}\Omega}{2}(\tilde{\rho}_{12} - \tilde{\rho}_{21}) + \tilde{\rho}_{22}\Gamma_2 \ , \tag{2.2}$$

$$\dot{\tilde{\rho}}_{12} = \frac{\mathrm{i}\Omega}{2}(\tilde{\rho}_{11} - \tilde{\rho}_{22}) + \tilde{\rho}_{12}\left(-\mathrm{i}\Delta - \frac{\Gamma_2}{2}\right) \ , \tag{2.3}$$

$$\dot{\tilde{\rho}}_{21} = \frac{\mathrm{i}\Omega}{2}(\tilde{\rho}_{22} - \tilde{\rho}_{11}) + \tilde{\rho}_{21}\left(\mathrm{i}\Delta - \frac{\Gamma_2}{2}\right) \ , \tag{2.4}$$

$$\dot{\tilde{\rho}}_{22} = \frac{\mathrm{i}\Omega}{2}(\tilde{\rho}_{21} - \tilde{\rho}_{12}) - \tilde{\rho}_{22}\Gamma_2 \ , \tag{2.5}$$

where the slow variables are $\tilde{\rho}_{11} = \rho_{11}$, $\tilde{\rho}_{12} = \rho_{12}e^{-\mathrm{i}\omega t}$, $\tilde{\rho}_{21} = \rho_{21}e^{\mathrm{i}\omega t}$ and $\tilde{\rho}_{22} = \rho_{22}$. By setting the derivatives of slow variables to zero ($\dot{\tilde{\rho}}_{11} = \dot{\tilde{\rho}}_{12} = \dot{\tilde{\rho}}_{21} = \dot{\tilde{\rho}}_{22} = 0$) we obtain the steady-state solutions. In the case of a closed two-level quantum system where $\rho_{11} + \rho_{22} = 1$, $\dot{\tilde{\rho}}_{11} + \dot{\tilde{\rho}}_{22}$ must equal 0, comparing equations 2.2 and 2.5 we can see that this statement is true. In the weak excitation limit we set $\tilde{\rho}_{11} = 1$ and $\tilde{\rho}_{22} = 0$, therefore the steady-state solution for the coherence terms is

$$\tilde{\rho}^*_{12} = \tilde{\rho}_{21} = -\frac{\mathrm{i}\Omega/2}{\Gamma/2 - \mathrm{i}\Delta} \ , \tag{2.6}$$

here we set $\Gamma_2 = \Gamma$, as from now on we will only be considering the lifetime from the excited state. Now we have the steady-state solution for the coherences of an ensemble of closed two-level atoms interacting with a classical field. Next we relate the microscopic and macroscopic properties for such a system via the susceptibility.

2.2.2 The susceptibility

The optical-Bloch equations allow us to calculate the interaction between a single closed two-level atom and a classical light field. Here we show the relation between the microscopic theory of such a system to a macroscopic property of an ensemble of atoms. The absorptive and dispersive properties of the ensemble can be described from the susceptibility in the macroscopic properties of dielectrics. The response of a dielectric to a linear applied external field $\hat{\mathcal{E}}$ can be written as [94]

$$\hat{P} = \epsilon_0 \chi(\Delta) \hat{\mathcal{E}} \ , \tag{2.7}$$

where $\chi(\Delta)$ is the frequency dependent susceptibility that is also complex, the real and imaginary parts describe the dispersive and absorption properties, respectively. Substituting for the classical electric field in the dipole approximation, $\hat{\mathcal{E}} = \mathcal{E}_0 \cos(\omega t)$, the response becomes

$$\hat{P} = \frac{1}{2}\epsilon_0 \mathcal{E}_0 \left(\chi^*(\Delta)e^{\mathrm{i}\omega t} + \chi(\Delta)e^{-\mathrm{i}\omega t}\right) \ . \tag{2.8}$$

In an ensemble of $\mathcal{N}$ dipoles per unit volume, the macroscopic polarisation, $\hat{P}$, can be written as [94]

$$\hat{P} = \mathcal{N} \langle \hat{\mu} \rangle \ , \tag{2.9}$$

where $\langle\hat{\mu}\rangle$ is the expectation value of the dipole moment operator. The expectation value of any operator is given by the general result [95]

$$\langle\hat{\mu}\rangle = \mathrm{Tr}\left(\hat{\rho}\hat{\mu}\right) = \mu\left(\rho_{12} + \rho_{21}\right) \ , \tag{2.10}$$

where $\mu = \mu_{12} = \mu_{21}$. Using the slow variables from section 2.2.1 the macroscopic polarisation becomes

$$\hat{P} = \mathcal{N}\mu\left(\tilde{\rho}_{12}e^{\mathrm{i}\omega t} + \tilde{\rho}_{21}e^{-\mathrm{i}\omega t}\right) \ . \tag{2.11}$$

Taking both forms of the polarisation allows us to calculate the electric susceptibility for a two-level quantum ensemble.

$$\frac{1}{2}\epsilon_0\mathcal{E}_0\left(\chi^*(\Delta)e^{\mathrm{i}\omega t} + \chi(\Delta)e^{-\mathrm{i}\omega t}\right) = \mathcal{N}\mu\left(\tilde{\rho}_{12}e^{\mathrm{i}\omega t} + \tilde{\rho}_{21}e^{-\mathrm{i}\omega t}\right) \ , \tag{2.12}$$

equating coefficients of $e^{-\mathrm{i}\omega t}$ leads to

$$\chi(\Delta) = \frac{2\mathcal{N}\mu}{\epsilon_0\mathcal{E}_0}\tilde{\rho}_{21} \ . \tag{2.13}$$

Substituting for the steady-state solution to the coherence terms (see equation 2.6) and the Rabi frequency (see equation 2.1) gives

$$\chi(\Delta) = -\frac{\mathcal{N}\mu^2}{\hbar\epsilon_0}\frac{1}{\Delta + \mathrm{i}\Gamma/2} \ , \tag{2.14}$$

$$= -\frac{\mathcal{N}\mu^2}{\hbar\epsilon_0}f_\Gamma\left(\Delta\right) \ , \tag{2.15}$$

where $f_\Gamma\left(\Delta\right)$ is the lineshape factor. The real, $\chi_R(\Delta)$, and imaginary, $\chi_I(\Delta)$, parts of the steady-state susceptibility are

$$\chi_R(\Delta) = -\frac{\mathcal{N}\mu^2}{\hbar\epsilon_0}\frac{\Delta}{\Delta^2 + \Gamma^2/4} \ , \tag{2.16}$$

$$\chi_I(\Delta) = \frac{\mathcal{N}\mu^2}{\hbar\epsilon_0}\frac{\Gamma/2}{\Delta^2 + \Gamma^2/4} \ . \tag{2.17}$$

Next we discuss the lineshape factor in more detail.

2.3 Lineshape factor

In section 2.3 we discuss the derived lineshape factor $f_\Gamma\left(\Delta\right)$ and show that the imaginary part is Lorentzian in shape and the real part has the form of a dispersion profile. We also consider how the Gaussian distribution due to thermal motion is incorporated into the lineshape factor, before showing that a convolution of both dependencies leads to a Voigt lineshape.

2.3.1 Lorentzian and dispersion lineshapes

The imaginary component of the lineshape is an even function centred around resonance, before dropping off rapidly either side and eventually decaying to zero. This is known as a Lorentzian lineshape. The real component of the lineshape is an odd function centred around resonance, with a positive value below and a negative value above resonance. This is known as a dispersion lineshape. The spread of frequencies is due to the finite lifetime τ of the excited state. The full width at half maximum (FWHM) of a Lorentzian function is given by Γ. This linewidth is related to the lifetime by $\Gamma = 1/\tau$. The natural linewidth (FWHM) of a closed two-level atom can be written as [92]

$$\Gamma = \frac{\omega_0^3}{3\pi\hbar\epsilon_0 c^3}\frac{g_1}{g_2}\mu^2 \ , \tag{2.18}$$

where ω_0 is the resonant angular frequency, μ is the dipole matrix element and g_1 and g_2 are the degeneracies of the ground and excited state, respectively. For Rb the natural linewidths (FWHM) are $\Gamma = 2\pi \times 5.746$ MHz [96] and $\Gamma = 2\pi \times 6.065$ MHz [96] for the D_1 and D_2 lines, respectively. For a closed two level system, where $g_1 = g_2 = 1$, it is possible to rewrite the dipole moment in terms of the decay rate of the excited state as $\mu^2 = 3\pi\hbar\epsilon_0\Gamma k^{-3}$, where $k = 2\pi/\lambda$ is the wavevector. Substituting this dipole moment into the real (equation 2.16) and imaginary (equation 2.17) parts of the susceptibility gives

$$\chi_R(\Delta) = -3\pi\mathcal{N}\Gamma k^{-3}\frac{\Delta}{\Delta^2 + \Gamma^2/4} \ , \tag{2.19}$$

$$\chi_I(\Delta) = 3\pi\mathcal{N}\Gamma k^{-3}\frac{\Gamma/2}{\Delta^2 + \Gamma^2/4} \ . \tag{2.20}$$

On resonance, $\Delta = 0$, χ is purely imaginary with a magnitude $6\pi\mathcal{N}k^{-3}$; this is a dimensionless factor, $\chi_0 \equiv \chi_I(\Delta = 0)$, which allows us to determine the magnitude of the susceptibility. If we now define a dimensionless factor s as the ratio Δ/Γ, the susceptibility of the real and imaginary parts can be expressed as

$$\chi_R(s) = -\chi_0\frac{s}{2s^2 + 1/2} \ . \tag{2.21}$$

$$\chi_I(s) = \chi_0\frac{1}{4s^2 + 1} \ . \tag{2.22}$$

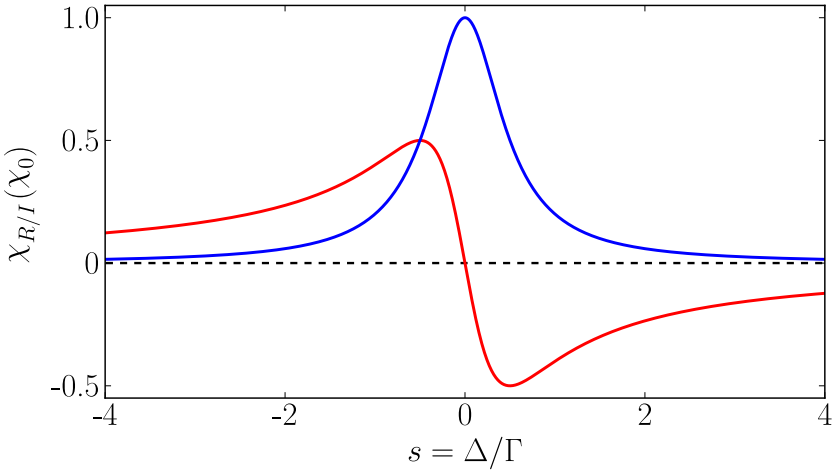

Figure 2.2: Normalised steady-state susceptibility in the weak excitation regime. The solid red (blue) line shows the real (imaginary) part of the susceptibility for an ensemble of two-level atoms.

In figure 2.2 we compare the real and imaginary parts of the susceptibility as a function of the dimensionless factor s. In chapter 5 we show that when $|\Delta| \gg \Gamma$ ($|s| \gg 1$) the real and imaginary parts reduce to $\chi_R \propto 1/\Delta$ and $\chi_I \propto 1/\Delta^2$, respectively. Therefore for large detunings dispersion effects dominate. In section 3.6.2 we show for large number densities the resonance imaginary susceptibility saturates to a constant value.

2.3.2 Gaussian lineshape

Atoms within a medium see a Doppler shift as a consequence of their thermal velocity. Along the z-axis of the beam, the probability, $P(v_z)\mathrm{d}v_z$, of an atom having a velocity, in the velocity group between v_z and $v_z + \mathrm{d}v_z$ is characterised by the well-known Maxwell-Boltzmann distribution [93]

$$P(v_z)\mathrm{d}v_z = \sqrt{\frac{m}{2\pi k_\mathrm{B} T}} \exp\left(-\frac{m v_z^2}{2k_\mathrm{B}T}\right) \mathrm{d}v_z \ , \tag{2.23}$$

where m is the atomic mass, k_B is the Boltzmann constant and T is the absolute temperature in Kelvin. This distribution is Gaussian in nature and has a 1/e width of $u = \sqrt{2k_\mathrm{B}T/m}$, such that

$$P(v_z)\mathrm{d}v_z = \sqrt{\frac{1}{\pi u^2}} \exp\left[-\left(\frac{v_z}{u}\right)^2\right] \mathrm{d}v_z \ . \tag{2.24}$$

Consider an atom with zero velocity that emits a photon of angular frequency ω_0. Now let the atom move along the same axis with a velocity v_z. Assuming the photon is emitted along this axis, the frequency, ω_0', seen by a stationary atom on the same axis is given by (see equation 15-34 in [97])

$$\omega_0' = \omega_0 \left(1 - \frac{v_z}{c}\right) \ . \tag{2.25}$$

Rearranging for the velocity v_z and substituting into equation 2.23, the following distribution centred on the resonant frequency, ω_0, can be obtained

$$\begin{aligned} P(\omega_0')\mathrm{d}\omega_0' &= \frac{c}{\omega_0}\sqrt{\frac{m}{2\pi k_\mathrm{B} T}} \exp\left[-\frac{mc^2}{2k_\mathrm{B}T\omega_0^2}\left(\omega_0' - \omega_0\right)^2\right] \mathrm{d}\omega_0' \ , \\ &= \frac{1}{ku}\sqrt{\frac{1}{\pi}} \exp\left[-\left(\frac{\omega_0' - \omega_0}{ku}\right)^2\right] \mathrm{d}\omega_0' \ . \end{aligned} \tag{2.26}$$

This Gaussian distribution has a FWHM of

$$\Delta\omega_\mathrm{D} = 2\sqrt{\ln 2}ku \ . \tag{2.27}$$

It is this motion along the z-axis which leads to Doppler broadening. Typically for room temperature (300°K) atoms, absorbing along the D_1 line ($\omega_0 = 2\pi \times$ 377.11 THz [98]) in ^{87}Rb (M = 86.91 amu), the FWHM is approximately $2\pi \times 500$ MHz, this is two orders of magnitude greater than the natural linewidth FWHM discussed in section 2.3.1. In chapter 3 we show for large number densities the self-broadening linewidth (FWHM) can be larger than the natural and Doppler broadened linewidths. To include the thermal motion in the lineshape factor, we start by substituting the angular frequency ω_L into equation 2.25 and then rewrite for the detuning Δ

$$\Delta' = \Delta - kv_z \ . \tag{2.28}$$

For an atomic vapour close to thermodynamic equilibrium (we assume the medium is illuminated by low light intensities) we can incorporate the Doppler effect for an atom moving along the direction of propagation of the beam by simply replacing the detuning in the lineshape factor (see equation 2.15) with the detuning described in equation 2.28, such that

$$\begin{aligned} \chi(\Delta - kv_z) &= -\frac{\mathcal{N}\mu^2}{\hbar\epsilon_0} f_\Gamma\left(\Delta - kv_z\right) \ , \\ &= -\frac{\mathcal{N}\mu^2}{\hbar\epsilon_0} \frac{1}{(\Delta - kv_z) + \mathrm{i}\Gamma/2} \ . \end{aligned} \tag{2.29}$$

Including both the modified susceptibility and the Gaussian distribution due to the longitudinal motion we can now derive the Voigt lineshape.

2.3.3 Voigt lineshape

The Voigt lineshape depends on two factors: the previously discussed Lorentzian and Gaussian lineshapes; and the strength, c^2, of a single transition. Here we include the strength of each transition as a prefactor in the generalised form of the susceptibility given by

$$\chi \;=\; c^2 \frac{\mathcal{N}\mu^2}{\hbar\epsilon_0} s\left(\Delta\right) \;, \tag{2.30}$$

where the Voigt lineshape, $s(\Delta)$, is the convolution of $f_\Gamma\left(\Delta - kv_z\right)$, the modified lineshape factor (see equation 2.29), and $P(v_z)$, the normalised Gaussian of longitudinal velocities (see equation 2.24). In the absence of magnetic field $c^2 = c^2_{m_F}$. The magnitude of $c^2_{m_F}$ will become apparent when we calculate the relative line-strengths for a Rb atom in section 2.5.1. Here we concentrate on the convolution integral given by

$$s(\Delta) = \int_{-\infty}^{+\infty} f_\Gamma\left(\Delta - kv_z\right) \times P(v_z)\mathrm{d}v_z \;. \tag{2.31}$$

To get this in the form of an integral we can use in the model, we substitute the dimensionless quantities, $y = \Delta/ku$, $x = v_z/u$ and $a = \Gamma/ku$ such that the convolution becomes

$$s(y) = \int_{-\infty}^{+\infty} f_a\left(y - x\right) \times P(x)\mathrm{d}x \;, \tag{2.32}$$

where $s(y)$ has units $(ku)^{-1}$ and $P(x)$ is normalised with a width of 1. The Voigt profile $s(y)$, is related to the Faddeeva function, $w(\mathrm{i}z)$ [99], via

$$s(y) = a\frac{\mathrm{i}\sqrt{\pi}}{\Gamma} w(\mathrm{i}z) \;. \tag{2.33}$$

This function of complex argument $z(y) = a/2 - \mathrm{i}y$, is given by

$$w(\mathrm{i}z) \;=\; \frac{\mathrm{i}}{\pi}\int_{-\infty}^{+\infty} \frac{e^{-x^2}}{\mathrm{i}z - x} dx = \exp(z^2)\mathrm{erfc}(z) \;, \tag{2.34}$$

where the complementary error function $\mathrm{erfc}(z)$ is defined as

$$\mathrm{erfc}(z) = \frac{2}{\sqrt{\pi}}\int_z^{+\infty} e^{-t^2}\mathrm{d}t \;. \tag{2.35}$$

The real and imaginary parts of the susceptibility can now be written in terms of the complementary error function. In summary, the Voigt lineshape

is given by a convolution of the Lorentzian and a Gaussian distribution incorporating the Doppler shift due to thermal motion. As this lineshape is identical for each transition of a particular isotope, we only need to calculate the Faddeeva function once in terms of these dimensionless quantities, y, x and a. Next we will determine the Hamiltonian for a many-level atom, which will allow us to calculate the relative line-strengths and consequently the magnitude of $c_{m_F}^2$.

2.4 Hamiltonian for a many-level atom

In section 2.4 we calculate the total atomic Hamiltonian for Rb. We have already defined the susceptibility for a closed two-level atom including the Doppler shift due to the thermal motion. Here we describe how the atomic structure arises and how we model such a system in the weak regime. Finally we show that a many level atom such as Rb, can be thought of as several closed two-level systems with different transition strengths.

2.4.1 Atomic structure

Fine structure $\hat{H}_{\text{fs}}$

Fine structure is the result of the spin angular momentum, S, coupling to the orbital angular momentum, L, of an electron via the spin-orbit interaction. The fine structure Hamiltonian, $\hat{H}_{\text{fs}}$, is (see equation 8.102 in [100])

$$\hat{H}_{\text{fs}} = \frac{\gamma_{\text{fs}}}{\hbar^2}\hat{L}\cdot\hat{S}\ , \tag{2.36}$$

where γ_{fs} is the spin-orbit constant. This interaction causes L and S to change, so that neither the electron orbital projection m_L nor the electron spin projection m_S remains constant. Here we introduce the quantum number that describes the total angular momentum, $J = L + S$, both J and its m_J projection remain constant. The eigenstates of the fine structure Hamiltonian are $|J, m_J\rangle$. Calculating the expectation value of $\left\langle \hat{H}_{\text{fs}} \right\rangle$ gives the eigenenergies

$$\text{E}_{\text{fs}} = \frac{\gamma_{\text{fs}}}{2}\left[J(J+1) - L(L+1) - S(S+1)\right]\ . \tag{2.37}$$

Term states, $n^{2S+1}L_J$, are specified by the quantum numbers n, L, S and J. For the ground term in ^{85}Rb and ^{87}Rb, $L = 0$ and $S = 1/2$, so $J = 1/2$; this gives rise to a $5^2S_{1/2}$ ground term. There is no fine structure splitting for $L = 0$ therefore the Hamiltonian, $\hat{H}_{\rm fs}$, is equal to 0. For the first excited 5P term, $L = 1$ and $S = 1/2$, so $J = 1/2$ or $J = 3/2$; this gives rise to the $5^2P_{1/2}$ and the $5^2P_{3/2}$ excited terms, respectively. The fine structure Hamiltonian, $\hat{H}_{\rm fs}$, is equal to $-\gamma_{\rm fs}$ and $\gamma_{\rm fs}/2$ (see appendix B.1) for $5^2P_{1/2}$ and $5^2P_{3/2}$ terms, respectively, where $\gamma_{\rm fs}/h$ (in THz) is 4.75.

The value of J determines the shift in energy of any particular terms, hence the 5S $\rightarrow$ 5P transition is split into two components. The D_1 line ($5^2S_{1/2} \rightarrow 5^2P_{1/2}$) and the D_2 line ($5^2S_{1/2} \rightarrow 5^2P_{3/2}$) transitions are the components of a fine-structure doublet. The D_1 transition has half the strength of the D_2 transition. This ratio arises because the strength of each component is proportional to the statistical weight of the levels $m_J = 2J + 1$. The centre of mass frequency for ^{85}Rb and ^{87}Rb on the D_1 and D_2 lines are 377.11 THz [101] and 384.23 THz [102], respectively. In the matrix representation these frequencies will correspond to zero detuning.

Hyperfine structure $\hat{H}_{\rm hfs}$

The hyperfine structure Hamiltonian, $\hat{H}_{\rm hfs}$, includes the effects of the magnetic dipole interaction, $\hat{H}_{\rm d}$ and electric quadrupole interaction $\hat{H}_{\rm q}$

$$\hat{H}_{\rm hfs} = \hat{H}_{\rm d} + \hat{H}_{\rm q} \ . \tag{2.38}$$

The magnetic dipole interaction between the nuclear dipole moment, μ_I, and the magnetic field, B_e, produced by the orbiting electrons is $\hat{H}_{\rm d} = -\mu_I \cdot B_e$, μ_I is related to the nuclear spin I by $\mu_I = g_I \mu_N \hat{I}/\hbar$, where g_I is the nuclear g-factor and μ_N is the nuclear magneton given in terms of the Bohr magneton, μ_B [100]

$$\mu_N = \mu_B \frac{m_e}{M_p} \approx \frac{\mu_B}{1840} \ . \tag{2.39}$$

As the magnetic field is produced by the motion of the atomic electrons i.e. their total angular momentum J, it has been shown that [103]

$$\hat{H}_{\rm d} = \frac{A_{\rm hfs}}{\hbar^2} \hat{I} \cdot \hat{J} \ , \tag{2.40}$$

where A_{hfs} is the magnetic dipole constant. This interaction has the largest contribution to the hyperfine structure Hamiltonian. The weaker electric quadrupole interaction is the result of the finite nuclear charge distribution and the electrostatic interaction between the protons and electrons. It has been shown that the electric quadrupole Hamiltonian can be written as [103]

$$\hat{H}_{\text{q}} = \frac{B_{\text{hfs}}}{2\hat{I}(2\hat{I}-1)\hat{J}(2\hat{J}-1)\hbar^2}\left[3(\hat{I}\cdot\hat{J})^2 + \frac{3}{2}(\hat{I}\cdot\hat{J}) - \hat{I}(\hat{I}+1)\hat{J}(\hat{J}+1)\right] , \tag{2.41}$$

where B_{hfs} is the electric quadrupole constant. The electric quadrupole Hamiltonian is zero for $I = 0$ or $1/2$ and $J = 0$ or $1/2$. Here we introduce the total angular momentum of the atom $F = I + J$. In analogy to the fine structure interaction, the hyperfine interaction causes I and J to change yet F to remain constant. Therefore the nuclear spin projection m_I and the total angular projection m_J are no longer good quantum numbers and instead the total angular momentum F and the projection m_F are a better description. The eigenstates of the hyperfine structure Hamiltonian are $|F, m_F\rangle$. The expectation value of $\left\langle \hat{H}_{\text{hfs}} \right\rangle$ gives the eigenenergies associated with the hyperfine interaction Hamiltonian

$$\Delta \text{E}_{\text{hfs}} = \frac{A_{\text{hfs}}}{2}K + \frac{B_{\text{hfs}}}{4}\frac{\frac{3}{2}K(K+1) - 2I(I+1)J(J+1)}{I(2I-1)J(2J-1)} , \tag{2.42}$$

where $K = F(F+1) - I(I+1) - J(J+1)$; see equation 9.60 in [104]. The constants A_{hfs} and B_{hfs} can be found in table 2.1 and the numerical values to this expression can be found in figure 2.3. In summary, for the $5^2\text{S}_{1/2}$ term of ^{87}Rb ($I = 3/2$), F can be 1 or 2 with a hyperfine splitting of 6.8 GHz, for the $5^2\text{P}_{1/2}$ term, F' can be 1, 2 with a hyperfine splitting of 810 MHz and for $5^2\text{P}_{3/2}$ term, F' can be 0, 1, 2 or 3 with hyperfine splittings between 70 and 270 MHz. For the $5^2\text{S}_{1/2}$ term of ^{85}Rb ($I = 5/2$), F can be 2 or 3 with a hyperfine splitting of 3.0 GHz, for the $5^2\text{P}_{1/2}$ term, F' can be 2, 3 with a hyperfine splitting of 360 MHz and for $5^2\text{P}_{3/2}$ term, F' can be 1, 2, 3 or 4 with hyperfine splittings between 30 and 120 MHz.

Table 2.2 shows a summary of the useful results for the fine structure, $\hat{H}_{\text{fs}}$ and hyperfine structure, $\hat{H}_{\text{hfs}}$ interactions. In figure 2.3 the fine structure, hyperfine structure and intervals for both isotopes are illustrated.

Isotope	Term	A_{hfs}/h (MHz)	B_{hfs}/h (MHz)
^{85}Rb	$5^2\mathrm{S}_{1/2}$	1011.91	-
	$5^2\mathrm{P}_{1/2}$	120.53	-
	$5^2\mathrm{P}_{3/2}$	25.04	26.01
^{87}Rb	$5^2\mathrm{S}_{1/2}$	3417.34	-
	$5^2\mathrm{P}_{1/2}$	407.24	-
	$5^2\mathrm{P}_{3/2}$	84.72	12.50

Table 2.1: The magnetic dipole constants, A_{hfs}, and electric quadrupole constants, B_{hfs}, for the $5^2\mathrm{S}_{1/2}, 5^2\mathrm{P}_{1/2}$ and $5^2\mathrm{P}_{3/2}$ terms of ^{85}Rb and ^{87}Rb. These constants were obtained from [102].

	Fine Structure $\hat{H}_{\mathrm{fs}}$	Hyperfine Structure $\hat{H}_{\mathrm{hfs}}$
Dominant interaction	$\frac{\gamma_{\mathrm{fs}}}{\hbar^2}\hat{L}\cdot\hat{S}$	$\frac{A_{\mathrm{hfs}}}{\hbar^2}\hat{I}\cdot\hat{J}$
Total angular momentum	$J = L + S$	$F = I + J$
Projection	$m_J = 2J + 1$	$m_F = 2F + 1$
Eigenstates	$\lvert J, m_J\rangle$	$\lvert F, m_F\rangle$
Eigenenergies	$\frac{\gamma_{\mathrm{fs}}}{2}\left[J(J+1) - L(L+1) - S(S+1)\right]$	$\frac{A_{\mathrm{hfs}}}{2}\left[F(F+1) - I(I+1) - J(J+1)\right]$
Intervals	$E_J - E_{J-1} = \gamma_{\mathrm{fs}} J$	$E_F - E_{F-1} = A_{\mathrm{hfs}} F$

Table 2.2: The analogy between the fine structure Hamiltonian, $\hat{H}_{\mathrm{fs}}$, in the $L-S$ coupling scheme and the hyperfine structure Hamiltonian, $\hat{H}_{\mathrm{hfs}}$, in the $I-J$ coupling scheme.

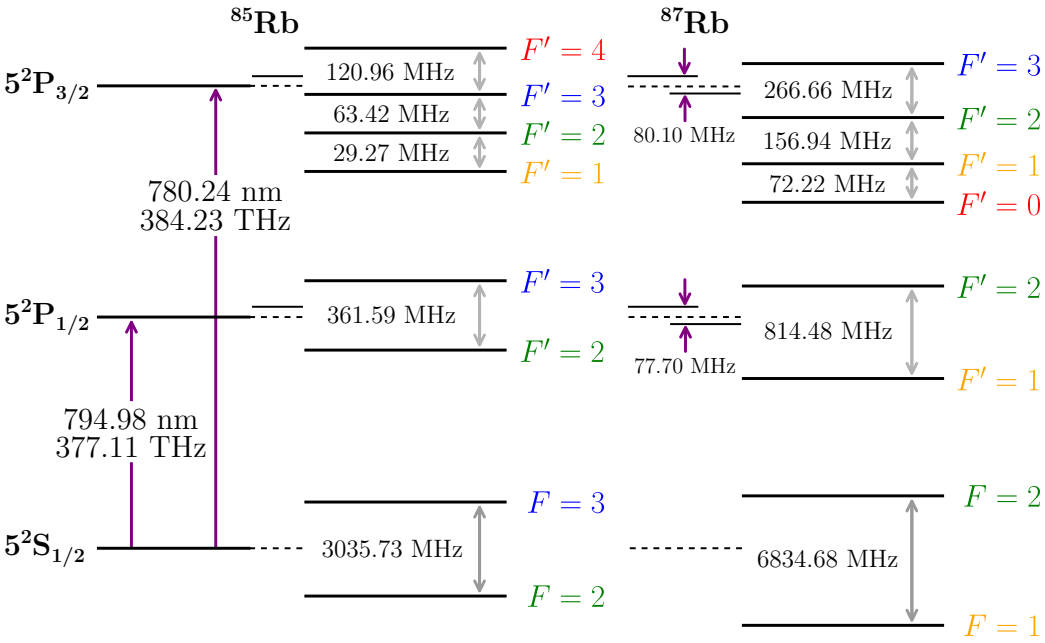

Figure 2.3: The hyperfine structure and intervals of ^{85}Rb and ^{87}Rb for the D_1 ($5^2S_{1/2} \rightarrow 5^2P_{1/2}$) and D_2 ($5^2S_{1/2} \rightarrow 5^2P_{3/2}$) lines. Due to the isotope shift, the $5^2P_{1/2}$ ($5^2P_{3/2}$) state in ^{85}Rb and ^{87}Rb is offset by 77.70(80.10) MHz, this is important when calculating the transition frequencies.

Interaction Hamiltonian

The interaction Hamiltonian for electric dipole transitions is described in terms of the dipole operator $-\hat{\mu}\cdot\hat{\mathcal{E}} = e\hat{r}\cdot\hat{\mathcal{E}}$ [100]. First we find it convenient to expand the classical light field, $\hat{\mathcal{E}}$, into its spherical components. In terms of the Cartesian components we write [105]

$$\hat{\mathcal{E}} = \begin{pmatrix} \mathcal{E}_L \\ \mathcal{E}_R \\ \mathcal{E}_0 \end{pmatrix} = \frac{1}{\sqrt{2}} \begin{pmatrix} -1 & -\mathrm{i} & 0 \\ 1 & -\mathrm{i} & 0 \\ 0 & 0 & \sqrt{2} \end{pmatrix} \cdot \begin{pmatrix} \mathcal{E}_x \\ \mathcal{E}_y \\ \mathcal{E}_z \end{pmatrix} . \tag{2.43}$$

The advantage of this decomposition is that the components $\mathcal{E}_L$ and $\mathcal{E}_R$ can be used in section 5.3.1 to help define the Stokes parameters for a circularly anisotropic medium. By convention [106], a $\mathcal{E}_L$ polarised wave rotates anti-clockwise around the axis, when viewed from the positive z-axis; and a $\mathcal{E}_R$ polarised wave rotates clockwise. Here we state that left circularly polarised light drives σ^+ transitions and right circularly polarised light drives σ^- transitions [105]. As wavefunctions are usually expressed in terms of spherical

polar coordinates, here we also find it convenient to expand the dipole operator in terms of its components in a similar basis. The dipole operator can be decomposed into the operators $C_{L,R,0}$, corresponding to σ^+, σ^- and π transitions, respectively. These operators can be written as (see equation 5.17 in [103])

$$\hat{\mu} = -e\hat{r} \quad = \quad -er\left(C_L + C_R + C_0\right) \ . \tag{2.44}$$

These operators are related to the spherical harmonics by $C_{L,R,0} = \sqrt{4\pi/3}Y_1^q$, where $q = -1$, $+1$ and 0 for L, R and 0, respectively. Next we consider the dipole matrix elements $\langle F, m_F|e\hat{r}|F', m_{F'}\rangle$ that describe the interaction between an atom and near-resonant electromagnetic radiation. The power of the Wigner-Eckart theorem [107] is that we can separate the dipole matrix elements into a reduced matrix element $\langle L \,\|er\|\, L'\rangle = d$ (see equation 5 in [92]) and an angular coupling element $\langle F, m_F|C_{L,R,0}|F', m_{F'}\rangle$ which we can calculate. In section 2.4.2 we write the coupled basis in terms of the completely uncoupled basis. Before we calculate the angular coupling part from the matrix representation we must consider the electric-dipole selection rules for transitions between states $|L\rangle$ and $|L'\rangle$, and $|m_L, m_S, m_I\rangle$ and $|m_{L'}, m_{S'}, m_{I'}\rangle$. Firstly, the interaction with the classical light field must conserve parity. As the operator $e\hat{r}$ has odd parity, the electromagnetic radiation must connect dipole matrix elements of opposite parity for it to be conserved. As we are only considering the interaction between S and P terms, there is always an odd change in the orbital angular momentum quantum number, with ΔL being ± 1. Secondly, depending on the polarisation of the light Δm_L must always be 0 or ± 1. Finally, the electron spin projection, m_S and nuclear spin projection m_I of the wavefunction must remain unchanged. The calculation for the angular coupling elements follows as

$$\begin{aligned}
&= \langle m_L, m_S, m_I|\, C_L \,|m_{L'} = m_L + 1, m_{S'}, m_{I'}\rangle \ , \\
&= \langle m_L, m_S, m_I|\, C_R \,|m_{L'} = m_L - 1, m_{S'}, m_{I'}\rangle \ , \\
&= \langle m_L, m_S, m_I|\, C_0 \,|m_{L'} = m_L, m_{S'}, m_{I'}\rangle \ , \\
&= c_{L,R,0} = c_{m_F} \ ,
\end{aligned} \tag{2.45}$$

where $c_{L,R,0}$ are the transition strength coefficients and in the absence of field are c_{m_F}. The strength of a transition is proportional to the square

of the transition strength coefficients, $c^2_{m_F}$. For each hyperfine transition $F \to F'$ the total transition strength, C^2_F, is denoted by the sum of transition strengths, $c^2_{m_F}$, of each $m_F \to m_{F'}$ transition in the hyperfine manifold. In section 2.4.2 we separate the angular coupling elements into the coupled ground states $\langle F, m_F|$ and the operator C_R acting on the coupled excited states $|F', m_{F'}\rangle$. Finally in section 2.5.1 we show how the total transition strengths are calculated from these two separate elements.

2.4.2 Matrix representation

The following section details the calculations of a matrix representation of the atomic Hamiltonian. The eigenenergies are calculated from a numerical diagonalisation of the matrix in the completely uncoupled $|m_L, m_S, m_I\rangle$ basis. The states are labeled according to the electron orbital angular momentum, m_L, electron spin angular momentum, m_S and nuclear spin angular momentum, m_I. The atomic Hamiltonian is written as

$$\hat{H} = \hat{H}_0 + \hat{H}_{\text{fs}} + \hat{H}_{\text{hfs}} \ , \tag{2.46}$$

where $\hat{H}_0$ is the coarse atomic structure; $\hat{H}_{\text{fs}}$ and $\hat{H}_{\text{hfs}}$ describes the fine and hyperfine structures. Here we take the example of the D_1 ($5^2S_{1/2} \to 5^2P_{1/2}$) line for ^{87}Rb ($I = 3/2$), as both the $5^2S_{1/2}$ and $5^2P_{1/2}$ terms give analytic solutions for eigenvalues and eigenfunctions. For the $5^2P_{3/2}$ term the calculation must be done numerically. We start by populating the $5^2S_{1/2}$ matrix and diagonalisation gives a list of eigenvalues and corresponding eigenvectors in the uncoupled basis. We then calculate the whole 5P matrix. Numerical diagonalisation allows one to separate the $5^2P_{1/2}$ and $5^2P_{3/2}$ terms[2]. Each nl term has a degeneracy of $D_{nl} = (2L+1)(2S+1)(2I+1)$, with a matrix of dimension $D_{nl} \times D_{nl}$. To simplify the calculation further we only consider the operator C_R acting on the excited uncoupled basis. The motivation for this is that in all the experiments in this thesis the quantisation axis of the magnetic field and wavevector of the laser are parallel, therefore the electric field drives linear combinations of σ^+ and σ^- transitions. After calculating

[2]The magnetic field interaction described in chapter 4 lifts the degeneracy of each hyperfine state allowing one to sort the whole matrix ensuring that the $5^2P_{1/2}$ and $5^2P_{3/2}$ terms can be separated.

the σ^- transitions the σ^+ transitions can be obtained from symmetry. No π transitions are driven in this thesis however for completeness the calculations for these transitions can be found in appendix B.3.

$5^2S_{1/2}$ matrix

For the $5^2S_{1/2}$ term a matrix of dimensions 8×8 is required. The coarse and fine structure Hamiltonians are zero, therefore the atomic Hamiltonian for the $5^2S_{1/2}$ term can be written as

$$\hat{H} = \frac{A_{\text{hfs}}}{\hbar^2} \hat{I} \cdot \hat{J} \ . \tag{2.47}$$

The $5^2S_{1/2}$ matrix for ^{87}Rb is populated as follows (see appendix B)

$$\hat{H} = A_{\text{hfs}} \begin{pmatrix} \frac{3}{4} & 0 & 0 & 0 & 0 & 0 & 0 & 0 \\ 0 & \frac{1}{4} & 0 & 0 & \frac{\sqrt{3}}{2} & 0 & 0 & 0 \\ 0 & 0 & -\frac{1}{4} & 0 & 0 & 1 & 0 & 0 \\ 0 & 0 & 0 & -\frac{3}{4} & 0 & 0 & \frac{\sqrt{3}}{2} & 0 \\ 0 & \frac{\sqrt{3}}{2} & 0 & 0 & -\frac{3}{4} & 0 & 0 & 0 \\ 0 & 0 & 1 & 0 & 0 & -\frac{1}{4} & 0 & 0 \\ 0 & 0 & 0 & \frac{\sqrt{3}}{2} & 0 & 0 & \frac{1}{4} & 0 \\ 0 & 0 & 0 & 0 & 0 & 0 & 0 & \frac{3}{4} \end{pmatrix} , \tag{2.48}$$

where A_{hfs} can be obtained from table 2.1. Analytic diagonlisation of this $\hat{I} \cdot \hat{J}$ matrix gives three eigenvalues with $-\frac{5}{4}$ and five eigenvalues with $\frac{3}{4}$. These two different values are the hyperfine ground states $F = 1$ and $F = 2$ with 3 and 5 m_F values, respectively. The corresponding eigenvectors are

$$A_{\text{hfs}} \left(\begin{array}{c|cccccccc} -\frac{5}{4} & 0 & \frac{1}{2} & 0 & 0 & -\sqrt{\frac{3}{4}} & 0 & 0 & 0 \\ -\frac{5}{4} & 0 & 0 & \sqrt{\frac{1}{2}} & 0 & 0 & -\sqrt{\frac{1}{2}} & 0 & 0 \\ -\frac{5}{4} & 0 & 0 & 0 & -\sqrt{\frac{3}{4}} & 0 & 0 & \frac{1}{2} & 0 \\ \hline \frac{3}{4} & 0 & 0 & 0 & 0 & 0 & 0 & 0 & 1 \\ \frac{3}{4} & 0 & 0 & 0 & \frac{1}{2} & 0 & 0 & \sqrt{\frac{3}{4}} & 0 \\ \frac{3}{4} & 0 & 0 & \sqrt{\frac{1}{2}} & 0 & 0 & \sqrt{\frac{1}{2}} & 0 & 0 \\ \frac{3}{4} & 0 & -\sqrt{\frac{3}{4}} & 0 & 0 & -\frac{1}{2} & 0 & 0 & 0 \\ \frac{3}{4} & 1 & 0 & 0 & 0 & 0 & 0 & 0 & 0 \end{array} \right) . \tag{2.49}$$

Now we choose to write the hyperfine states $|F, m_F\rangle$ in the coupled basis as a linear combination of the states $|m_L, m_S, m_I\rangle$ in the uncoupled basis. Two basis sets of orthonormal eigenfunctions can be related by a unitary transformation [100].

$$\begin{aligned} |F, m_F\rangle &= \sum_{m_L=-L}^{L} \sum_{m_S=-S}^{S} \sum_{m_I=-I}^{I} \langle m_L, m_S, m_I | F, m_F\rangle \, |m_L, m_S, m_I\rangle \ , \\ |F, m_F\rangle &= T^F_{LSI} \cdot |m_L, m_S, m_I\rangle \ , \end{aligned} \tag{2.50}$$

where $\langle m_L, m_S, m_I | F, m_F\rangle$ are the Clebsch-Gordan coefficients and T^F_{LSI} is the transformation matrix from the F basis into the L, S, I basis. The $|F, m_F\rangle$ basis is ordered as follows

$$\begin{aligned} |F, m_F\rangle = \quad & |1, +1\rangle \, ; |1, +0\rangle \, ; |1, -1\rangle \, ; \\ & |2, -2\rangle \, ; |2, -1\rangle \, ; |2, +0\rangle \, ; |2, +1\rangle \, ; |2, +2\rangle \ . \end{aligned} \tag{2.51}$$

The $|m_L, m_S, m_I\rangle$ basis is ordered as follows

$$\begin{aligned} |m_L, m_S, m_I\rangle = \quad & \left|0, +\frac{1}{2}, +\frac{3}{2}\right\rangle ; \left|0, +\frac{1}{2}, +\frac{1}{2}\right\rangle ; \left|0, +\frac{1}{2}, -\frac{1}{2}\right\rangle ; \left|0, +\frac{1}{2}, -\frac{3}{2}\right\rangle ; \\ & \left|0, -\frac{1}{2}, +\frac{3}{2}\right\rangle ; \left|0, -\frac{1}{2}, +\frac{1}{2}\right\rangle ; \left|0, -\frac{1}{2}, -\frac{1}{2}\right\rangle ; \left|0, -\frac{1}{2}, -\frac{3}{2}\right\rangle \ . \end{aligned} \tag{2.52}$$

The transformation matrix for the $5^2\mathrm{S}_{1/2}$ term is

$$T^F_{LSI} = \begin{pmatrix} 0 & \frac{1}{2} & 0 & 0 & -\sqrt{\frac{3}{4}} & 0 & 0 & 0 \\ 0 & 0 & \sqrt{\frac{1}{2}} & 0 & 0 & -\sqrt{\frac{1}{2}} & 0 & 0 \\ 0 & 0 & 0 & -\sqrt{\frac{3}{4}} & 0 & 0 & \frac{1}{2} & 0 \\ 0 & 0 & 0 & 0 & 0 & 0 & 0 & 1 \\ 0 & 0 & 0 & \frac{1}{2} & 0 & 0 & \sqrt{\frac{3}{4}} & 0 \\ 0 & 0 & \sqrt{\frac{1}{2}} & 0 & 0 & \sqrt{\frac{1}{2}} & 0 & 0 \\ 0 & -\sqrt{\frac{3}{4}} & 0 & 0 & -\frac{1}{2} & 0 & 0 & 0 \\ 1 & 0 & 0 & 0 & 0 & 0 & 0 & 0 \end{pmatrix} . \tag{2.53}$$

Decomposing the $|F, m_F\rangle$ states into the $|m_L, m_S, m_I\rangle$ basis and Clebsch-Gordan coefficients gives

$$|1,+1\rangle = \frac{1}{2}\left|0,+\frac{1}{2},+\frac{1}{2}\right\rangle - \sqrt{\frac{3}{4}}\left|0,-\frac{1}{2},+\frac{3}{2}\right\rangle , \tag{2.54}$$

$$|1,+0\rangle = \sqrt{\frac{1}{2}}\left|0,+\frac{1}{2},-\frac{1}{2}\right\rangle - \sqrt{\frac{1}{2}}\left|0,-\frac{1}{2},+\frac{1}{2}\right\rangle , \tag{2.55}$$

$$|1,-1\rangle = -\sqrt{\frac{3}{4}}\left|0,+\frac{1}{2},-\frac{3}{2}\right\rangle + \frac{1}{2}\left|0,-\frac{1}{2},-\frac{1}{2}\right\rangle , \tag{2.56}$$

$$|2,-2\rangle = \left|0,-\frac{1}{2},-\frac{3}{2}\right\rangle , \tag{2.57}$$

$$|2,-1\rangle = \frac{1}{2}\left|0,+\frac{1}{2},-\frac{3}{2}\right\rangle + \sqrt{\frac{3}{4}}\left|0,-\frac{1}{2},-\frac{1}{2}\right\rangle , \tag{2.58}$$

$$|2,+0\rangle = \sqrt{\frac{1}{2}}\left|0,+\frac{1}{2},-\frac{1}{2}\right\rangle + \sqrt{\frac{1}{2}}\left|0,-\frac{1}{2},+\frac{1}{2}\right\rangle , \tag{2.59}$$

$$|2,+1\rangle = -\sqrt{\frac{3}{4}}\left|0,+\frac{1}{2},+\frac{1}{2}\right\rangle - \frac{1}{2}\left|0,-\frac{1}{2},+\frac{3}{2}\right\rangle , \tag{2.60}$$

$$|2,+2\rangle = \left|0,+\frac{1}{2},+\frac{3}{2}\right\rangle . \tag{2.61}$$

Now we have written the hyperfine ground states for the $5^2S_{1/2}$ term, next we calculate the operator C_R acting on the hyperfine excited states for the $5^2P_{1/2}$ term.

$5^2\mathbf{P}_{1/2}$ matrix

For the 5P term a matrix of dimensions 24×24 is required. The atomic Hamiltonian including fine structure is

$$\begin{aligned}\hat{H} = \quad & \frac{\gamma_{\rm fs}}{\hbar^2}\hat{L}\cdot\hat{S} + \frac{A_{\rm hfs}}{\hbar^2}\hat{I}\cdot\hat{J} \\ & + \frac{B_{\rm hfs}}{2\hat{I}(2\hat{I}-1)\hat{J}(2\hat{J}-1)\hbar^2}\left[3(\hat{I}\cdot\hat{J})^2 + \frac{3}{2}(\hat{I}\cdot\hat{J}) - \hat{I}(\hat{I}+1)\hat{J}(\hat{J}+1)\right] .\end{aligned} \tag{2.62}$$

As we are only interested in $5^2P_{1/2}$, the last term in this Hamiltonian can be ignored as the electric quadrupole constant is zero. Here we introduce an additional Hamiltonian that allows for the centre of mass frequency of the D_1 line to correspond to zero detuning about which the hyperfine interaction is important. In section 2.4.1 and appendix B.1 we showed the fine structure

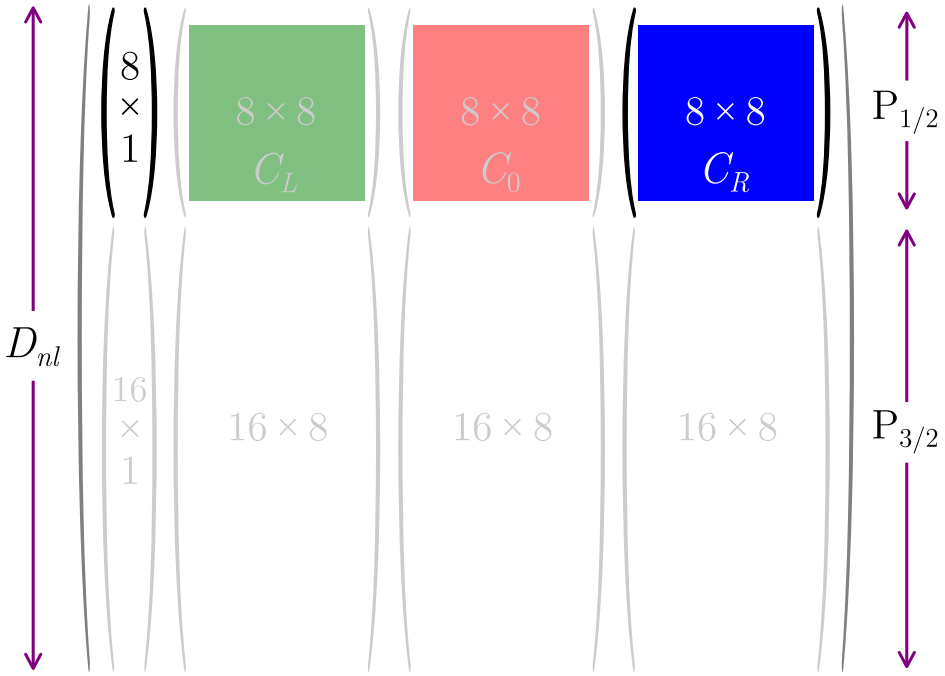

Figure 2.4: A matrix of dimensions 24×24 for the 5P term of Rb. The matrix is sorted by the addition of a single column of 24 rows for the eigenvalues for each state. The first 8 rows correspond to the $5^2P_{1/2}$ term and the final 16 rows correspond to the $5^2P_{3/2}$ term. Columns 2 - 9, 10 - 17 and 18 - 25 hold the elements for the operators C_L, C_0 and C_R acting on the uncoupled basis, respectively.

splittings for the $5^2P_{1/2}$ and $5^2P_{3/2}$ terms to be $-\gamma_{\rm fs}$ and $\gamma_{\rm fs}/2$, respectively. For the $5^2P_{1/2}$ term the modified atomic Hamiltonian can be written as

$$\hat{H} \;=\; \frac{\gamma_{\rm fs}}{\hbar^2}\hat{L}\cdot\hat{S} + 2\frac{\gamma_{\rm fs}}{\hbar^2} \;\otimes\; \mathbb{1}_{D_{nl}} + \frac{A_{\rm hfs}}{\hbar^2}\hat{I}\cdot\hat{J}\;. \tag{2.63}$$

where $\mathbb{1}_{D_{nl}}$ is an identity matrix with dimensions $D_{nl} \times D_{nl}$. Alternatively if we wanted to address the $5^2P_{3/2}$ term instead, we would introduce the additional Hamiltonian $-\gamma_{\rm fs}/\hbar^2 \;\otimes\; \mathbb{1}_{D_{nl}}$.

Figure 2.4 shows a schematic of the eigenvalues and corresponding eigenvectors calculated from the diagonalisation of the populated 5P matrix. Column 1 is arranged such that the first 8 eigenvalues correspond to the $5^2P_{1/2}$ term and the final 16 eigenvalues correspond to the $5^2P_{3/2}$ term. Columns 2 - 25 correspond to the eigenvectors for each hyperfine state. As before, each state in the coupled basis can be written as a linear combination of the states in the uncoupled basis, however to simplify the calculation we take the operator C_R acting on the $|F', m_{F'}\rangle$ excited states which are listed in columns 18 - 25.

In summary, we therefore take the first 8 rows and the final 8 columns. This sub-matrix for the $5^2\mathrm{P}_{1/2}$ term is

$$A_{\mathrm{hfs}} \left(\begin{array}{c|cccccccc} -\frac{5}{4} & -\sqrt{\frac{1}{2}} & 0 & 0 & 0 & 0 & 0 & 0 & 0 \\ -\frac{5}{4} & 0 & -\sqrt{\frac{1}{3}} & 0 & 0 & 0 & 0 & 0 & 0 \\ -\frac{5}{4} & 0 & 0 & -\sqrt{\frac{1}{6}} & 0 & 0 & 0 & 0 & 0 \\ \hline \frac{3}{4} & 0 & 0 & 0 & \sqrt{\frac{2}{3}} & 0 & 0 & 0 & 0 \\ \frac{3}{4} & 0 & 0 & -\sqrt{\frac{1}{2}} & 0 & 0 & 0 & 0 & 0 \\ \frac{3}{4} & 0 & -\sqrt{\frac{1}{3}} & 0 & 0 & 0 & 0 & 0 & 0 \\ \frac{3}{4} & \sqrt{\frac{1}{6}} & 0 & 0 & 0 & 0 & 0 & 0 & 0 \\ \frac{3}{4} & 0 & 0 & 0 & 0 & 0 & 0 & 0 & 0 \end{array}\right) \tag{2.64}$$

where the eignevalues of the $5^2\mathrm{P}_{1/2}$ matrix correspond to the hyperfine excited states $F' = 1$ and $F' = 2$ with 3 and 5 $m_{F'}$ values, respectively. For the $5^2\mathrm{P}_{1/2}$ term the $|F', m_{F'}\rangle$ basis is ordered as follows

$$\begin{aligned} |F', m_{F'}\rangle = \quad & |1,+1\rangle\,; |1,+0\rangle\,; |1,-1\rangle\,; \\ & |2,-2\rangle\,; |2,-1\rangle\,; |2,+0\rangle\,; |2,+1\rangle\,; |2,+2\rangle \ . \end{aligned} \tag{2.65}$$

The $|m_{L'}, m_{S'}, m_{I'}\rangle$ basis is ordered as follows

$$\begin{aligned} |m_{L'}, m_{S'}, m_{I'}\rangle = \quad & \left|-1,+\frac{1}{2},+\frac{3}{2}\right\rangle; \left|-1,+\frac{1}{2},+\frac{1}{2}\right\rangle; \left|-1,+\frac{1}{2},-\frac{1}{2}\right\rangle; \\ & \left|-1,+\frac{1}{2},-\frac{3}{2}\right\rangle; \left|-1,-\frac{1}{2},+\frac{3}{2}\right\rangle; \left|-1,-\frac{1}{2},+\frac{1}{2}\right\rangle; \\ & \left|-1,-\frac{1}{2},-\frac{1}{2}\right\rangle; \left|-1,-\frac{1}{2},-\frac{3}{2}\right\rangle \ . \end{aligned} \tag{2.66}$$

Note that in order to calculate the angular coupling elements described in section 2.4.1 we need $C_R\,|F', m_{F'}\rangle$. For the operator C_R acting on the hyperfine excited states $|F', m_{F'}\rangle$ the decomposition into the uncoupled basis and

Clebsch-Gordan coefficients is written as follows

$$C_R\,|1,+1\rangle = -\sqrt{\frac{1}{2}}\left|-1,+\frac{1}{2},+\frac{3}{2}\right\rangle , \tag{2.67}$$

$$C_R\,|1,+0\rangle = -\sqrt{\frac{1}{3}}\left|-1,+\frac{1}{2},+\frac{1}{2}\right\rangle , \tag{2.68}$$

$$C_R\,|1,-1\rangle = -\sqrt{\frac{1}{6}}\left|-1,+\frac{1}{2},-\frac{1}{2}\right\rangle , \tag{2.69}$$

$$C_R\,|2,-2\rangle = \sqrt{\frac{2}{3}}\left|-1,+\frac{1}{2},-\frac{3}{2}\right\rangle , \tag{2.70}$$

$$C_R\,|2,-1\rangle = -\sqrt{\frac{1}{2}}\left|-1,+\frac{1}{2},-\frac{1}{2}\right\rangle , \tag{2.71}$$

$$C_R\,|2,+0\rangle = -\sqrt{\frac{1}{3}}\left|-1,+\frac{1}{2},+\frac{1}{2}\right\rangle , \tag{2.72}$$

$$C_R\,|2,+1\rangle = \sqrt{\frac{1}{6}}\left|-1,+\frac{1}{2},+\frac{3}{2}\right\rangle , \tag{2.73}$$

$$C_R\,|2,+2\rangle = 0\,. \tag{2.74}$$

Here we note that the operator C_L acting on the hyperfine excited states $|F', m_{F'}\rangle$ can be obtained from symmetry. The decomposition for the operator C_0 is given in appendix B.3. These states are similar to the ones written in section 2.4.2.

2.5 Using the matrix representation

In section 2.5 we use the matrix representation to calculate the relative line-strength factors and transition frequencies of Rb, before showing that the absorption and dispersion coefficients can be used to calculate a macroscopic property such as transmission.

2.5.1 Relative line-strength factors

Using the matrix representation we show for example how the total transition strength is calculated for σ^- transitions on $F = 1 \rightarrow F' = 1$ line in ^{87}Rb. In section 2.4.2 we wrote the operator C_R acting on the the coupled basis for the $5^2\mathrm{P}_{1/2}$ term. The matrix diagonalisation of the entire 5P term leads

to a representation of all three operators. By choosing specific parts of the matrix we need to reduce the strength of the angular coupling elements by a 1/3. This value is the result of the three operators C_L, C_0 and C_R. For σ^- transitions on the $F = 1 \rightarrow F' = 1$ line we have $m_F = +0 \rightarrow m_{F'} = -1$ and $m_F = +1 \rightarrow m_{F'} = +0$. The calculation for total transition strength is

$$C_F^2 = \frac{1}{3}\sum_{m_F=-F}^{F} c_{m_F}^2 = \frac{1}{3}\left[\langle 1,+0|C_R|1,-1\rangle^2 + \langle 1,+1|C_R|1,+0\rangle^2\right] , \tag{2.75}$$

where

$$\begin{aligned} C_F^2 = \quad & \frac{1}{3}\left[\left(\sqrt{\frac{1}{2}}\left\langle 0,+\frac{1}{2},-\frac{1}{2}\right| - \sqrt{\frac{1}{2}}\left\langle 0,-\frac{1}{2},+\frac{1}{2}\right|\right)\right. \\ & \left. C_R\left(-\sqrt{\frac{1}{6}}\left|-1,+\frac{1}{2},-\frac{1}{2}\right\rangle\right)\right]^2 \\ & + \frac{1}{3}\left[\left(\frac{1}{2}\left\langle 0,+\frac{1}{2},+\frac{1}{2}\right| - \sqrt{\frac{3}{4}}\left\langle 0,-\frac{1}{2},+\frac{3}{2}\right|\right)\right. \\ & \left. C_R\left(-\sqrt{\frac{1}{3}}\left|-1,+\frac{1}{2},+\frac{1}{2}\right\rangle\right)\right]^2 , \end{aligned} \tag{2.76}$$

applying the electric-dipole selection rules we have

$$\begin{aligned} C_F^2 = \quad & \frac{1}{3}\left(-\sqrt{\frac{1}{2}}\sqrt{\frac{1}{6}}\left\langle 0,+\frac{1}{2},-\frac{1}{2}\right| C_R \left|-1,+\frac{1}{2},-\frac{1}{2}\right\rangle\right)^2 \\ & + \frac{1}{3}\left(-\frac{1}{2}\sqrt{\frac{1}{3}}\left\langle 0,+\frac{1}{2},+\frac{1}{2}\right| C_R \left|-1,+\frac{1}{2},+\frac{1}{2}\right\rangle\right)^2 , \end{aligned} \tag{2.77}$$

substituting for equation 2.45, the total transition strength is

$$\begin{aligned} C_F^2 &= \frac{1}{3}\left(\frac{1}{12}+\frac{1}{12}\right) , \\ &= \frac{1}{18} . \end{aligned} \tag{2.78}$$

Figure 2.5 shows the relative line-strengths, $c_{m_F}^2$, of each $m_F \rightarrow m_{F'}$ transition for linearly polarised light driving π transitions and left and right circularly polarised light driving σ^+ and σ^- transitions, respectively, on the $F = 1 \rightarrow F' = 1$ line in ^{87}Rb. Table 2.3 shows the total strengths for σ^- transitions on the $F \rightarrow F'$ lines in Rb.

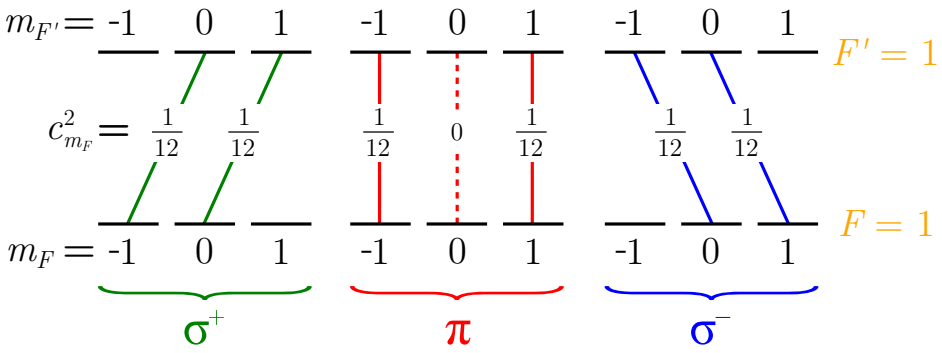

Figure 2.5: Calculated relative line-strengths, $c^2_{m_F}$, for each $m_F \rightarrow m_{F'}$ transition for linearly polarised light driving π transitions and left and right circularly polarised light driving σ^+ and σ^- transitions, respectively, on the $F = 1 \rightarrow F' = 1$ line in ^{87}Rb.

2.5.2 Transition frequencies

Now we have the relative line-strengths the next step is to calculate the transition frequencies using the matrix representation. The matrices in section 2.4.2 are arranged according to their eigenvalues. It is these eigenvalues that allow us to calculate the relative detunings. The energy of the $5^2S_{1/2}$ and $5^2P_{1/2}$ terms are given by

$$\mathrm{E}_{5^2\mathrm{S}_{1/2}/5^2\mathrm{P}_{1/2}} = \pm A_{\mathrm{hfs}}(5^2\mathrm{S}_{1/2}/5^2\mathrm{P}_{1/2})\lambda_{5^2\mathrm{S}_{1/2}/5^2\mathrm{P}_{1/2}} \ , \tag{2.79}$$

where $A_{\mathrm{hfs}}(5^2\mathrm{S}_{1/2})$ and $A_{\mathrm{hfs}}(5^2\mathrm{P}_{1/2})$ are the magnetic dipole constants of the $5^2S_{1/2}$ and $5^2P_{1/2}$ terms (listed in table 2.1) and $\lambda_{5^2\mathrm{S}_{1/2}/5^2\mathrm{P}_{1/2}}$ are the eigenvalues calculated from the diagonalisation of each matrix. Here we introduce the isotope shift due to the abundance of ^{85}Rb (C_{85}) and ^{87}Rb (C_{87}) in the medium (see appendix A). A natural cell (72% ^{85}Rb, 28% ^{87}Rb) has isotope shifts, $\Delta_{\mathrm{isotope}}$, of +21.62 MHz and −56.08 MHz for ^{85}Rb and ^{87}Rb on the D_1 line, respectively. Here we show for example the calculation for the detuning value for the $F = 1$ to $F' = 1$ transition of ^{87}Rb on the D_1 line. The detuning (in MHz) is calculated as follows

$$\begin{aligned}
\Delta_{F=1\rightarrow F'=1} &= -\frac{A_{\mathrm{hfs}}(5^2\mathrm{S}_{1/2})}{h}\lambda_{\mathrm{F}=1} + \frac{A_{\mathrm{hfs}}(5^2\mathrm{P}_{1/2})}{h}\lambda_{\mathrm{F}'=1} - \Delta_{\mathrm{isotope}} \ , \\
&= -3417.34 \times \left(-\frac{5}{4}\right) + 407.24 \times \left(-\frac{5}{4}\right) + 56.08 \ , \\
&= 3818.71 \text{ MHz} \ .
\end{aligned} \tag{2.80}$$

		D_1 Line		D_2 Line	
Line	F'	Detuning (MHz)	C_F^2	Detuning (MHz)	C_F^2
^{87}Rb	1	-3015.98	$\frac{5}{18}$	-2735.05	$\frac{1}{18}$
$F = 2 \rightarrow F' =$	2	-2201.50	$\frac{5}{18}$	-2578.11	$\frac{5}{18}$
	3			-2311.45	$\frac{14}{18}$
^{85}Rb	2	-1497.44	$\frac{35}{81}$	-1371.16	$\frac{10}{81}$
$F = 3 \rightarrow F' =$	3	-1135.85	$\frac{28}{81}$	-1307.74	$\frac{35}{81}$
	4			-1186.78	$\frac{81}{81}$
^{85}Rb	1			1635.30	$\frac{27}{81}$
$F = 2 \rightarrow F' =$	2	1538.29	$\frac{10}{81}$	1664.57	$\frac{35}{81}$
	3	1899.88	$\frac{35}{81}$	1727.99	$\frac{28}{81}$
^{87}Rb	0			4027.41	$\frac{2}{18}$
$F = 1 \rightarrow F' =$	1	3818.71	$\frac{1}{18}$	4099.63	$\frac{5}{18}$
	2	4633.18	$\frac{5}{18}$	4256.57	$\frac{5}{18}$

Table 2.3: Transition frequencies and total strengths, C_F^2, for the σ^- transitions on the D_1 and D_2 lines in a natural-abundant cell of Rb. Zero detuning ($\Delta = 0$) corresponds to the weighted centre of the lines.

The detunings of the atomic transitions relative to the centre of mass frequencies are listed in table 2.3.

2.5.3 Absorption and dispersion coefficients

The absorption and dispersion coefficients are calculated from the real and imaginary parts of the susceptibility. Here we introduce the complex refractive index, $n = n_R + in_I$. The susceptibility describing the optical properties is related to the refractive index by [108]

$$n = \sqrt{1+\chi} \approx 1 + \frac{\chi}{2} \,. \tag{2.81}$$

This approximation is valid because $|\chi| \ll 1$. Keaveney *et al.* [3] have shown that for a high density Rb vapour $\chi_{max} = 0.3$. Hence the real and imaginary parts can be written as

$$n_R = 1 + \frac{\chi_R}{2} \,, \tag{2.82}$$

$$n_I = \frac{\chi_I}{2} \,. \tag{2.83}$$

The refractive index and hence the susceptibility modifies the propagation of a classical light field along the z-direction in the following way

$$\hat{\mathcal{E}}(z) = \mathcal{E}_0 e^{\mathrm{i}(nkz-\omega t)} = \mathcal{E}_0 e^{\mathrm{i}(\sqrt{1+\chi}kz-\omega t)} \ , \tag{2.84}$$

substituting for the real and imaginary parts leads to

$$\hat{\mathcal{E}}(z) = \mathcal{E}_0 e^{\mathrm{i}(kz-\omega t)} e^{\mathrm{i}(\chi_{\mathrm{R}}kz/2)} e^{-\chi_{\mathrm{I}}kz/2} \ . \tag{2.85}$$

Here the field is attenuated by the medium due to the imaginary part of the susceptibility. The relative phase of the field changes due to the real part of the susceptibility. The phase changing part due to the real susceptibility will be investigated in chapter 5. The absorption of a propagating light beam along the z-direction of a medium is given by the Beer-Lambert law [109]

$$I(z) = I_0 \exp(-\alpha z) \ , \tag{2.86}$$

where $I(z)$ is the beam intensity at position z, α is the total absorption coefficient and I_0 is the initial beam intensity before the medium. Using the relation $I(z) = \frac{1}{2}\epsilon_0 c \left|\mathcal{E}(z)\right|^2$ [110] we can see that the absorption coefficient in terms of the imaginary part of the susceptibility, $\chi_I(\Delta)$ is

$$\alpha = k\chi_I(\Delta) \ , \tag{2.87}$$

where k is the wavevector of the beam. Now we concentrate on developing the absorption coefficient for a particular hyperfine transition $F \to F'$. The imaginary part of the susceptibility, $\chi_I(\Delta)$, was discussed in detail in section 2.3. In summary, it has the form of the imaginary part of the Faddeeva function, $s_{\mathrm{I}}(y)$, multiplied by the transition strength and prefactors which depend on the resonant transition. The lineshape factor is identical for each transition of a particular isotope, therefore in the theoretical model we need only calculate the Faddeeva function once. Recalling equation 2.30 the absorption coefficient for each transition can be written as

$$\begin{aligned} \alpha_{F\to F'} &= k \times \text{strength} \times \text{prefactor} \times \text{Voigt profile} \ , \\ &= k \frac{C_F^2}{2(2I+1)} \frac{\mathcal{N}\mu^2}{\hbar\epsilon_0} \frac{s_{\mathrm{I}}(y)}{ku} \ , \end{aligned} \tag{2.88}$$

where k is the wavevector, the strength factor includes the degeneracy, $2(2I+1)$, of the ground state of a particular isotope (see appendix A)

and the calculated C_F^2 coefficients from section 2.5.1. The degeneracy factor is included under the assumption that the population is evenly distributed amongst the ground-state Zeeman sublevels. The prefactor and Voigt profile were discussed in detail in section 2.3.3.

Transmission

For a medium of length, L, the transmission, T, is defined as

$$T = \frac{I(L)}{I_0} = \exp(-\alpha L) \ . \tag{2.89}$$

For beam intensities under one-thousandth of the saturation intensity, I_{SAT}, the absorption coefficient is independent of intensity [92] , where I_{SAT} is [108]

$$I_{\mathrm{SAT}} = hc\frac{\Gamma k^3}{24\pi^2} \ , \tag{2.90}$$

here $I_{\mathrm{SAT}} = 1.50$ mWcm^{-2} and 1.67 mWcm^{-2} for the D_1 and D_2 lines in Rb, respectively. If the probe beam is intense i.e. $I \geq I_{\mathrm{SAT}}$, the approximation that all the atoms reside in the ground states breaks down. This familiar exponential decay is then replaced by a polynomial dependence on the distance [111]. Nevertheless, the focus of part I is to ensure that the condition of $I \ll I_{SAT}$ for the probe beam is satisfied. The total absorption coefficient is given by the sum over all the electric-dipole-allowed transitions. For a medium with multiple transitions ($F \rightarrow F'$) the transmission is now defined as

$$T = \exp(-\sum \alpha_{F\rightarrow F'} L) \ , \tag{2.91}$$

where $\alpha_{F\rightarrow F'}$, is the absorption coefficient for each electric-dipole-allowed transition. The expected transmission profile can now be calculated as a function of detuning. Figure 2.6 shows theoretical transmission plots for a Rb vapour cell of length, $L = 75$ mm, on the D_1 and D_2 lines at a temperature of 35°C.

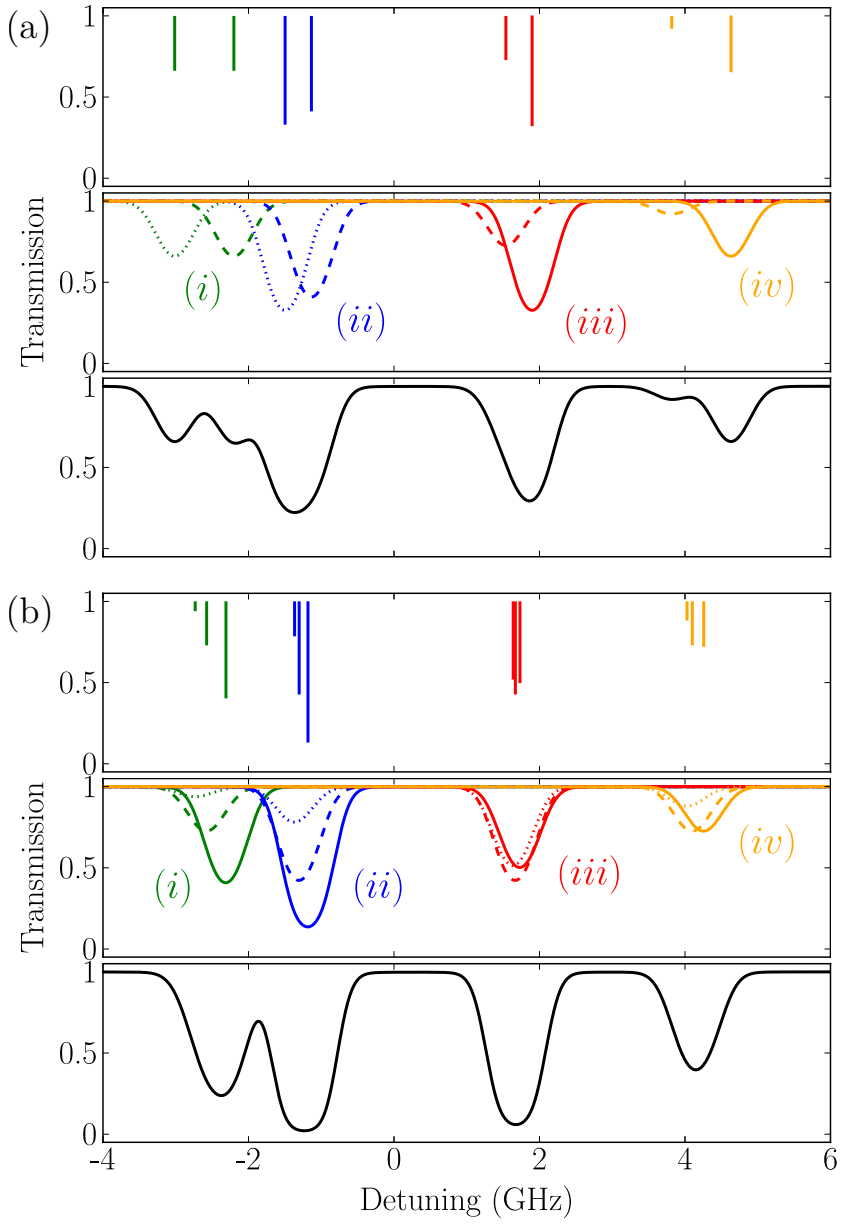

Figure 2.6: Transmission plots for a thermal Rb vapour cell of length 75 mm as a function of linear detuning, $\Delta/2\pi$. Zero detuning corresponds to the weighted centre of the lines. Plots (a) and (b) show the D_1 and D_2 lines at 35°C, respectively. The stick plots correspond to the energy levels and strengths calculated from the atomic Hamiltonian. The curves (i), (ii), (iii) and (iv) show the transmission for the transitions ^{87}Rb $F = 2 \rightarrow F'$ (green), ^{85}Rb $F = 3 \rightarrow F'$ (blue), ^{85}Rb $F = 2 \rightarrow F'$ (red) and ^{87}Rb $F = 1 \rightarrow F'$ (orange), respectively. The solid, dashed and dotted curves show the transitions between the hyperfine states $F \rightarrow F' = F + 1$, $F \rightarrow F' = F$ and $F \rightarrow F' = F - 1$, respectively. The solid black curves show the total transmission for both lines.

2.6 Experimental methods and results

In section 2.6 we describe the experimental apparatus used to measure the absolute Doppler-broadened transmission which we finally compare with the theoretical model.

2.6.1 Experimental apparatus

Figure 2.7 shows a schematic of the experimental apparatus used to observe the absolute Doppler-broadened transmission on the D_1 and D_2 transitions of Rb. Two external cavity diode laser systems (ECDL) (Toptica DL100) with wavelengths of 795 nm and 780 nm were used for these measurements. Both beams pass through a polarisation beam splitter providing linearly polarised light with $1/e^2$ radii of 0.77 $\pm$ 0.02 mm and 0.66 $\pm$ 0.02 mm for the D_1 and D_2 beams, respectively. Knowing that the the probe beams have to be weak in order for there to be agreement between the theoretical model and the experimental measurements, neutral-density filters are then used to ensure that optical pumping processes which redistribute population amongst the hyperfine levels of the ground term do not occur [112, 113]. After attenuation the beam powers are 20 nW and 15 nW with corresponding I/I_{SAT} equal to 0.006 and 0.007 for the D_1 and D_2 lines, respectively. The beams are then sent through 75 mm vapour cells containing Rb in its natural abundance (72% ^{85}Rb, 28% ^{87}Rb). After traversing the experiment cell both beams impinge on calibrated photodiodes. The frequency scan is linearised with a Fabry-Perot etalon (not shown), and calibrated by the use of hyperfine/saturated absorption spectroscopy [112, 113] in a natural-abundant room-temperature reference cell: this technique is discussed in detail in appendix C.

2.6.2 Comparing theory and experiment

Figure 2.8 shows plots for the transmission of (a) the Rb D_1 and (b) the Rb D_2 lines versus linear detuning, $\Delta/2\pi$. The zero of the detuning axis for both lines is taken to be the centre of mass frequency of the transitions in the absence of hyperfine splitting, taking into account the natural abundance of

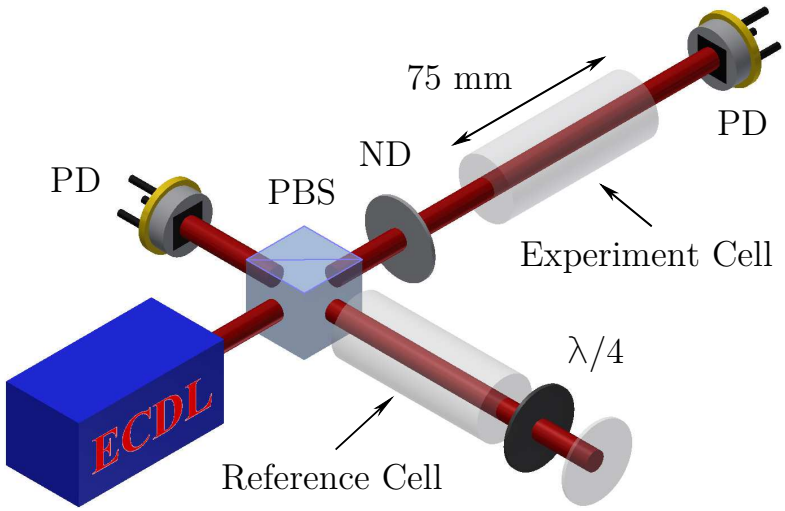

Figure 2.7: Schematic of the experimental apparatus in a long vapour cell. Both beams pass through a polarisation beam splitter (PBS), providing linearly polarised light. A small fraction of each beam is used to perform sub-Doppler spectroscopy in a room-temperature reference cell. The probe beams are attenuated with neutral-density filters (ND) before passing through 75 mm vapour cells and being collected on photodiodes (PD).

each isotope. The solid (black) and dotted (red) lines show the measured and theoretical transmissions, respectively. The data are measured on calibrated photodiodes: the technique adopted to normalise these data sets is discussed in appendix C. In figure 2.8(a) and 2.8(b) the corresponding theory curves are generated using the natural Lorentzian linewidths $\Gamma = 2\pi \times 5.746$ MHz [96] and $\Gamma = 2\pi \times 6.065$ MHz [96] and temperatures of 20.7°C and 20.9°C, which are in excellent agreement with the thermocouple measurements. For both curves there is excellent agreement between theory and experiment at the 0.1% rms level.

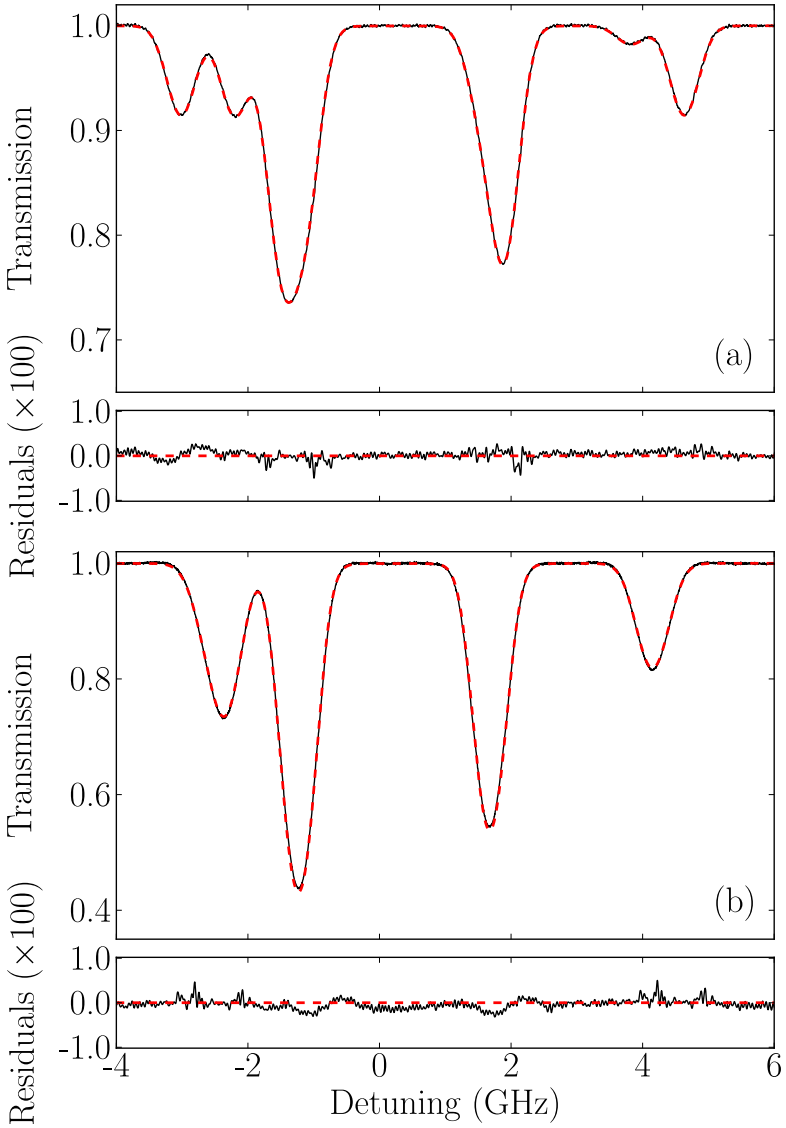

Figure 2.8: Transmission plots for the comparison between experiment and theory for (a) the Rb D_1 line and (b) the Rb D_2 line, through a 75 mm vapour cell as a function of linear detuning, $\Delta/2\pi$. The zero of the detunings are taken to be the centre-of-mass frequencies of each transition. Solid (black) and dotted (red) lines show measured and expected transmission, respectively. (a) has a temperature of 20.7°C with $\Gamma = 2\pi \times 5.746$ MHz and (b) has a temperature of 20.9°C with $\Gamma = 2\pi \times 6.065$ MHz. Below the main figures are plots of the residuals (the difference in transmission between theory and experiment). The magnitude of the residuals confirm an excellent fit between the theoretical model and the experimental data.

2.7 Discussion

In summary, we have developed a theoretical model for the electric susceptibility that will allow us to make quantitative predictions for the absorptive and dispersive properties of a Rb vapour in the vicinity of the D lines. Measurements of the frequency dependence of the absolute Doppler-broadened transmission are in excellent agreement between theory and experiment at the 0.1% rms level. After all this work we now have a code that precisely predicts the macroscopic optical properties of a Rb vapour cell. This will be the fundamental basis for all future investigations in part I of the thesis. Next we consider the modification to the medium's susceptibility as a consequence of resonant dipole-dipole interactions in a high density atomic media.

Chapter 3

Including resonant dipole-dipole interactions

This chapter is based on the following publication

L. Weller, R. J. Bettles, P. Siddons, C. S. Adams, and I. G. Hughes, *Absolute absorption on the rubidium D_1 line including resonant dipole-dipole interactions*, J. Phys. B: At. Mol. Opt. Phys. **44**, 195006 (2011), 10.1088/0953-4075/44/19/195006

Here we report on measurements of the absolute absorption spectra of dense rubidium vapour on the D_1 line in the weak-probe regime for temperatures up to 170° C and number densities up to 3×10^{14} cm^{-3}. In such vapours, modifications to the homogeneous linewidth of optical transitions arise due to dipole-dipole interactions between identical atoms, in superpositions of the ground and excited terms. Absolute absorption spectra were recorded with deviation of 0.1% between experiment and a theory incorporating resonant dipole-dipole interactions. The manifestation of dipole-dipole interactions is a self-broadening contribution to the homogeneous linewidth, which grows linearly with number density of atoms. Analysis of the absolute absorption spectra allow us to ascertain the value of the self-broadening coefficient for the rubidium D_1 line: $\beta/2\pi = (0.69 \pm 0.04) \times 10^{-7}$ Hz cm^3, in excellent agreement with the theoretical prediction.

3.1 Introduction

In chapter 2 we developed a model for the electric susceptibility that allowed us to make quantitative predictions for the absorptive and dispersive properties of a thermal Rb vapour probed in the vicinity of the D lines. Resonant dipole-dipole interactions among Rb atoms were not included in the model, as they do not become important unless the vapour has a temperature exceeding ~ 125°C. However, there is a strong motivation to working at higher temperature as in this case high optical depths are accessible even in cells with lengths of only a few millimetres or a few microns [18]. In this chapter we show that by including self broadening in the model for susceptibility, experiment and theory agree to within 0.1% up to densities of 3×10^{14} cm^{-3}. At these higher densities the resonant dipole-dipole interactions between two identical atoms, in superpositions of the ground and excited terms, gives rise to the phenomenon of self-broadening [114]. The modification of the medium's susceptibility as a consequence of the dipole-dipole interactions is the subject of this chapter. In this chapter we also extend the theoretical and experimental study of the absolute absorption spectroscopy of Rb on the D_1 line for temperatures up to ~ 170°C, corresponding to a number density four orders of magnitude larger than in chapter 2.

3.2 Resonant dipole-dipole interactions

In section 3.2 the form of the resonant dipole-dipole interaction between two identical atoms is considered. We then develop an understanding for how these interactions contribute to the susceptibility, before differentiating both the quasi-static and impact regimes for a thermal Rb vapour.

3.2.1 Form of the interaction

In chapter 2 we started by considering the properties of many two-level atoms and showed that the homogeneous lineshape for such a system is of a finite width, Γ_0. In dense atomic vapours the interaction between identical atoms causes a modification in this linewidth. This interrupts the process of light

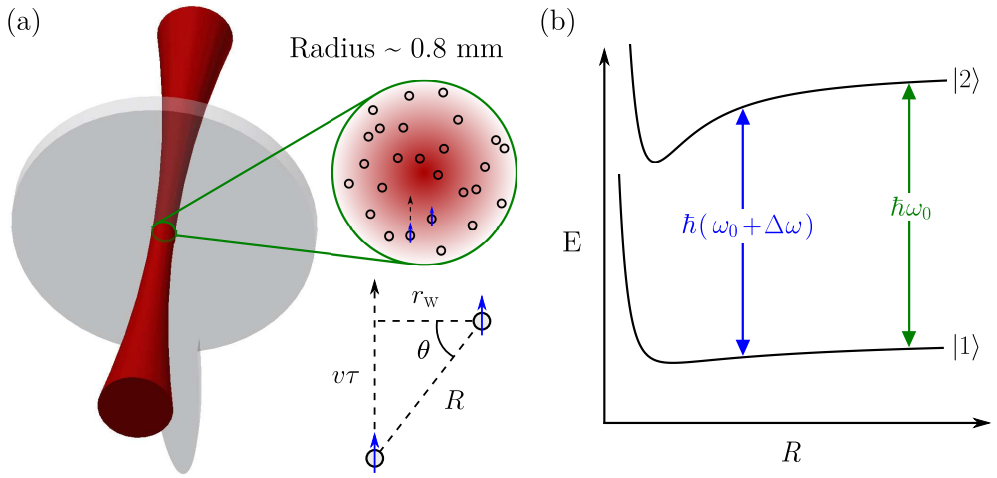

Figure 3.1: (a) Schematic of a beam through a cell of Rb atoms. The straight line trajectory of a neutral single perturber moving past an excited atom is also shown. (b) Energy levels of a two-level atom as a function of distance, R, from a perturbing atom. The levels $|1\rangle$ and $|2\rangle$ begin parallel with an energy separation $\hbar\omega_0$. For smaller R the potential curves are modified and there is an instantaneous change, $\Delta\omega$, in the angular frequency.

emission and can shorten the effective lifetime of the excited state. Figure 3.1 shows the influence of a single perturber on an excited atom separated by a distance R. At long range the energy separation, $\hbar\omega_0$, is the same as for a single two-level atom. Here we introduce $V^{|1\rangle}(R)$ and $V^{|2\rangle}(R)$ as the change in the energies of the ground and excited terms, respectively. The resonant angular frequency at large distance, ω_0, is changed by an instantaneous frequency, $\Delta\omega$, where $\hbar\Delta\omega = V^{|2\rangle}(R) - V^{|1\rangle}(R)$. The change in the energies of the ground and excited terms can be represented by a potential of the form $V^{|1,2\rangle}(R) = C_n^{1,2}/R^n$ where $C_n^{1,2}$ is a constant which depends on state 1 or 2. Here we note that for $n = 3$, this refers to the dominant resonant dipole-dipole interactions between identical atoms, in superpositions of the ground and excited terms.

The form of the interaction described so far refers to a binary system in superpositions of the ground and excited terms. For an ensemble of atoms there are many perturbers with different orientations and separations. In 1933 Weisskopf showed that disruption to light emission may be explained by a change in the phase of the light field before and after a collision. The

phase change for a collision is given by the expression [103]

$$n(r_{\rm w}) = \int_{-\infty}^{\infty} \Delta\omega {\rm d}\tau \ , \tag{3.1}$$

where $r_{\rm w}$ is the Weisskopf radius and $\Delta\omega$ is the instantaneous change in the angular frequency. For the dominant resonant dipole-dipole interactions it has be shown that $\Delta\omega = C_3/R^3$ [103], where $\hbar C_3$ is the difference between the excited, $C_3^{|2\rangle}$ and ground $C_3^{|1\rangle}$ terms of a given transition. In figure 3.1 we show the straight line trajectory of an atom with mean relative velocity, v, moving past a radiating atom, where the separation between both atoms is R. The phase for the emitted radiation becomes

$$n(r_{\rm w}) = \int_{-\infty}^{\infty} \frac{C_3}{R^3} {\rm d}\tau \ , \tag{3.2}$$

where $R = \sqrt{r_{\rm w}^2 + v^2\tau_{\rm tot}^2}$, hence

$$n(r_{\rm w}) = \int_{-\infty}^{\infty} \frac{C_3}{\left(r_{\rm w}^2 + v^2\tau^2\right)^{3/2}} {\rm d}\tau \ . \tag{3.3}$$

Using trigonometry for figure 3.1, $v\tau = r_{\rm w}\tan\theta$ and ${\rm d}\tau = r_{\rm w}\sec^2\theta {\rm d}\theta/v$, the integral can be rearranged to give

$$\begin{aligned} n(\theta) &= \int_{-\frac{\pi}{2}}^{\frac{\pi}{2}} \frac{C_3 r_{\rm w}\sec^2\theta}{v\left(r_{\rm w}^2 + r_{\rm w}^2\tan^2\theta\right)^{3/2}} {\rm d}\theta \ , \\ &= \frac{C_3}{v r_{\rm w}^2} \int_{-\frac{\pi}{2}}^{\frac{\pi}{2}} \frac{\sec^2\theta}{\left(1+\tan^2\theta\right)^{3/2}} {\rm d}\theta \ , \\ &= \frac{C_3}{v r_{\rm w}^2} \int_{-\frac{\pi}{2}}^{\frac{\pi}{2}} \cos\theta {\rm d}\theta \ , \\ &= \frac{2C_3}{v r_{\rm w}^2} \ . \end{aligned} \tag{3.4}$$

Weisskopf then assumed a phase change equal to 1 or greater would result in a completely incoherent process, the Weisskopf radius is defined as follows

$$r_{\rm w} = \sqrt{\frac{2C_3}{v}} \ . \tag{3.5}$$

A two-body collision occurs when both atoms are separated by a distance less than the Weisskopf radius.

3.2.2 Contribution to the susceptibility

The susceptibility we developed in chapter 2 is calculated by summing the contributions from all dipole-allowed transitions [92]. Each transition has a Voigt profile with two contributions: a homogeneous Lorentzian lineshape arising from spontaneous emission from the excited state (with natural linewidth Γ_0), and an inhomogeneous Gaussian lineshape to account for the atomic motion. At the higher densities considered here there is a significant contribution to the total Lorentzian linewidth, $\Gamma_{\rm tot}$, from the interaction among the atoms:

$$\Gamma_{\rm tot} = \Gamma_0 + \Gamma_{\rm self} = \Gamma_0 + \beta\mathcal{N} \ , \tag{3.6}$$

where β is the self-broadening coefficient and $\mathcal{N}$ is the number density. The dominant effect arises from the dipole-dipole interaction between two identical atoms, in superpositions of the ground and excited terms. The binary dipole-dipole approximation remains valid for densities up to $\frac{4\pi}{3}\mathcal{N}r_{\rm w}^3 \ll 1$ (see equation 10.23 in [115]) where the Weisskopf radius is (see equation 8.30 in [103])

$$r_{\rm w} = \sqrt{\frac{\beta}{2\pi v}} \ , \tag{3.7}$$

and v is the mean relative velocity in the vapour given by [103]

$$v = \sqrt{\frac{8k_{\rm B}T}{\pi\mu}} = \sqrt{\frac{8}{\pi}}u \approx 1.6u \ . \tag{3.8}$$

where $\mu = m/2$ and u is the mean speed of a single Rb atom. This gives $\mathcal{N} \geq 1.6 \times 10^{17}$ cm^{-3} (corresponding to a temperature ~ 380°C) which is valid for the D_1 line considered in this work. Above this number density multiperturber effects become important, these are beyond the scope of this thesis. Equating equations 3.5 and 3.7 for the Weisskopf radii, the relation that connects β and the effective C_3 coefficient is

$$C_3 \ = \ \frac{1}{2}\frac{\beta}{2\pi} \ . \tag{3.9}$$

Experimental measurements for the C_3 coefficient for the D_1 and D_2 lines in Rb [116] are consistent with theoretical predictions of equations 3.21 and 3.22 combined with equation 3.9.

Length Scale	Formula	$C = 1$ (at 145°C)	$C = 1000$ (at 350°C)
r_{w}	$\sqrt{\frac{\beta}{2\pi v}}$	13 nm	11 nm
d_0	$v\tau_0$	13×10^3 nm	15×10^3 nm
d_{tot}	$v\tau_{\mathrm{tot}}$	6300 nm	15 nm
L_C	$\frac{\lambda/2\pi}{\sqrt[3]{C}}$	130 nm	13 nm
l	$\frac{5}{9}\sqrt[3]{\frac{1}{\mathcal{N}}}$	130 nm	13 nm

Table 3.1: Several length scales at two different cooperativity (defined in section 3.3.2) parameters and corresponding temperatures for D_1 line in ^{87}Rb. Here we compare the Weisskopf radius, r_{w}, the distance travelled in the absence, d_0, and presence, d_{tot}, of a collision, the cooperative length, L_C and the nearest neighbour, l. At $C = 1$ (at 145°C) and $C = 1000$ (at 350°C) the mean relative velocities are 450 ms^{-1} and 550 ms^{-1}, respectively.

3.2.3 Impact and quasi-static regimes

When the duration of a collision is much greater than the time between collisions i.e. $r_{\mathrm{w}} \gg d_{\mathrm{tot}}$, this is known as the quasi-static approximation. The line broadening is produced over a short distance and therefore the thermal motion of the perturber can be ignored. This is likely to be the case when we have high densities, where the mean time between collisions τ_{tot} is small and at low temperatures, where the mean relative velocity v is small. When the conditions for the quasi-static approximation are valid we say that the medium is in constant state of collision. When the duration of a collision is short compared with the time between collisions i.e. $r_{\mathrm{w}} \ll d_{\mathrm{tot}}$, this is known as the impact approximation. This is likely to be the case when we have low densities, where the mean time between collisions τ_{tot} is large and at high temperatures, where v is large. The two approximations are formally divided by the duration of one collision given by the Weisskopf time

$$\tau_{\mathrm{w}} = \frac{r_{\mathrm{w}}}{v} \ . \tag{3.10}$$

Table 3.1 compares the different length scales for D_1 line in ^{87}Rb at two different cooperativity (defined in section 3.3.2) parameters and corresponding temperatures. Here we state that for the number densities and temperatures under investigation the conditions for the impact approximation are valid.

The impact regime may also be defined by the inequality $|\Delta| < \omega_{\rm w}$, where Δ is the detuning of the laser light from resonance, ($\Delta = \omega_{\rm L} - \omega_0$, with $\omega_{\rm L}$ the laser angular frequency, and ω_0 the angular frequency of the resonance transition), and $\omega_{\rm w}$ is the Weisskopf angular frequency. For the Rb D_1 line the Weisskopf angular frequency defined by $\omega_{\rm w} = 1/\tau_{\rm w} = 2\pi \times \sqrt{v^3/2\pi\beta}$ [117], is approximately $2\pi \times 6$ GHz for the temperatures studied here. The detunings from resonance accessible with our apparatus are less than the Weisskopf frequency, therefore we need to evaluate the self-broadening parameter β in the impact regime within the binary-collision approximation.

3.3 The self-broadening parameter

In section 3.3 the calculations for the impact self-broadening parameter of the D_1 and D_2 lines in Rb are shown. We calculate the total Lorentzian linewidth in terms of the cooperativity parameter, which defines the magnitude of the resonant dipole-dipole interactions. Finally we compare the homogeneous and inhomogeneous FWHM and show that Doppler-broadening dominates for the temperatures considered here, however the Lorentzian profile dominates in the wings of the absorption profile.

3.3.1 Calculating the self-broadening parameter

In a comprehensive treatment of collisional line broadening Lewis [118] provides an expression for the self-broadening parameter for alkali-metal atoms in the binary-collision approximation, which is $\beta = 2\,f\,c\,r_0\,\lambda\,\sqrt{g_1/g_2}$. Here, f is the absorption oscillator strength for the transition; c is the speed of light; r_0 is the classical radius of the electron; λ is the resonance transition wavelength; g_1 and g_2 are the degeneracies of the ground and excited terms, respectively. To highlight the physical mechanism underpinning the interaction we begin by writing the formula for the self-broadening coefficient in terms of the degeneracies $2J+1$ and $2J'+1$ for the ground and excited terms of Rb, respectively.

$$\beta = 2fcr_0\lambda\sqrt{\frac{2J+1}{2J'+1}}\ . \tag{3.11}$$

The absorption oscillator strength, f, is a dimensionless quantity that describes the strength of a particular transition. The strength f of a transition from a lower state J to an upper state J' may be defined by [118]

$$f = \frac{2\pi\epsilon_0 m_e c^3}{e^2\omega_0^2}\frac{2J'+1}{2J+1}\Gamma_0 \ , \tag{3.12}$$

where Γ_0 is the natural linewidth (see equation 2.18)

$$\Gamma_0 = \frac{\omega_0^3}{3\pi\epsilon_0\hbar c^3}\frac{2J+1}{2J'+1}\mu^2 \ , \tag{3.13}$$

and μ is the dipole matrix element from chapter 2. If we now substitute equation 3.13 into equation 3.12 we get [119]

$$f = \frac{2}{3}\frac{m_e\omega_0}{\hbar e^2}\mu^2. \tag{3.14}$$

The dipole matrix element, μ, can be written in terms of the reduced dipole matrix element, d, using the relation [92]

$$\mu \ = \ (-1)^{J'+L+S+1} \times \sqrt{(2J'+1)(2L+1)} \begin{Bmatrix} L & L' & 1 \\ J & J' & S \end{Bmatrix} d. \tag{3.15}$$

The Wigner $6-j$ coefficient and prefactor, both of which are independent of the F and m_F quantum numbers, can be calculated for the D_1 and D_2 lines

$$\mu_1 \ = \ \sqrt{\frac{1}{3}}d_1 \ , \tag{3.16}$$

$$\mu_2 \ = \ \sqrt{\frac{2}{3}}d_2 \ , \tag{3.17}$$

where $d_1 = 5.182ea_0$ and $d_2 = 5.177ea_0$ for Rb D_1 and D_2 lines, respectively. For the Rb D_1 and D_2 lines we can now write the absorption oscillator strength f in terms of the reduced dipole matrix element, d. Substituting equations 3.17 and 3.16 into 3.14 we get [120]

$$f_1 \ = \ \frac{2}{9}\frac{m_e\omega_0}{\hbar e^2}d_1^2 = 0.3420 \ , \tag{3.18}$$

$$f_2 \ = \ \frac{4}{9}\frac{m_e\omega_0}{\hbar e^2}d_2^2 = 0.6956 \ , \tag{3.19}$$

where the ratio f_2/f_1 is approximately equal to 2. This ratio arises because the strength of each component is proportional to the statistical weight of the levels $m_{J'} = 2J'+1$ which are 2 and 4 for the $5^2P_{1/2}$ and $5^2P_{3/2}$ terms,

respectively. If we finally substitute equations 3.18 and 3.19, and the classical radius of the electron

$$r_0 = \frac{1}{4\pi\epsilon_0}\frac{e^2}{m_e c^2} \ , \tag{3.20}$$

into equation 3.11 we can write the formulae for the self-broadening coefficients for the Rb D_1 and D_2 lines as

$$\beta_1 = \frac{2}{9\hbar\epsilon_0} d_1^2 = 2\pi \times \Gamma_1 \left(\frac{\lambda_1}{2\pi}\right)^3 \ , \tag{3.21}$$

$$\beta_2 = \sqrt{2}\frac{2}{9\hbar\epsilon_0} d_2^2 = 2\pi \times \sqrt{2}\ \Gamma_2 \left(\frac{\lambda_2}{2\pi}\right)^3 \ , \tag{3.22}$$

where d_1, d_2, Γ_1, Γ_2 and λ_1, λ_2, are the reduced dipole matrix elements, natural linewidths and wavelengths for the D_1 and D_2 lines, respectively, for alkali-metal atoms. The d^2 terms in these equations highlight the dipole-dipole origin of the self-broadening interaction. The dependence on Γ demonstrates that the lines broaden by an amount equal to the natural-broadening per atom within a volume equal to the reduced wavelength cubed. Note also that the self-broadening coefficient is $\sqrt{2}$ larger for the D_2 line compared to the D_1 line.

3.3.2 Total Lorentzian linewidth

Now let us reconsider the total Lorentzian linewidth from section 3.2.2. For the D_1 and D_2 transitions the natural linewidths, Γ_0, are calculated as follows: $\omega_{1,2} = k_{1,2}c$, the dipole matrix elements are $\mu_1 = \sqrt{1/3}d_1$ and $\mu_2 = \sqrt{2/3}d_2$, where d_1 and d_2 are the reduced dipole matrix elements. For the D_1 line $J = 1/2$, $J' = 1/2$ and for the D_2 line $J = 1/2$, $J' = 3/2$, hence

$$\Gamma_1 = \frac{d_1^2 k_1^3}{9\pi\hbar\epsilon_0} \ , \tag{3.23}$$

$$\Gamma_2 = \frac{d_2^2 k_2^3}{9\pi\hbar\epsilon_0} \ , \tag{3.24}$$

where $\Gamma_1 = 2\pi \times 5.746$ MHz and $\Gamma_2 = 2\pi \times 6.065$ MHz for the D_1 and D_2 lines, respectively. The self-broadening linewidths, Γ_{self}, for the D_1 and D_2 transitions are calculated using equations 3.21 and 3.22

$$\Gamma_{\text{self}} = \beta_1 \mathcal{N} = \frac{2d_1^2\mathcal{N}}{9\hbar\epsilon_0} \ , \tag{3.25}$$

$$\Gamma_{\text{self}} = \beta_2 \mathcal{N} = \sqrt{2}\frac{2d_2^2\mathcal{N}}{9\hbar\epsilon_0} \ . \tag{3.26}$$

The total linewidth for the D_1 and D_2 transitions are

$$\Gamma_{\rm tot} = \frac{d_1^2 k_1^3}{9\pi\hbar\epsilon_0}(1 + 2\pi\mathcal{N}k_1^{-3}) \,, \tag{3.27}$$

$$\Gamma_{\rm tot} = \frac{d_2^2 k_2^3}{9\pi\hbar\epsilon_0}(1 + \sqrt{2}\ 2\pi\mathcal{N}k_2^{-3}) \,, \tag{3.28}$$

At high densities resonant dipole-dipole interactions dominate for low lying excited terms. The magnitude of these interactions can now be defined by introducing the cooperativity parameter, $C_{1,2} = 2\pi\mathcal{N}k_{1,2}^{-3}$. It follows that the total Lorentzian linewidths can be written as

$$\Gamma_{\rm tot} = \Gamma_1(1 + C_1) \,, \tag{3.29}$$

$$\Gamma_{\rm tot} = \Gamma_2(1 + \sqrt{2}\ C_2) \,. \tag{3.30}$$

In chapter 7 we measure the enhancement of energy transfer in a high-density thermal vapour as a function of the defined cooperativity parameter.

3.3.3 Homogeneous and inhomogeneous FWHM

To illustrate how the density maps on to the vapour temperature, figure 3.2 shows the natural, Γ_0, Doppler, $\Gamma_{\rm D}$, and self-broadened, $\Gamma_{\rm self}$, full-widths half-maximum (FWHM) for the ^{87}Rb D_1 line as a function of temperature. The Rb number density [121] is also plotted. For temperatures below ~ 145°C the Doppler width is two orders of magnitude larger than the homogeneous linewidth, and natural-broadening exceeds self-broadening; for temperatures above ~ 265°C self-broadening dominates; and in the intermediate regime self-broadening dictates the homogeneous width. The optical depth on resonance increases rapidly with temperature, therefore for experiments where it is desirable for a large fraction of the light to be transmitted this necessitates working far from resonance. In the range of temperatures to which we gain access in the experiments we report here, the Doppler-broadening exceeds the total homogeneous (natural- and self-) broadening; however, in the wing of the absorption line the profile is expected to have a Lorentzian profile [122].

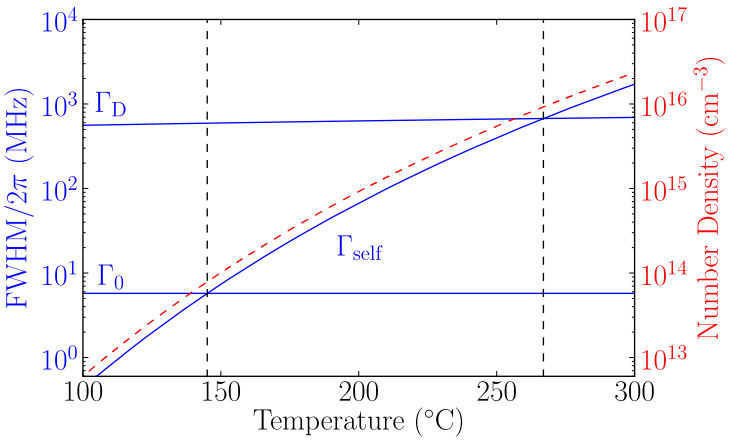

Figure 3.2: The solid blue lines show natural, Γ_0, Doppler, Γ_D, and self-broadened, Γ_{self}, FWHM for the ^{87}Rb D_1 line as a function of temperature. The dotted red line shows number density [121] as a function of temperature. The dotted black lines define the regimes where $\Gamma_D > \Gamma_0 > \Gamma_{self}$ (leftmost region), $\Gamma_D > \Gamma_{self} > \Gamma_0$ (central region), and $\Gamma_{self} > \Gamma_D > \Gamma_0$ (rightmost region).

3.4 Experimental methods and results

In section 3.4 we discuss the experimental apparatus and the cell heater required to investigate resonance line self-broadening on the D_1 line of Rb. Initial comparisons between theory and experiment show disagreement as the Lorentzian width due to self-broadening is not included in the theoretical model.

3.4.1 Experimental apparatus

Figure 3.3 shows a schematic of the experimental apparatus used to observe the resonance line self-broadening on the D_1 transition of Rb. An external cavity diode laser system (ECDL) with a wavelength of 795 nm was used for these measurements. The beam had $1/e^2$ radius 0.77 ± 0.02 mm and passed through a polarisation beam splitter providing linearly polarised light. After attenuation by a neutral-density filter the beam was sent through a 2 mm heated vapour cell containing Rb in its natural abundance (72% ^{85}Rb, 28% ^{87}Rb). After traversing the experiment cell the light impinges on a calibrated photodiode. The frequency scan was linearised with a Fabry-Perot etalon (not shown), and calibrated by the use of hyperfine/saturated absorption

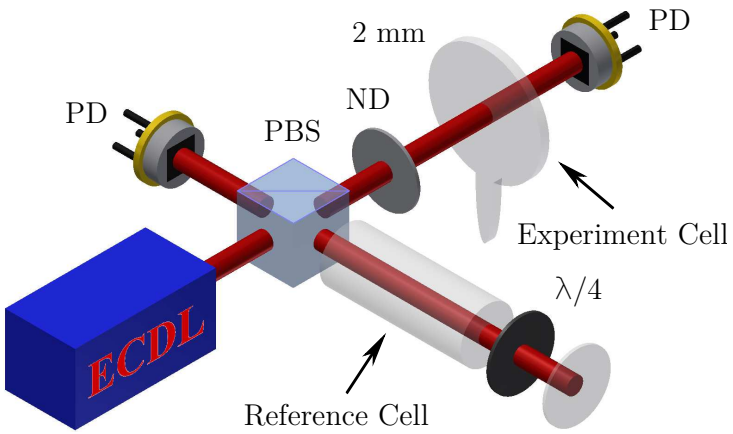

Figure 3.3: Schematic of the experimental apparatus. A beam passes through a polarisation beam splitter (PBS), providing linearly polarised light. A small fraction of the beam is used to perform sub-Doppler spectroscopy in a room-temperature reference cell. The probe beam is attenuated with a neutral-density filter (ND) before passing through a heated vapour cell and being collected on a photodiode (PD).

spectroscopy [112, 113] in a natural-abundant room-temperature reference cell: this technique is discussed in detail in appendix C.

3.4.2 2 mm cell heater

The cell was placed in an oven (see figure 3.4) which has two sections, one containing the body of the cell, the other the metal reservoir. The oven is made from non-magnetic stainless steel and polyether ether ketone (PEEK); the latter is used owing to its heat-insulating properties. The two oven sections are resistively (ceramic body wirewound resistors) heated independently. In this investigation a constant temperature difference of $\sim 5°C$ was maintained between the body of the cell and the reservoir; this is to prevent Rb from condensing on the windows. The body and reservoir temperatures were measured with thermocouples.

To obtain good agreement between theory and experiment it is important that the atoms in the cell traversing the laser beam do not undergo hyperfine pumping into the other ground term hyperfine level. This is achieved by working with a probe beam power much less than 100 nW [92, 111]. We

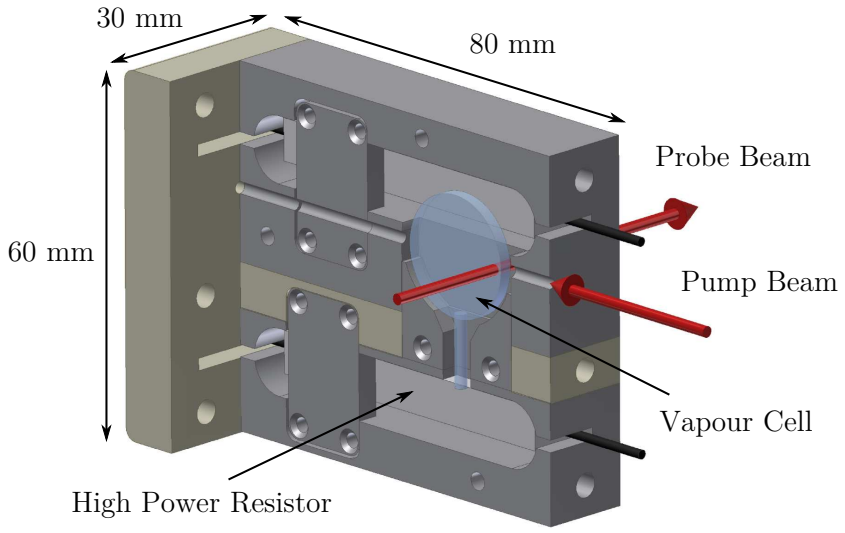

Figure 3.4: A schematic of the oven assembly for a 2 mm vapour cell, including the relevant dimensions. The oven has two non-magnetic stainless steel sections separated by a layer of polyether ether ketone (PEEK). One of the sections contains the body of the cell and the other the metal reservoir. Both sections are heated independently with high power resistors. Owing to the heat-insulating properties of the PEEK layer, a constant temperature difference of 5°C is usually maintained between the body of the cell and the reservoir. This temperature gradient prevents the Rb from condensing on the windows of the cell.

measured transmission spectra for a range of temperatures from room temperature up to $\sim$ 170°C. For each temperature five spectra were recorded and analysed.

3.4.3 Comparing theory and experiment

Figure 3.5 shows a plot of the transmission of the Rb D_1 line versus linear detuning $\Delta/2\pi$. The zero of the detuning axis is taken to be the centre of mass frequency of the transition in the absence of hyperfine splitting, taking into account the natural abundance of each isotope. The solid (black) and dotted (red) lines show the measured and theoretical transmission, respectively, using the susceptibility of chapter 2. The two theory curves are generated assuming that the Lorentzian width is Γ_0, the natural width and with temperatures 55°C and 170°C in agreement with thermocouple measurements. There is excellent agreement between theory and experiment for the lower

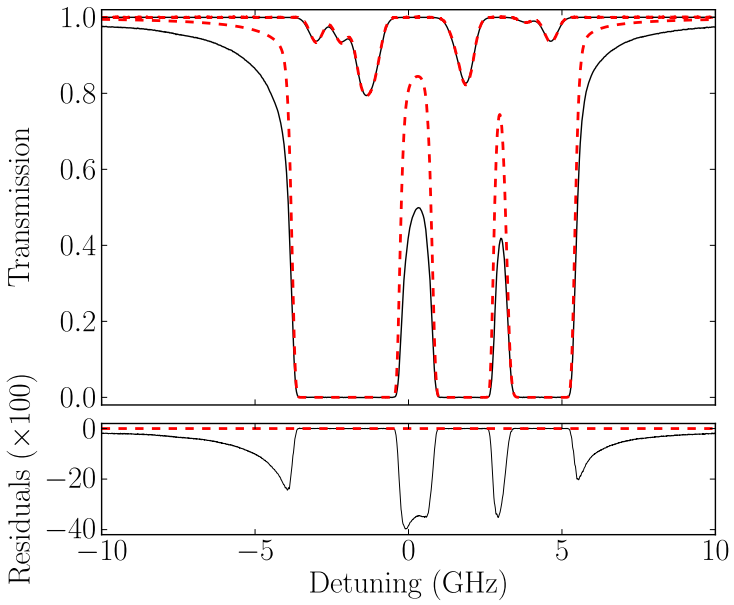

Figure 3.5: Transmission plot for the comparison between experiment and theory for the Rb D_1 line, through a 2 mm vapour cell as a function of linear detuning, $\Delta/2\pi$. The zero of detuning is taken to be the centre-of-mass frequency of the transition. Solid (black) and dotted (red) lines show measured and expected transmission, respectively, for a temperature of 55°C and 170°C with $\Gamma_0/2\pi = 5.746$ MHz [96]. Below the main figure is a plot of the residuals (the difference in transmission between theory and experiment) for the higher temperature. The structure and magnitude of the residuals confirm how poor a fit the theory is to the data.

temperature; however, at the higher temperature agreement is poor. The discrepancy at the higher temperature is not surprising when recalling figure 3.2; self-broadening is expected to provide the dominant contribution to the homogeneous width in this regime.

3.5 Modified form of the susceptibility

In section 3.5 the additional Lorentzian width due to self-broadening is included and excellent agreement between theory and experiment is shown. With this agreement we then measure the self-broadening parameter for the D_1 line in Rb and compare other measured values with the theoretical predictions of equations 3.21 and 3.22.

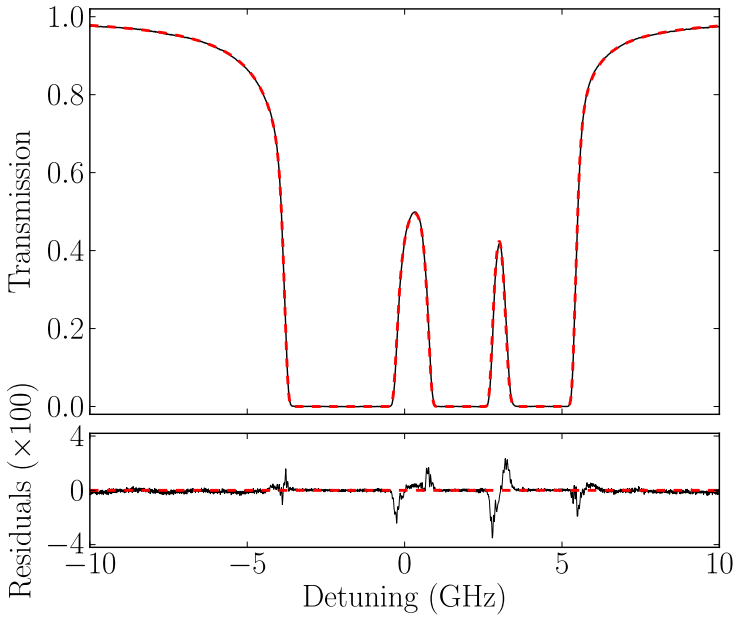

Figure 3.6: Transmission plot for the comparison between experiment and theory for the Rb D_1 line, through a 2 mm vapour cell as a function of linear detuning, $\Delta/2\pi$. The zero of detuning is taken to be the centre-of-mass frequency of the transition. Solid (black) and dotted (red) lines show measured and expected transmission, respectively, for a temperature of (171.8 ± 0.2)°C with $\Gamma_{\text{tot}}/2\pi$ = (23.7 ± 0.2) MHz. Below the main figure is a plot of the difference in transmission between theory and experiment. There is excellent agreement between model and data, with the exception of a small number of glitches where the linearisation of the laser scan was not adequate.

3.5.1 Modified total homogeneous linewidth

Based on the discussion in section 3.2.2 we modify the form of the susceptibility in our theoretical model. We expect the total Lorentzian linewidth to be a function of density, and hence temperature. Both isotopes have two values of F in the ground $5^2S_{1/2}$ term (^{85}Rb has $F = 2$ and 3; ^{87}Rb has $F =$ 1 and 2). The susceptibilities for transitions from each F are allowed to have variable Lorentzian linewidths. Figure 3.6 shows a comparison of the data and modified theoretical prediction. A least-squares fit[1] of the data to the modified theory allows the total homogeneous linewidths, Γ_{tot}, and temperature to be determined from the spectrum. The agreement between theory

[1]The Marquardt-Levenberg method [123] was used to perform a least-squares fit and extract the optimised parameters and their uncertainties (see appendix D).

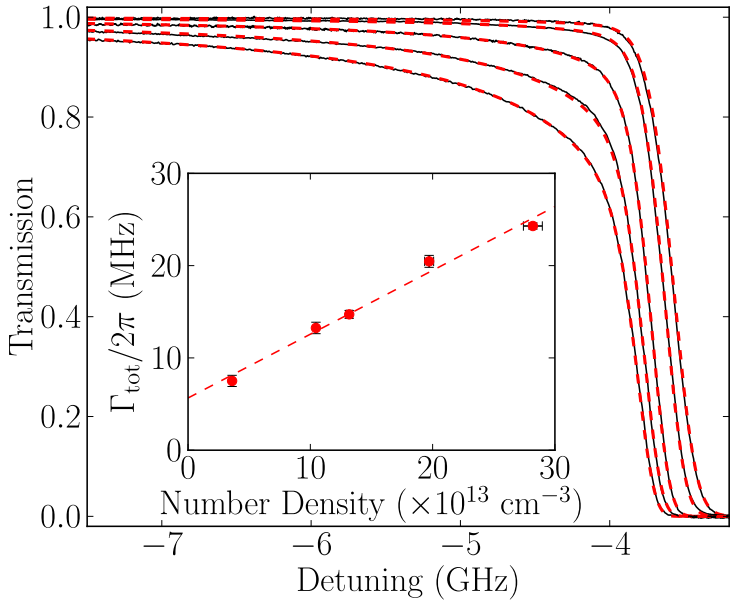

Figure 3.7: Transmission plots for the comparison between experiment and theory for the $F = 2 \rightarrow F' = 1, 2$ in ^{87}Rb, through a 2 mm natural abundant vapour cell, as a function of linear detuning, $\Delta/2\pi$. Solid (black) and dotted (red) lines show measured and expected transmission for several different number densities. The insert shows total homogeneous linewidth versus number density. The dotted red line shows a linear relationship between the two axes, with a gradient of $\beta/2\pi = (0.69 \pm 0.04) \times 10^{-7}$ Hz cm^3 and an intercept of $\Gamma_0/2\pi = (5.7 \pm 0.7)$ MHz.

and experiment is excellent. There are minor glitches in the residuals where the transmission varies most rapidly - this is a manifestation of the imperfect linearisation of the laser scan. Ignoring those anomalies, the deviation between theory and experiment is at the 0.1% rms level.

3.5.2 Measuring the self-broadening parameter

Five spectra were taken for each temperature value, and the statistical uncertainty in the twenty measurements of the total homogeneous linewidth, Γ_{tot}, was calculated as the standard error. In figure 3.7 the transmission as a function of linear detuning through a 2 mm natural abundant vapour cell is measured in the red-detuned wing for several different temperatures. Despite being in the regime where the Doppler width exceeds the homoge-

	D_1 in 10^{-7} Hz cm^3		D_2 in 10^{-7} Hz cm^3	
Element	Theory	Measured	Theory	Measured
Na	0.51	0.49±0.07 [117]	0.72	0.74±0.11 [117]
Rb	0.73	0.69±0.04 present	1.03	1.10±0.17 [124]
Cs	0.83	0.75±0.11 [125]	1.16	1.15±0.23 [126]

Table 3.2: Theoretical and measured values of the impact self-broadening coefficients $\beta_{1,2}/2\pi$ for Na, Rb and Cs on the D_1 and D_2 lines. Theoretical predictions are from equations 3.21 and 3.22. Note all self-broadening coefficients are of the order 1×10^{-13} MHz cm^3, this is equivalent to approximately 3 GHz Torr^{-1} which is useful when considering the buffer gas broadening in section 4.5.3.

neous width, as discussed in section 3.3.3, the absorption profile far from resonance has a Lorentzian profile. Measuring the total homogeneous width as a function of temperature allows us to evaluate the self-broadening coefficient. For each temperature, the Rb number density is deduced from [121], and the total homogeneous linewidth and its uncertainty are extracted from the least-squares fit. For the density range investigated the inset to figure 3.7 shows that the spectral width Γ_{tot} is linear in number density, as expected from equation 3.6. From the slope we find a value for the self-broadening coefficient for the Rb D_1 line $\beta/2\pi = (0.69 \pm 0.04) \times 10^{-7}$ Hz cm^3, and infer a natural linewidth $\Gamma_0/2\pi = (5.7 \pm 0.7)$ MHz from the intercept of the fit. The experimentally determined self-broadening coefficient is in excellent agreement with the theoretical prediction presented in table 3.2.

In table 3.2 we have collated experimental measurements of the D_1 and D_2 self-broadening coefficients for Na, Rb and Cs, and compared these measurements with the theoretical predictions of equations 3.21 and 3.22. A variety of experimental techniques were used for the measurements (line-wing absorption, and reflection spectroscopy); all of the values are in excellent agreement with the theoretical prediction within the quoted uncertainty. The statistical variation in the Rb density evaluated from the five spectra in each series of measurements is very small (0.6%); two possible systematic errors in the evaluation of number density are the accuracy of the vapour pressure formula in [121] and the small difference between the temperature of the atoms interacting with the light and the atoms in the metal reservoir.

The centre of the Rb absorption lines are shifted in dense vapour owing to local-field effects [127]. Next we show that the shift is expected to be proportional to the atomic density [128], and for the highest density studied in this work is of the order of 18 MHz - too small to be evident. In addition we will also show that at densities of the order of 10^{16} cm^{-3} dipole-dipole interactions can lead to the saturation of the resonance susceptibility [18].

3.6 Shifts and saturation

In section 3.6 the Lorentz-Lorenz and collisional shifts of the resonance lines are discussed and are shown to be too small to be evident. We also write the saturated susceptibility on resonance for a large number density medium.

3.6.1 Lorentz-Lorenz and collisional shifts

Transfer of optical coherence from an excited state atom to a ground state atom can lead to a shift of the resonance line. In alkali-metal atoms the density dependence of the line shift has been studied extensively [125, 129–132]. In high density vapours the total line shift is given by the Lorentz-Lorenz, $\Delta_{\rm LL}$, and collisional, $\Delta_{\rm col}$, shifts, which are both proportional to the total atomic density and therefore difficult to distinguish experimentally. Keaveney *et al.* [18] has shown the collisional shift to be $\Delta_{\rm col} = \alpha\mathcal{N}$ where $\alpha/2\pi = (-0.25 \pm 0.01) \times 10^{-7}$ Hz cm^3 in a nanothickness atomic vapour layer for similar conditions. For the number densities studied in this work the collisional shift is of the order of 8 MHz. In addition they have shown a shift in the resonance frequency due to dipole-dipole interactions can be given by the Lorentz shift [133]

$$\Delta_{\rm LL} = -\frac{\mathcal{N}\mu^2}{3\hbar\epsilon_0} \ . \tag{3.31}$$

For the D_1 and D_2 lines of Rb where $\mu_1^2 = d_1^2/3$ and $\mu_2^2 = 2d_2^2/3$, respectively, $\Delta_{\rm LL}$ can be written in terms of the self-broadened linewidth as

$$\Delta_{\rm LL}(D_1) = -\frac{d_1^2\mathcal{N}}{9\hbar\epsilon_0} = -\frac{\Gamma_{\rm self}}{2} \ , \tag{3.32}$$

$$\Delta_{\rm LL}(D_2) = -\frac{2d_2^2\mathcal{N}}{9\hbar\epsilon_0} = -\frac{\Gamma_{\rm self}}{\sqrt{2}} \ . \tag{3.33}$$

The total red shift including the collisional shift for a thermal ensemble on the D_1 line of Rb is 18 MHz for the temperatures studied here. In the calibration of the frequency axis we expect an error similar to the magnitude of this shift. Therefore this shift will be too small to be evident. We also note that the self-broadened width, $\Gamma_{\rm self}$, is 2 and $\sqrt{2}$ times the Lorentz shift, $\Delta_{\rm LL}$, for the D_1 and D_2 lines, respectively.

3.6.2 Saturation of the resonance susceptibility

In section 2.2.2 we wrote the real and imaginary parts of the susceptibility. On resonance, $\Delta = 0$, χ_R is zero and χ_I is equal to

$$\chi_I = \frac{\mathcal{N}\mu^2}{\hbar\epsilon_0}\frac{2}{\Gamma_0} , \tag{3.34}$$

Substituting for the reduced dipole matrix elements and replacing the natural linewidth, Γ_0 with the total Lorentzian linewidth, $\Gamma_{\rm tot}$ gives the imaginary susceptibility for the D_1 and D_2 lines as

$$\chi_I(\mathrm{D}_1) = \frac{\mathcal{N}d_1^2}{3\hbar\epsilon_0}\frac{2}{\Gamma_{\rm tot}} , \tag{3.35}$$

$$\chi_I(\mathrm{D}_2) = \frac{\mathcal{N}d_2^2}{3\hbar\epsilon_0}\frac{4}{\Gamma_{\rm tot}} . \tag{3.36}$$

Substituting for the natural linewidths, equations 3.29 and 3.30 and the cooperativity parameter the imaginary susceptibilities for the Rb D lines are

$$\chi_I(\mathrm{D}_1) = \frac{3C_1}{1+C_1} , \tag{3.37}$$

$$\chi_I(\mathrm{D}_2) = \frac{6C_2}{1+\sqrt{2}C_2} . \tag{3.38}$$

At high densities where $C_{1,2} \gg 1$, the resonance susceptibility saturates and the final expressions tend to

$$\chi_I(\mathrm{D}_1) \to 3 , \tag{3.39}$$

$$\chi_I(\mathrm{D}_2) \to 3\sqrt{2} . \tag{3.40}$$

Therefore for a non-interacting medium the susceptibility increases linearly with atomic density, for an interacting medium the susceptibility saturates. For a thin dipolar layer it has been shown that however many scatterers you add, the medium never becomes opaque [134].

3.7 Discussion

In summary, we have experimentally shown that for hot Rb vapour with density up to 3×10^{14} cm^{-3} the Lorentzian component of the D_1 line is modified as the result of dipole-dipole interactions. The off-resonant absorption lineshape is sensitive to the total homogeneous linewidth, which grows linearly with the number density of atoms. We have shown that a simple modification of the theoretical model for electric susceptibility to take into account self-broadening leads to excellent agreement between theory and experiment. Absolute absorption spectra have been measured for detunings of the order of the Weisskopf frequency or less and for temperatures up to ~ 170°C with deviation of 0.1% between theory and experiment. These measurements allowed us to ascertain the value of the self-broadening coefficient for the Rb D_1 line to be $\beta/2\pi = (0.69 \pm 0.04) \times 10^{-7}$ Hz cm^3, which is in excellent agreement with the theoretical impact self-broadening coefficient. Our results give new insight into the resonant dipole-dipole collision physics in dense atomic vapours. Next we include the magnetic interaction Hamiltonian for the matrix representation discussed in chapter 2. We also outline the experimental procedures with which we choose to investigate the absorption and dispersion properties of an atomic ensemble in an external magnetic field.

Chapter 4

Including the magnetic field interaction

This chapter is based on the following publication

L. Weller, K. S. Kleinbach, M. A. Zentile, S. Knappe, C. S. Adams, and I. G. Hughes, *Absolute absorption and dispersion of a rubidium vapour in the hyperfine Paschen-Back regime*, J. Phys. B: At. Mol. Opt. Phys. **45**, 215005 (2012), 10.1088/0953-4075/45/21/215005

Here we report on measurements of the absolute absorption and dispersion properties of an isotopically pure ^{87}Rb vapour for magnetic fields up to and including 0.6 T. We discuss the various regimes that arise when the hyperfine and Zeeman interactions have different magnitudes, and show that we enter the hyperfine Paschen-Back regime for fields greater than 0.33 T on the Rb D_2 line. The experiment uses a compact 1 mm^3 microfabricated vapour cell that makes it easy to maintain a uniform and large magnetic field with a small and inexpensive magnet. We find excellent agreement between the experimental results and numerical calculations of the weak probe susceptibility where the line positions and strengths are calculated by matrix diagonalisation.

4.1 Introduction

In chapters 2 and 3 a detailed description of the model used to calculate atomic susceptibility incorporating the energy levels and transition probabilities of the Rb ensemble is shown. In summary, the lineshape around resonance is given by a convolution of the Lorentzian (accounting for natural and self-broadening) and a Gaussian distribution incorporating the Doppler shift due to thermal motion. The medium's susceptibility, χ, is then calculated by summing over the electric-dipole-allowed transitions. From the atomic susceptibility we are able to model the absorptive and dispersive properties of the medium. The refractive index and absorption coefficients can be calculated by use of the real, $n = 1 + \chi_{\mathrm{R}}/2$, and imaginary, $\alpha = k\chi_{\mathrm{I}}$, parts of the susceptibility, respectively, where k is the wavevector. In the absence of field, absolute Doppler-broadened absorption [40, 92] (see chapter 2) in the low density regime, and dipole-dipole interactions [22] in the binary-collision regime (see chapter 3) have been tested. The absorption and dispersion of an atomic ensemble in an external magnetic field can also be calculated from the atomic susceptibility. The motivation for chapter 4 is to include the presence of a magnetic field for the absolute susceptibility in a ^{87}Rb vapour on the D_2 line. Here we will outline the procedures used to compare experimental results and numerical calculations for absolute absorption and dispersion for fields up to and including 0.6 T. It should be noted that at such fields the nuclear spin, I, and total electronic angular momentum, J, are decoupled for both ground and excited terms and the total angular momentum, F, is no longer a good quantum number; this is known as the hyperfine Paschen-Back regime [135].

4.2 Atomic Hamiltonian

The atomic Hamiltonian can be written as

$$\hat{H} = \hat{H}_0 + \hat{H}_{\mathrm{fs}} + \hat{H}_{\mathrm{hfs}} + \hat{H}_{\mathrm{Z}} \ , \tag{4.1}$$

where $\hat{H}_0$ is the coarse atomic structure; $\hat{H}_{\mathrm{fs}}$ and $\hat{H}_{\mathrm{hfs}}$ describes the fine and hyperfine interactions and $\hat{H}_{\mathrm{Z}}$; represents the atomic interaction with

an external magnetic field. The zero detuning frequencies in the absence of hyperfine splitting for ^{87}Rb and ^{85}Rb on the D_1 ($5^2S_{1/2} \rightarrow 5^2P_{1/2}$) and D_2 ($5^2S_{1/2} \rightarrow 5^2P_{3/2}$) lines are 377.11 THz [101] and 384.23 THz [102], respectively. The splittings associated with the hyperfine interaction Hamiltonian around the zero-detuning energies can be calculated by use of the following expression (see equation 2.42)

$$\Delta E_{hfs} = \frac{A_{hfs}}{2}K + \frac{B_{hfs}}{4}\frac{\frac{3}{2}K(K+1) - 2I(I+1)J(J+1)}{I(2I-1)J(2J-1)} , \tag{4.2}$$

where A_{hfs} is the magnetic dipole constant, B_{hfs} is the electric quadrupole constant and $K = F(F+1) - I(I+1) - J(J+1)$; see equation 9.60 in [104]. The numerical values to this expression can be found in, for example, figure 2.3 of chapter 2. For an external magnetic field the magnetic interaction Hamiltonian has a linear and quadratic term in $\hat{B}$ [100]. For typical laboratory magnetic fields, quadratic shifts for terms with a low principal quantum number, n, are extremely difficult to observe. Therefore the quadratic term in $\hat{B}$ can usually be ignored; however, with high n terms the dependence is very much evident [1]. The magnetic interaction Hamiltonian for an external field has the form

$$\hat{H}_Z = -(\hat{\mu}_L + \hat{\mu}_S + \hat{\mu}_I) \cdot \hat{B} , \tag{4.3}$$

where $\hat{\mu}_L$, $\hat{\mu}_S$ and $\hat{\mu}_I$ are the magnetic moments of the orbital motion due to the electron, the spin of the electron and the nucleus, respectively. The magnetic moments are related to the orbital and electron spins by $\hat{\mu}_L = \mu_B g_L L/\hbar$ and $\hat{\mu}_S = \mu_B g_S S/\hbar$, with the nuclear spin given by $\hat{\mu}_I = \mu_N g_I I/\hbar$. We can ignore the contribution due to the magnetic moment of the nucleus, $\hat{\mu}_I$, because g_I is very small (see table 4.1) and the nuclear magneton is three orders of magnitude smaller than the Bohr magneton (see equation 2.39). Therefore the final form of the interaction Hamiltonian for an external magnetic field is

$$\hat{H}_Z = \frac{\mu_B}{\hbar}\left(g_L\hat{L} + g_S\hat{S}\right) \cdot \hat{B} . \tag{4.4}$$

The different spacings ΔE_Z associated with the magnetic interaction Hamiltonian are discussed in section 4.4.

[1] The topic of diamagnetic shifts in Rydberg atoms has been studied for many years. For magnetic fields of about 0.6 T the shifts become evident for terms above $n \approx 56$ [136].

g-factor	Symbol	^{87}Rb	^{85}Rb
Electron spin	g_S	2.002 [137]	
Electron orbital	g_L	0.999 [138]	
Nuclear	g_I	-0.000995 [102]	-0.000294 [102]
Fine structure Landé	$g_J(5^2S_{1/2})$	2.002	
	$g_J(5^2P_{1/2})$	0.666	
	$g_J(5^2P_{3/2})$	1.336	

Table 4.1: The electron orbital, electron spin, nuclear spin and fine structure Landé g-factors for the $5^2S_{1/2}$, $5^2P_{1/2}$ and $5^2P_{3/2}$ terms in ^{87}Rb and ^{85}Rb. The fine structure Landé g-factors are calculated using equation 4.6.

4.3 Matrix representation of $\hat{H}_Z$

In chapter 2 we obtained numerical values for the susceptibility from a matrix representation of the Hamiltonian for the fine and hyperfine interactions, which are calculated in the completely uncoupled $|m_L, m_S, m_I\rangle$ basis. The frequency detunings and transition strengths were calculated from a numerical diagonalisation of this matrix. Here we include the Hamiltonian describing the atomic interaction with a magnetic field along the z-direction

$$\hat{H}_Z = \frac{\mu_B}{\hbar}\left(g_L L_z + g_S S_z\right) B_z \ , \tag{4.5}$$

where μ_B is the Bohr magneton and g_L and g_S are the the electron orbital and electron spin g-factors that account for various modifications to the corresponding magnetic dipole moments. The fine structure Landé g-factors are calculated as follows [139]

$$\begin{aligned} g_J = \quad & g_L \frac{J(J+1) - S(S+1) + L(L+1)}{2J(J+1)} \\ & + g_S \frac{J(J+1) + S(S+1) - L(L+1)}{2J(J+1)} \ . \end{aligned} \tag{4.6}$$

Table 4.1 shows the values of the electron orbital g-factor, g_L, the electron spin g-factor, g_S and fine structure Landé g-factor, g_J for the $5^2S_{1/2}$, $5^2P_{1/2}$ and $5^2P_{3/2}$ terms in ^{87}Rb and ^{85}Rb. Now we take the example in chapter 2 of the D_1 ($5^2S_{1/2} \rightarrow 5^2P_{1/2}$) line for ^{87}Rb ($I = 3/2$). We start by including the magnetic interaction Hamiltonian for the $5^2S_{1/2}$ term. The eigenvalues

are given by the analytic Breit-Rabi formula [140], with eigenfunctions being calculated and generalised for any value of B_z. We then include the magnetic interaction Hamiltonian for both the $5^2P_{1/2}$ and $5^2P_{3/2}$ terms. For the $5^2P_{1/2}$ term as $J' = 1/2$, we can again use the analytic Breit-Rabi formula for the eigenvalues. Here for the operator C_R acting on the coupled $|F', m_{F'}\rangle$ basis we also show generalised coefficients. For the $5^2P_{3/2}$ term the eigenvalues and eigenfunctions must be calculated numerically.

4.3.1 $5^2S_{1/2}$ matrix

For the $5^2S_{1/2}$ term, where $L = 0$ and $S = 1/2$, the magnetic interaction Hamiltonian is

$$\hat{H}_Z = \frac{g_S \mu_B B_z}{\hbar} S_z \ , \tag{4.7}$$

Including the $\hat{H}_{hfs}$ matrix from chapter 2 the Hamiltonian is written as

$$\hat{H} = \hat{H}_{hfs} + \hat{H}_Z = \frac{A_{hfs}}{\hbar^2} I \cdot J + \frac{g_S \mu_B B_z}{\hbar} S_z \ . \tag{4.8}$$

The $5^2S_{1/2}$ matrix is populated as follows

$$\hat{H} = A_{hfs} \begin{pmatrix} \frac{3}{4} & 0 & 0 & 0 & 0 & 0 & 0 & 0 \\ 0 & \frac{1}{4} & 0 & 0 & \frac{\sqrt{3}}{2} & 0 & 0 & 0 \\ 0 & 0 & -\frac{1}{4} & 0 & 0 & 1 & 0 & 0 \\ 0 & 0 & 0 & -\frac{3}{4} & 0 & 0 & \frac{\sqrt{3}}{2} & 0 \\ 0 & \frac{\sqrt{3}}{2} & 0 & 0 & -\frac{3}{4} & 0 & 0 & 0 \\ 0 & 0 & 1 & 0 & 0 & -\frac{1}{4} & 0 & 0 \\ 0 & 0 & 0 & \frac{\sqrt{3}}{2} & 0 & 0 & \frac{1}{4} & 0 \\ 0 & 0 & 0 & 0 & 0 & 0 & 0 & \frac{3}{4} \end{pmatrix}$$
$$+ g_S \mu_B B_z \begin{pmatrix} \frac{1}{2} & 0 & 0 & 0 & 0 & 0 & 0 & 0 \\ 0 & \frac{1}{2} & 0 & 0 & 0 & 0 & 0 & 0 \\ 0 & 0 & \frac{1}{2} & 0 & 0 & 0 & 0 & 0 \\ 0 & 0 & 0 & \frac{1}{2} & 0 & 0 & 0 & 0 \\ 0 & 0 & 0 & 0 & -\frac{1}{2} & 0 & 0 & 0 \\ 0 & 0 & 0 & 0 & 0 & -\frac{1}{2} & 0 & 0 \\ 0 & 0 & 0 & 0 & 0 & 0 & -\frac{1}{2} & 0 \\ 0 & 0 & 0 & 0 & 0 & 0 & 0 & -\frac{1}{2} \end{pmatrix} \ , \tag{4.9}$$

where A_{hfs} and g_S can be obtained from table 2.1 and 4.1, respectively, and B_z is the magnetic field along the z-direction. The matrices are ordered as in section 2.4.2. Analytic diagonalisation leads to the well-known Breit-Rabi solution for a generalised matrix of eigenvalues and eigenfunctions given by

(4.10)

$$
\begin{array}{c|cccccccccc}
 & \lambda_-^{+1} & \lambda_-^{0} & \lambda_-^{-1} & \lambda_+^{-2} & \lambda_+^{-1} & \lambda_+^{0} & \lambda_+^{+1} & \lambda_+^{+2} \\
\hline
\lambda_-^{+1} & 0 & \frac{\sqrt{3}}{\sqrt{3+\left|g_+^{+1}\right|^2}} & 0 & 0 & 0 & 0 & 0 & 0 \\
\lambda_-^{0} & \frac{\sqrt{3}}{\sqrt{3+\left|g_+^{+1}\right|^2}} & 0 & \frac{2}{\sqrt{4+\left|g_+^{+0}\right|^2}} & 0 & 0 & 0 & 0 & 0 \\
\lambda_-^{-1} & 0 & \frac{2}{\sqrt{4+\left|g_+^{+0}\right|^2}} & 0 & -\frac{\sqrt{3}}{\sqrt{3+\left|g_+^{-1}\right|^2}} & 0 & 0 & 0 & 0 \\
\hline
\lambda_+^{-2} & 0 & 0 & -\frac{\sqrt{3}}{\sqrt{3+\left|g_+^{-1}\right|^2}} & 0 & \frac{\sqrt{3}}{\sqrt{3+\left|g_-^{-1}\right|^2}} & 0 & 0 & 1 \\
\lambda_+^{-1} & 0 & 0 & 0 & \frac{\sqrt{3}}{\sqrt{3+\left|g_-^{-1}\right|^2}} & 0 & \frac{2}{\sqrt{4+\left|g_-^{+0}\right|^2}} & 0 & 0 \\
\lambda_+^{0} & 0 & 0 & 0 & 0 & \frac{2}{\sqrt{4+\left|g_-^{+0}\right|^2}} & 0 & \frac{\sqrt{3}}{\sqrt{3+\left|g_-^{+1}\right|^2}} & 0 \\
\lambda_+^{+1} & 0 & 0 & 0 & 0 & 0 & \frac{\sqrt{3}}{\sqrt{3+\left|g_-^{+1}\right|^2}} & 0 & 0 \\
\lambda_+^{+2} & 1 & 0 & 0 & 0 & 0 & 0 & 0 & 0
\end{array}
$$

Here $\lambda_{\pm}^{m}$ are the eigenvalues given by the Breit-Rabi formula [140]

$$\lambda_{\pm}^{m} = -\frac{1}{4} \pm \sqrt{1 + m x_g + x_g^2}\,, \tag{4.11}$$

where $m = m_F = m_I + m_J$ (see page 192 in [104]) and x_g is the ratio of the Zeeman to hyperfine interactions given by

$$x_g = \frac{g_S \mu_{\mathrm{B}} B_z}{2A_{\mathrm{hfs}}}\,. \tag{4.12}$$

To avoid sign ambiguity we write the eigenvalues for $m = \pm 2$ as

$$\lambda_{+}^{\pm 2} \;=\; \frac{3}{4} \pm x_g\,. \tag{4.13}$$

The coefficients are given by

$$g_{\pm}^{m} \;=\; m + 2x_g \pm 2\sqrt{1 + m x_g + x_g^2}\,. \tag{4.14}$$

Note that the coefficients for $|2,-2\rangle$ and $|2,+2\rangle$ are always equal to one. Therefore the decomposition is always written as

$$|2,-2\rangle \;=\; \left|0,-\frac{1}{2},-\frac{3}{2}\right\rangle\,, \tag{4.15}$$

$$|2,+2\rangle \;=\; \left|0,+\frac{1}{2},+\frac{3}{2}\right\rangle\,. \tag{4.16}$$

These are referred to as stretched states (see page 71 in [103]). As these states are made up from only one combination of m_L, m_S and m_I, they have constant magnetic moments and therefore are straight lines on the Breit-Rabi diagram. Figure 4.1 shows the Breit-Rabi diagram for the $5^2\mathrm{S}_{1/2}$ term of ^{87}Rb. The solid (black) lines show the energy levels calculated using equation 4.11 as a function of magnetic field. The solid (red) lines show the stretched $|2,-2\rangle$ and $|2,+2\rangle$ states calculated using equation 4.13 with gradients -1 and 1, respectively. The dashed (grey) line with a gradient $1/2$ describes the $|1,-1\rangle$ if it was a stretched state. For fields smaller and bigger than the intercept with the $|2,-2\rangle$ state we define different regimes. In table 4.3 we give values for these intercepts for the $5^2\mathrm{S}_{1/2}$, $5^2\mathrm{P}_{1/2}$ and $5^2\mathrm{P}_{3/2}$ terms in ^{85}Rb and ^{87}Rb. The $|F, m_F\rangle$ basis and $|m_L, m_S, m_I\rangle$ basis are ordered the same as in chapter 2. Decomposing this basis gives generalised Clebsch-Gordan coefficients which vary as a function of magnetic field.

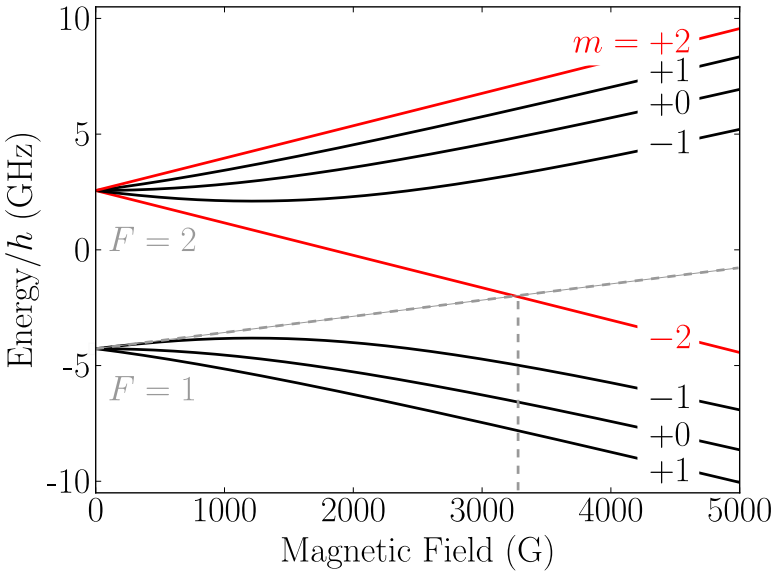

Figure 4.1: Breit-Rabi diagram for the $5^2S_{1/2}$ term of ^{87}Rb. The solid (black) lines show the energy levels as a function of magnetic field. The solid (red) lines are the stretched states. The levels are grouped according to $F = 1$ or $F = 2$ states for low-fields and $m_J = 1/2$ or $m_J = -1/2$ states for high-fields. The sub-levels are given by $m = m_F = m_I + m_J$. The dashed (grey) lines allow one to extract a magnetic field value where the interaction is best described by the $|m_J, m_I\rangle$ basis.

$$|1,+1\rangle = \frac{\sqrt{3}}{\sqrt{3+\left|g_+^{+1}\right|^2}}\left|0,+\frac{1}{2},+\frac{1}{2}\right\rangle - \frac{g_+^{+1}}{\sqrt{3+\left|g_+^{+1}\right|^2}}\left|0,-\frac{1}{2},+\frac{3}{2}\right\rangle \ , \tag{4.17}$$

$$|1,+0\rangle = \frac{2}{\sqrt{4+\left|g_+^{+0}\right|^2}}\left|0,+\frac{1}{2},-\frac{1}{2}\right\rangle - \frac{g_+^{+0}}{\sqrt{4+\left|g_+^{+0}\right|^2}}\left|0,-\frac{1}{2},+\frac{1}{2}\right\rangle \ , \tag{4.18}$$

$$|1,-1\rangle = \frac{g_+^{-1}}{\sqrt{3+\left|g_+^{-1}\right|^2}}\left|0,-\frac{1}{2},-\frac{1}{2}\right\rangle - \frac{\sqrt{3}}{\sqrt{3+\left|g_+^{-1}\right|^2}}\left|0,+\frac{1}{2},-\frac{3}{2}\right\rangle \ , \tag{4.19}$$

$$|2,-2\rangle = \left|0,-\frac{1}{2},-\frac{3}{2}\right\rangle \ , \tag{4.20}$$

$$|2,-1\rangle = \frac{\sqrt{3}}{\sqrt{3+\left|g_-^{-1}\right|^2}}\left|0,+\frac{1}{2},-\frac{3}{2}\right\rangle - \frac{g_-^{-1}}{\sqrt{3+\left|g_-^{-1}\right|^2}}\left|0,-\frac{1}{2},-\frac{1}{2}\right\rangle \ , \tag{4.21}$$

$$|2,+0\rangle = \frac{2}{\sqrt{4+\left|g_-^{+0}\right|^2}}\left|0,+\frac{1}{2},-\frac{1}{2}\right\rangle - \frac{g_-^{+0}}{\sqrt{4+\left|g_-^{+0}\right|^2}}\left|0,-\frac{1}{2},+\frac{1}{2}\right\rangle \ , \tag{4.22}$$

$$|2,+1\rangle = \frac{g_-^{+1}}{\sqrt{3+\left|g_-^{+1}\right|^2}}\left|0,-\frac{1}{2},+\frac{3}{2}\right\rangle - \frac{\sqrt{3}}{\sqrt{3+\left|g_-^{+1}\right|^2}}\left|0,+\frac{1}{2},+\frac{1}{2}\right\rangle \ , \tag{4.23}$$

$$|2,+2\rangle = \left|0,+\frac{1}{2},+\frac{3}{2}\right\rangle \ . \tag{4.24}$$

In appendix E we plot the Breit-Rabi diagrams for the $5^2S_{1/2}$, $5^2P_{1/2}$ and $5^2P_{3/2}$ terms in ^{85}Rb and ^{87}Rb. In the absence of magnetic field, $x_g = 0$ and equation 4.11 reduces to

$$\lambda_{\pm} = -\frac{1}{4} \pm 1 \,, \tag{4.25}$$

which are the eigenvalues $-\frac{5}{4}$ and $\frac{3}{4}$, corresponding to the 3 and 5 m_F values for the $F = 1$ and $F = 2$ states, respectively. In addition, when $x_g = 0$ the coefficients given by equation 4.14 for m_F values -1, 0 and 1 are

$$g_{\pm}^{-1} = -1 \pm 2 \,, \tag{4.26}$$

$$g_{\pm}^{+0} = \pm 2 \,, \tag{4.27}$$

$$g_{\pm}^{+1} = 1 \pm 2 \,. \tag{4.28}$$

Substituting both the eigenvalues and coefficients into the generalised matrix given by 4.10 we get matrix 2.49, which is the same one calculated in chapter 2. For a magnetic field, $B_z = 0.6$ T ($x_g/h = 2.46$) coefficients are

$$g_{\pm}^{-1} = 3.92 \pm 4.28 \,, \tag{4.29}$$

$$g_{\pm}^{+0} = 4.92 \pm 5.31 \,, \tag{4.30}$$

$$g_{\pm}^{+1} = 5.92 \pm 6.16 \,, \tag{4.31}$$

and the matrix is

$$\left(\begin{array}{c|cccccccc}
-3.33 & 0 & 0.142 & 0 & 0 & -0.990 & 0 & 0 & 0 \\
-2.90 & 0 & 0 & 0.192 & 0 & 0 & -0.981 & 0 & 0 \\
-2.39 & 0 & 0 & 0 & 0.207 & 0 & 0 & -0.978 & 0 \\
-1.71 & 0 & 0 & 0 & 0 & 0 & 0 & 0 & 1 \\
\hline
1.89 & 0 & 0 & 0 & 0.978 & 0 & 0 & 0.207 & 0 \\
2.40 & 0 & 0 & 0.981 & 0 & 0 & 0.192 & 0 & 0 \\
2.83 & 0 & -0.990 & 0 & 0 & -0.142 & 0 & 0 & 0 \\
3.21 & 1 & 0 & 0 & 0 & 0 & 0 & 0 & 0
\end{array}\right) . \tag{4.32}$$

Here the diagonlisation gives four negative eigenvalues and four positive eigenvalues. These eigenvalues can be described by the m_J quantum numbers $-1/2$ or $1/2$, with m_I being $-3/2$, $-1/2$, $1/2$ and $3/2$. Hence, in this regime the $|m_J, m_I\rangle$ basis best describes the interaction.

4.3.2 $5^2P_{1/2}$ matrix

For the $5^2P_{1/2}$ term the analysis for the eigenvalues and eigenfunctions is slightly different. In order to calculate the angular coupling element $\langle F, m_F|C_{L,R,0}|F', m_{F'}\rangle$ we need two parts. The first part was calculated in section 4.3.1 and are the $\langle F, m_F|$ states for the $5^2S_{1/2}$ term. For the second part we need to consider the large matrix shown in figure 2.4 that describes the $|F', m_{F'}\rangle$ states for the $5^2P_{1/2}$ and $5^2P_{3/2}$ terms. As in chapter 2 to simplify the calculation here we chose to calculate the operator C_R acting on the coupled $|F', m_{F'}\rangle$ basis.

A Hamiltonian for the 5P matrix was calculated in chapter 2. Here we discuss the inclusion of the magnetic interaction Hamiltonian for the $5^2P_{1/2}$ term. For the $5^2P_{1/2}$ term, where $L = 1$ and $S = 1/2$, the magnetic interaction Hamiltonian is written as

$$\hat{H}_Z = \frac{\mu_B B_z}{\hbar}\left(g_L L_z + g_S S_z\right) . \tag{4.33}$$

If we now include this Hamiltonian with the calculated Hamiltonian from chapter 2 we have

$$\begin{aligned}\hat{H} &= \hat{H}_{fs} + \hat{H}_{hfs} + \hat{H}_Z ,\\ \hat{H} &= \frac{\gamma_{fs}}{\hbar^2}\hat{L}\cdot\hat{S} + 2\frac{\gamma_{fs}}{\hbar^2} \otimes \mathbb{1}_{D_{nl}} + \frac{A_{hfs}}{\hbar^2}\hat{I}\cdot\hat{J} + \frac{\mu_B B_z}{\hbar}\left(g_L L_z + g_S S_z\right) .\end{aligned} \tag{4.34}$$

Analytic diagonalisation of this modified Hamiltonian leads to the well-known Breit-Rabi solution for a generalised matrix $C_R\,|F', m_{F'}\rangle$ given by 4.35. For this matrix $g = e$ and the eigenvalues, $\lambda_\pm^m$, are given by equation 4.11 with the ratio x_e given by equation 4.12. Note $g_S = g_J$ when $L = 1$. For the $5^2P_{1/2}$ state g_J is shown in table 4.1 and A_{hfs} is given in table 2.1. The coefficients, $e_\pm^m$, are calculated using equation 4.14. Here also N is a factor that arises from the diagonalisation of the Hamiltonian for the $5^2P_{1/2}$ and $5^2P_{3/2}$ terms. In section 4.3.3 we discuss in detail the origin and magnitude of this factor. In the absence of magnetic field ($x_e = 0$) the matrix is equal to 2.64. The $|F', m_{F'}\rangle$ basis and $|m_{L'}, m_{S'}, m_{I'}\rangle$ basis are ordered the same as in chapter 2.

$$\left(\begin{array}{c|cccccccc}
\lambda_-^{+1} & \frac{Ne_+^{+1}}{\sqrt{3+\left|e_+^{+1}\right|^2}} & 0 & 0 & 0 & 0 & 0 & 0 & 0 \\
\lambda_-^{+0} & 0 & \frac{Ne_+^{+0}}{\sqrt{4+\left|e_+^{+0}\right|^2}} & 0 & 0 & 0 & 0 & 0 & 0 \\
\lambda_-^{-1} & 0 & 0 & \frac{Ne_+^{-1}}{\sqrt{3+\left|e_+^{-1}\right|^2}} & 0 & 0 & 0 & 0 & 0 \\
\hline
\lambda_+^{-2} & 0 & 0 & 0 & -N & 0 & 0 & 0 & 0 \\
\lambda_+^{-1} & 0 & 0 & -\frac{Ne_-^{-1}}{\sqrt{3+\left|e_-^{-1}\right|^2}} & 0 & 0 & 0 & 0 & 0 \\
\lambda_+^{+0} & 0 & -\frac{Ne_-^{+0}}{\sqrt{4+\left|e_-^{+0}\right|^2}} & 0 & 0 & 0 & 0 & 0 & 0 \\
\lambda_+^{+1} & -\frac{Ne_-^{+1}}{\sqrt{3+\left|e_-^{+1}\right|^2}} & 0 & 0 & 0 & 0 & 0 & 0 & 0 \\
\lambda_+^{+2} & 0 & 0 & 0 & 0 & 0 & 0 & 0 & 0
\end{array}\right) , \tag{4.35}$$

Decomposing into the $|m_{L'}, m_{S'}, m_{I'}\rangle$ basis gives generalised Clebsch-Gordan coefficients which vary as a function of magnetic field.

$$C_R\,|1,+1\rangle = \frac{Ne_+^{+1}}{\sqrt{3+\left|e_+^{+1}\right|^2}}\left|-1,+\frac{1}{2},+\frac{3}{2}\right\rangle , \tag{4.36}$$

$$C_R\,|1,+0\rangle = \frac{Ne_+^{+0}}{\sqrt{4+\left|e_+^{+0}\right|^2}}\left|-1,+\frac{1}{2},+\frac{1}{2}\right\rangle , \tag{4.37}$$

$$C_R\,|1,-1\rangle = \frac{Ne_+^{-1}}{\sqrt{3+\left|e_+^{-1}\right|^2}}\left|-1,+\frac{1}{2},-\frac{1}{2}\right\rangle , \tag{4.38}$$

$$C_R\,|2,-2\rangle = -N\left|-1,+\frac{1}{2},-\frac{3}{2}\right\rangle , \tag{4.39}$$

$$C_R\,|2,-1\rangle = -\frac{Ne_-^{-1}}{\sqrt{3+\left|e_-^{-1}\right|^2}}\left|-1,+\frac{1}{2},-\frac{1}{2}\right\rangle , \tag{4.40}$$

$$C_R\,|2,+0\rangle = -\frac{Ne_-^{+0}}{\sqrt{4+\left|e_-^{+0}\right|^2}}\left|-1,+\frac{1}{2},+\frac{1}{2}\right\rangle , \tag{4.41}$$

$$C_R\,|2,+1\rangle = -\frac{Ne_-^{+1}}{\sqrt{3+\left|e_-^{+1}\right|^2}}\left|-1,+\frac{1}{2},+\frac{3}{2}\right\rangle , \tag{4.42}$$

$$C_R\,|2,+2\rangle = 0\ . \tag{4.43}$$

For a magnetic field, $B_z = 0.6$ T ($x_e/h = 6.87$) the coefficients are

$$e_{\pm}^{-1} = 12.8 \pm 12.9 \,, \tag{4.44}$$

$$e_{\pm}^{+0} = 13.8 \pm 13.9 \,, \tag{4.45}$$

$$e_{\pm}^{+1} = 14.8 \pm 14.9 \,, \tag{4.46}$$

and the matrix is

$$\left(\begin{array}{c|cccccccc} -7.68 & 0.815 & 0 & 0 & 0 & 0 & 0 & 0 & 0 \\ -7.20 & 0 & 0.814 & 0 & 0 & 0 & 0 & 0 & 0 \\ -6.68 & 0 & 0 & 0.815 & 0 & 0 & 0 & 0 & 0 \\ -6.12 & 0 & 0 & 0 & -0.816 & 0 & 0 & 0 & 0 \\ \hline 6.18 & 0 & 0 & -0.055 & 0 & 0 & 0 & 0 & 0 \\ 6.70 & 0 & -0.059 & 0 & 0 & 0 & 0 & 0 & 0 \\ 7.17 & -0.048 & 0 & 0 & 0 & 0 & 0 & 0 & 0 \\ 7.62 & 0 & 0 & 0 & 0 & 0 & 0 & 0 & 0 \end{array}\right) . \tag{4.47}$$

Here the diagonlisation gives four negative eigenvalues and four positive eigenvalues. These eigenvalues can be described by the $m_{J'}$ quantum numbers $-1/2$ or $1/2$, with $m_{I'}$ being $-3/2$, $-1/2$, $1/2$ and $3/2$. Hence, in this regime the $|m_{J'}, m_{I'}\rangle$ basis best describes the interaction.

4.3.3 Relative line-strengths and transition frequencies

In section 4.3.2 we introduced a factor N that arises from the diagonalisation of the 5P matrix. Figure 4.2 shows the relative line-strengths in the hyperfine Paschen-Back regime for σ^- transitions on the $m_J \rightarrow m_{J'}$ lines in Rb. The relative line-strengths are calculated using the same method described in section 2.5.1. Here it is evident that this N factor arises due to the fact that the $m_J = 1/2$ quantum number for the $5^2S_{1/2}$ term couples to both the $5^2P_{1/2}$ and $5^2P_{3/2}$ terms in the excited manifold, whereas the $m_J = -1/2$ quantum number only couples to the $5^2P_{3/2}$ term. For the $5^2P_{1/2}$ term $N = \sqrt{2/3}$ and for the $5^2P_{3/2}$ term factors of $N = \sqrt{1/3}$ and $N = 1$ arise from diagonalisation. Note the sum of the relative strengths is always 2 and the D_2 line is twice as strong as the D_1 line.

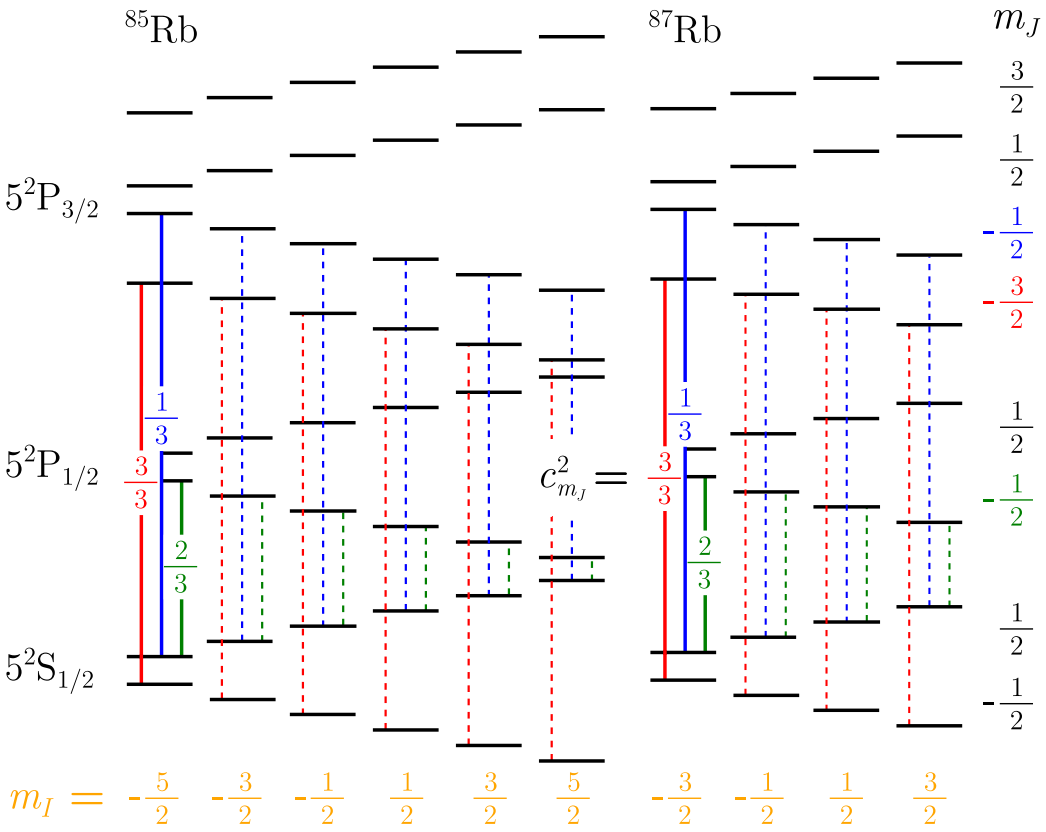

Figure 4.2: Relative line-strengths for σ^- transitions on the $m_J \rightarrow m_{J'}$ lines for ^{85}Rb and ^{87}Rb in the hyperfine Paschen-Back (HPB) regime. The $m_J = 1/2$ quantum number in the $5^2S_{1/2}$ term couples to both the $5^2P_{1/2}$ and $5^2P_{3/2}$ terms with strengths 2/3 and 1/3, respectively. The $m_J = -1/2$ quantum number in the $5^2S_{1/2}$ term only couples to the $5^2P_{3/2}$ term with a strength of 1.

Now we understand the relative line-strengths the next step is to calculate the frequencies for each dipole allowed transition. As in section 2.5.2 the detunings (in GHz) are calculated as follows

$$\Delta_{m\rightarrow m'} = -\frac{A_{\rm hfs}(5^2S_{1/2})}{h}\lambda_m + \frac{A_{\rm hfs}(5^2P_{1/2})}{h}\lambda_{m'} - \Delta_{\rm isotope}\ , \quad (4.48)$$

where $A_{\rm hfs}(5^2S_{1/2})$ and $A_{\rm hfs}(5^2P_{1/2})$ can be found in table 2.1, and the λ_m and $\lambda_{m'}$ eigenvalues are calculated using equation 4.11. For σ^- transitions on the D_1 line in ^{87}Rb we have

$$\begin{aligned}\Delta_{m\rightarrow m'} = &- 3417.34 \times \left(-\frac{1}{4} \pm \sqrt{1 + m x_g + x_g^2}\right) \\ &+ 407.24 \times \left(-\frac{1}{4} \pm \sqrt{1 + m' x_e + x_e^2}\right) + 56.08\ , \quad (4.49)\end{aligned}$$

Line		D_1			D_2		
$m_J \to m_{J'}$	$m_{I/I'}$	Detuning (GHz) ^{87}Rb	^{85}Rb	$c^2_{m_J}$	Detuning (GHz) ^{87}Rb	^{85}Rb	$c^2_{m_J}$
$\frac{1}{2} \to -\frac{1}{2}$	$\frac{5}{2}$		-12.6	$\frac{2}{3}$		-15.3	$\frac{1}{3}$
	$\frac{3}{2}$	-14.0	-12.1	$\frac{2}{3}$	-16.6	-14.9	$\frac{1}{3}$
	$\frac{1}{2}$	-12.6	-11.6	$\frac{2}{3}$	-15.2	-14.4	$\frac{1}{3}$
	$-\frac{1}{2}$	-10.9	-11.1	$\frac{2}{3}$	-13.7	-13.9	$\frac{1}{3}$
	$-\frac{3}{2}$	-8.9	-10.5	$\frac{2}{3}$	-11.9	-13.4	$\frac{1}{3}$
	$-\frac{5}{2}$		-9.9	$\frac{2}{3}$		-12.8	$\frac{1}{3}$
$-\frac{1}{2} \to -\frac{3}{2}$	$-\frac{5}{2}$					-9.6	$\frac{3}{3}$
	$-\frac{3}{2}$				-10.7	-9.0	$\frac{3}{3}$
	$-\frac{1}{2}$				-8.5	-8.5	$\frac{3}{3}$
	$\frac{1}{2}$				-6.9	-8.1	$\frac{3}{3}$
	$\frac{3}{2}$				-5.5	-7.6	$\frac{3}{3}$
	$\frac{5}{2}$					-7.2	$\frac{3}{3}$

Table 4.2: Transition frequencies and total transition strengths, $c^2_{m_J}$, in the hyperfine Paschen-Back (HPB) regime for σ^- transitions on the $m_J \to m_{J'}$ line for D_1 and D_2 lines in Rb. These detuning values are calculated for a field of 0.6 T. Zero detuning ($\Delta = 0$) corresponds to the weighted centre of the lines.

where $x_g/h = 2.46$ and $x_e/h = 6.87$ are calculated using equation 4.12. For the $|2, +1\rangle \to |1, +0\rangle$ transition, the detuning is

$$\begin{aligned} \Delta_{m=+1\to m'=+0} &= -3417.34 \times (2.83) + 407.24 \times (-7.20) + 56.08 \ , \\ &= -12.6 \text{ GHz} \ , \end{aligned} \tag{4.50}$$

Here we state that the $|2, +1\rangle \to |1, +0\rangle$ detuning value corresponds to the $|1/2, 1/2\rangle \to |-1/2, 1/2\rangle$ detuning value. In chapter 6 we show that there are several weak transitions that also couple these states. Table 4.2 shows the numerical detunings and relative line strengths for a magnetic field of 0.6 T. Next we discuss the various magnetic regimes available for this thesis.

4.4 Various magnetic regimes

In section 4.4 we investigate three cases: the hyperfine linear Zeeman (HLZ) regime, where the magnetic interaction is treated as a perturbation to the hyperfine interaction, $\Delta E_Z < \Delta E_{hfs}$; the hyperfine Paschen-Back (HPB) regime where the magnetic interaction is larger than the hyperfine interaction, yet smaller than the fine interaction, $\Delta E_{hfs} < \Delta E_Z$; and the fine Paschen-Back (FPB) regime where the magnetic interaction dominates both the fine and hyperfine interaction, $\Delta E_{hfs} < \Delta E_{fs} < \Delta E_Z$.

4.4.1 HLZ and HPB regimes

Figure 4.3 shows the energy level evolution as a function of magnetic field for ^{87}Rb ($I = 3/2$) on the D_2 line. In the weak-field regime the nuclear spin, I, and total electronic angular momentum, J, couple to give the total angular momentum, F, which has $2J + 1$ values for $J \leq I$. For the $5^2S_{1/2}$ term of ^{87}Rb, F can be 1 or 2 with a hyperfine splitting of 6.8 GHz, for the $5^2P_{1/2}$ term of ^{87}Rb, F can be 1 or 2 with a hyperfine splitting of 810 MHz, whereas for the $5^2P_{3/2}$ term, F can be 0, 1, 2 or 3 with hyperfine intervals between 70 and 270 MHz. For weak magnetic fields each hyperfine level, F, is split into $2F + 1$ levels (m_F) symmetrically about the zero field level, $\Delta E_Z = g_F m_F \mu_B B$; this is known as the HLZ regime. In this regime the $|F, m_F\rangle$ basis best describes the interaction. For large magnetic fields the total angular momentum decouples into I and J; this is known as the HPB regime. The effect introduces $2I + 1$ levels (m_I) with each m_J value, for the $5^2S_{1/2}$ term, m_J is equal to $1/2$ or $-1/2$, for the $5^2P_{1/2}$ term, m_J is equal to $1/2$ or $-1/2$, and for the $5^2P_{3/2}$ term, m_J can be $3/2$, $1/2$, $-1/2$ or $-3/2$. In this regime the $|m_J, m_I\rangle$ basis best describes the interaction. The spacings of the levels are proportional to the values of m_J and m_I, $\Delta E_Z = (g_J m_J + g_I m_I)\mu_B B$. A detailed theoretical discussion of this regime can be found in [100]. For intermediate magnetic fields all symmetry is lost and there is no good basis to describe the interaction.

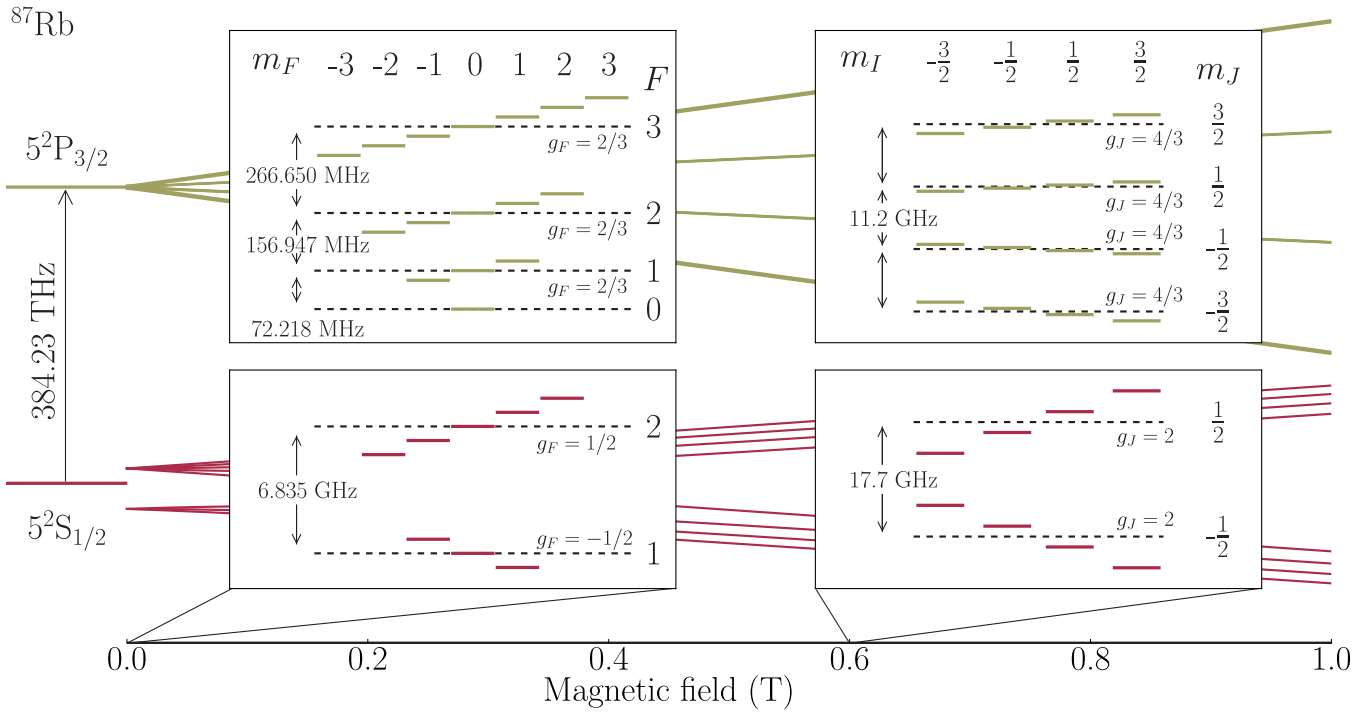

Figure 4.3: Diagram showing the shift in the energy levels as a function of magnetic field for the $5^2S_{1/2}$ and $5^2P_{3/2}$ terms in ^{87}Rb. In the (weak-field) hyperfine linear Zeeman (HLZ) regime, the energy levels can be described by the F and m_F quantum numbers (shown in the left plot). At intermediate fields there are no good quantum numbers to label all of the energy levels. At large fields (0.6 T) m_I and m_J become good quantum numbers due to the nuclei and electronic spins decoupling (shown in the right plot); this case is referred to as the hyperfine Paschen-Back (HPB) regime. Not to scale.

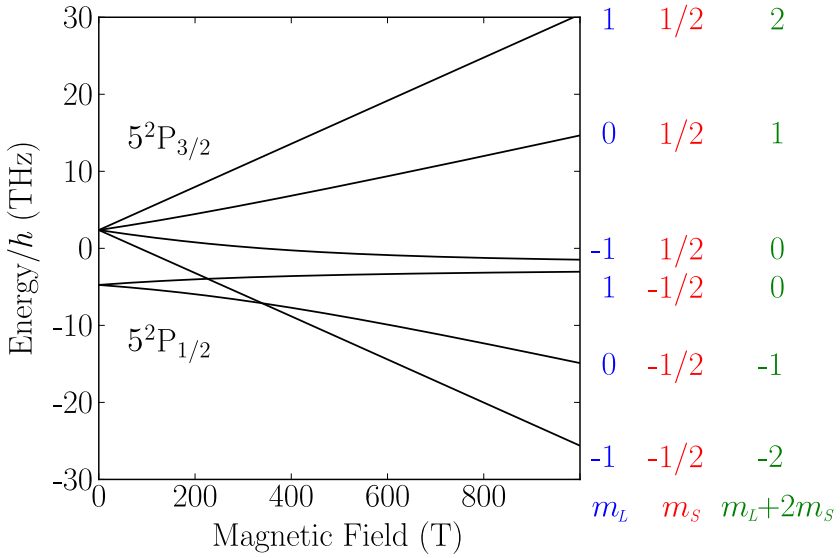

Figure 4.4: Shift in the energy levels as a function of magnetic field for the $5^2P_{1/2}$ and $5^2P_{3/2}$ terms in ^{87}Rb. For fields typically larger than 218 T, m_L and m_S become good quantum numbers due to the orbital and electronic spins decoupling; this case is referred to as the fine Paschen-Back (FPB) regime.

4.4.2 FPB regime

Figure 4.4 shows the energy level evolution as a function of magnetic field for the $5^2P_{1/2}$ and $5^2P_{3/2}$ terms in ^{87}Rb. In section 4.4.3 we discuss the calculation that describes the fields required to gain access to each regime. For fields typically larger than 218 T, J decouples into the total orbital angular momentum, L, and total spin angular momentum, S; this is known as the FPB regime. This effect introduces $2L+1$ levels (m_L) for each of the 2 orientations of m_S for a single electron. These are known as Lorentz triplets when $L = 1$. The spacings of the levels are proportional to the values of m_L and m_S, $\Delta E_Z = (g_L m_L + g_S m_S)\mu_B B$.

4.4.3 Summary

Table 4.3 shows the typical calculated magnetic fields to gain access to the HLZ, HPB and FPB regimes of the linear magnetic interaction term of ^{87}Rb and ^{85}Rb. In addition, the fields and principal quantum number required to see any quadratic effects are noted. To calculate the fields we equate the

Isotope	Term	Linear				Quadratic
		HLZ / HPB			FPB	
		A_{hfs}/h (MHz)	B_{hfs}/h (MHz)	B (T)	B (T)	B (T)
^{87}Rb	$5^2S_{1/2}$	3417.34	-	0.33	-	$\approx 9.4 \times 10^3$
	$5^2P_{1/2}$	407.24	-	0.12	218	
	$5^2P_{3/2}$	84.72	12.50	0.01		
^{85}Rb	$5^2S_{1/2}$	1011.91	-	0.13	-	
	$5^2P_{1/2}$	120.32	-	0.05	218	
	$5^2P_{3/2}$	25.00	25.79	0.005		
	$n \approx 56$					0.6

Table 4.3: The magnetic fields required to gain access to the linear and quadratic terms of the magnetic interaction Hamiltonian for Rb. For a field of 0.6 T and $n = 5$ state only the hyperfine linear Zeeman (HLZ) and hyperfine Paschen-Back (HPB) regimes are accessible in this work. The magnetic dipole constants, A_{hfs}, and electric quadrupole constants, B_{hfs}, were obtained from [102]. The fine Paschen-Back (FPB) regime is also shown. The $n \approx 56$ state would need to be investigated to see any quadratic effects for the field under investigation, or a field of $\approx 9.4 \times 10^3$ T would be required to investigate the $n = 5$ state.

hyperfine energy splitting to the sum of the Zeeman shift of the lowest m_F state of the upper F value and the highest m_F state of the lower F value. The HLZ and HPB regimes are accessed for fields much smaller and bigger than the calculated values, respectively. A similar procedure is adapted to calculate the fields required to access the FPB regime. For the low-lying $n = 5$ state, fields of $\approx 9.4 \times 10^3$ T are required to observe the quadratic term of the magnetic interaction Hamiltonian. For 0.6 T we would need to gain access to Rydberg states with $n \approx 56$ to measure any interaction.

4.5 Experimental methods

In section 4.5 we describe in detail the main experimental components: permanent neodymium magnets; aluminum holder; commercial 2 mm Rb vapour cell and microfabricated ^{87}Rb vapour cell. We also outline the three experimental procedures used to investigate the magnetic field interaction with a thermal Rb vapour. In the first investigation we measure the Stokes param-

eters for light near resonance and extend the work to include the Poincaré representation. In the second investigation we measure the absorption and dispersion properties of a high density medium in the described hyperfine Paschen-Back (HPB) regime. Exploiting these dispersion properties we realise an optical isolator, which forms the basis for our final investigation.

4.5.1 Permanent neodymium magnets

Here we describe the two different permanent neodymium magnets used to investigate the magnetic field interaction. In this work all the magnets were purchased from kj magnetics. To investigate moderate magnetic fields two axial magnetised countersunk permanent neodymium magnets were chosen. Figure 4.5 shows the relevant dimensions and a photograph of a single countersunk permanent magnet. We also show the measured solid (black) circles for the axial variation of the z-component of magnetic field. The diameter, $D = 25$ mm, length, $L = 20$ mm, outer diameter, $d_o = 11$ mm, and inner diameter, $d_i = 7$ mm, describe the dimensions of the magnet. The direction of the beam in the experiments using these magnets is parallel to the z-component of the magnetic field. The magnetic field profile is measured with a Hall probe (Magnetic Instruments GM04 Gaussmeter). The variation of the dimensions across the magnet make it difficult to fit an analytic formula to the measured field. Inside the magnet we measure the largest fields where the circular bore has the smallest diameter. Outside the magnet the field profile reaches a minimum before finally decaying to zero at large distances.

To gain access to magnetic fields to investigate the HPB regime, an axial magnetised annular permanent neodymium magnet with a circular bore was chosen. The direction of the beam in the experiments using these magnets is also parallel to the z-component of the magnetic field. There is an analytic solution for the axial field of a uniformly magnetised annular magnet (the full derivation for this equation is shown in appendix F), which is [141]

$$\begin{aligned} B(z) &= \frac{B_r}{2}\left(\frac{z+z_0+t}{\sqrt{(z+z_0+t)^2+R^2}} - \frac{z+z_0-t}{\sqrt{(z+z_0-t)^2+R^2}}\right) \\ &- \frac{B_r}{2}\left(\frac{z+z_0+t}{\sqrt{(z+z_0+t)^2+r^2}} - \frac{z+z_0-t}{\sqrt{(z+z_0-t)^2+r^2}}\right), \end{aligned} \tag{4.51}$$

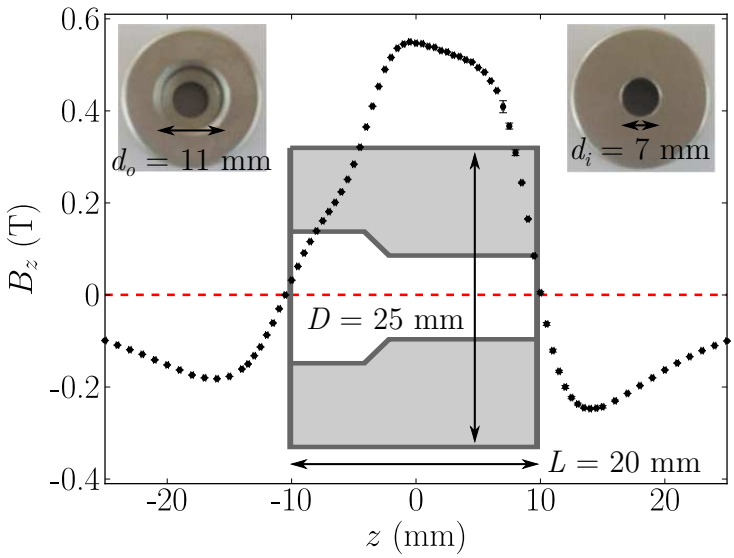

Figure 4.5: Dimensions of a single countersunk permanent neodymium magnet and axial variation of the magnetic field component, B_z, as a function of z. The diameter, D, length, L, outer diameter, d_o, and inner diameter, d_i, describe the dimensions of the magnet. The measured solid (black) circles are achieved by use of a Hall probe along the z-axis.

where z_0 is the z-axis offset, $2t$ is the length, $d = 2r$ is the inner diameter of the magnet, $D = 2R$ is the outer diameter and B_r is the remanence of the magnetic material. Figure 4.6 shows the measured solid (blue) circles and theoretical solid (black) line comparison for the axial variation of the z-component of magnetic field. The error on the measured field and position is less than the size of the data point. Values of $z_0 = (0.05 \pm 0.01)$ mm, $2t = (6.18 \pm 0.12)$ mm, $d = (7.98 \pm 0.10)$ mm and $D = (25.0 \pm 0.6)$ mm were extracted from a Marquardt-Levenberg fit [123] by allowing the dimensions of the magnet to be free parameters (see appendix D). The parameters are consistent with the physical dimensions of the magnet, with the deviation between theory and experiment at the 0.3 mT rms level. The excellent agreement validates the assumption of a uniform magnetisation for the magnet. The best-fit remanence for this magnet is $B_r = (1.42 \pm 0.07)$ T. Now we have described both magnets, the next experimental component to consider is the aluminum magnet holder.

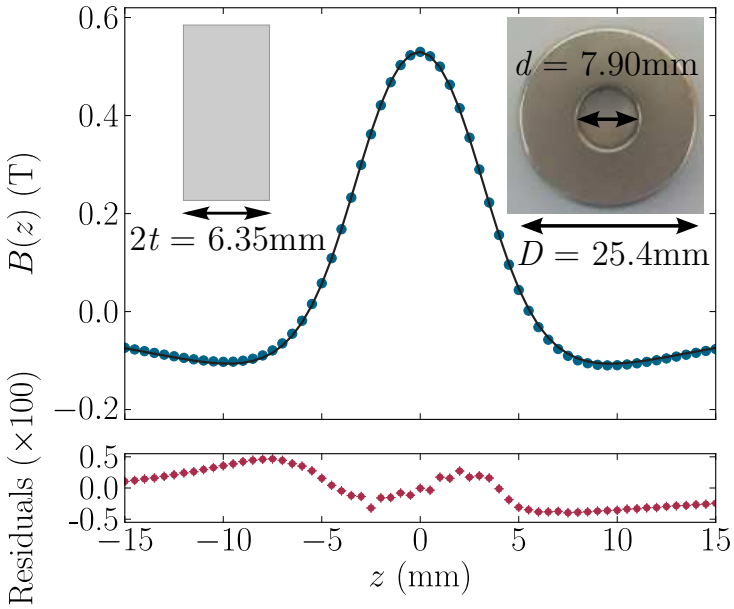

Figure 4.6: Dimensions of a neodymium magnet and axial variation of the z-component of magnetic field. The z-axis offset, z_0, length, $2t$, inner diameter, d, and outer diameter, D, describe the dimensions of the magnet, and the remanence, B_r, characterises the strength of the material. The measured solid (blue) circles are achieved by use of a Hall probe along the z-axis, and the theoretical solid (black) line is obtained from equation 4.51. Below the main graph is a plot of the residuals (solid red circles), that show excellent agreement between theory and experiment, with an rms deviation of 0.3 mT. From a Marquardt-Levenberg fit, the parameters were found to be: $z_0 = (0.05 \pm 0.01)$ mm, $2t = (6.18 \pm 0.12)$ mm, $d = (7.98 \pm 0.10)$ mm, $D = (25.0 \pm 0.6)$ mm and $B_r = (1.42 \pm 0.07)$ T.

4.5.2 Aluminum magnet holder

Here we describe the aluminum magnet holder used to vary the magnetic field for both described permanent neodymium magnets. Figure 4.7 shows the schematic and relevant dimensions for the magnet holder used to control the magnitude of the magnetic field between two countersunk neodymium magnets. Two permanent magnets are held in two columns, positioned on two separate translational stages made from aluminum. By varying the separation between each column the magnetic field profile for both magnets can be measured. Note both magnets have central holes for the probe beam to pass through. Figure 4.14 shows the magnet holder that was used to gain access to the large magnetic fields required to investigate the HPB regime.

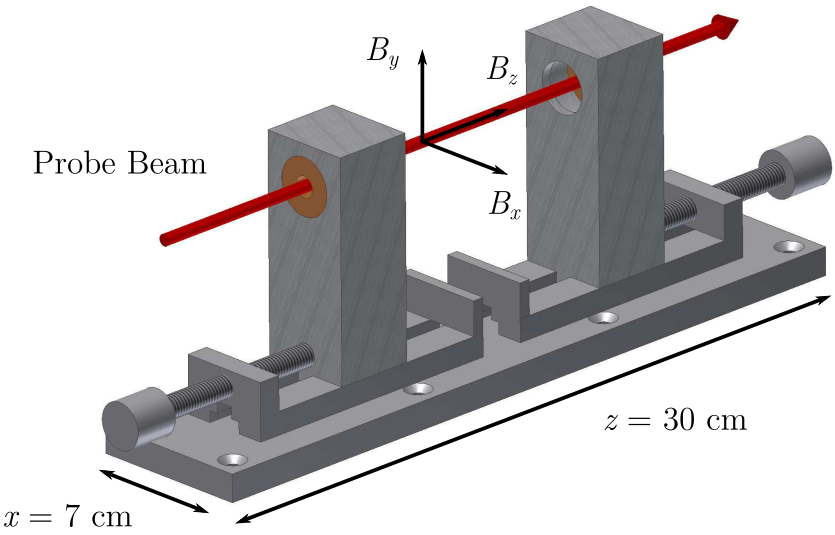

Figure 4.7: Schematic and relevant dimensions of the aluminum magnet holder. The magnitude of the field is controlled by the separation between the permanent magnets which are held in each column.

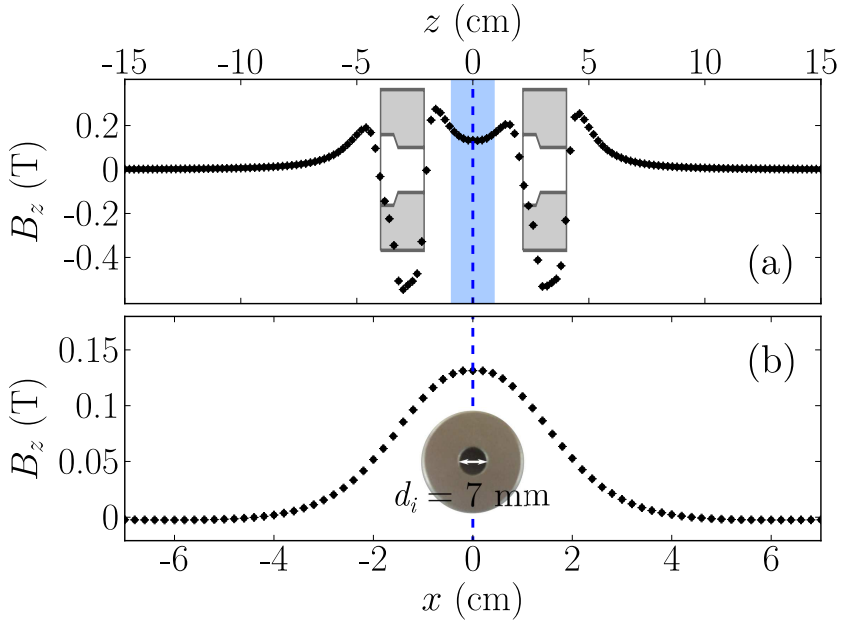

Figure 4.8: (a) Axial variation of the z-component of magnetic field for two countersunk permanent neodymium magnets at their closest separation, $z = 3$ cm. In figure 4.9 the magnetic field profiles are measured across the shaded (blue) area at various separations. (b) z-component of magnetic field as a function of x for $z = 0$. The dashed (blue) lines correspond to the magnetic field at the origin. Across the inner diameter, d_i, the magnetic field is uniform.

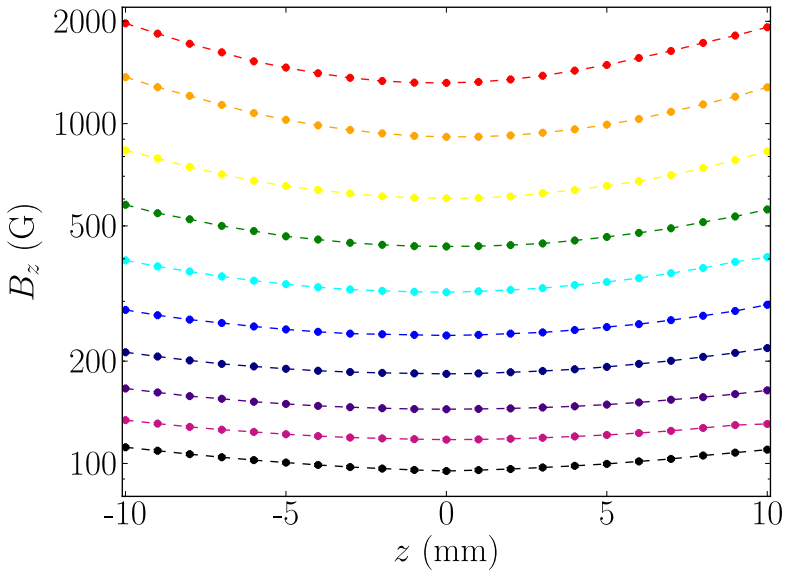

Figure 4.9: Measured magnetic field profiles along the z-axis of the cell for various separations. Separations between the permanent magnets are varied between 3 cm (Red), 4 cm (Orange), 5 cm (Yellow), 6 cm (Green), 7 cm (Cyan), 8 cm (Blue), 9 cm (Navy), 10 cm (Indigo), 11 cm (Violet) and 12 cm (Black).

Figure 4.8(a) shows the axial variation of the z-component of magnetic field for two countersunk neodymium magnets held for the Helmholtz configuration at closest separation, $z = 3$ cm. The measured field profile of the magnet holder shows small fields at large distances and negative fields inside either magnets. Results also show that the strengths of both magnets are very similar. Figure 4.8(b) shows the measured z-component of magnetic field as a function of x for $z = 0$. Across the inner diameter, d_i, of the magnets the field profile is uniform at the 1% level. Adjusting both stages carefully allows for the magnetic field profiles at various separations to be measured.

Figure 4.9 shows the measured magnetic field profiles as a function of z at several separations. The permanent neodymium magnets are held between separations of 3 and 12 cm. At each separation the magnetic field profile between both magnets is measured. The adjustable stages allow for a closest separation of 3 cm, at this distance the z-component of magnetic field is approximately 0.13 T at the origin. In figure 4.10, a graph of the magnetic field at $z = 0$ as a function of separation distance is shown. A guide to the eye fit enables one to extrapolate an approximate magnetic field value for a specific separation. The described cell heater in chapter 3 has a total width

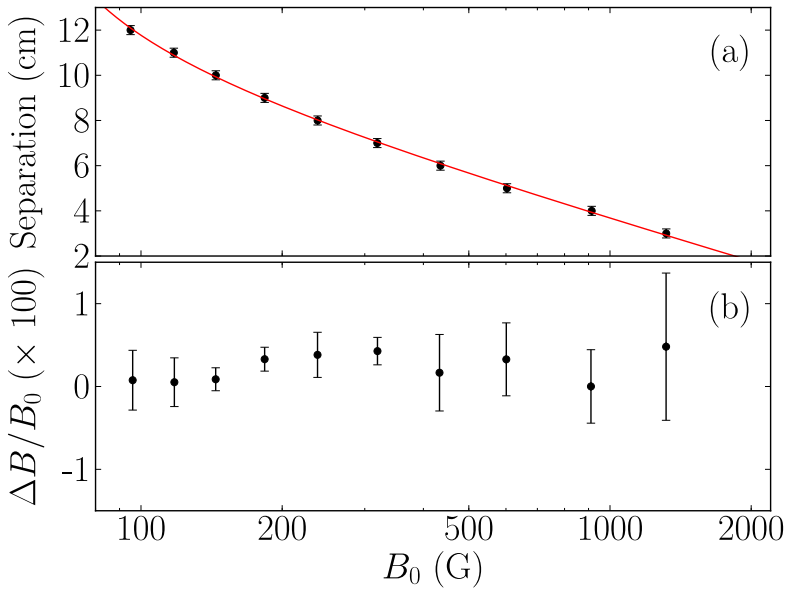

Figure 4.10: (a) The measured magnetic field at $z = 0$ mm as a function of the various separations. The solid (red) line is a logarithmic function of the form $y = a - b\ln((x - c)/d)$, where $a = 11.99$, $b = 2.64$, $c = 56.13$ and $d = 40.39$. This function is not an analytic solution but one chosen because it provides a good guide. (b) The magnetic field uniformity over a cell of length 2 mm. Results show an error of less than approximately 1% for all separations.

of approximately 4.2 cm giving a maximum field for investigation of around 0.08 T. Over the length of the cell the field is uniform at the 1% level. In chapter 5 we experimentally measure the magnetic field for a 2 mm vapour cell and compare values with these measurements taken with a Hall probe.

4.5.3 Vapour cells

Here we describe both the commercial and microfabricated Rb vapour cells used to investigate the magnetic field interaction. Figure 4.11 shows photographs of both vapour cells with their relevant dimensions. Figure 4.11(a) shows the commercial 2 mm Rb vapour cells that are purchased from photonics technologies. For this thesis we use natural abundant and isotopically pure ^{87}Rb vapour cells. The cells have two sections, one containing the body of the cell, the other the metal reservoir. Figure 4.11(b) shows the $1 \times 1 \times 1$ mm^3 microfabricated ^{87}Rb vapour cell held between two plates of silica. The metal reservoir is contained within the body of the cell. This

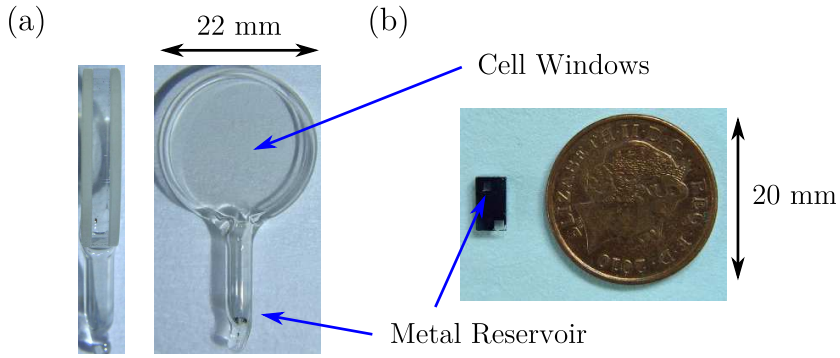

Figure 4.11: Photographs of the Rb vapour cells. (a) shows the commercial 2 mm Rb vapour cells. (b) shows the 1 × 1 × 1 mm^3 microfabricated ^{87}Rb vapour cell.

cell is inherited from NIST.

The 1 × 1 × 1 mm^3 heated isotopically pure ^{87}Rb microfabricated vapour cell [142] contains buffer gases including hydrogen (H_2) and methane (CH_4) with low partial pressure, this arises during the fabrication process[2]. To obtain the optical depths required to compare theoretical and measured absorption spectra, the cell was placed in an oven allowing the number density, $\mathcal{N}$, to vary over several orders of magnitude. Note careful heating of the cell is required to prevent condensation on the windows. Figure 4.12 shows a plot of the transmission through the heated vapour cell on the Rb D_2 line. The solid (red) and dashed (black) lines show the measured and theoretical transmission, respectively, for several temperatures and number densities. Based on the discussion in chapter 3 we have previously accounted for a number-density-dependent increase in the Lorentzian width due to dipole-dipole interactions; however, we must now also include the broadening and shift due to the buffer gases. The collisional broadening and shift of the Rb D_1 and D_2 lines by rare gases have previously been measured [143]. For the Rb D_2 line and buffer gases H_2 and CH_4, the broadening, $\Gamma_{\text{buffer}}/2\pi$, equals 26.4 MHz Torr^{-1}, 26.2 MHz Torr^{-1} and the line shift, $\Delta_{\text{buffer}}/2\pi$, equals −3.8 MHz Torr^{-1}, −7.0 MHz Torr^{-1}, respectively. From the analysis of the broadening in figure 4.12 we learn that the cell contains 99% ^{87}Rb, 1% ^{85}Rb, and a total pressure of ≈ 1 Torr of H_2 and CH_4. As in section 3.6 the shift is too small to be evident.

[2] S. Knappe private communications.

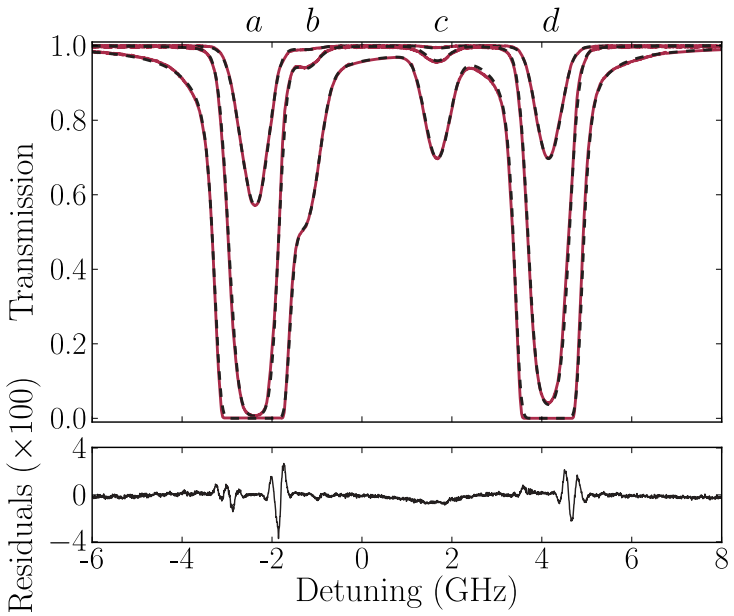

Figure 4.12: Transmission plots for comparison between experiment and theory for the Rb D_2 transitions (*a*) ^{87}Rb $F = 2 \rightarrow 1, 2, 3$, (*b*) ^{85}Rb $F = 3 \rightarrow 2, 3, 4$, (*c*) ^{85}Rb $F = 2 \rightarrow 1, 2, 3$, and (*d*) ^{87}Rb $F = 1 \rightarrow 0, 1, 2$, through a 1 mm vapour cell (99% ^{87}Rb, 1% ^{85}Rb) as a function of linear detuning, $\Delta/2\pi$, for three different temperatures. The solid (red) and dashed (black) lines show measured and expected transmission, respectively. The temperatures of the vapours were extracted from a Marquardt-Levenberg fit [123] and were found to be (60.4 ± 0.2)°C ($\mathcal{N} = 3.49 \times 10^{11}$ cm^{-3}) (top), (90.1 ± 0.5)°C ($\mathcal{N} = 3.13 \times 10^{12}$ cm^{-3}) (middle) and (127.4 ± 0.8)°C ($\mathcal{N} = 3.08 \times 10^{13}$ cm^{-3}) (bottom). The broadening due to the buffer gases were found to be $\Gamma_{\text{buffer}}/2\pi = (23.7 \pm 1.2)$ MHz, for all three temperatures. Below the main figure is a plot of the residuals between experiment and theory for the middle measurement. There is excellent agreement between the data and model, with an rms deviation of 0.5%. There is, however, a small number of glitches due to the linearisation of the laser scan being inadequate.

4.5.4 Details for moderate magnetic fields

Figure 4.13 shows a schematic of the experimental apparatus used to observe the modification to the absorptive and dispersive properties of the atoms in the presence of a moderate magnetic field. An external cavity diode laser system (Toptica DL100) was used for these measurements with a wavelength of 780 nm and scanned across the Rb D_2 transition. The laser output passes through a polarisation beam splitter providing linearly polarised light with

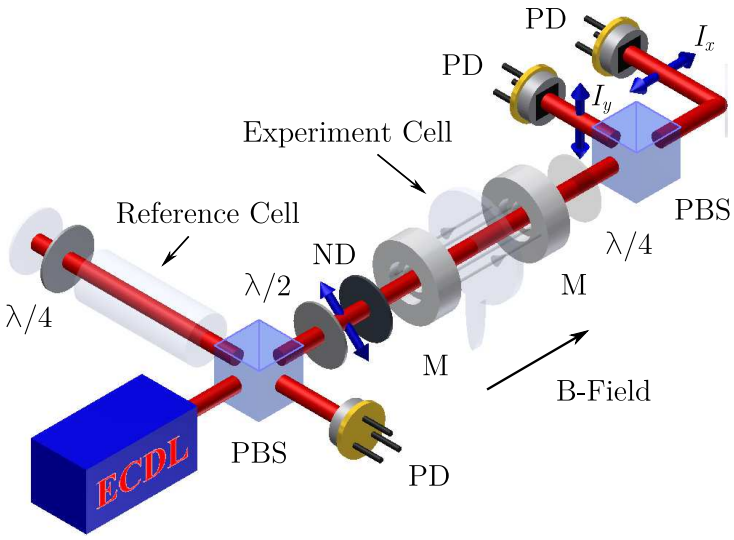

Figure 4.13: Schematic of the experimental apparatus. A beam passes through a polarisation beam splitter (PBS), providing linearly polarised light. A small fraction of the beam is used to perform hyperfine/saturated absorption spectroscopy in a room-temperature reference cell. A half-wave plate ($\lambda/2$) is set at $-\pi/8$ rads to the linearly polarised light. The probe beam is attenuated with a neutral-density filter (ND) before passing through a heated experiment cell and two magnets (M). It is then separated into its horizontal and vertical components and collected on each photodiode (PD). The magnetic field is applied axially along the direction of the beam and an optional quarter-wave plate ($\lambda/4$) is available for measuring the Stokes parameters.

a $1/e^2$ radius of 0.68 ± 0.03 mm. A Fabry-Perot etalon (not shown) was used to linearise the frequency scan with a small fraction of the beam passing through a natural-abundant room temperature reference cell performing hyperfine/saturated absorption spectroscopy [112, 113] to calibrate the scan: this technique is discussed in detail in appendix C. A half-wave plate ($\lambda/2$) is set at $-\pi/8$ rads to the linearly polarised light such that in the absence of any optical rotation the differencing signal is zero, as the light intensities of the horizontal, I_x, and vertical, I_y, channels of light incident on the individual detectors are equal [144]. A neutral-density filter then attenuates the probe beam before it traverses a 2 mm heated experiment cell containing Rb either in its natural abundance (72% ^{85}Rb, 28% ^{87}Rb) or an isotopically pure ^{87}Rb cell. For powers much less than 100 nW, the atoms in the cell traversing the probe beam do not undergo hyperfine pumping into the other ground

term hyperfine level and good agreement between theory and experiment is obtained [40, 92, 111].

The cells were placed in the oven described in section 3.4.2. Two countersunk neodymium magnets (see section 4.5.1) are held at various separations either side of the oven using the aluminum magnet holder described in section 4.5.2. After traversing the experiment cell and magnet holder a polarisation beam splitter separates the light into horizontal and vertical components before the light impinges on calibrated photodiodes: the technique adopted to normalise these data sets is discussed in appendix C. To observe all four Stokes parameters a quarter-wave plate ($\lambda/4$) must also be inserted. In chapter 5 transmission spectra are measured in the absence and presence of a large magnetic field as a function of number density and magnet separation. The Stokes parameters are measured with the laser red detuned from the D_2 ^{87}Rb $F = 2 \rightarrow F'$ transitions in the binary-collision regime for a modest magnetic field.

4.5.5 Details for large magnetic fields

Figure 4.14 shows a schematic of the experimental apparatus used to investigate the HPB regime. An external cavity diode laser (Toptica DL100) was used to scan across the Rb D_2 transition ($5^2S_{1/2} \rightarrow 5^2P_{3/2}$) at a wavelength of 780 nm. After passing through a polarisation beam splitter (PBS) the output beam was linearly polarised along the horizontal direction with a $1/e^2$ radius of 80 μm. A weak beam [92, 111] with a power of 10 nW traverses a $1 \times 1 \times 1$ mm heated ^{87}Rb cell described in section 4.5.3. The cell was held in an oven allowing the laser beam to pass through. A power of 11 W was used to heat a copper block where the cell was placed, however this was far from optimised. The described aluminum holder in section 4.5.2 was modified to hold a single annular neodymium magnet. The field profile of the neodymium magnet is shown in figure 4.6. Over the length of the cell, the field was uniform at the 2% level. The frequency axis is calibrated by use of the method described in appendix C; for detunings over 60 GHz, two scans were stitched together in this experiment. Transmission spectra are measured using a single calibrated photodiode. Dispersion spectra use a bal-

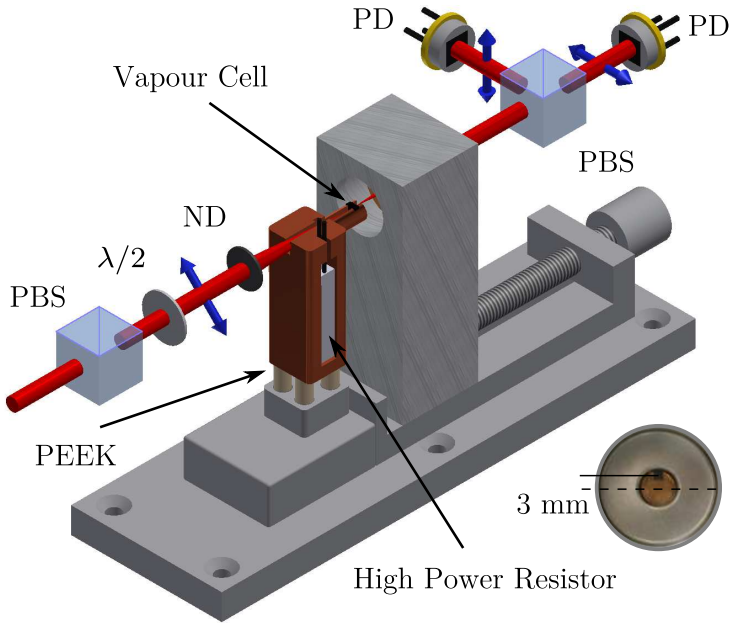

Figure 4.14: Schematic of the experimental apparatus used to investigate the HPB regime. A weak probe beam passes through a $1 \times 1 \times 1$ mm^3 ^{87}Rb vapour cell held in an oven. A high power resistor was used to heat a copper block where the cell was placed, and PEEK provides insulation from the rest of the magnet holder. The axial magnetised annular permanent neodymium magnet with a circular bore was held in the magnet holder which can be adjusted over the cell. The photograph shows the typical displacement from the axis of the magnet.

anced polarimeter to measure the light intensities of the horizontal, I_x, and vertical, I_y, channels after a polarisation beam splitter. A half-wave plate ($\lambda/2$) is set to $-\pi/8$ such that in the absence of rotation both channels of light are equal [144].

Owing to the physical constraints of the cell heater the centre of the cell is typically radially displaced by ≈ 3 mm from the axis of the magnet. At this location the field value is larger than the maximum seen in figure 4.6. The transverse field is three orders of magnitude smaller than the axial field. Having outlined the procedure for investigating large magnetic fields, in chapter 6 we perform spectroscopy in the HPB regime.

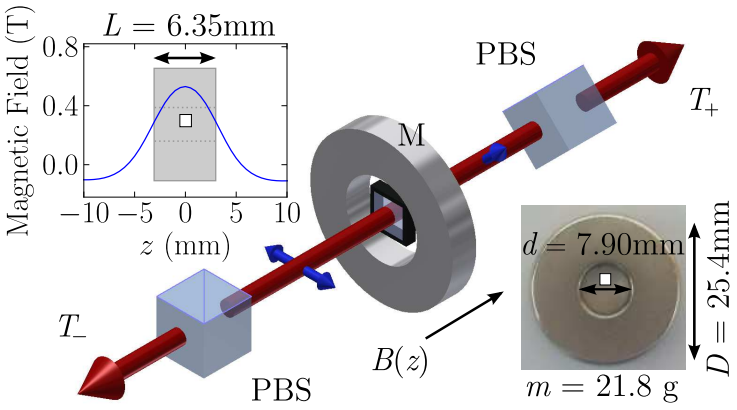

Figure 4.15: Schematic of the experimental apparatus and measured magnetic field profile through the center of the neodymium magnet. The dimensions and mass of a typical magnet used in this investigation are also shown. A beam passes through a polarisation beam splitter (PBS) providing linearly polarised light along the horizontal axis. The beam then passes through a heated micro-fabricated cell held in the center of the magnet (M), which provides an axial field. A second PBS is set to $\pi/4$ to allow high transmission, T_+, along $+z$ and low transmission, T_-, along $-z$.

4.5.6 Details for optical isolation

The experimental procedure used to investigate optical isolation is described in section 4.5.5. Figure 4.15 shows a schematic of the experimental apparatus along with details of the neodymium magnet. In summary, we use a linear polarised weak-beam [111] with a power of 10 nW and $1/e^2$ radius of 80 μm propagating along the z-direction. The laser traverses a microfabricated cell of length $L = 1$ mm (see section 4.5.3). After traversing the cell and magnet we carry out two experiments in chapter 6: firstly, a PBS was set to 0 such that for an induced rotation of $\pi/4$ both channels of light were equal; and secondly, a PBS was set to $\pi/4$, allowing high transmission along $+z$ for an induced rotation of $\pi/4$. With this second arrangement one would also expect isolation along $-z$. In addition this is the arrangement shown in figure 4.15.

4.6 Discussion

In summary, we have discussed the magnetic field interaction Hamiltonian and how it is included in the theoretical model. As a function of magnetic field we have outlined the possible regimes for investigation. We also described the main experimental components together with the details for investigating the Stokes parameters of light propagating through an atomic ensemble in chapter 5, and the hyperfine Paschen-Back (HPB) regime with an optical isolator based on an atomic medium in chapter 6. Next we carry out the described experiments and compare measurements with the theoretical model.

Chapter 5

Measuring the Stokes parameters of light propagating through an atomic ensemble

This chapter is based on the following publication

L. Weller, T. Dalton, P. Siddons, C. S. Adams, and I. G. Hughes, *Measuring the Stokes parameters for light transmitted by a high-density rubidium vapour in large magnetic fields*, J. Phys. B: At. Mol. Opt. Phys. **45**, 055001 (2012), 10.1088/0953-4075/45/5/055001

Here we report on measurements of the absolute absorption and dispersion of light in a dense rubidium vapour on the D_2 line in the weak-probe regime with an applied magnetic field. A model for the electric susceptibility of the vapour is presented which includes both dipole-dipole interactions and the Zeeman effect. The predicted susceptibility is comprehensively tested by comparison to experimental spectra for fields up to 800 G. The dispersive properties of the medium are tested by comparison between experimental measurements and theoretical prediction of the Stokes parameters as a function of the atom-light detuning.

5.1 Introduction

In chapters 2, 3 and 4 we developed a model for the absolute susceptibility that allows us to make quantitative predictions for the absorptive and dispersive properties in the vicinity of the D lines. The model has successfully accounted for absolute Doppler-broadened absorption in the low-density regime [92] (see chapter 2) and absolute absorption including dipole-dipole interactions in the binary-collision regime [22] (see chapter 3). The motivation for chapter 5 is to include the effect of an axial magnetic field up to 800 G in the model for susceptibility and to measure the modification to the optical absorptive and dispersive properties of the atoms. Note that the field is sufficiently large that the angular momentum F is partially uncoupled for the ground terms, and F' and $m_{F'}$ are not good quantum numbers for the excited states. The absorptive properties are comprehensively tested through measuring experimental Doppler-broadened absorption spectra for both low-density and binary-collision regimes, and as a function of magnet field. In addition the dispersive properties are investigated by measuring the Stokes parameters of the transmitted light.

5.2 Comparing theory and experiment for moderate fields

In section 5.2 we compare theory and experiment for the procedure described in section 4.5.4. We start by measuring magnetic field values for both low density and binary collision regimes, before fixing the density and varying the magnetic field for different magnet separations.

5.2.1 As a function of number density

Figure 5.1 shows a plot of the transmission of the Rb D_2 line versus linear detuning, $\Delta/2\pi$. The zero of the detuning axis is taken to be the centre-of-mass frequency of the transition in the absence of hyperfine splitting, taking into account the natural abundance of each isotope. The solid (black) lines

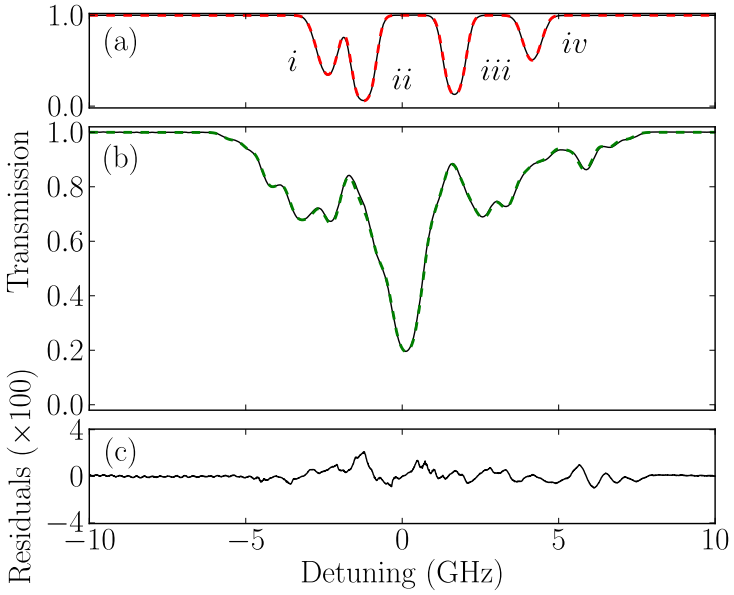

Figure 5.1: Transmission plots for the comparison between experiment and theory for the Rb D_2 transitions (i) ^{87}Rb $F = 2 \rightarrow F'$, (ii) ^{85}Rb $F = 3 \rightarrow F'$, (iii) ^{85}Rb $F = 2 \rightarrow F'$ and (iv) ^{87}Rb $F = 1 \rightarrow F'$, through a vapour cell of length 2 mm as a function of linear detuning, $\Delta/2\pi$. Zero detuning is taken to be the centre-of-mass frequency of the transition. Plots (a) and (b) show the transmission for the transitions in the absence and presence of a magnetic field, respectively. Solid (black) and dashed (red and green) lines show measured and expected transmission, for a Lorentzian width of $\Gamma_0/2\pi = 6.065$ MHz [96], with a temperature of (76.7 ± 0.1)°C ($\mathcal{N} = 1.22 \times 10^{12}$ cm^{-3}) in a magnetic field of (766 ± 5) G. Plot (c) shows the residuals for (b). There is excellent agreement between the data and model, with an rms deviation of 0.4%.

show the transmission measured by one of the photodiodes before the PBS in (a) the absence, and (b) the presence of a magnetic field, at the same temperature. The dashed (red and green) lines are the corresponding theoretical transmission spectra using the susceptibility of chapter 4. The two theory curves are generated with a Lorentzian width of Γ_0 and a Doppler width which is allowed to vary. A least-squares fit [123] allows us to extract the temperature. Five spectra are recorded for each temperature to allow the statistical variation to be quantified; for the parameters which were used to generate figure 5.1 the fits yield a temperature of (76.7 ± 0.1)°C ($\mathcal{N} = 1.22 \times 10^{12}$ cm^{-3}), which is consistent with a thermocouple measurement. In figure 5.1(b) the presence of the field means that the spectrum is very

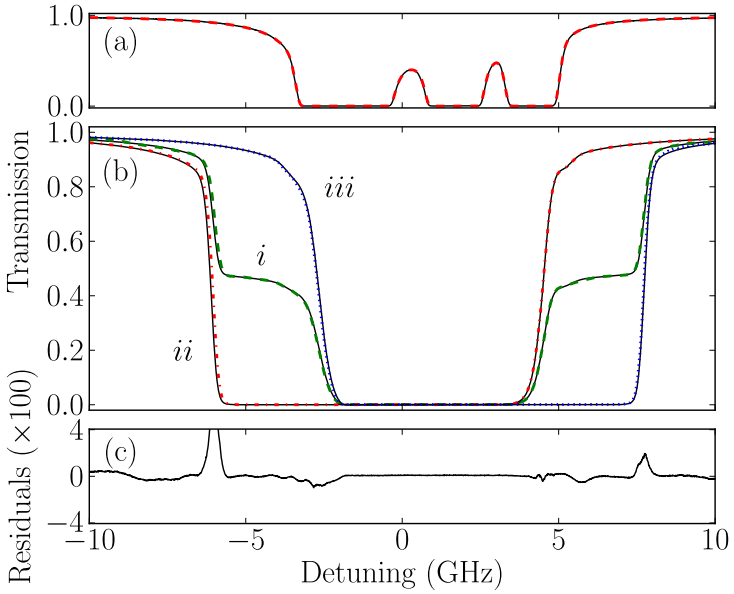

Figure 5.2: Transmission plots for the comparison between experiment and theory for the Rb D_2 line, through a vapour cell of length 2 mm as a function of linear detuning, $\Delta/2\pi$. Plots (a) and (b) show the transmission including resonant dipole-dipole interactions, in the absence and presence of an applied magnetic field, respectively. The three spectra are (*i*) the total transmission (dashed green) and (*ii*) the transmission of the right (dot-dashed red) and (*iii*) left (dotted blue) circular polarisation components. The fits yield a Lorentzian width of $\Gamma/2\pi = (23.3 \pm 0.4)$ MHz, with a temperature of $(159.8 \pm 0.2)^{\circ}$C ($\mathcal{N} = 1.62 \times 10^{14}$ cm^{-3}) in a magnetic field of (774 ± 4) G. Plot (c) shows the residuals of the total transmission demonstrating that there is excellent agreement between the data and model (with the exception of a small number of glitches where the linearisation of the laser scan was not adequate), with an rms deviation of 0.7%.

rich; there are many spectral features, all of which are accounted for in the theoretical model. Figure 5.1(c) shows the residuals which demonstrate that there is excellent agreement between the data and model with an rms deviation of 0.4%. Five spectra are recorded for each value of magnetic field, and for the parameters of figure 5.1(b) we extract (766 ± 5) G which is consistent with measurements with a Hall probe. For this magnitude of field the angular momentum F is partially uncoupled for the ground terms, and F' and $m_{F'}$ are not good quantum numbers for the excited states – this is the origin of the numerous spectral features in figure 5.1(b).

Figure 5.2 shows the transmission spectrum of the Rb D_2 line at elevated

temperature where dipole-dipole interactions become important [22] and the Lorentzian width has an additional density-dependent term as well as the natural contribution. The solid (black) lines show the measured transmission in (a) the absence, and (b) presence of a magnetic field. Three transmission spectra are recorded in the presence of field: the dashed (green) curve with a single photodiode placed before the PBS, and the dot-dashed (red) and dotted (blue) recorded on the two photodiodes after a quarter waveplate is added to show the transmission of light driving σ^- and σ^+ transitions, respectively. The least-squares fits to the four theory curves yield a Lorentzian width of $\Gamma/2\pi = (23.3 \pm 0.4)$ MHz, a temperature of (159.8 ± 0.2)°C in a magnetic field of (774 ± 4) G for figure 5.2(b). There is excellent agreement between the data and model except for some minor glitches in the residuals where the transmission varies most rapidly, an rms deviation of 0.7% was measured. Note that the absorption spectra of figure 5.2(b) have simpler profiles than the lower-temperature spectrum of 5.1(b). In particular on either side of the resonance there are spectral windows approximately 4 GHz wide where one circular polarisation component is nearly fully transmitted and the orthogonal component nearly fully absorbed.

5.2.2 As a function of magnet separation

Figure 5.3 shows the transmission spectrum for comparison between experiment and the theory for various magnetic fields on the Rb D_1 line, as a function of linear detuning, $\Delta/2\pi$. A weak probe beam is sent through two permanent neodymium magnets held in an aluminum holder either side of an isotopically pure ^{87}Rb vapour cell of length 2 mm (see chapter 4). Using the holder, the separation between both magnets is systematically varied and an axial magnetic field value can be extracted from a fit between the measured data and theoretical model. The solid (black) and dashed (green) lines show the measured and theoretical transmissions, respectively. Plot (a) shows the transmission in the absence of an applied magnetic field. Plots (b) to (f) show the transmission in the presence of an applied magnetic field between 200 G and 800 G. Fits to each spectrum yield a temperature of (76.7 ± 0.1)°C ($\mathcal{N} = 1.22 \times 10^{12}$ cm^{-3}).

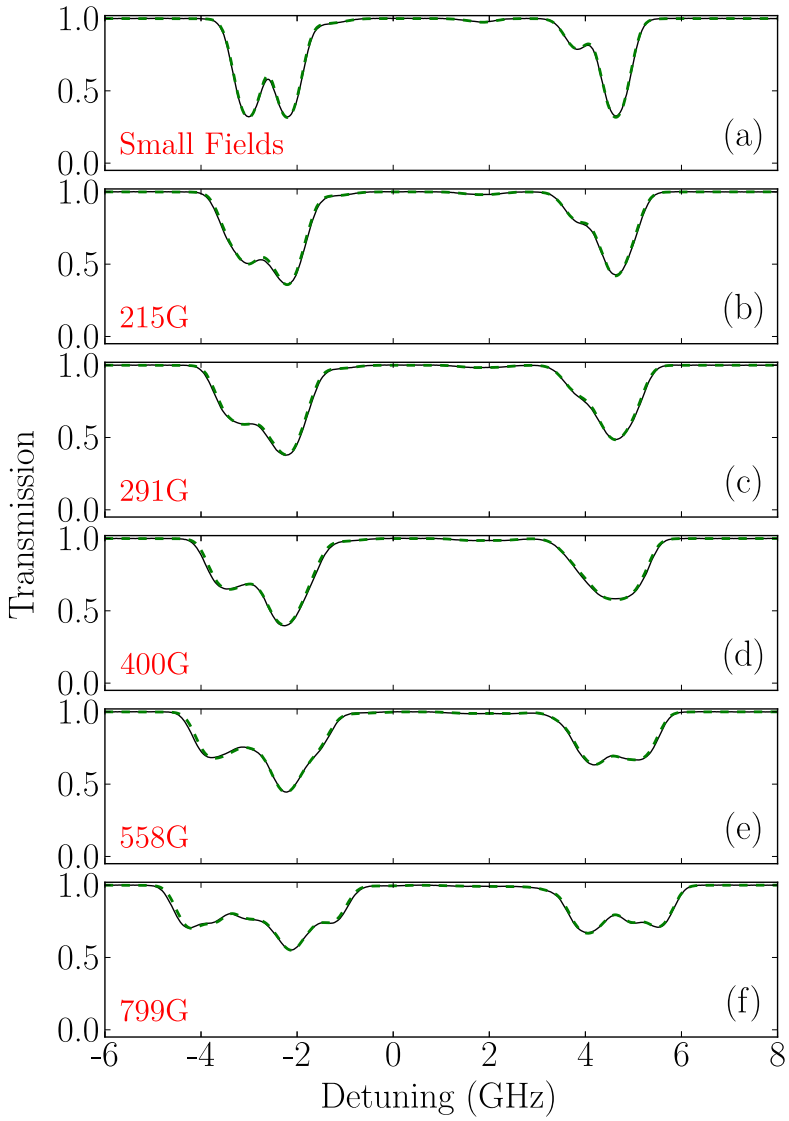

Figure 5.3: Transmission plots for comparison between experiment and theory for various magnetic fields on the Rb D_1 line, through an isotopically pure (99% ^{87}Rb, 1% ^{85}Rb) vapour cell of length 2 mm, as a function of linear detuning, $\Delta/2\pi$. The solid (black) and dashed (green) lines show the measured and theoretical transmissions, respectively. Plot (a) shows the transmission in small applied magnetic fields. The fit yields a temperature of $(76.7 \pm 0.1)^{\circ}$C ($\mathcal{N} = 1.22 \times 10^{12}$ cm^{-3}). Plots (b) to (f) show the transmission in the presence of an applied magnetic field. The fits yield magnetic field values between 200 G and 800 G. For small fields the transmission spectrum looks very similar to a zero field spectrum. For larger fields however, they are richer in structure.

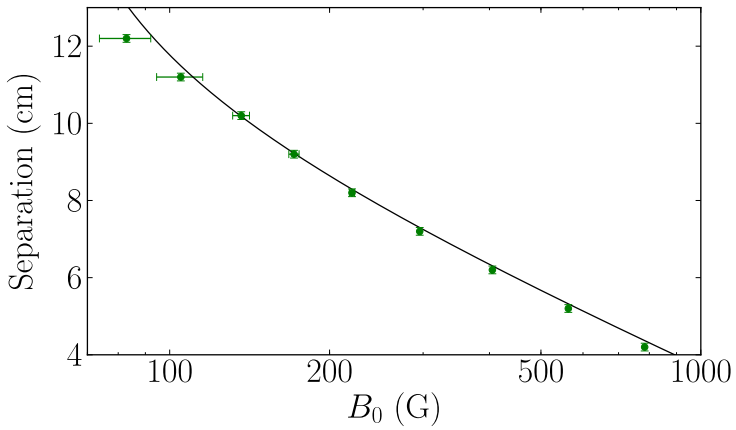

Figure 5.4: Comparison between the measured magnetic field values from figure 5.3 and the fit to the Hall probe measurements from section 4.5.2. The solid (black) line is the logarithmic function from figure 4.10. The solid (green) circles are the extracted magnetic field values at different separations. There are larger errors for small field values because the transmission spectrum is very similar to the zero field spectrum.

The spectra obtained in large fields are rich in structure giving accurate values for measured fields. Due to the Doppler width however, the transmission spectrum for low fields are not too dissimilar to a zero field spectrum. At such temperatures comparing measured transmission spectrum to a theoretical model is not a reliable method for extracting magnetic field values.

In section 5.3 we show that the dispersion signal and more specifically the Stokes parameters are a more effective tool for obtaining smaller field values. Figure 5.4 shows magnetic field values at zero position for the Hall probe and transmission spectrum measurements. The solid (black) line is the logarithmic fit to the Hall probe measurements in section 4.5.2. The solid (green) circles are the transmission spectrum measurements described in figure 5.3. The extracted magnetic field values are measured between 4.2 cm and 12.2 cm due to the cell heater and magnet holder limitations. At moderate magnetic fields and close separations fitting to transmission spectrum is a useful technique for extracting values, however, for small fields and large separations the transmission spectrum are very similar to the spectrum in absence of field, making it difficult to extract a realistic field value. Nevertheless, figure 5.4 shows good agreement between the Hall probe measurements and the fields extracted from a comparison to theory.

5.3 Stokes parameters

In section 5.3 we discuss the properties of a circularly anisotropic media and define the Stokes parameters for light propagating through such a media. We compare experimental measurements of the Stokes parameters with theoretical predictions from the model. In addition we plot the rotation in the absence of dichroism, 2φ, along with the angle that defines the ellipticity and chirality, 2ϑ.

5.3.1 Circularly anisotropic media

A linearly polarised light beam is made up of right and left circularly polarised components, each one of which interacts with a circularly anisotropic medium. To calculate the Stokes parameters of the system we start by defining the quantisation axis to be in the z-direction. For each hyperfine level, F, there are integer values of magnetic sub-levels, m_F, in the range $-F \rightarrow +F$. The electric dipole selection rules govern the change in magnetic sub-level for a transition between a ground and excited hyperfine level as

$$\Delta m_F = 0, \pm 1. \tag{5.1}$$

For $\Delta m_F = 0$ linearly polarised light drives π transitions with the electric field parallel to the magnetic field. In the case where the electric field and magnetic field are perpendicular left- and right- circularly polarised light drives σ^+ and σ^- transitions corresponding to $\Delta m_F = \pm 1$, respectively. Along the direction of the quantisation $\sigma^\pm$ transitions transfer ± 1 unit of angular momentum. Figure 5.5(a) shows for degenerate magnetic sublevels with equal population, σ^+ and σ^- transitions have identical dispersive and absorptive properties. Once the degeneracy is lifted a difference in these properties is visible, as can be clearly seen in figure 5.2(b). Figure 5.5(b) shows a linearly polarised beam at an angle θ_0 to the x-axis. This beam can be described in terms of the horizontal and vertical components

$$\begin{pmatrix} \mathcal{E}_x \\ \mathcal{E}_y \end{pmatrix} = \mathcal{E}_0 \begin{pmatrix} \cos\theta_0 \\ \sin\theta_0 \end{pmatrix} = \frac{\mathcal{E}_0}{2\mathrm{i}} \begin{pmatrix} \mathrm{i}(e^{\mathrm{i}\theta_0} + e^{-\mathrm{i}\theta_0}) \\ e^{\mathrm{i}\theta_0} - e^{-\mathrm{i}\theta_0} \end{pmatrix} . \tag{5.2}$$

Using the transformation described by equation 2.43, we find the horizontal and vertical electric field components can be written in the left- and right-

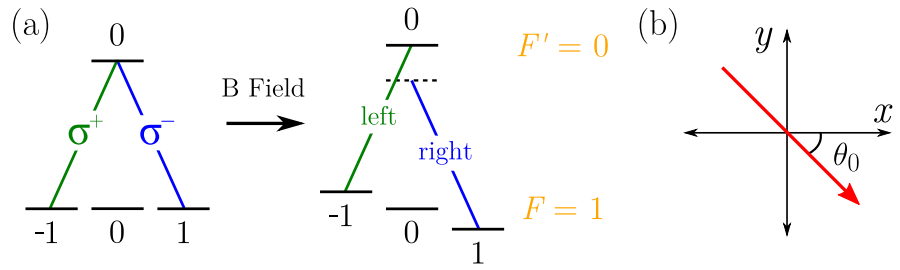

Figure 5.5: (a) Energy level diagrams to show the configurations for circular birefringence. The energies of the σ^+ and σ^- transitions are degenerate, and the m_F states are equally populated, therefore no asymmetry is seen for circularly polarised light. An applied magnetic field lifts the degeneracy such that the σ^+ transition is resonant and the σ^- transition is detuned further from resonance. (b) A linearly polarised light beam at an angle θ_0 to the x-axis.

basis (see equation 5.3 in [103])

$$\begin{pmatrix} \mathcal{E}_L \\ \mathcal{E}_R \end{pmatrix} = \frac{1}{\sqrt{2}} \begin{pmatrix} -1 & -\mathrm{i} \\ 1 & -\mathrm{i} \end{pmatrix} \begin{pmatrix} \mathcal{E}_x \\ \mathcal{E}_y \end{pmatrix} = \frac{\mathcal{E}_0}{\sqrt{2}} \begin{pmatrix} -e^{\mathrm{i}\theta_0} \\ e^{-\mathrm{i}\theta_0} \end{pmatrix} . \tag{5.3}$$

After propagating through a medium of length L the left- $(+)$ and right- $(-)$ circularly polarised components of the light field experience a phase shift $\phi^{\pm} = kn^{\pm}L$ and transmission $e^{-\frac{1}{2}\alpha^{\pm}L}$, where $\alpha^{\pm}$ $(n^{\pm})$ is the absorption coefficient (refractive index) of the particular transition which are calculated in chapter 2.

$$\begin{pmatrix} \mathcal{E}_L \\ \mathcal{E}_R \end{pmatrix} = \frac{\mathcal{E}_0}{\sqrt{2}} \begin{pmatrix} -e^{\mathrm{i}(\phi^+ + \theta_0) - \frac{1}{2}\alpha^+ L} \\ e^{\mathrm{i}(\phi^- - \theta_0) - \frac{1}{2}\alpha^- L} \end{pmatrix} , \tag{5.4}$$

To calculate the Stokes parameters in section 5.3.2 we need the electric field in all three bases: left and right; $+\pi/4$ and $-\pi/4$ and horizontal and vertical. Using the transformations

$$\begin{pmatrix} \mathcal{E}_{+\frac{\pi}{4}} \\ \mathcal{E}_{-\frac{\pi}{4}} \end{pmatrix} = \frac{1}{\sqrt{2}} \begin{pmatrix} e^{-\mathrm{i}\frac{3\pi}{4}} & e^{-\mathrm{i}\frac{\pi}{4}} \\ e^{-\mathrm{i}\frac{\pi}{4}} & e^{-\mathrm{i}\frac{3\pi}{4}} \end{pmatrix} \begin{pmatrix} \mathcal{E}_L \\ \mathcal{E}_R \end{pmatrix} , \tag{5.5}$$

$$\begin{pmatrix} \mathcal{E}_x \\ \mathcal{E}_y \end{pmatrix} = \frac{1}{\sqrt{2}} \begin{pmatrix} 1 & -1 \\ 1 & 1 \end{pmatrix} \begin{pmatrix} \mathcal{E}_{+\frac{\pi}{4}} \\ \mathcal{E}_{-\frac{\pi}{4}} \end{pmatrix} , \tag{5.6}$$

the output electric fields are

$$\begin{pmatrix} \mathcal{E}_{+\frac{\pi}{4}} \\ \mathcal{E}_{-\frac{\pi}{4}} \end{pmatrix} = \frac{\mathcal{E}_0}{2} \begin{pmatrix} -e^{\mathrm{i}(\phi^+ + \theta_0 - \frac{3\pi}{4}) - \frac{1}{2}\alpha^+ L} + e^{\mathrm{i}(\phi^- - \theta_0 - \frac{\pi}{4}) - \frac{1}{2}\alpha^- L} \\ -e^{\mathrm{i}(\phi^+ + \theta_0 - \frac{\pi}{4}) - \frac{1}{2}\alpha^+ L} + e^{\mathrm{i}(\phi^- - \theta_0 - \frac{3\pi}{4}) - \frac{1}{2}\alpha^- L} \end{pmatrix} , \quad (5.7)$$

$$\begin{pmatrix} \mathcal{E}_x \\ \mathcal{E}_y \end{pmatrix} = \frac{\mathcal{E}_0}{2} \begin{pmatrix} e^{\mathrm{i}(\phi^+ + \theta_0) - \frac{1}{2}\alpha^+ L} + e^{\mathrm{i}(\phi^- - \theta_0) - \frac{1}{2}\alpha^- L} \\ e^{\mathrm{i}(\phi^+ + \theta_0 + \frac{\pi}{2}) - \frac{1}{2}\alpha^+ L} - e^{\mathrm{i}(\phi^- - \theta_0 + \frac{\pi}{2}) - \frac{1}{2}\alpha^- L} \end{pmatrix} . \quad (5.8)$$

From chapter 2 the definition describing the intensity is $I = \frac{1}{2} c \epsilon_0 \left| \hat{\mathcal{E}} \right|^2$, hence the output intensities in the three relevant bases are

$$\begin{pmatrix} I_L \\ I_R \end{pmatrix} = \frac{I_0}{2} \begin{pmatrix} e^{-\alpha^+ L} \\ e^{-\alpha^- L} \end{pmatrix} , \quad (5.9)$$

$$\begin{pmatrix} I_{+\frac{\pi}{4}} \\ I_{-\frac{\pi}{4}} \end{pmatrix} = \frac{I_0}{4} \begin{pmatrix} e^{-\alpha^+ L} + e^{-\alpha^- L} + 2\sin(2\varphi) e^{-\frac{1}{2}(\alpha^+ + \alpha^-)L} \\ e^{-\alpha^+ L} + e^{-\alpha^- L} - 2\sin(2\varphi) e^{-\frac{1}{2}(\alpha^+ + \alpha^-)L} \end{pmatrix} , \quad (5.10)$$

$$\begin{pmatrix} I_x \\ I_y \end{pmatrix} = \frac{I_0}{4} \begin{pmatrix} e^{-\alpha^+ L} + e^{-\alpha^- L} + 2\cos(2\varphi) e^{-\frac{1}{2}(\alpha^+ + \alpha^-)L} \\ e^{-\alpha^+ L} + e^{-\alpha^- L} - 2\cos(2\varphi) e^{-\frac{1}{2}(\alpha^+ + \alpha^-)L} \end{pmatrix} , \quad (5.11)$$

where $I_0 = \frac{1}{2} c \epsilon_0 |\mathcal{E}_0|^2$ and the rotation angle $\varphi = \frac{1}{2}(\phi^+ - \phi^-) + \theta_0 = \theta + \theta_0$ is the angle at which the plain of polarisation of the light is rotated with respect to the x-axis. Note $I_{+\frac{\pi}{4}}$ and $I_{-\frac{\pi}{4}}$ will be used in chapter 6 when defining T_+ and T_- for the optical isolator.

5.3.2 Stokes Theory

We can represent the polarisation state of transmitted light via the Stokes parameters [145, 146]. Combinations of the observable intensities of various polarisation components allow us to measure the four Stokes parameters, which are defined as:

$$S_0 = I_R + I_L = \frac{I_0}{2} \left(e^{-\alpha^- L} + e^{-\alpha^+ L} \right) , \quad (5.12)$$

$$S_1 = I_x - I_y = I_0 \cos(2\varphi)\, e^{-\frac{1}{2}(\alpha^+ + \alpha^-)L} , \quad (5.13)$$

$$S_2 = I_{+\frac{\pi}{4}} - I_{-\frac{\pi}{4}} = I_0 \sin(2\varphi)\, e^{-\frac{1}{2}(\alpha^+ + \alpha^-)L} , \quad (5.14)$$

$$S_3 = I_R - I_L = \frac{I_0}{2} \left(e^{-\alpha^- L} - e^{-\alpha^+ L} \right) . \quad (5.15)$$

The parameter S_0 describes the total intensity of the transmitted light field. S_1 describes the intensity difference between horizontal and vertical linearly

polarised light. S_2 describes the intensity difference between linearly polarised light at an angle $+\pi/4$ rad and $-\pi/4$ rad to the x-axis. S_3 describes the intensity difference between right- and left-circularly polarised light. I_0 is the initial intensity and φ is the rotation angle with respect to the x-axis. Note that the parameter S_0 can be the sum of the intensity components in any of the three described bases. For balanced polarimetry the initial rotation angle θ_0 is set to $-\pi/4$ rad, such that the S_1 parameter tends to zero when θ tends to zero i.e. far from resonance. Note the S_1 parameter is referred to as the differencing signal in the rest of the thesis. Independent of dichroism the ratio of the S_2 and S_1 parameters gives a measurement of the rotation angle, φ,

$$\frac{S_2}{S_1} = \tan 2\varphi = \frac{\sin(2\varphi)\, e^{-\frac{1}{2}\left(\alpha^+ + \alpha^-\right)L}}{\cos(2\varphi)\, e^{-\frac{1}{2}(\alpha^+ + \alpha^-)L}} \,. \tag{5.16}$$

The ratio of the S_3 and S_0 parameters gives a measurement of the ellipticity and chirality angle, ϑ,

$$\frac{S_3}{S_0} = \sin 2\vartheta = \frac{e^{-\alpha^- L} - e^{-\alpha^+ L}}{e^{-\alpha^- L} + e^{-\alpha^+ L}} \,. \tag{5.17}$$

Both the rotation angle and ellipticity angle are defined on the Poincaré sphere in section 5.4.1. For $\alpha^- = \alpha^+$ and $n^- \neq n^+$ light remains linear whilst experiencing a rotation around the equator of the sphere. For $\alpha^- \neq \alpha^+$ and $n^- \neq n^+$ circular dichroism is evident and the light moves off the equator towards one of the hemispheres.

5.3.3 Results

Figure 5.6 shows the comparison between experimental and theoretical Stokes parameters for a Doppler-broadened medium of natural Rb atoms with a Lorentzian width of $\Gamma/2\pi = (23.3 \pm 0.4)$ MHz, at a temperature of (159.8 ± 0.2)°C ($\mathcal{N} = 1.62 \times 10^{14}$ cm^{-3}) in a magnetic field of (82 ± 2) G, red detuned from the D$_2$ ^{87}Rb $F = 2 \rightarrow F'$ transitions. Far detuned from resonance (**A**) the absorptive and dispersive properties of Rb are negligible. As the light is tuned closer to resonance (**B**) dispersive properties dominate the light-matter interaction, leading to birefringence and a varying S_1 and

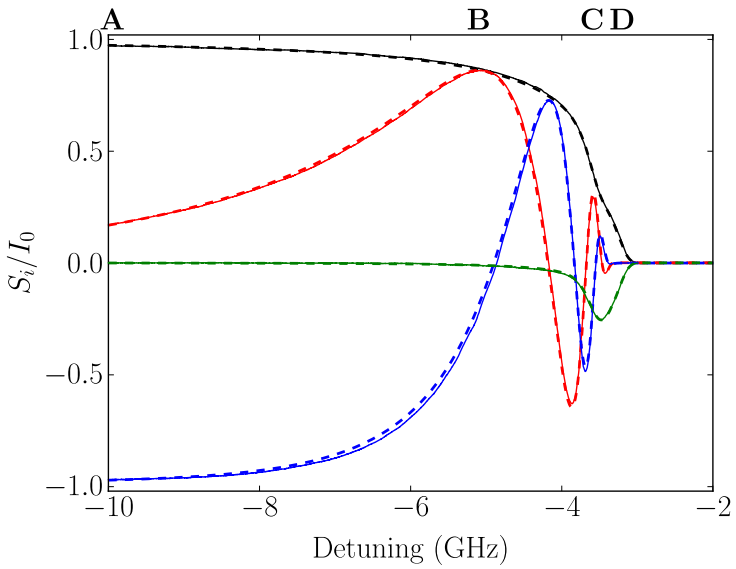

Figure 5.6: Comparison between experimental and theoretical Stokes parameters for the Rb D_2 line, through a vapour cell of length 2 mm as a function of linear detuning, $\Delta/2\pi$, red detuned from the D_2 ^{87}Rb $F = 2 \rightarrow F'$ transitions. Solid and dashed lines show measured and expected S_0 (black), S_1 (red), S_2 (blue) and S_3 (green) signals, for a Lorentzian width of $\Gamma/2\pi = (23.3 \pm 0.4)$ MHz, at a temperature of (159.8 ± 0.2)°C ($\mathcal{N} = 1.62 \times 10^{14}$ cm^{-3}) in a magnetic field of (82 ± 2) G. **A**, **B**, **C** and **D** are four different frequencies showing how the polarisation state of light evolves as a function of detuning.

S_2 signal. As S_0 and S_3 depend only on the absorption, and not the refractive index of the medium, they are both very similar to their extreme far from resonance values. Closer to resonance (**C**) absorptive properties become apparent, circular dichroism expresses itself resulting in a change in the S_3 signal. Even closer to resonance the right-circular component is completely absorbed (**D**) because the σ^- transition is at a higher red-detuning than the σ^+ transition and the S_1 and S_2 signals stop varying. At this detuning the transmitted light has left-circular polarisation. For detunings closer still to resonance the medium is optically thick to both polarisations and all four Stokes parameters are zero. There is excellent agreement between the experimental and theoretical Stokes parameters, which demonstrates that our theoretical model accounts successfully for both the absorptive and dispersive components of the atom-light interaction in a moderate magnetic field. Any discrepancy is likely due to the different detectors used in the measurement

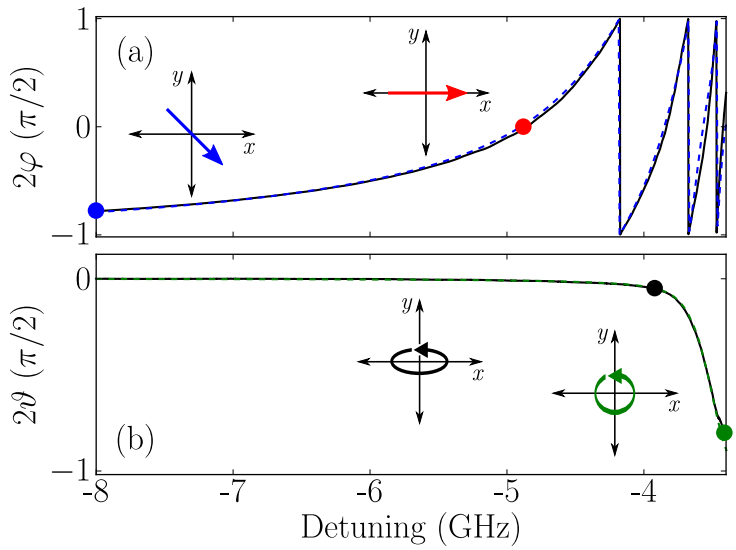

Figure 5.7: Comparison between experimental and theoretical birefringence-induced rotation angles experienced by incident light for the Rb D_2 line, through a vapour cell of length 2 mm as a function of linear detuning, $\Delta/2\pi$, red detuned from the D_2 ^{87}Rb $F = 2 \rightarrow F'$ transitions. Solid (black) and dashed (blue/green) lines show measured and expected rotation, respectively. Both are proportional to the difference between the phase shifts experienced by individual circular components. (a) shows the rotation in the absence of dichroism, light initially remains linear whilst experiencing a rotation. (b) shows that the polarisation becomes highly elliptical, before becoming purely left-circularly polarised near resonance.

of I_x and I_y and the calibration of the frequency axis.

Figure 5.7 shows the comparison between experimental and theoretical birefringence-induced rotation for a Doppler-broadened medium of natural Rb atoms with the same parameters as figure 5.6. Figure 5.7(a) shows the rotation in the absence of dichroism, 2φ, and at large detunings the incident light retains its linear polarisation while being rotated. Figure 5.7(b) shows the angle that defines the ellipticity and chirality, 2ϑ and highlights the region near resonance that experiences greater rotation at the expense of becoming highly elliptical and finally circular. The solid (black) and dashed (blue/green) lines are calculated using equations 5.16 and 5.17, along with the measured and theoretical Stokes parameters from figure 5.6.

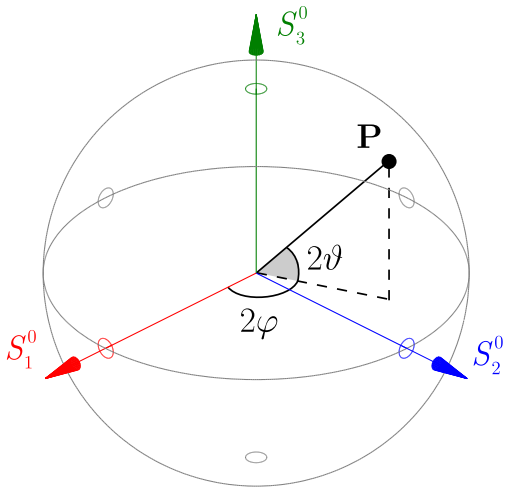

Figure 5.8: Illustration of the Poincaré sphere. For polarised light we define a normalised Poincaré vector given by $\mathbf{P} = (S_1^0, S_2^0, S_3^0)$. The angle 2ϑ is a measure of the ellipticity and chirality of the polarisation. 2φ denotes the angle between the major axis of the ellipse and the horizontal axis.

5.4 The Poincaré representation

In section 5.4 we describe the three-dimensional Poincaré sphere, before plotting a normalised measured and calculated Poincaré sphere for a Doppler-broadened medium of natural Rb atoms.

5.4.1 Poincaré sphere

The Poincaré sphere is a graphical way to represent the polarisation state of light [144]. For polarised light we can present a normalised Poincaré vector $\mathbf{P} = (S_1^0, S_2^0, S_3^0)$ where $S_i^0 = S_i/S_0$ for $i = 1, 2, 3$. The magnitude of the vector describes the total intensity of the polarised light. Figure 5.8 shows a general normalised Poincaré vector $(\cos 2\vartheta \cos 2\varphi, \cos 2\vartheta \sin 2\varphi, \sin 2\vartheta)$ that connects the origin to a point on the surface of a Poincaré sphere. The angle 2ϑ is a measure of the ellipticity and chirality of the polarisation. The north $(2\vartheta = \pi/2)$ and south $(2\vartheta = -\pi/2)$ poles denote right- and left-circularly polarised light, respectively; linearly polarised light is mapped to the equator $(2\vartheta = 0)$; on every other point on the sphere the light is elliptically polarised with the chirality of the hemisphere it resides in. The angle 2φ is between the major axis of the ellipse and the horizontal axis; for linearly polarised

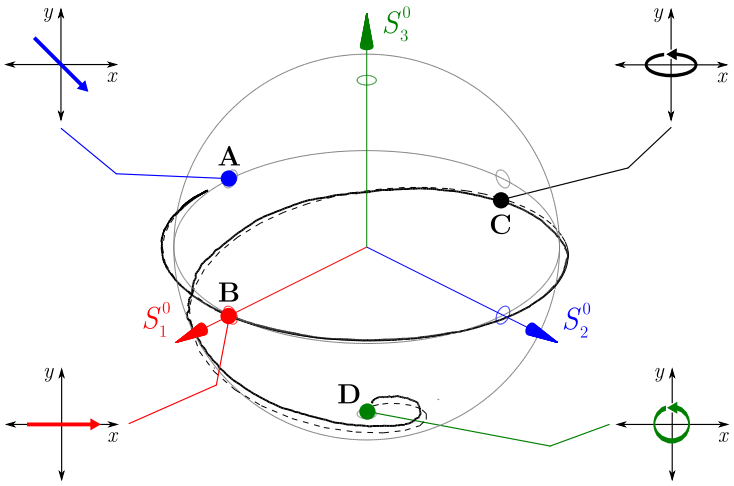

Figure 5.9: Representation of the polarisation state of light on the Poincaré sphere. The normalised Poincaré vector (S_1^0, S_2^0, S_3^0) is measured and calculated for a Doppler-broadened medium of natural Rb atoms with a Lorentzian width of $\Gamma/2\pi = (23.3 \pm 0.4)$ MHz, at a temperature of (159.8 ± 0.2)°C ($\mathcal{N} = 1.62 \times 10^{14}$ cm^{-3}) in a magnetic field of (82 ± 2) G, red detuned from the D_2 ^{87}Rb $F = 2 \rightarrow F'$ transitions. The poles represent right- and left-circular polarisation, the equator linear polarization and intermediate points elliptical polarisation. **A**, **B**, **C** and **D** are four different frequencies showing how the polarisation state of light evolves as a function of detuning.

light on the equator this is simply the rotation angle. Note antipodal points represent the orthogonality of this vector space, i.e., **P** is orthogonal to $-$**P**.

5.4.2 Measured and calculated Poincaré sphere

Figure 5.9 shows a normalised Poincaré sphere measured and calculated for a Doppler-broadened medium of natural Rb atoms with a Lorentzian width of $\Gamma/2\pi = (23.3 \pm 0.4)$ MHz, at a temperature of (159.8 ± 0.2)°C ($\mathcal{N} = 1.62 \times 10^{14}$ cm^{-3}) in a magnetic field of (82 ± 2) G, red detuned from the D_2 ^{87}Rb $F = 2 \rightarrow F'$ transitions. (**A**) shows the initial linearly polarised state at an angle $-\pi/4$ rad to the x-axis. As the light is tuned closer to resonance (**B**) the polarisation state of the light initially remains linear whilst experiencing a rotation around the equator of the sphere. Closer to resonance (**C**) the polarisation state moves off the equator and becomes highly elliptical, before becoming purely left-circularly polarised at the southern hemisphere

(**D**). The magnetic field chosen for the data sets of figures 5.6, 5.7 and 5.9 is an order of magnitude smaller than that used to generate the data for figures 5.1 and 5.2. The motivation for this is the clarity of figure 5.9. For a larger field there would be many more rotations around the vertical axis of the Poincaré sphere. The excellent agreement between the experimental and theoretical trajectories on the Poincaré sphere confirm the accuracy of the predictions of the absorptive and dispersive properties of our model for the electric susceptibility of the dense atomic vapour including an external field.

5.5 Discussion

In summary, we have discussed the physics underlying the transmission of light through a dense atomic vapour, accounting for self-broadening and the application of a moderate axial magnetic field. We showed excellent agreement between experimental and theoretical absorption spectra of rubidium vapour on the D_2 line, and of the spectral dependence of the Stokes parameters red detuned from the ^{87}Rb $F = 2 \rightarrow F'$ transitions. These results demonstrate that our theoretical model of the electric susceptibility of the atomic vapour accounts successfully for both the absorptive and dispersive components of the atom-light interaction in a moderate magnetic field. The Poincaré sphere was shown to be a useful representation of the spectral dependence of the polarisation of a probe beam transmitted through the medium. Next we investigate the absorptive and dispersive properties of a Rb vapour in the hyperfine Paschen-Back (HPB) regime.

Chapter 6

Spectroscopy of a Rb vapour in the hyperfine Paschen-Back (HPB) regime

This chapter is based on the following publications

L. Weller, K. S. Kleinbach, M. A. Zentile, S. Knappe, C. S. Adams, and I. G. Hughes, *Absolute absorption and dispersion of a rubidium vapour in the hyperfine Paschen-Back regime*, J. Phys. B: At. Mol. Opt. Phys. **45**, 215005 (2012), 10.1088/0953-4075/45/21/215005

Here we report on measurements of the absolute absorption and dispersion properties of an isotopically pure ^{87}Rb vapour for magnetic fields up to and including 0.6 T. We discuss the various regimes that arise when the hyperfine and Zeeman interactions have different magnitudes, and show that we enter the hyperfine Paschen-Back regime for fields greater than 0.33 T on the Rb D_2 line. The experiment uses a compact 1 mm^3 microfabricated vapour cell that makes it easy to maintain a uniform and large magnetic field with a small and inexpensive magnet. We find excellent agreement between the experimental results and numerical calculations of the weak probe susceptibility where the line positions and strengths are calculated by matrix diagonalisation.

L. Weller, K. S. Kleinbach, M. A. Zentile, S. Knappe, I. G. Hughes, and C. S. Adams, *Optical isolator using an atomic vapour in the hyperfine Paschen-Back regime*, Opt. Lett. **37**, 3405 (2012), 10.1364/OL.37.003405

A light, compact optical isolator using an atomic vapour in the hyperfine Paschen-Back regime is presented. Absolute transmission spectra for experiment and theory through an isotopically pure ^{87}Rb vapour cell show excellent agreement for fields of 0.6 T. We show $\pi/4$ rotation for a linearly polarised beam in the vicinity of the D_2 line and achieve an isolation of 30 dB with a transmission > 95 %.

6.1 Introduction

As we saw in chapters 4 and 5 the absorption and dispersion of an atomic ensemble in an external magnetic field can be calculated from the atomic susceptibility. In the absence of field, absolute Doppler-broadened absorption [40, 92] (see chapter 2) in the low density regime, and dipole-dipole interactions [22] (see chapter 3) in the binary-collision regime have been tested. In the presence of field, Stokes parameters for fields up to 0.08 T [41] (see chapter 5) have also been investigated. To the best of our knowledge the work presented in this chapter is the first study highlighting excellent agreement between experimental results and numerical calculations for absolute absorption and dispersion for fields up to and including 0.6 T. In chapter 6 we use the model for absolute susceptibility for the Rb D_2 line to predict the performance of an optical isolator based on a compact magnet producing a field of the order of 0.6 T. At such fields the vapour becomes transparent to light resonant with the D_2 line due to large Zeeman shifts. However there remains a large refractive index difference between left- and right- circular polarisations in the vicinity of resonance. We measure rotation and transmission and confirm the theoretical predictions and thereby demonstrate the feasibility of using resonant atomic media for optical isolation. Although here we focus on the Rb D_2 line, using the same principle, resonant atomic isolators can be implemented for other atomic vapours.

6.2 Absorption and dispersion in the HPB regime

In section 6.2 we measure the absolute optical depths and compare the measured and theoretical dispersion and absorption signals for the D_2 line in a ^{87}Rb vapour in the hyperfine Paschen-Back (HPB) regime.

6.2.1 Absorption in the HPB regime

Figure 6.1 shows the measured absolute optical depths as a function of detuning and magnetic field on the D_2 line in a ^{87}Rb vapour. The model for the susceptibility yields the solid (grey) theoretical lines corresponding to the evolution of the transition frequencies as a function of magnetic field.

In the zero-field regime, the solid (blue) measured absolute optical depths are shown at a temperature of $(116 \pm 1)^{\circ}$C ($\mathcal{N} = 1.61 \times 10^{13}$ cm^{-3}), the two large features are the Doppler-broadened ^{87}Rb transitions from the $F = 1$ and $F = 2$ states. The other two very small features arise from the 1% of ^{85}Rb in the cell.

In the intermediate regime, the solid (olive) measured absolute optical depths are shown at a temperature of $(116 \pm 1)^{\circ}$C ($\mathcal{N} = 1.61 \times 10^{13}$ cm^{-3}) and for a field of (0.180 ± 0.001) T, where the error bar represents the uncertainty in the mean value and is not the deviation of values across the cell. For this spectrum the magnetic field was achieved with the countersunk permanent neodymium magnet described in section 4.5.1. There are many spectral features; assigning quantum numbers to the transitions is difficult because there is no suitable basis set: the excited terms are completely decoupled, whereas the ground terms are only partially uncoupled.

In the HPB regime, the solid (red) measured absolute optical depths are shown at a temperature of $(116 \pm 1)^{\circ}$C ($\mathcal{N} = 1.61 \times 10^{13}$ cm^{-3}) and for a field of (0.618 ± 0.002) T. The spectrum remains very rich in structure; however, the $|m_J, m_I\rangle$ basis best describes the interaction, with the expected 16 strong transitions at this field being clearly visible. Note that as the Zeeman shift exceeds the hyperfine interaction, the spectrum becomes symmetric

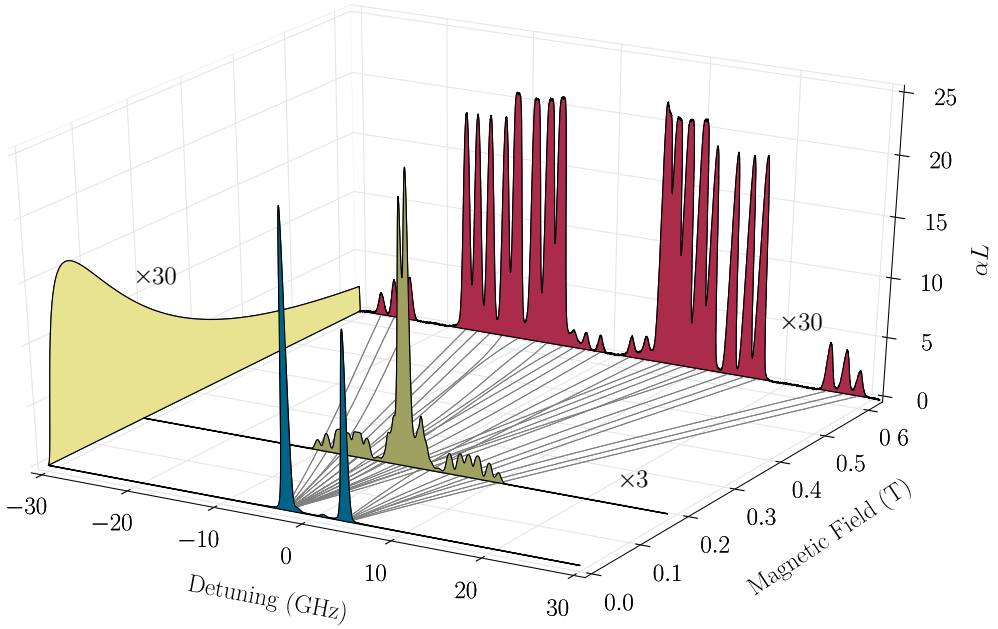

Figure 6.1: Experimentally measured absolute optical depths for the Rb D_2 line, through a vapour cell (99% ^{87}Rb, 1% ^{85}Rb) of length, $L = 1$ mm, as a function of linear detuning, $\Delta/2\pi$, at three different magnetic field values. All three spectra were measured at a temperature of (116 ± 1)°C. The solid (blue) measured spectrum was taken in the absence of magnetic field. The solid (olive) measured spectrum was taken at a field of (0.180 ± 0.001) T in the intermediate regime. The solid (red) measured spectrum was measured at a field of (0.618 ± 0.002) T in the hyperfine Paschen-Back (HPB) regime. The solid (grey) theoretical lines show the transition frequencies as a function of magnetic field. Also plotted is the solid (yellow) theoretical transition strength of the outermost weak transitions as a function of magnetic field. The normalisation factors (×3 and ×30) compensate for a decrease in the transition strengths.

with respect to detuning. The other weaker transitions arise as a consequence of the ground state still not being completely decoupled. For example, the second-highest energy state in the ground-level manifold asymptotes to being $|1/2, 1/2\rangle$ at large field in the $|m_J, m_I\rangle$ basis. However, at 0.618 T the composition of the state is $0.99\,|1/2, 1/2\rangle + 0.14\,|-1/2, 3/2\rangle$. The weak component of this state couples via an allowed $\Delta m_J = -1$, $\Delta m_I = 0$ transition to the lowest energy level of the excited manifold $|-3/2, 3/2\rangle$. The theoretical transition strength for the outermost of the weak transitions is shown as the solid (yellow) curve for all fields. Numerically diagonalising the atomic

Hamiltonian matrix allows one to predict the energy levels and probabilities for all the features. The 16 strong transitions ($\Delta m_J = \pm 1$) are easily obtained from the solid (grey) lines describing the transition frequencies in figure 6.1; however, the advantage of our technique is that the detunings and absolute linestrengths of the 12 weakly allowed transitions are also given. In section 6.3 we discuss in detail the origin of these weak transitions.

6.2.2 Dispersion in the HPB regime

Figure 6.2 shows the measured and theoretical absolute dispersion and absorption in the HPB regime as a function of detuning on the D_2 line in a ^{87}Rb vapour. Plot (a) shows solid (red) measured and dashed (black) theoretical absolute transmission at a temperature of (127.4 ± 0.8)°C ($\mathcal{N} = 3.08 \times 10^{13}$ cm^{-3}), showing the Rb absorption features in the absence of a magnetic field. Plot (b) shows solid (blue) measured and dashed (black) theoretical absolute transmission at a temperature of (114.8 ± 0.6)°C ($\mathcal{N} = 1.50 \times 10^{13}$ cm^{-3}) in the presence of a magnetic field of (0.618 ± 0.003) T. The transmission signal describing the absorptive properties of the medium, was measured using a single photodiode after the cell[1]. Below the main plot are the residuals showing excellent agreement over 60 GHz, with an rms of 0.9 %. Plot (c) shows the solid (olive) measured and dashed (black) theoretical absolute dispersion at a temperature of (126.0 ± 0.8)°C ($\mathcal{N} = 2.85 \times 10^{13}$ cm^{-3}) in the presence of a magnetic field of (0.599 ± 0.003) T. The differencing signal describing the dispersive properties of the medium, was measured using a balanced polarimeter[1]. Here a half-wave plate is set such that in the absence of rotation both channels of light are equal. Below the main plot, residuals show good agreement over 60 GHz, with an rms of 3.3 %. In the theoretical and measured signals the additional weak features are clearly visible, verifying the prediction (of section 6.2.1) that the ground terms are not completely decoupled. Such a result highlights the strength of a model for understanding the energy levels and transition probabilities of such an ensemble. In contrast to the zero crossings associated with the dispersive features of the off-resonant Faraday effect [39], the various features

[1]Note for detunings over 60 GHz, two scans were stitched together in this experiment.

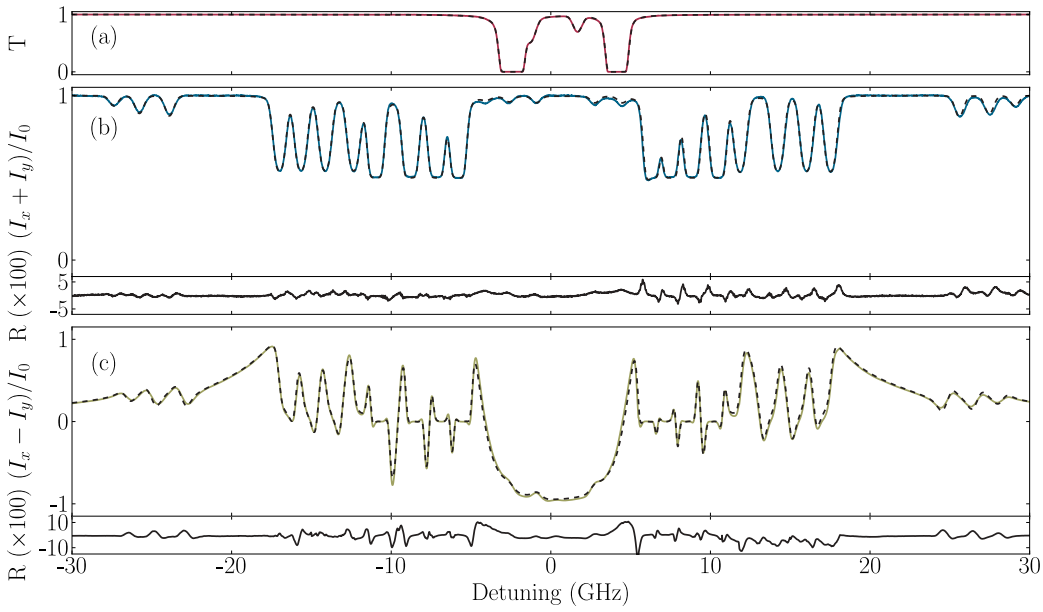

Figure 6.2: Measured and theoretical absolute dispersion and absorption spectra in the hyperfine Paschen-Back (HPB) regime for the Rb D_2 line, through a ^{87}Rb vapour cell of length $L = 1$ mm, as a function of linear detuning, $\Delta/2\pi$. Plot (a) shows solid (red) measured and dashed (black) theoretical transmission in the absence of field at a temperature of (127.4 ± 0.8)°C and a width of $\Gamma_{\text{buffer}}/2\pi$ = (23.7 ± 1.2) MHz. Plot (b) shows solid (blue) measured and dashed (black) theoretical transmission in the presence of a field of (0.618 ± 0.003) T, at a temperature of (114.8 ± 0.6)°C and a width of $\Gamma_{\text{buffer}}/2\pi$ = (47 ± 10) MHz. Below is a plot of residuals showing the excellent agreement between theory and experiment in plot (b), with an rms of 0.9 %. Plot (c) shows solid (olive) measured and dashed (black) theoretical differencing signals in the presence of a field of (0.599 ± 0.003) T at a temperature of (126.0 ± 0.8)°C and a width of $\Gamma_{\text{buffer}}/2\pi$ = (63 ± 12) MHz. The bottom plot is the residuals for (c), with an rms of 3.3 %. There was no attempt made to add in any shift due to the buffer gases.

in figure 6.2 are associated with Zeeman shift resonances and are therefore expected to be less sensitive to temperature. Consequently this opens up the possibility for locking far off-resonance.

For the D_2 line the relative line-strengths and transitions frequencies are calculated numerically. Next we discuss the origin for the weak transitions using the D_1 line in ^{87}Rb, here we solve the problem analytically and show generalised relative line-strengths for any magnetic field value.

6.3 Origin of the weak transitions

In section 6.3 we outline the origin for the weak transitions and calculate the relative line-strength factors and transition frequencies for the D_1 line in ^{87}Rb for a field of 0.6 T.

6.3.1 Relative line-strength factors

In the hyperfine Paschen-Back (HPB) regime the $|m_J, m_I\rangle$ basis best describes the magnetic interaction. In section 6.3 we take the example of the D_1 line for ^{87}Rb and in particular the σ^- transition $|1/2, 1/2\rangle \rightarrow |-1/2, 1/2\rangle$. In chapter 4 we defined the coupled basis in terms of the completely uncoupled basis and generalised Clebsch-Gordan coefficients. Here we calculate the relative line strength factors for each transition $|1/2, 1/2\rangle \rightarrow |-1/2, 1/2\rangle$, which are coupled via the C_R operator. Figure 6.3 shows the relative line strengths in (a) the hyperfine Paschen-Back (HPB) regime and (b) the zero field regime. We start by considering the σ^- transitions on $|F, m_F\rangle \rightarrow |F', m_{F'}\rangle$ lines. We can see immediately from equations 4.17 $\rightarrow$ 4.24 in chapter 4 that there are four transitions that couple the correct $|m_J, m_I\rangle$ states and these are the $|1, +1\rangle \rightarrow |1, +0\rangle$; $|1, +1\rangle \rightarrow |2, +0\rangle$; $|2, +1\rangle \rightarrow |1, +0\rangle$ and $|2, +1\rangle \rightarrow |2, +0\rangle$ transitions. The relative line-strengths are given by

$$c_1{}^2 = \langle 1, +1|C_R|1, +0\rangle^2 \ , \tag{6.1}$$

$$c_2{}^2 = \langle 1, +1|C_R|2, +0\rangle^2 \ , \tag{6.2}$$

$$c_3{}^2 = \langle 2, +1|C_R|1, +0\rangle^2 \ , \tag{6.3}$$

$$c_4{}^2 = \langle 2, +1|C_R|2, +0\rangle^2 \ . \tag{6.4}$$

where for the $5^2S_{1/2}$ term

$$\langle 1, +1| = \frac{\sqrt{3}}{\sqrt{3 + \left|g_+^{+1}\right|^2}} \left\langle 0, +\frac{1}{2}, +\frac{1}{2}\right| - \frac{g_+^{+1}}{\sqrt{3 + \left|g_+^{+1}\right|^2}} \left\langle 0, -\frac{1}{2}, +\frac{3}{2}\right| \ , \tag{6.5}$$

$$\langle 2, +1| = -\frac{\sqrt{3}}{\sqrt{3 + \left|g_-^{+1}\right|^2}} \left\langle 0, +\frac{1}{2}, +\frac{1}{2}\right| + \frac{g_-^{+1}}{\sqrt{3 + \left|g_-^{+1}\right|^2}} \left\langle 0, -\frac{1}{2}, +\frac{3}{2}\right| \ , \tag{6.6}$$

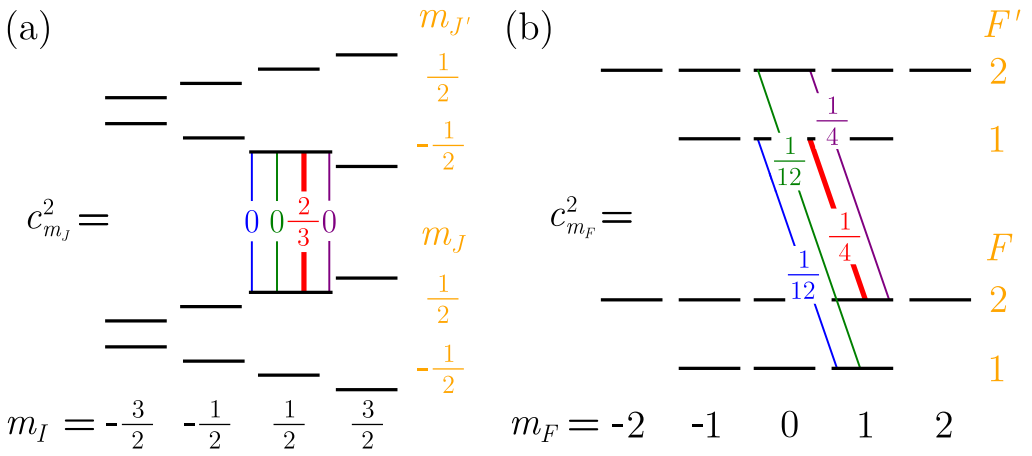

Figure 6.3: Energy level diagrams to show the basis that best describes the interaction in (a) the hyperfine Paschen-Back (HPB) regime and (b) the zero field regime. For the σ^- transition $|1/2, 1/2\rangle \rightarrow |-1/2, 1/2\rangle$ in the HPB regime, there are four possible transitions in the zero field regime that describe this interaction. For large fields the $|2, +1\rangle \rightarrow |1, +0\rangle$ transition is dominant and the other three transitions decay to zero. Note the sum of the relative transitions in the coupled basis equals the sum of the relative transitions in the uncoupled basis.

and for the $5^2P_{1/2}$ term

$$C_R \left|1, +0\right\rangle = \frac{N e_+^{+0}}{\sqrt{4 + \left|e_+^{+0}\right|^2}} \left|-1, +\frac{1}{2}, +\frac{1}{2}\right\rangle , \tag{6.7}$$

$$C_R \left|2, +0\right\rangle = -\frac{N e_-^{+0}}{\sqrt{4 + \left|e_-^{+0}\right|^2}} \left|-1, +\frac{1}{2}, +\frac{1}{2}\right\rangle . \tag{6.8}$$

Applying the electric-dipole selection rules we get

$$c_1{}^2 = \left(\frac{\sqrt{3}}{\sqrt{3 + \left|g_+^{+1}\right|^2}} \frac{N e_+^{+0}}{\sqrt{4 + \left|e_+^{+0}\right|^2}} \left\langle 0, +\frac{1}{2}, +\frac{1}{2} \right| C_R \left| -1, +\frac{1}{2}, +\frac{1}{2} \right\rangle \right)^2 , \tag{6.9}$$

$$c_2{}^2 = \left(-\frac{\sqrt{3}}{\sqrt{3 + \left|g_+^{+1}\right|^2}} \frac{N e_-^{+0}}{\sqrt{4 + \left|e_-^{+0}\right|^2}} \left\langle 0, +\frac{1}{2}, +\frac{1}{2} \right| C_R \left| -1, +\frac{1}{2}, +\frac{1}{2} \right\rangle \right)^2 , \tag{6.10}$$

$$c_3{}^2 = \left(\frac{\sqrt{3}}{\sqrt{3 + \left|g_-^{+1}\right|^2}} \frac{N e_+^{+0}}{\sqrt{4 + \left|e_+^{+0}\right|^2}} \left\langle 0, +\frac{1}{2}, +\frac{1}{2} \right| C_R \left| -1, +\frac{1}{2}, +\frac{1}{2} \right\rangle \right)^2 , \tag{6.11}$$

$$c_4{}^2 = \left(-\frac{\sqrt{3}}{\sqrt{3+\left|g_-^{+1}\right|^2}} \frac{Ne_-^{+0}}{\sqrt{4+\left|e_-^{+0}\right|^2}} \left\langle 0,+\frac{1}{2},+\frac{1}{2}\right| C_R \left|-1,+\frac{1}{2},+\frac{1}{2}\right\rangle \right)^2 . \tag{6.12}$$

Substituting for equation 2.45 and $N^2 = 2/3$, the generalised transition strengths are

$$c_1{}^2 = \frac{2\left|e_+^{+0}\right|^2}{12+4\left|g_+^{+1}\right|^2+3\left|e_+^{+0}\right|^2+\left|g_+^{+1}\right|^2\left|e_+^{+0}\right|^2} , \tag{6.13}$$

$$c_2{}^2 = \frac{2\left|e_-^{+0}\right|^2}{12+4\left|g_+^{+1}\right|^2+3\left|e_-^{+0}\right|^2+\left|g_+^{+1}\right|^2\left|e_-^{+0}\right|^2} , \tag{6.14}$$

$$c_3{}^2 = \frac{2\left|e_+^{+0}\right|^2}{12+4\left|g_-^{+1}\right|^2+3\left|e_+^{+0}\right|^2+\left|g_-^{+1}\right|^2\left|e_+^{+0}\right|^2} , \tag{6.15}$$

$$c_4{}^2 = \frac{2\left|e_-^{+0}\right|^2}{12+4\left|g_-^{+1}\right|^2+3\left|e_-^{+0}\right|^2+\left|g_-^{+1}\right|^2\left|e_-^{+0}\right|^2} . \tag{6.16}$$

In the absence of field, $g_+^{+1} = 3$, $g_-^{+1} = -1$, $e_+^{+0} = 2$ and $e_-^{+0} = -2$, these are calculated using the generalised coefficients defined in chapter 4, it follows that the strengths are $c_1{}^2 = c_2{}^2 = \frac{1}{12}$ and $c_3{}^2 = c_4{}^2 = \frac{1}{4}$. For 0.6 T ($x_g/h = 2.46$ and $x_e/h = 6.87$), the coefficients are $g_+^{+1} = 12.1$, $g_-^{+1} = -0.25$, $e_+^{+0} = 27.6$ and $e_-^{+0} = -0.14$, with the relative transition strengths being

$$c_1{}^2 = 1.3\times10^{-2} , \tag{6.17}$$

$$c_2{}^2 = 7.0\times10^{-5} , \tag{6.18}$$

$$c_3{}^2 = 6.5\times10^{-1} , \tag{6.19}$$

$$c_4{}^2 = 3.4\times10^{-3} . \tag{6.20}$$

For extremely high fields the fourth, second, third and first terms dominate in the denominator for the $c_1{}^2, c_2{}^2, c_3{}^2$ and $c_4{}^2$ coefficients, respectively. Therefore for high fields, the relative line strengths tend to

$$c_1{}^2 = \frac{2}{\left|g_+^{+1}\right|^2} \to 0 , \tag{6.21}$$

$$c_2{}^2 = \frac{\left|e_-^{+0}\right|^2}{2\left|g_+^{+1}\right|^2} \to 0 , \tag{6.22}$$

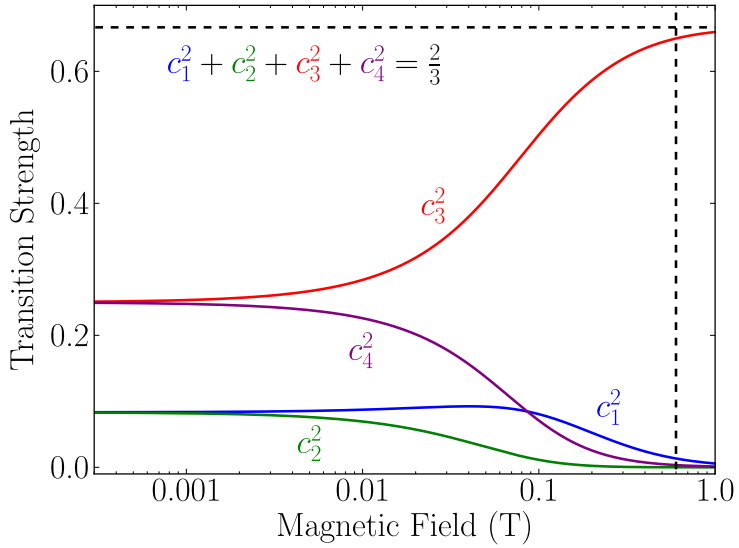

Figure 6.4: The calculated strengths for the four relevant transitions that couple the $|1/2, 1/2\rangle \rightarrow |-1/2, 1/2\rangle$ transition as a function of magnetic field. The solid (coloured) lines correspond to the calculated strengths, ${c_1}^2, {c_2}^2, {c_3}^2$ and ${c_4}^2$ for the $|1, +1\rangle \rightarrow |1, +0\rangle$; $|1, +1\rangle \rightarrow |2, +0\rangle$; $|2, +1\rangle \rightarrow |1, +0\rangle$ and $|2, +1\rangle \rightarrow |2, +0\rangle$ transitions, respectively. In absence of field ${c_1}^2$ and ${c_2}^2$ begin at 1/12, whereas ${c_3}^2$ and ${c_4}^2$ begin at 1/4. For high fields the ${c_1}^2$, ${c_2}^2$ and ${c_4}^2$ coefficients tend to zero, and ${c_3}^2$ tends to 2/3. Note for any magnetic field value the sum of all four transitions is 2/3.

$$ {c_3}^2 = \frac{2\left|e_+^{+0}\right|^2}{3\left|e_+^{+0}\right|^2} \rightarrow \frac{2}{3} , \tag{6.23} $$

$$ {c_4}^2 = \frac{\left|e_-^{+0}\right|^2}{6} \rightarrow 0 . \tag{6.24} $$

Figure 6.4 shows the relative line strengths for these four transitions as a function of magnetic field. The solid (coloured) lines show the ${c_1}^2, {c_2}^2, {c_3}^2$ and ${c_4}^2$ coefficients for the $|1, +1\rangle \rightarrow |1, +0\rangle$; $|1, +1\rangle \rightarrow |2, +0\rangle$; $|2, +1\rangle \rightarrow |1, +0\rangle$ and $|2, +1\rangle \rightarrow |2, +0\rangle$ transitions, respectively. For high fields the ${c_3}^2$ coefficient dominates and the other three decay to zero. For the fields under investigation in this work the weak transitions are a direct consequence of these decaying coefficients still being finite.

6.3.2 Transition frequencies

Now we have the transition strengths the next step is to calculate the frequencies for each dipole-allowed transition. In section 4.3.3 the method adopted for calculating the detunings (in MHz) is shown. For the $|1,+1\rangle \rightarrow |1,+0\rangle$; $|1,+1\rangle \rightarrow |2,+0\rangle$; $|2,+1\rangle \rightarrow |1,+0\rangle$ and $|2,+1\rangle \rightarrow |2,+0\rangle$ transitions, the detunings are

$$\begin{aligned}
\Delta_{m=1\rightarrow m'=0} &= -3417.34 \times (-3.33) + 407.24 \times (-7.20) + 56.08 \ , \\
&= 8.5 \text{ GHz} \ , \qquad (6.25) \\
\Delta_{m=1\rightarrow m'=0} &= -3417.34 \times (-3.33) + 407.24 \times (6.70) + 56.08 \ , \\
&= 14.2 \text{ GHz} \ , \qquad (6.26) \\
\Delta_{m=1\rightarrow m'=0} &= -3417.34 \times (2.83) + 407.24 \times (-7.20) + 56.08 \ , \\
&= -12.6 \text{ GHz} \ , \qquad (6.27) \\
\Delta_{m=1\rightarrow m'=0} &= -3417.34 \times (2.83) + 407.24 \times (6.70) + 56.08 \ , \\
&= -6.9 \text{ GHz} \ . \qquad (6.28)
\end{aligned}$$

The $|2,+1\rangle \rightarrow |1,+0\rangle$ detuning value corresponds to the $|1/2,1/2\rangle \rightarrow |-1/2,1/2\rangle$ detuning value calculated in table 4.2.

6.4 Optical isolator in the HPB regime

Optical isolators were discussed in detail in section 1.4. In section 6.4 we compare calculated and measured rotation in the region of high transmission and large dispersion described in section 6.2. Exploiting the magneto-optical properties of a ^{87}Rb vapour we realise an optical isolator in the hyperfine Paschen-Back (HPB) regime. Concluding by defining the major characteristics of an isolator for our system and discussing the optimised theoretical parameters.

6.4.1 Properties of the medium

Figure 6.5 shows the absolute transmission spectra for the Rb D_2 line through (a) a natural-abundant (72% ^{85}Rb, 28% ^{87}Rb) cell in the absence of an ap-

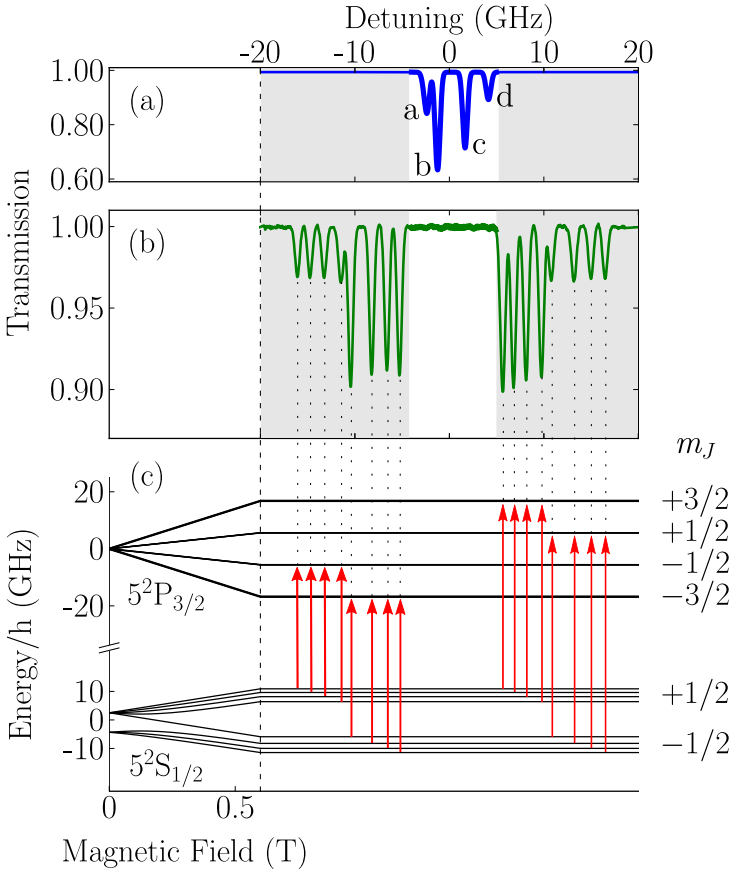

Figure 6.5: Transmission spectra of atomic vapour (a) without and (b) with an applied field illustrating the opening of a transparency window over resonance. Panel (a) shows the theoretical (solid blue) transmission spectra at a temperature of 60.4°C through a natural-abundant cell, highlighting the four absorption peaks of interest for isolation. Panel (b) shows the measured (solid green) line transmission spectra at a magnetic field of 0.576 T and a temperature of (60.4 ± 0.2)°C through a ^{87}Rb cell. Panel (c) shows the energy-level splittings for the ground ($5^2S_{1/2}$) and excited terms ($5^2P_{3/2}$) of ^{87}Rb on the D_2 line. In the hyperfine Paschen-Back regime m_J is now a good quantum number, the transitions with $\Delta m_J = \pm 1$ correspond to the 16 absorption peaks we measure in panel (b).

plied magnetic field and (b) a ^{87}Rb cell[2] in the presence of an applied magnetic field of 0.576 T. For this field (the hyperfine Paschen-Back regime [135]) the Zeeman shift is large compared with the hyperfine splitting of the ground and excited terms, and m_J is the good quantum number. In (b) we observe the 16 absorption peaks corresponding to the $\Delta m_J = \pm 1$ transitions. Mag-

[2]Note this is the described NIST cell in section 4.5.3.

netic fields of such magnitude force a large splitting in the transition frequencies, giving a region of high transmission and large dispersion [122] where we would normally expect absorption on the Rb D_2 line: this is the basis for our isolator. Now we have a thorough understanding of the absorption properties of the medium, next we need to calculate the theoretical rotation angles and compare them to experimental measurements for the peak absorption detuning values described in figure 6.5(a). These values correspond to the (a) ^{87}Rb $F = 2 \rightarrow F' = 1, 2, 3$ ($\Delta = -2.47$ GHz), (b) ^{85}Rb $F = 3 \rightarrow F' = 2, 3, 4$ ($\Delta = -1.23$ GHz), (c) ^{85}Rb $F = 2 \rightarrow F' = 1, 2, 3$ ($\Delta = 1.68$ GHz) and (d) ^{87}Rb $F = 1 \rightarrow F' = 0, 1, 2$ ($\Delta = 4.15$ GHz) transitions.

6.4.2 Theoretical and experimental rotation

Figure 6.6 shows the calculated transmission plots as a function of temperature and magnetic field for the D_2 line in a ^{87}Rb vapour cell of length 1 mm. Plots (a), (b), (c) and (d) refer to the absorption detuning values described in section 6.4.1. The solid (black) lines show the required magnetic field and temperature values to give $\pi/4$ rotation. For a magnetic field value of 0.576 T we require temperatures of approximately 119°C, 121°C, 121°C and 115°C for each detuning, respectively. For this field value and corresponding temperatures we expect a minimum transmission of $\approx$ 95%. In section 6.4.3 we discuss the possibility for larger transmission for a larger magnetic field value. Now we have calculated the temperatures required to measure $\pi/4$ rotation, the next step is to measure them experimentally.

The S_1 signal describes the intensity difference between the horizontal, I_x and vertical, I_y linearly polarisations after a polarising beam splitter (PBS). For figure 6.2 the initial polarisation before the cell is $-\pi/4$ such that in the absence of any rotation the signal is zero. In figures 6.7 and 6.10 the initial polarisation is horizontal, such that for a PBS set to zero, the signal is normalised to +1 in the absence of any rotation. To realise an optical isolator we require that a PBS after the cell and magnet be set to $\pi/4$ for an initial horizontally polarised beam. For an induced rotation of $\pi/4$ this arrangement provides high transmission in one direction and isolation in the other.

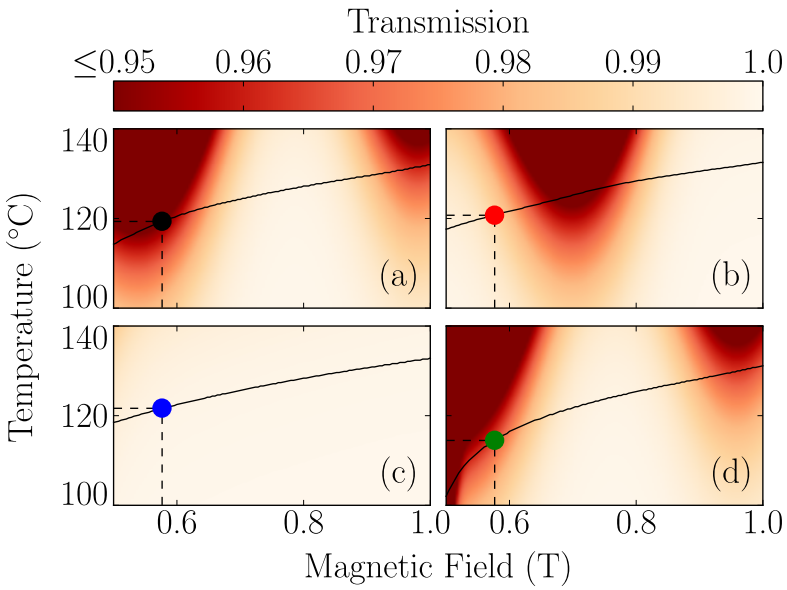

Figure 6.6: Simulated transmission plots as a function of temperature and magnetic field for the D_2 line in a ^{87}Rb vapour cell of length 1 mm. Plots (a), (b), (c) and (d) refer to peak absorption detuning values described in figure 6.5(a). The solid (black) lines correspond to the magnetic field and temperature values where the initial horizontal plane of polarisation is rotated by $\pi/4$ (45°). The dotted (black) lines and solid (coloured) circles highlight the required temperatures for $\pi/4$ rotation at a magnetic field value of 0.576 T.

Figure 6.7 shows the measured and theoretical S_1 signals for the D_2 line in a ^{87}Rb vapour cell as a function of linear detuning, $\Delta/2\pi$. The solid (coloured) and dotted (coloured) lines are the measured and theoretical S_1 signals for a magnetic field of 0.576 T, respectively. For this magnetic field we measure $\pi/4$ rotation for temperatures of (119.0 ± 0.7)°C, (120.7 ± 0.7)°C, (121.2 ± 0.9)°C and (114.8 ± 0.8)°C for plots (a), (b), (c) and (d) corresponding to the detuning values described in figure 6.5(a), respectively. The dashed (coloured) lines show $\pi/4$ rotation when the S_1 signal crosses zero. The excellent agreement between the theoretical rotation and experimental measurements once again highlights the strength of a model for understanding the absorption and dispersion properties of the atomic vapour. Now we have a thorough understanding of the dispersion properties for the medium, next we describe the signals one would expect to see for an optical isolator with a PBS set to $\pi/4$ after the cell and magnet (see figure 4.15).

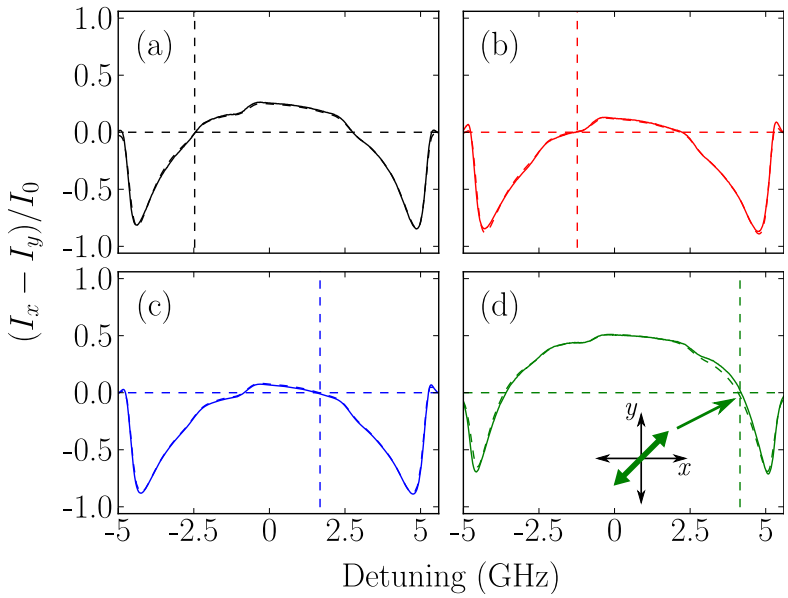

Figure 6.7: Comparing the measured and theoretical S_1 signals on the D_2 line in a ^{87}Rb vapour cell as a function of linear detuning, $\Delta/2\pi$. The solid (coloured) and dotted (coloured) lines are the measured and theoretical rotation signals for a magnetic field of 0.576 T, respectively. The dotted (coloured) lines meet for $\pi/4$ rotation at the detunings described in figure 6.5(a). Plots (a), (b), (c) and (d) show $\pi/4$ rotation for temperatures of (119.0 ± 0.7)°C, (120.7 ± 0.7)°C, (121.2 ± 0.9)°C and (114.8 ± 0.8)°C, respectively.

Figure 6.8 shows absolute transmission spectra for the Rb D_2 line. Panel (a) shows the theoretical (solid black) transmission through a natural-abundant cell in the absence of field and at a temperature of 60.4°C. Panels (b), (c) and (d) show comparisons between experiment (solid coloured) and theory (dashed black) for the rotation of light describing the high transmission along $+z$ (blue), low transmission along $-z$ (green) and extinction values of the isolator (red), respectively. The theoretical T_+ and T_- signals are calculated using equation 5.10 in chapter 5. For an arrangement where a PBS is set to $\pi/4$ after a vapour cell and magnet, the T_+ and T_- signals are given by

$$T_+ = \frac{I_{+\frac{\pi}{4}}}{I_0} = \frac{1}{4}\left(e^{-\alpha^+ L} + e^{-\alpha^- L} + 2\sin(2\varphi)e^{-\frac{1}{2}(\alpha^+ + \alpha^-)L}\right) , \qquad (6.29)$$

$$T_- = \frac{I_{-\frac{\pi}{4}}}{I_0} = \frac{1}{4}\left(e^{-\alpha^+ L} + e^{-\alpha^- L} - 2\sin(2\varphi)e^{-\frac{1}{2}(\alpha^+ + \alpha^-)L}\right) , \qquad (6.30)$$

All three spectra are obtained for an isotopically pure ^{87}Rb cell with a fixed field of 0.576 T and a temperature value of (121.5 ± 0.4)°C, which corre-

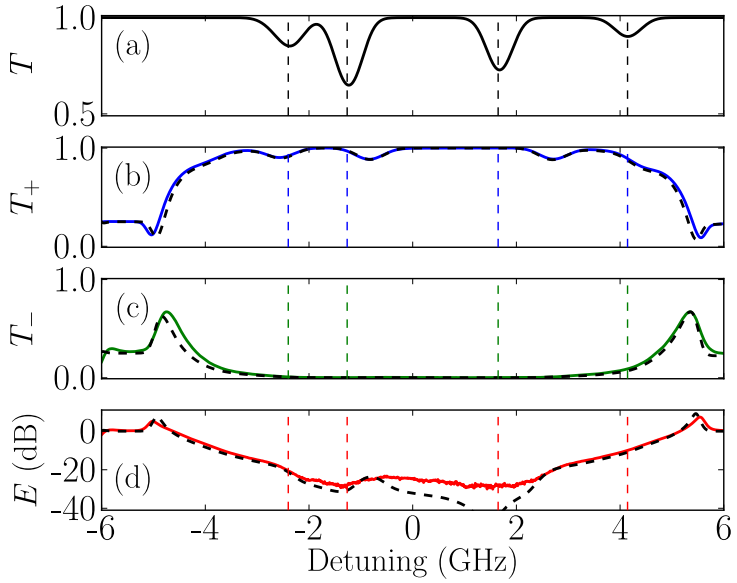

Figure 6.8: Forward T_+ and backward T_- transmission illustrating the isolator effect as a function of detuning around resonance. Panel (a) shows the theoretical (solid black) transmission through a natural-abundant cell in the absence of field and at a fixed temperature of 60.4°C. The four absorption peaks highlight the required detuning values for isolation. Panels (b), (c) and (d) show comparisons between experiment (solid coloured) and theory (dashed black) through an isotopically pure ^{87}Rb cell in the presence of a fixed field of 0.576 T and a temperature value of (121.5 ± 0.4)°C, which corresponds to a region where we expect $\pi/4$ rotation.

sponds to a region where we expect $\pi/4$ rotation (see figure 6.6). These spectra demonstrate the narrow-band nature of isolators based on atomic vapours, as there is only a constant extinction over a range of 4 GHz. The increased structure in the T_+ signal, which is present in the theoretical and measured signals, is the result of additional weak absorption features owing to the fact that the ground terms are not completely decoupled; a detailed study of these features has been discussed in section 6.3. In comparison with other isolators next we discuss the characteristics for our optical isolator based on an atomic medium.

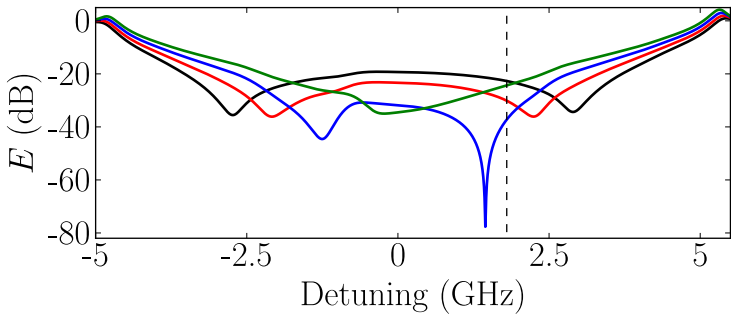

Figure 6.9: Theoretical extinction values at four different temperatures for the D_2 line in an isotopically pure ^{87}Rb vapour cell as a function of linear detuning, $\Delta/2\pi$. These extinction values are calculated using equation 6.31. The solid lines are the theoretical extinction values for a magnetic field value of 0.576 T and temperatures of 120°C (black), 121°C (red), 122°C (blue) and 123°C (green).

6.4.3 Characteristics for our optical isolator

Important characteristics for isolators are their ability to extinguish back scattered light, power threshold and temperature stability. The isolation of the device described in figure 6.8(d) was defined as

$$E = -10 \log \left(\frac{T_+}{T_-} \right) \text{ dB} , \tag{6.31}$$

where T_+ is the transmitted light along $+z$ and T_- is the transmission along $-z$. Previous examples of crystal isolators have measured extinctions of 47 dB for a single device [147] and 60 dB for a back-to-back device [141]. In figure 6.8(d) the extinction for some detuning values had poor agreement with the theoretical predictions. The maximum predicted extinction value was approximately 70 dB, much larger than we can measure experimentally. In this experiment Glan-Thompson polarisers were used with measured extinction values of better than 10^{-4} (40 dB), therefore the only other obvious source for the large disagreement with the predicted extinction is the cell windows. It is well known that these microfabricated cells exhibit birefringence when heated to large temperatures [148, 149]. To the best of our knowledge, this is the first resonant atomic vapour isolator, and we achieve a 30 dB suppression, limited by the birefringence of the windows.

Figure 6.9 shows theoretical extinction values at four different temperatures to show the narrow-band nature of isolators based on atomic vapours. The

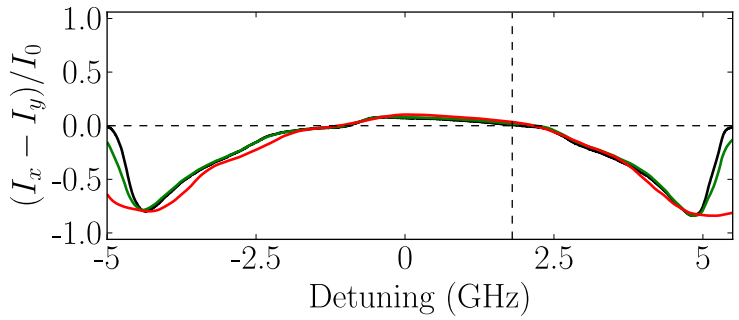

Figure 6.10: Measured S_1 signals for three powers on the D_2 line in an isotopically pure ^{87}Rb vapour cell as a function of linear detuning, $\Delta/2\pi$. All three signals correspond to a temperature of (121.2 ± 0.9)°C and a magnetic field of 0.576 T. For these parameters we achieve $\pi/4$ rotation for the detuning corresponding to the $F = 2 \rightarrow F' = 1, 2, 3$ ($\Delta = 1.68$ GHz) absorption peak in ^{85}Rb. The solid lines correspond to powers of 10 nW (black), 53 μW (green) and 1.6 mW (red).

solid lines are the theoretical extinction values for a magnetic field value of 0.576 T and temperatures of 120°C (black), 121°C (red), 122°C (blue) and 123°C (green). Owing to the strong temperature dependence of the birefringent properties of the medium, a device utilising this effect would require the vapour cell to be temperature stabilised, as there is a theoretical sensitivity of ≈ 6 dB/°C.

Figure 6.10 shows measured S_1 signals for a measured temperature of (121.2 ± 0.9)°C and a magnetic field of 0.576 T. The solid lines correspond to powers of 10 nW (black), 53 μW (green) and 1.6 mW (red). For each power, $\pi/4$ rotation is measured for the detuning corresponding to the $F = 2 \rightarrow F' = 1, 2, 3$ ($\Delta = 1.68$ GHz) transitions in ^{85}Rb. The S_1 signals are very similar in the region of high transmission and large dispersion. However, closer to the transition frequencies the change in power evidently alters the absorptive properties of the medium. The excellent agreement between theory and our model is typically achieved in the weak-probe regime. However, when the power of the beam was increased by 6 orders of magnitude, the extinction in figure 6.10 changed by less than 8 dB.

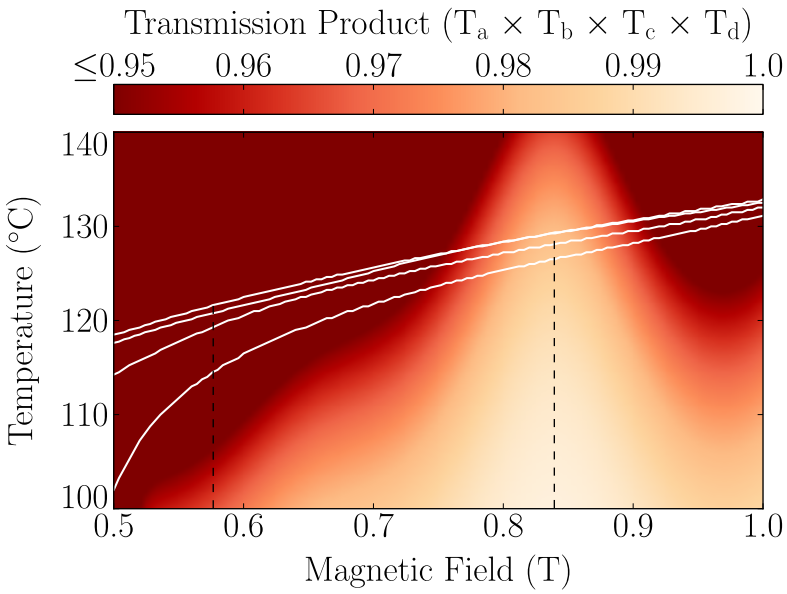

Figure 6.11: Simulated transmission plot for the product of the four transmission plots described in figure 6.6. For a magnetic field value of 0.84 T a transmission above $\approx$ 98% is possible for each detuning whilst measuring $\pi/4$ rotation. The solid (white) lines show the required magnetic field and temperature values to give $\pi/4$ rotation for each detuning. The upper one is the ^{87}Rb $F = 2 \rightarrow F' = 1, 2, 3$ transition and in sequence they are the ^{85}Rb $F = 3 \rightarrow F' = 2, 3, 4$, ^{85}Rb $F = 2 \rightarrow F' = 1, 2, 3$ and ^{87}Rb $F = 1 \rightarrow F' = 0, 1, 2$ transitions.

6.4.4 Ideal parameters

Figure 6.11 shows the simulated products of the four transmission plots described in figure 6.6 for the D_2 line in an isotopically pure ^{87}Rb vapour cell. The product of the four transmission plots shows that a larger transmission value could be achieved for an optical isolator with a larger magnetic field. For a magnetic field value of 0.84 T one would achieve a transmission above $\approx$ 98% whilst maintaining the $\pi/4$ rotation for isolation. The solid (white) lines show the required magnetic field and temperature values to give $\pi/4$ rotation for each described detuning value. Note in this regime the temperatures required to give the required rotation are closer. In chapter 4 we wrote the analytic solution for the axial field of a uniformly magnetised annular magnet. In appendix F we show that a magnetic field value of 0.84 T can be achieved with a magnet that has similar dimensions to the one used in this investigation however with an inner diameter of $d = 4.00$ mm instead.

6.5 Discussion

In summary, we have tested our model for the electric susceptibility of Rb vapour for magnetic fields up to and including 0.6 T, which corresponds to the HPB regime on the D_2 line. We have demonstrated excellent agreement between the theoretical predictions and the experimental measurements of the absolute absorption and dispersion properties of the medium. Our study extends the range of magnetic fields for which the theoretical model has been tested by an order of magnitude compared to chapter 5. Understanding the optical properties of atomic vapours in the HPB regime will find utility in many applications, such as measuring magnetic fields with submicron spatial resolution [135], and constructing tunable atomic frequency references [135]. We have also demonstrated the principle of an optical isolator for the Rb D_2 line by exploiting the magneto-optical properties of an isotopically pure ^{87}Rb vapour in the hyperfine Paschen-Back regime and shown $\pi/4$ rotation for linearly polarised light in the vicinity of the D_2 line, realising an optical isolator with an isolation of 30 dB.

In the second part of the thesis, we concern ourselves with an atomic medium subject to strong excitation. We have already shown in chapter 3 that in a high density medium of Rb dipole-dipole interactions are significant for low lying n states [22]. In chapter 7 we show cooperative effects give rise to a threshold for non-linear effects such as frequency up-conversion.

Part II

Cooperative effects

Chapter 7

Cooperative enhancement of energy transfer in a high-density thermal vapour

This chapter closely relates to the following publication

L. Weller, R. J. Bettles, C. Vaillant, M. A. Zentile, R. M. Potvliege, C. S. Adams and I. G. Hughes, *Cooperative enhancement of energy transfer in a high-density thermal vapour*, in preparation,

We present a study of energy transfer in a thermal vapour as a function of atomic density. We use confocal microscopy and input light resonant with either the D_1 or D_2 lines of Rb to measure fluorescence over the visible and near infra red regions. Low-density transfer arises due to the energy-pooling effect: collisions between two identical optically excited atoms in their first excited terms. At high densities we observe a dramatic enhancement of the population of high-lying excited states which cannot be accounted for by energy pooling. A threshold value of cooperativity of $\sqrt{2}$ and 2 for D_2 and D_1 excitation, respectively is evident, and is hypothesised to be the result of cooperative effects due to enhanced interactions. Analysis of the fluorescence of the $6^2P_{1/2,3/2} \rightarrow 5^2S_{1/2}$ transitions as a function of the number density shows a single-atom response in the cooperatively-enhanced regime.

7.1 Introduction

In part I we developed a theoretical model that allowed us to compare experimental measurements for the absolute absorption and dispersion properties of the Rb D lines in the weak-probe regime through a dense thermal vapour in the absence and presence of an applied magnetic field. In chapter 3 we showed that in dense vapours modifications to the homogeneous linewidth (self-broadening) in the D lines arises due to resonant dipole-dipole interactions between identical atoms. In part II (chapter 7) we show that field enhancement due to resonant dipole-dipole interactions in a dense atomic vapour gives rise to a threshold for non-linear effects such as frequency up-conversion. This threshold corresponds to the condition where there is more than one atom per reduced wavelength cubed, i.e., $C = 2\pi\mathcal{N}k^{-3} > 1$, where $\mathcal{N}$ is the atomic number density and $\lambda = 2\pi/k$ is the optical wavelength. Note this is the same cooperativity parameter that was derived in section 3.3.2. The field enhancement can be interpreted in terms of radiation trapping and in many respects is analogous to the enhancement produced by optical cavities. Above threshold one observes enhanced emission from higher excited states. Populating these states from collisions of 5P atoms is kinematically disallowed.

7.2 Experimental methods

In section 7.2 we outline both procedures for investigating cooperative enhancement of energy transfer in a high-density vapour. We begin by describing confocal microscopy, before discussing the technique of side-imaging.

7.2.1 Method

Figure 7.1 shows a schematic of the experimental apparatus required to observe cooperative enhancement of energy transfer. Light resonant with either the D_1 ($5^2S_{1/2} \rightarrow 5^2P_{1/2}$) or D_2 ($5^2S_{1/2} \rightarrow 5^2P_{3/2}$) lines was sent through a 2 mm thermal vapour cell containing Rb atoms in their natural abundance (72% ^{85}Rb, 28% ^{87}Rb). The vapour cell is contained in an oven with the same

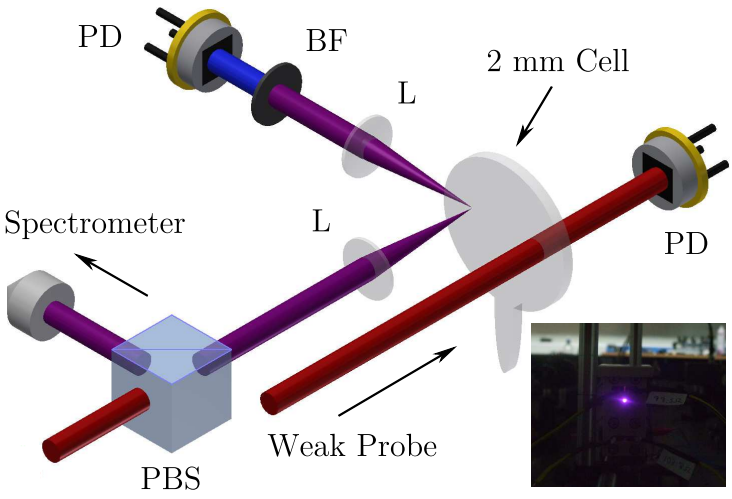

Figure 7.1: Schematic of the confocal microscopy and side-imaging experiments. A polarising beam splitter (PBS) provides linear light resonant with either the D_1 or D_2 lines, which is sent through a 2 mm thermal vapour cell containing Rb atoms in their natural abundance. For confocal microscopy, atoms illuminated in the focal plane of a lens (L) are imaged onto a broadband multi-mode fiber connected to a spectrometer. For side-imaging, a single bandpass filter (BF) is used to select the blue fluorescence from the cell, which is then incident on a calibrated photodiode (PD). A weak-probe beam sent through the cell was used to measure the atomic density as a function of the oven temperature. The inset shows a photograph of the visible fluorescence seen with infra-red input.

design as in section 3.4.2. Here we note that the cell heater has two extra holes which are used in this investigation. A side hole (see figure 3.4) which will be used for the side-imaging experiments and an additional front hole (see figure 7.1) which will be used for weak probe measurements. Using absolute absorption spectroscopy [92], the atomic density of the heated vapour can be measured as a function of the oven temperature. Varying the oven temperature between 20°C and 250°C allows us to investigate the fluorescence counts as a function of the cooperativity parameter. In a natural-abundant room-temperature reference cell hyperfine/saturated absorption spectroscopy was used to calibrate the detuning, Δ, of the resonant light: this technique is discussed in detail in appendix C. We then carry out two experiments: confocal microscopy [150] is first used to investigate the fluorescence lines over the visible and near infra-red regions and side-imaging is used to measure the spectral dependence of the $6^2P_{1/2,3/2} \rightarrow 5^2S_{1/2}$ transitions.

7.2.2 Confocal microscopy

For confocal microscopy the frequencies were centered on the $F = 3 \rightarrow F' = 3$ transitions of ^{85}Rb for the D_1 ($\Delta = -1.14$ GHz) and D_2 ($\Delta = -1.31$ GHz) lines. Beam widths of $1/e^2$ radius 5.94 ± 0.10 μm and 6.64 ± 0.16 μm, with beam powers of 60 mW and 80 mW, gave maximum beam intensities of 3.75×10^7 mW cm^{-2} and 4.00×10^7 mW cm^{-2} for the D_1 and D_2 lines, respectively. We use confocal microscopy to ensure the collection of fluorescence from a well-defined region. The backward fluorescence was then imaged onto a broadband multi-mode fiber connected to a USB4000-VIS-NIR Ocean Optics spectrometer. The spectrometer has a bandwidth of ~ 700 nm (348 - 1036 nm) over the visible and near infra-red regions, with a FWHM spectral resolution of ~ 1.5 nm.

7.2.3 Side-imaging

For side-imaging experiments, light with wavelength of 780 nm was scanned in the vicinity of the D_2 line. The cell heater described in section 3.4.2 has a side hole which can be used to image the illuminated atoms along the length of the cell. A lens was used to collimate the fluorescence onto a calibrated photodiode (Hamamatsu GaP diode 2.3 mm $\times$ 2.3 mm) that has large gain over the visible regions. To filter out all other colours except for the blue 420.30 nm ($6^2P_{3/2} \rightarrow 5^2S_{1/2}$) and 421.67 nm ($6^2P_{1/2} \rightarrow 5^2S_{1/2}$) lines we also add a single bandpass filter (Semrock Brightline single-band 4501-425/30-25) before the photodiode. Here the temperatures and corresponding number densities are recorded slightly differently. For a given voltage on a thermocouple held close to the cell reservoir we can extract a temperature from a calibrated curve using absolute-absorption spectroscopy. The advantage of this is that we could take multiple measurements without the need of carrying out many theoretical fits to weak-probe measurements. We use side-imaging as we found it was the best way to separate single transitions i.e. the blue lines.

7.3 Energy levels and fluorescence spectra

Figure 7.2 shows the energy levels and fluorescence spectra for the measured dipole-dipole induced energy transfer for two Rb atoms. Figure 7.2(a) shows the partial term diagram for a single Rb atom showing the (black) energy levels (THz) for the total orbital angular momentum states S, P, D and F ($L = 0$, 1, 2 and 3) as a function of n. The quasi-two-photon (dashed purple) resonances of 780.24 nm and 794.98 nm highlight the close proximity of the $5^2\mathrm{D}_J$ ($J = 3/2, 5/2$) energy levels. Figure 7.3 also shows the potential energy curves of these resonances due to dipole-dipole interactions for atoms at close separation. The (solid purple) line at 1010.03 THz (in figure 7.2) is the ionisation energy level for a single Rb atom. The (solid coloured) lines labeled $a - u$ show the allowed transitions, these can also be found in table 7.1. Note that b ($4^2\mathrm{D}_J$ ($J = 3/2, 5/2$) $\rightarrow 5^2\mathrm{S}_{1/2}$) is a weakly allowed quadrupole transition [151] largely due to second-order decays.

Figure 7.2(b) shows the normalised measured fluorescence counts as a function of wavelength and frequency for the resonant D_2 excitation of ^{85}Rb. This spectrum was measured for a number density of 9×10^{14} cm^{-3}, with a corresponding temperature of 200°C. The (solid white) measured fluorescence lines correspond to the labelled transitions in figure 7.2(a). The counts were normalised to the maximum saturated fluorescence of the 780.24 nm line. All of the 21 lines are visible with an exposure time of 500 ms on the spectrometer. In order to see all of the lines the large amount of resonant fluorescence on the spectrometer bleaches across several wavelengths. Similar spectra are measured for resonant D_1 light.

Table 7.1 shows the measured and calculated fluorescence in a thermal Rb vapour. Each transition (or group of transitions when the lines are indistinguishable) are assigned a label $a - u$, which are associated with the lines in figure 7.2. These energy levels were calculated from [152]. Transfer to the $5^2\mathrm{D}_J$ ($J = 3/2, 5/2$) states due to energy-pooling processes was expected [76]. However to the best of our knowledge no previous work has seen the other forest of visible lines.

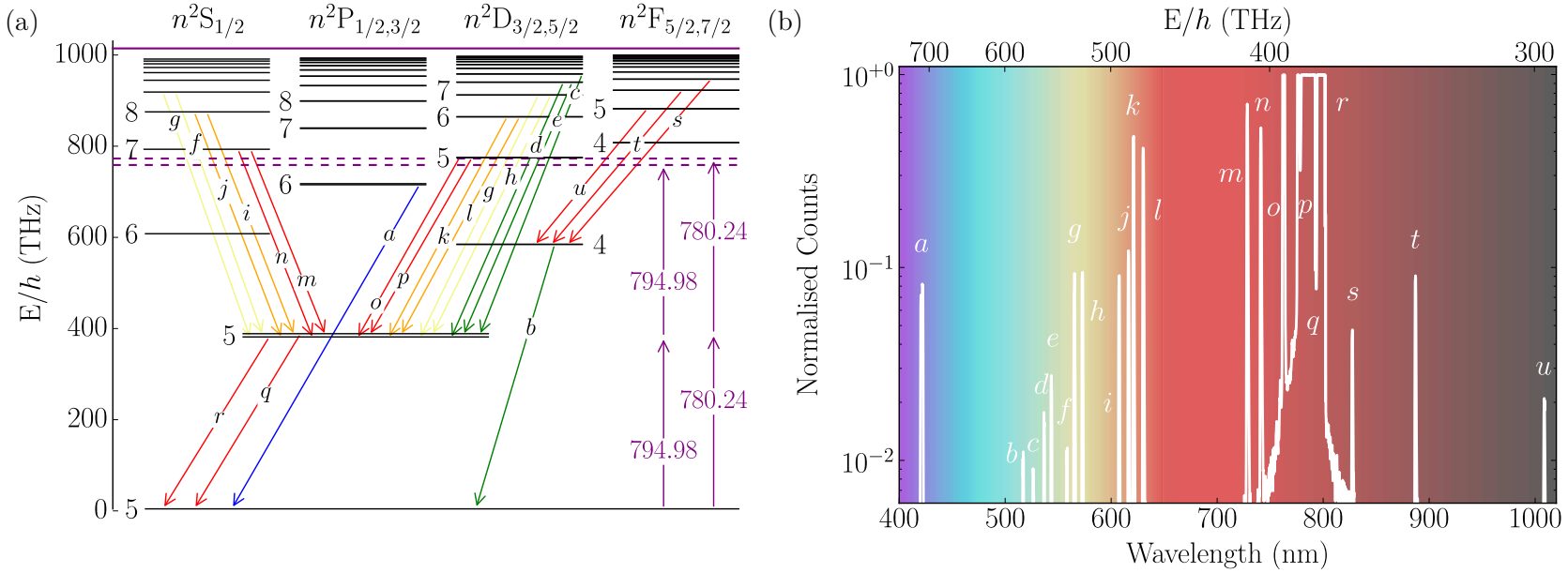

Figure 7.2: Energy levels and fluorescence spectrum for Rb. (a) shows the partial term diagram for a Rb atom. The (dashed purple) quasi-two-photon resonances are for the 780.24 nm and 794.98 nm lines. (b) shows the (solid white) normalised measured counts as a function of wavelength and frequency for the resonant D_2 line of ^{85}Rb. This spectrum was measured for a number density of 9×10^{14} cm^{-3}, with a corresponding temperature of 200°C. The (solid coloured) lines labeled $a-u$ are the measured and allowed fluorescence transitions.

Label	Wavelength (nm)	E/h (THz)	Transition
a	420.30	713.29	$6^2P_{3/2} \rightarrow 5^2S_{1/2}$
	421.67	710.96	$6^2P_{1/2} \rightarrow 5^2S_{1/2}$
b	516.65	580.27	$4^2D_{3/2} \rightarrow 5^2S_{1/2}$
	516.66	580.25	$4^2D_{5/2} \rightarrow 5^2S_{1/2}$
c	526.15	569.79	$9^2D_{5/2} \rightarrow 5^2P_{3/2}$
	526.17	569.77	$9^2D_{3/2} \rightarrow 5^2P_{3/2}$
d	536.41	558.89	$8^2D_{3/2} \rightarrow 5^2P_{1/2}$
e	543.30	551.80	$8^2D_{5/2} \rightarrow 5^2P_{3/2}$
	543.33	551.77	$8^2D_{3/2} \rightarrow 5^2P_{3/2}$
f	558.03	537.23	$9^2S_{1/2} \rightarrow 5^2P_{1/2}$
g	564.93	530.67	$7^2D_{3/2} \rightarrow 5^2P_{1/2}$
	565.53	530.11	$9^2S_{1/2} \rightarrow 5^2P_{3/2}$
h	572.57	523.59	$7^2D_{5/2} \rightarrow 5^2P_{3/2}$
	572.62	523.55	$7^2D_{3/2} \rightarrow 5^2P_{3/2}$
i	607.24	493.70	$8^2S_{1/2} \rightarrow 5^2P_{1/2}$
j	616.13	486.57	$8^2S_{1/2} \rightarrow 5^2P_{3/2}$
k	620.80	482.91	$6^2D_{3/2} \rightarrow 5^2P_{1/2}$
l	630.00	475.85	$6^2D_{5/2} \rightarrow 5^2P_{3/2}$
	630.09	475.79	$6^2D_{3/2} \rightarrow 5^2P_{3/2}$
m	728.20	411.69	$7^2S_{1/2} \rightarrow 5^2P_{1/2}$
n	741.02	404.57	$7^2S_{1/2} \rightarrow 5^2P_{3/2}$
o	762.10	393.38	$5^2D_{3/2} \rightarrow 5^2P_{1/2}$
p	775.97	386.34	$5^2D_{5/2} \rightarrow 5^2P_{3/2}$
	776.16	386.25	$5^2D_{3/2} \rightarrow 5^2P_{3/2}$
q	780.24	384.23	$5^2P_{3/2} \rightarrow 5^2S_{1/2}$
r	794.98	377.11	$5^2P_{1/2} \rightarrow 5^2S_{1/2}$
s	827.37	362.34	$7^2F_{5/2} \rightarrow 4^2D_{5/2}$
	827.37	362.34	$7^2F_{7/2} \rightarrow 4^2D_{5/2}$
	827.40	362.33	$7^2F_{5/2} \rightarrow 4^2D_{3/2}$
t	887.09	337.95	$6^2F_{5/2} \rightarrow 4^2D_{5/2}$
	887.09	337.95	$6^2F_{7/2} \rightarrow 4^2D_{5/2}$
	887.13	337.94	$6^2F_{5/2} \rightarrow 4^2D_{3/2}$
u	1007.80	297.47	$5^2F_{5/2} \rightarrow 4^2D_{5/2}$
	1007.80	297.47	$5^2F_{7/2} \rightarrow 4^2D_{5/2}$
	1007.85	297.46	$5^2F_{5/2} \rightarrow 4^2D_{3/2}$

Table 7.1: Wavelengths and frequencies of the measured and calculated fluorescence as a consequence of the energy transfer in a thermal Rb vapour. Each transition or group of transitions are assigned a label associated with the lines in figure 7.2.

7.4 Theoretical considerations

In section 7.4 we summarise the calculations used to help explain the experimental observations. Note these calculations were carried out by Christophe Vaillant, Robert J Bettles and Mark A Zentile and are only included in the thesis for completeness. We start by plotting the potential energy curves around the $5^2\mathrm{P}_J + 5^2\mathrm{P}_{J'}$ states. We then discuss the emission for highly-excited states from a kinetic-theory perspective. Finally we discuss the enhancement in the electric field between two atoms in the cooperative regime.

7.4.1 Potential-energy curves

The potential-energy curve calculations were done by Christophe Vaillant[1]. In summary, the theoretical model depends on the calculation of the dipole-dipole interactions using an effective Hamiltonian method. The pair state energies are given by the sum of the energies of the individual atomic states at infinite separation. The dipole-dipole interaction terms are proportional to the radial dipole matrix elements, internuclear distance, state-dependent angular factors [153] and damping functions [154]. Figure 7.3 shows the potential energy (in THz) curves of Rb around the $5^2\mathrm{P}_J + 5^2\mathrm{P}_{J'}$ curves at close separation. In any given moment in a gas, the constituent particles will have varying distances between themselves and their nearest neighbor. Assuming the particles are placed randomly and are non-interacting, we get the following probability distribution for the distance, R, to the nearest neighbor [155],

$$P(R) = 4\pi\mathcal{N}R^2 \exp\left[-\frac{4\pi\mathcal{N}}{3}R^3\right]. \tag{7.1}$$

The mean of this distribution is at $\Gamma\left(\frac{4}{3}\right)\left(\frac{3}{4\pi\mathcal{N}}\right)^{1/3} \approx \frac{5}{9}\mathcal{N}^{-1/3}$ [155, 156]. At $C = 1$ the atoms within the vapour are separated by a distance of $\lambda/2\pi$ (see table 3.1) and the resonant dipole-dipole interactions are of the order of MHz. As the form of the dipole-dipole interaction is R^{-3}, shifts on the order of THz can be measured for two orders of magnitude decrease in the separation i.e. $(\lambda/2\pi)/100$.

[1] A PhD student in our research group.

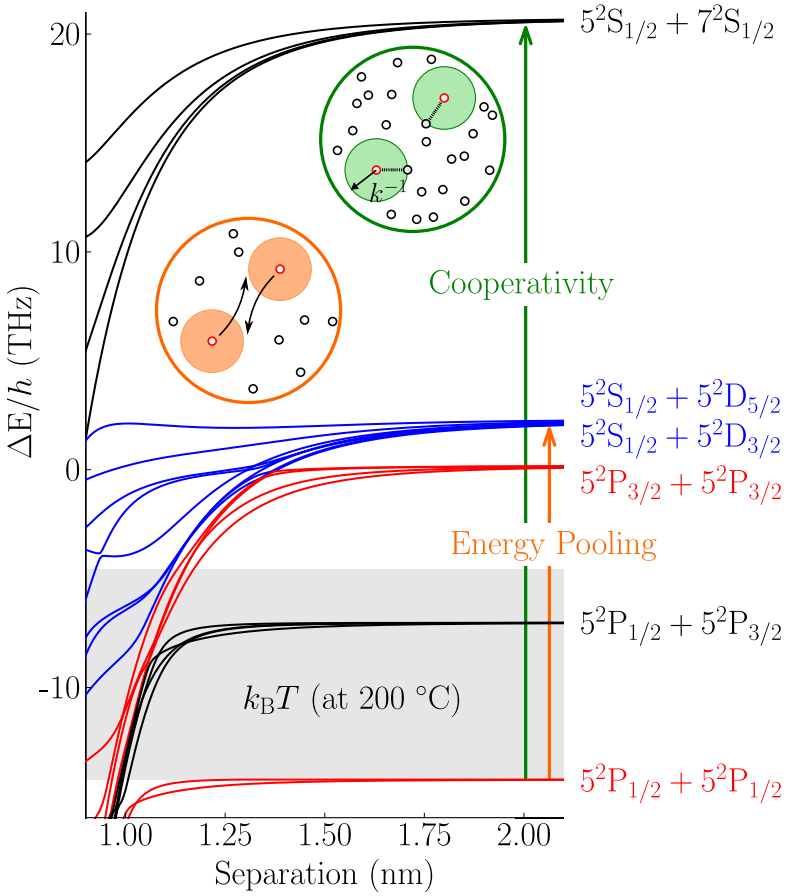

Figure 7.3: Potential energy curves for Rb around $5^2P_J + 5^2P_{J'}$ resonances at close separation. The solid (grey) box shows the average kinetic energy available for two Rb atoms at 200°C. The inset shows the two regimes of interest for state energy transfer. In the low density regime (orange) energy pooling between two identical atoms in their first excited states is the main process. In the high density regime (green) cooperative transfer for atoms in superpositions of the ground and excited states is the dominant mechanism.

7.4.2 Kinetic theory

The kinetic theory calculations were done by Mark A Zentile[2]. In an ideal gas, the probability density for a single particle to have a (non-relativistic) speed, is given by the well known Maxwell-Boltzmann speed distribution [157]. However, for two particle collisions the distribution of relative speeds v is a more useful quantity. We can reduce this two-body problem to an effective

[2]A PhD student in our research group.

one-body problem by simply replacing the mass m of the individual particles with the reduced mass $\mu = m/2$ [158]. So from the Maxwell-Boltzmann distribution we find

$$f_v(v) = 4\pi \left(\frac{m}{4\pi k_\mathrm{B} T}\right)^{\frac{3}{2}} v^2 \exp\left[-\frac{mv^2}{4k_\mathrm{B}T}\right] \ , \tag{7.2}$$

where k_B is the Boltzmann constant and T is the thermodynamic temperature. The mean of this distribution is described by equation 3.8. When considering whether certain inelastic collisions or reactions are allowed by energy conservation, we want to compare the total energy before and after. This is most convenient in the centre of mass (CM) frame since in this frame the momentum sums to zero so no energy is required to be carried away by kinetic energy after the process. Since the centre of mass lies equidistant between the two particles of equal mass, we can immediately see that the speed of two colliding particles of equal mass should be $u_1' = u_2' = v/2$, where u_1' and u_2' are the CM frame speeds of particle 1 and 2, respectively. From this we can derive an expression for the total kinetic energy, E, in the centre of mass frame,

$$\begin{aligned} \mathrm{E} &= \frac{1}{2} m\, u_1'^2 + \frac{1}{2} m\, u_2'^2 \ , \\ &= m \left(\frac{v}{2}\right)^2 \ . \end{aligned} \tag{7.3}$$

We now make use of the following result from probability theory [159]

$$f_y(y) = f_x(x) \left|\frac{dx}{dy}\right| \ , \tag{7.4}$$

where y is some function of the random variable x and f_y & f_x are the probability distributions of y & x, respectively. This, along with equation 7.2, allows us to arrive at the result

$$\begin{aligned} f_\mathrm{E}(v) &= \frac{8\pi}{m} \left(\frac{m}{4\pi k_\mathrm{B} T}\right)^{\frac{3}{2}} v \exp\left[-\frac{mv^2}{4k_\mathrm{B}T}\right] \ , \\ f_\mathrm{E}(\mathrm{E}) &= 2\sqrt{\frac{\mathrm{E}}{\pi}} \left(\frac{1}{k_\mathrm{B} T}\right)^{\frac{3}{2}} \exp\left[-\frac{\mathrm{E}}{k_\mathrm{B}T}\right] \ . \end{aligned} \tag{7.5}$$

Integrating equation 7.5 with limits of E equal to the threshold energy ΔE and infinity, will give the fraction of all collisions ΔF that have at least ΔE kinetic energy in the CM frame,

$$\Delta\mathrm{F} = \mathrm{erfc}\left(\sqrt{\frac{\Delta\mathrm{E}}{k_\mathrm{B}T}}\right) + 2\sqrt{\frac{\Delta\mathrm{E}}{\pi k_\mathrm{B}T}} \exp\left[\frac{-\Delta\mathrm{E}}{k_\mathrm{B}T}\right] \ , \tag{7.6}$$

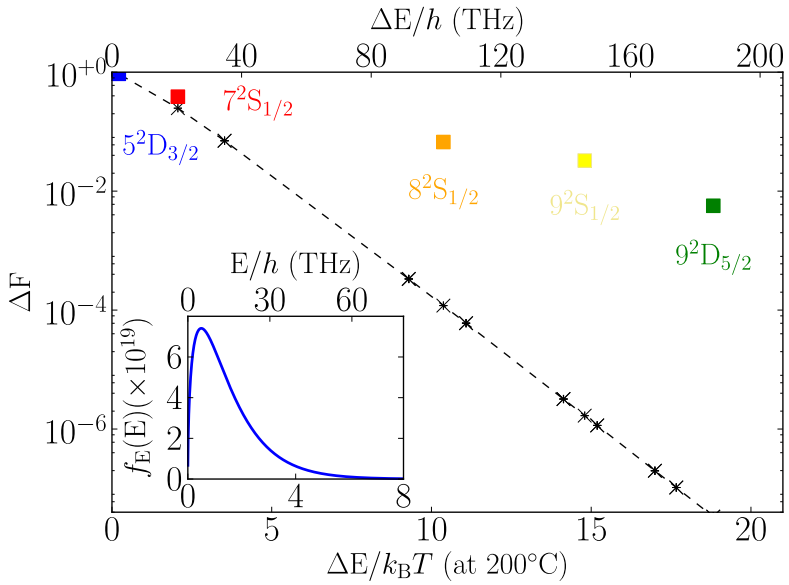

Figure 7.4: Two particle kinetic energy distribution, $f_{\mathrm{E}}(\mathrm{E})$, and fraction of collisions, $\Delta\mathrm{F}$, with the threshold energy as a function of the energy in terms of THz and $k_{\mathrm{B}}T$ (at 200°C). For large energy defects $\Delta\mathrm{E}/h = 185.56$ THz ($5^2\mathrm{P}_{3/2} + 5^2\mathrm{P}_{3/2} + \Delta\mathrm{E}_2 \rightarrow 9^2\mathrm{D}_{5/2} + 5^2\mathrm{S}_{1/2}$) one would expect eight orders of magnitude fewer particles with enough energy for state transfer. However only two orders of magnitude decrease in the amount of fluorescence is measured compared to the energy transfer to $5^2\mathrm{D}_{3/2}$ state.

where erfc denotes the complimentary error function [159]. Figure 7.4 shows the two particle kinetic energy distribution and the fraction of collisions as a function of threshold energy in terms of THz and $k_{\mathrm{B}}T$ (at 200°C). The solid (black) crosses are the theoretical fraction of collisions calculated using equation 7.6 and the energy defects $\Delta\mathrm{E}$ from table 7.3. The solid (coloured) squares are measured fluorescence taken from figure 7.2 where the $5^2\mathrm{D}_{3/2}$ state has been normalised to one. In the inset the solid (blue) line shows the two particle energy distribution calculated using equation 7.5 at 200°C. In tables 7.2 and 7.3 we list pair interactions for two excited Rb atoms, highlighting the energy required in terms of THz and $k_{\mathrm{B}}T$ (at 200°C = 9.86 THz) to reach the high-lying n states. The fraction of collisions with enough energy, $\Delta\mathrm{F}$, are also shown.

$\Delta E/h$ (THz)	ΔE_1 $\Delta E/k_B T$ (at 200°C)	ΔF (at 200°C)	States
-754.21	-76.50	1.00	$5^2S_{1/2} + 5^2S_{1/2}$
-377.10	-38.25	1.00	$5^2P_{1/2} + 5^2S_{1/2}$
-369.98	-37.53	1.00	$5^2P_{3/2} + 5^2S_{1/2}$
-173.96	-17.65	1.00	$4^2D_{5/2} + 5^2S_{1/2}$
-173.94	-17.64	1.00	$4^2D_{3/2} + 5^2S_{1/2}$
-150.65	-15.28	1.00	$6^2S_{1/2} + 5^2S_{1/2}$
-43.25	-4.39	1.00	$6^2P_{1/2} + 5^2S_{1/2}$
-40.93	-4.15	1.00	$6^2P_{3/2} + 5^2S_{1/2}$
0.00	0.00	1.00	$5^2P_{1/2} + 5^2P_{1/2}$
7.12	0.72	0.70	$5^2P_{3/2} + 5^2P_{1/2}$
14.25	1.44	0.41	$5^2P_{3/2} + 5^2P_{3/2}$
16.27	1.65	0.35	$5^2D_{3/2} + 5^2S_{1/2}$
16.36	1.66	0.35	$5^2D_{5/2} + 5^2S_{1/2}$
34.59	3.51	0.07	$7^2S_{1/2} + 5^2S_{1/2}$
49.00	4.97	0.02	$4^2F_{7/2} + 5^2S_{1/2}$
49.00	4.97	0.02	$4^2F_{5/2} + 5^2S_{1/2}$
105.81	10.73	8.43×10^{-5}	$6^2D_{3/2} + 5^2S_{1/2}$
105.88	10.74	8.37×10^{-5}	$6^2D_{5/2} + 5^2S_{1/2}$
116.52	11.82	2.97×10^{-5}	$8^2S_{1/2} + 5^2S_{1/2}$
123.51	12.53	1.50×10^{-5}	$5^2F_{7/2} + 5^2S_{1/2}$
123.52	12.53	1.50×10^{-5}	$5^2F_{5/2} + 5^2S_{1/2}$
153.56	15.58	7.90×10^{-7}	$7^2D_{3/2} + 5^2S_{1/2}$
153.61	15.58	7.86×10^{-7}	$7^2D_{5/2} + 5^2S_{1/2}$
160.13	16.24	4.14×10^{-7}	$9^2S_{1/2} + 5^2S_{1/2}$
163.99	16.63	2.83×10^{-7}	$6^2F_{7/2} + 5^2S_{1/2}$
163.99	16.63	2.83×10^{-7}	$6^2F_{5/2} + 5^2S_{1/2}$
181.78	18.44	4.89×10^{-8}	$8^2D_{3/2} + 5^2S_{1/2}$
181.81	18.44	4.87×10^{-8}	$8^2D_{5/2} + 5^2S_{1/2}$
188.39	19.11	2.54×10^{-8}	$7^2F_{7/2} + 5^2S_{1/2}$
188.39	19.11	2.54×10^{-8}	$7^2F_{5/2} + 5^2S_{1/2}$
199.78	20.26	8.23×10^{-9}	$9^2D_{3/2} + 5^2S_{1/2}$
199.81	20.27	8.21×10^{-9}	$9^2D_{5/2} + 5^2S_{1/2}$

Table 7.2: Pair interactions for two excited Rb atoms ($5^2P_{1/2} + 5^2P_{1/2} + \Delta E_1 \rightarrow$ States), highlighting the energy required in terms of THz and $k_B T$ (at 200°C = 9.86 THz) to reach the high-lying n states. The fraction of collisions with enough energy, ΔF, is also shown.

ΔE_2			
$\Delta E/h$ (THz)	$\Delta E/k_B T$ (at 200°C)	ΔF (at 200°C)	States
-768.46	-77.95	1.00	$5^2S_{1/2} + 5^2S_{1/2}$
-391.35	-39.70	1.00	$5^2P_{1/2} + 5^2S_{1/2}$
-384.23	-38.97	1.00	$5^2P_{3/2} + 5^2S_{1/2}$
-188.21	-19.09	1.00	$4^2D_{5/2} + 5^2S_{1/2}$
-188.19	-19.09	1.00	$4^2D_{3/2} + 5^2S_{1/2}$
-164.90	-16.73	1.00	$6^2S_{1/2} + 5^2S_{1/2}$
-57.50	-5.83	1.00	$6^2P_{1/2} + 5^2S_{1/2}$
-55.18	-5.60	1.00	$6^2P_{3/2} + 5^2S_{1/2}$
-14.25	-1.44	1.00	$5^2P_{1/2} + 5^2P_{1/2}$
-7.12	-0.72	1.00	$5^2P_{3/2} + 5^2P_{1/2}$
0.00	0.00	1.00	$5^2P_{3/2} + 5^2P_{3/2}$
2.02	0.20	0.94	$5^2D_{3/2} + 5^2S_{1/2}$
2.11	0.21	0.93	$5^2D_{5/2} + 5^2S_{1/2}$
20.34	2.06	0.25	$7^2S_{1/2} + 5^2S_{1/2}$
34.75	3.52	0.07	$4^2F_{7/2} + 5^2S_{1/2}$
34.75	3.52	0.07	$4^2F_{5/2} + 5^2S_{1/2}$
91.56	9.29	3.35×10^{-4}	$6^2D_{3/2} + 5^2S_{1/2}$
91.63	9.29	3.33×10^{-4}	$6^2D_{5/2} + 5^2S_{1/2}$
102.27	10.37	1.19×10^{-4}	$8^2S_{1/2} + 5^2S_{1/2}$
109.26	11.08	6.03×10^{-5}	$5^2F_{7/2} + 5^2S_{1/2}$
109.27	11.08	6.02×10^{-5}	$5^2F_{5/2} + 5^2S_{1/2}$
139.31	14.13	3.20×10^{-6}	$7^2D_{3/2} + 5^2S_{1/2}$
139.36	14.14	3.19×10^{-6}	$7^2D_{5/2} + 5^2S_{1/2}$
145.88	14.80	1.68×10^{-6}	$9^2S_{1/2} + 5^2S_{1/2}$
149.74	15.19	1.15×10^{-6}	$6^2F_{7/2} + 5^2S_{1/2}$
149.74	15.19	1.15×10^{-6}	$6^2F_{5/2} + 5^2S_{1/2}$
167.53	16.99	1.99×10^{-7}	$8^2D_{3/2} + 5^2S_{1/2}$
167.56	17.00	1.99×10^{-7}	$8^2D_{5/2} + 5^2S_{1/2}$
174.14	17.66	1.04×10^{-7}	$7^2F_{7/2} + 5^2S_{1/2}$
174.14	17.66	1.04×10^{-7}	$7^2F_{5/2} + 5^2S_{1/2}$
185.53	18.82	3.37×10^{-8}	$9^2D_{3/2} + 5^2S_{1/2}$
185.56	18.82	3.36×10^{-8}	$9^2D_{5/2} + 5^2S_{1/2}$

Table 7.3: Pair interactions for two excited Rb atoms ($5^2P_{3/2} + 5^2P_{3/2} + \Delta E_2 \rightarrow$ States), highlighting the energy required in terms of THz and $k_B T$ (at 200°C = 9.86 THz) to reach the high-lying n states. The fraction of collisions with enough energy, ΔF, is also shown.

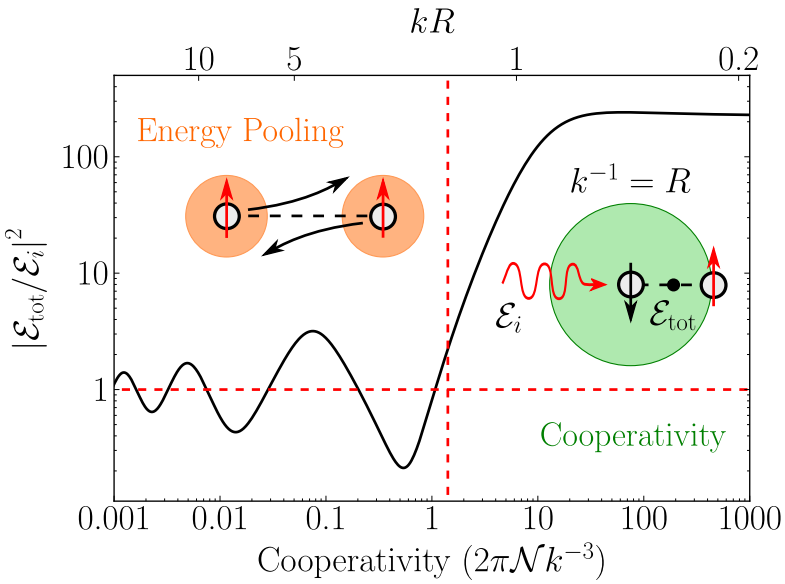

Figure 7.5: Enhancement in the electric field midway between two atoms as a function of the cooperativity parameter and their separation. The total electric field, $\mathcal{E}_{\rm tot}$, is calculated by summing the driving field, $\mathcal{E}_{\rm i}$, and the fields produced by each of the atomic dipoles. The two atoms resemble an optical cavity, producing enhancements in the electric field of over two orders of magnitude for a cooperativity larger than $\sqrt{2}$ (dotted vertical red line).

7.4.3 Enhancement in the electric field

The electric field calculations were done by Robert J Bettles[3]. In summary, the model is a semi-classical model that includes an oscillating classical electric field that drives dipole transitions in a pair of two-level atoms separated in the direction of propagation of the driving field. A matrix is generated which couples each atom to the driving field as well as to the field produced by the other atom. This matrix is then diagonalised and we extract each of the dipole moments. The total electric field, $\mathcal{E}_{\rm tot}$, midway between these two atoms is calculated by summing the driving field, $\mathcal{E}_{\rm i}$, and the fields produced by each of the atomic dipoles. Figure 7.5 shows the total electric field as a function of cooperativity and separation. For cooperativities larger than $\sqrt{2}$ we see a dramatic increase in the total electric field.

[3]A PhD student in our research group.

7.5 Dependencies with number density

In section 7.5 we show dependencies with number density for the confocal microscopy and side-imaging experiments discussed in section 7.2.

7.5.1 Confocal microscopy results

Figure 7.6 shows the normalised measured fluorescence counts as a function of the cooperativity parameter and temperature for the resonant D_2 (crosses) excitation of ^{85}Rb. For each measured value of the cooperativity parameter an uncertainty in the number density is extracted from a least-squares fit using absolute absorption spectroscopy [22]. The uncertainty in the fluorescence measurements is given by the square root of the number of counts. Figure 7.6(a), (b), (c) and (d) show the (red) normalised measured fluorescence for the 780.24 nm ($5^2P_{3/2} \rightarrow 5^2S_{1/2}$), 794.98 nm ($5^2P_{1/2} \rightarrow 5^2S_{1/2}$), 762.10 nm ($5^2D_{3/2} \rightarrow 5^2P_{1/2}$) and 776.16/775.97 nm ($5^2D_{3/2,5/2} \rightarrow 5^2P_{3/2}$) transitions, respectively.

For $C \leq \sqrt{2}$ the increase in the amount of fluorescence is a result of state transfer due to energy-pooling processes. For two excited Rb atoms with thermal energy 9.86 THz (at 200°C) the energy defects of 2.02 THz and 2.11 THz for the $5^2D_{3/2}$ and $5^2D_{5/2}$ states are easily compensated. Therefore population transfer to these states is always expected for a thermal Rb vapour. When $C \geq \sqrt{2}$ the dependencies on the amount of fluorescence for each line is rather different. For figures 7.6(a) and (d) the amount of the 780.24 nm and 776.16/775.97 nm fluorescence decreases, this can be attributed to the fact that the amount of population transferred to the higher states is greatly increased (see figure 7.7) removing population from these states. For figures 7.6(b) and (c) the amount of the 794.98 nm and 762.10 nm fluorescence increases, this can be attributed to the fact that the amount of population transferred to the higher states provides an increase amount of second-order decays via these states.

Figure 7.7 shows the normalised measured fluorescence counts as a function of the cooperativity parameter and temperature for the resonant D_1 (circles) and D_2 (crosses) excitations of ^{85}Rb. Since the cooperativity parameter scales

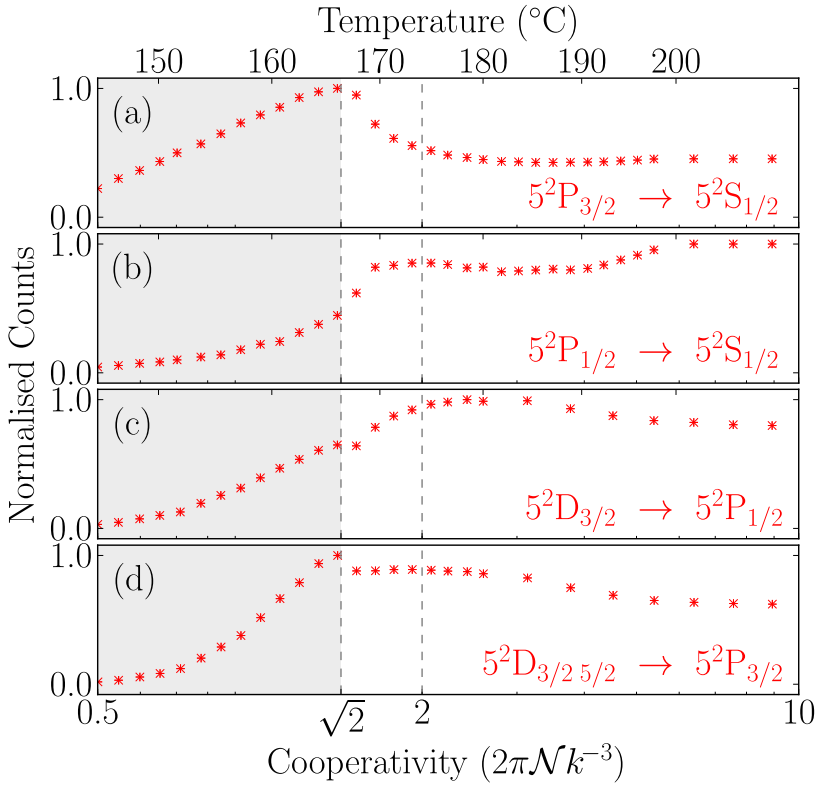

Figure 7.6: Fluorescence transitions as a function of the cooperativity parameter and temperature for the resonant D_2 (crosses) excitation. (a), (b), (c) and (d) show the (red) normalised measured fluorescence for the 780.24 nm, 794.98 nm, 762.10 nm and 776.16/775.97 nm transitions, respectively. For $C \leq \sqrt{2}$ the energy-pooling process is the dominant mechanism for state transfer. For $C \geq \sqrt{2}$ transfer of population to higher states and second-order decays from these higher states results in a change in the amount of measured fluorescence.

with wavevector here we chose the temperature axis to be calculated for the D_1 wavevector. The uncertainty in the number density which defines the cooperativity parameter is calculated as in figure 7.6. Figures 7.7(a), (b) and (c) show the normalised measured fluorescence for the 421.67 nm (blue) ($6^2P_{1/2} \rightarrow 5^2S_{1/2}$), 630.09 nm (orange) ($6^2D_{3/2} \rightarrow 5^2P_{3/2}$) and 728.20 nm (red) ($7^2S_{1/2} \rightarrow 5^2P_{1/2}$) transitions, respectively.

In figure 7.7(a) the $6^2P_{1/2}$ state can be populated via several state transfers. For $C \leq 2$ the rapid rise in the amount of 421.67 nm fluorescence is a result of energy-pooling processes. For a negative energy defect, two excited (5^2P_J ($J = 1/2, 3/2$)) atoms can produce a $5^2S_{1/2}$ atom and a $6^2P_{1/2}$

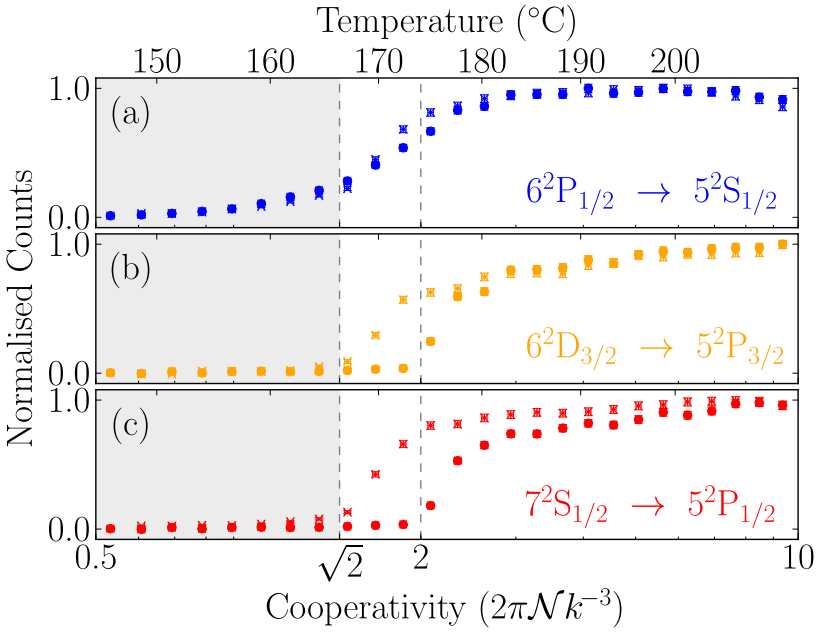

Figure 7.7: Fluorescence transitions as a function of the cooperativity parameter and temperature for the resonant D_1 (circles) and D_2 (crosses) excitation. (a), (b) and (c) show the normalised measured fluorescence for the 421.67 nm (blue), 630.09 nm (orange) and 728.20 nm (red) transitions, respectively. For (a) the state can be accessed via the energy-pooling process with a negative energy defect, therefore this is the dominant mechanism for state transfer. A monotonic increase in fluorescence as a function of density is observed until the cooperative-enhancement mechanism becomes active for other lines thus reducing the number of excited $6^2P_{1/2}$ atoms. For larger temperatures the medium becomes optically thick for the blue light and radiation trapping occurs. For (b) and (c) the population of the excited state via energy pooling is kinematically forbidden as the energy defect is many times larger than the collisional energy. Very little signal is seen from these two lines until a dramatic turn on occurs for a cooperativity of $\sqrt{2}$ and 2 for D_2 and D_1 excitations, respectively.

atom. In addition we have already shown (see figure 7.6) that there is always enough thermal kinetic energy to compensate the defect to the $5^2D_{3/2,5/2}$ states. When $C \geq 2$ the amount of 421.67 nm fluorescence saturates as a consequence of an increased population to the higher n states. These highly-populated states preferably cascade down via the $5^2P_{1/2}/5^2P_{3/2}$ states. For $C \gg 2$ self-absorption [78] on the 421.67 nm transition becomes dominant and a decrease in the number of counts is observed.

In figures 7.7(b) and (c) within the sensitivity of the apparatus no fluorescence is measured for $C \ll \sqrt{2}$ and 2 for the D_2 and D_1 excitations, respectively. As C increases, as long as the energy defect can be compensated, the number of atoms with enough thermal energy to state transfer increases exponentially. However in contrast to the $6^2P_{1/2}$ state the energy defect for $7^2S_{1/2}$ and $6^2D_{3/2}$ states is far too big for energy-pooling processes to be responsible for transfer. Transfer to these higher lying n states is hypothesised to be the result of cooperative effects due to resonant dipole-dipole interactions. Further evidence for the role of cooperative enhancement is obtained from a comparison of the D_1 and D_2 excitation. The magnitude of these interactions are well-known to be $\sqrt{2}$ larger for the D_2 line [118]. Using equations 3.29 and 3.30 we see that

$$C_1 = 2\pi\mathcal{N}k_1^{-3} = \frac{\Gamma_{\text{self}}}{\Gamma_1}\ , \tag{7.7}$$

$$C_2 = 2\pi\mathcal{N}k_2^{-3} = \frac{\Gamma_{\text{self}}}{\sqrt{2}\Gamma_2}\ . \tag{7.8}$$

In figures 7.7(b) and (c) we see that an enhancement in the fluorescence is observed when $C = \sqrt{2}$ and $C = 2$, where resonant dipole-dipole interactions become important for the D_2 and D_1 line, respectively.

7.5.2 Side-imaging results

Figure 7.8 shows the spectral dependence of the measured fluorescence for the $6^2P_{1/2,3/2} \rightarrow 5^2S_{1/2}$ transition as a function of the number density and temperature for input light resonant with the D_2 line. For small temperatures and number densities the collective thermal energy of two excited Rb atoms is far too small for state transfer to occur. The solid (grey) lines in figure 7.8(a) show the solid (black) measured fluorescence in figures 7.8(b), (c) and (d) for temperatures and corresponding number densities of 163.6°C ($\mathcal{N} = 1.94 \times 10^{14}$ cm^{-3}), 164.5°C ($\mathcal{N} = 2.02 \times 10^{14}$ cm^{-3}) and 166.4°C ($\mathcal{N} = 2.22 \times 10^{14}$ cm^{-3}), respectively. The theoretical optical depth curves in figures 7.8(b), (c) and (d) are calculated using the absorption coefficient from the model in part I of the thesis and a length scale of 15 μm. This length scale was extract from a fit to figure 7.8(b) and is fixed for the other two data sets.

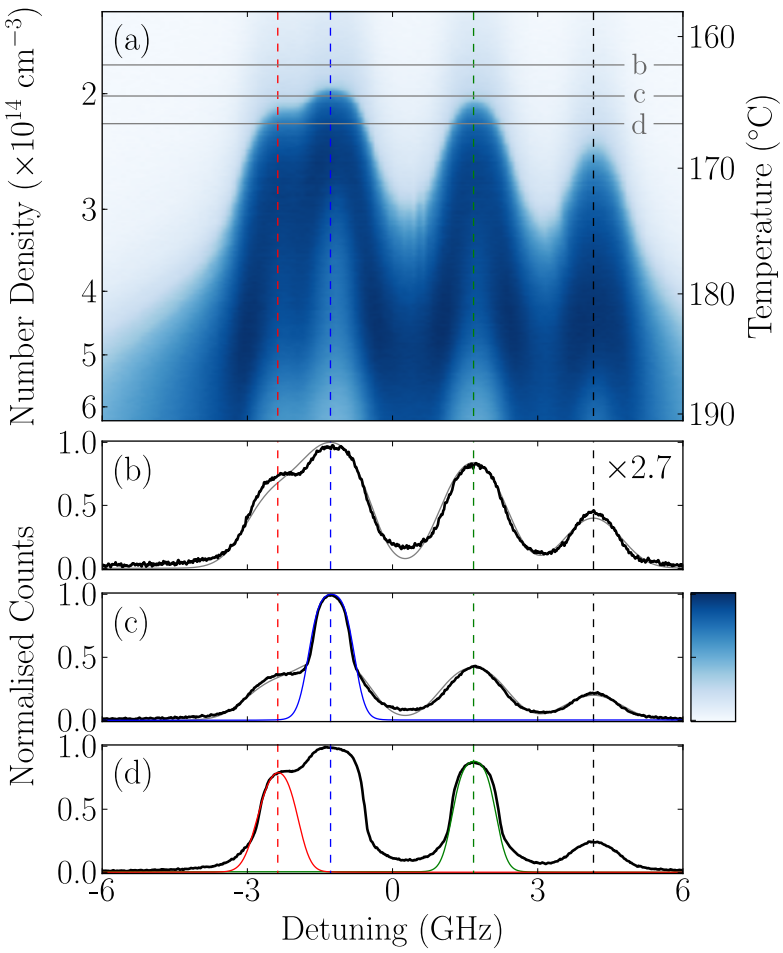

Figure 7.8: (a) Spectral dependence of the $6^2P_{1/2,3/2} \rightarrow 5^2S_{1/2}$ transitions as a function of the number density and temperature for input light resonant with the D_2 line. The dashed (blue) and (green) lines correspond to the maximum fluorescence for the $F = 3 \rightarrow F' = 2, 3, 4$ ($\Delta = -1.23$ GHz) and $F = 2 \rightarrow F' = 1, 2, 3$ ($\Delta = 1.68$ GHz) transitions of ^{85}Rb, respectively. The dashed (red) and (black) lines correspond to the maximum fluorescence for the $F = 2 \rightarrow F' = 1, 2, 3$ ($\Delta = -2.47$ GHz) and $F = 1 \rightarrow F' = 0, 1, 2$ ($\Delta = 4.15$ GHz) transitions of ^{87}Rb, respectively. Plots (b), (c) and (d) show the normalised measured fluorescence for temperatures and corresponding number densities of 163.63°C, 164.50°C and 166.35°C, respectively. A normalisation factor 2.7 is used in plot (b). The solid (grey) line in plots (b) and (c) has been calculated for a Doppler width of $2kv$. The solid (coloured) lines in plots (c) and (d) have been calculated for Doppler widths of kv.

We have already shown that atoms transfer their states if the energy defects can be compensated by the total thermal energy of two excited atoms. The

solid (grey) line in figure 7.8(b) has a Doppler width of $2kv$. Comparison between experiment and theory conclude that the mechanism for transfer must involve two excited atoms as the Gaussian width is twice as wide as for a single absorption profile. The solid (blue) line in figure 7.8(c) has a Doppler width of kv. For this number density resonant dipole-dipole interactions are dominant and enhanced state transfer is observed. Comparison between experiment and theory shows a clear narrowing of the spectral dependence for this regime and hints towards a single atom mechanism being responsible for the enhancement. We see no evidence for the medium having become a hot plasma [160], nor for other possible population transfer mechanisms such as multi-photon ionisation or dimer formation [83]. Figure 7.8(d) demonstrates that different spectral lines are enhanced at different temperatures; note that the peak at a detuning of 4.15 GHz has yet to be enhanced. The reason for this is that the cooperativity parameter has a dependence on the degeneracy of the ground state and the amount of each isotope has to be taken into account. Also note that for higher temperatures and number densities radiation trapping is clearly visible on resonance.

7.6 Discussion

In summary, we have extended the previous experimental and theoretical studies of state transfer due to energy-pooling processes in alkali-metal systems. Low-density transfer arises due to the well-known energy-pooling effect between two identical atoms, in their first excited states. We provide evidence for the enhancement of energy transfer and attribute this to resonant dipole-dipole interactions in the cooperative regime. The 2 and $\sqrt{2}$ for the D_1 and D_2 excitation corroborates this mechanism. Blue fluorescence hints at single-atom emission; certainly not a hot plasma. Cooperative effects in alkali-metal atoms allows a deeper understanding of complex systems in the real world. These observations open interesting prospects for exploiting dipole-dipole enhanced fields in non-linear optics and quantum optics.

Chapter 8

Conclusions and Outlook

8.1 Conclusion

Here we provide a brief summary of the work investigated in this thesis. Our main concern in part I of the thesis was the demonstration of excellent agreement between a theoretical model and experimental measurements of the absorptive and dispersive properties of a dense thermal Rb vapour in the absence and presence of a magnetic field.

In the absence of a magnetic field we have experimentally shown agreement for measurements of the absolute Doppler-broadened transmission for densities up to 3×10^{14} cm^{-3} (170°C). For densities above 8×10^{13} cm^{-3} (145°C) the Lorentzian component of the D lines needs to be modified as the result of dipole-dipole interactions. We have shown that a simple modification of the theoretical model for electric susceptibility to take into account the extra Lorentzian component allowed us to ascertain the value of the self-broadening coefficient for the Rb D_1 line to be $\beta/2\pi = (0.69 \pm 0.04) \times 10^{-7}$ Hz cm^3, which was in agreement with the theoretical prediction.

In the presence of a magnetic field we have tested our model for the electric susceptibility of Rb vapour. For the absorption and dispersion properties we showed agreement for transmission spectra and differencing spectra of rubidium vapour on the D_2 line for magnetic fields up to and including 0.6 T, which corresponds to the HPB regime on the D lines. Also for the dispersion properties we showed agreement for Stokes parameters red detuned from

the D_2 ^{87}Rb $F = 2 \rightarrow F'$ transitions for magnetic fields up to 0.08 T. The excellent agreement between theory and experiment gives confidence in the model; this allowed us to demonstrate the principle of an optical isolator for the Rb D_2 line by exploiting the spectral region of high transmission and large dispersion where we would normally expect absorption.

In part II of the thesis we considered an atomic medium of Rb subject to strong excitation. Here we carried out a comparative study of state energy transfer. We found that low density transfer arose due to the well-known energy-pooling effect between two identical atoms, in their first excited terms and cooperative enhancement of transfer is the result of dipole-dipole interactions in high density media.

8.2 Outlook

Here we discuss some possible investigations that would easily be accessible with the current apparatus and theoretical models. Firstly, the theoretical model could be generalised for all group I elements. As more group I elements are investigated in the research group at Durham and elsewhere, one can imagine a general model that only requires knowledge of what element and isotope, and which spectral line to compare theory and experiment. Secondly, using the model we have already predicted the ideal parameters for an optical isolator using an atomic medium (see section 6.4.4). Ideally we would now like to show this experimentally with a more compact heater and a permanent magnet with optimised dimensions. Finally, we would attempt to produce heralded single photons with a 4 wave mixing scheme using $5^2S_{1/2}$, $5^2P_{1/2}$, $5^2P_{3/2}$, $5^2D_{3/2,5/2}$ terms in Rb. It has already been shown that it is possible to produce an efficient heralded single photon source in a thermal atomic vapour [161]. Here we would develop a system where the cooperative enhancement described in chapter 7 would help eliminate one of the wavelengths (762 nm) required to populate the $5^2D_{3/2,5/2}$ terms and hopefully one could imagine two correlated 780 nm photons being emitted. For quantum optics in dense thermal vapours the future's bright; the future's blue[1].

[1] other colours are available: see figure 7.2(b).

Appendix A

Rubidium atomic & spectroscopic data

In appendix A we write the vapour pressure and number density formulae for Rb, also listing the essential atomic and spectroscopic data.

A.1 Vapour pressure and number density

The vapour pressure (in Torr), P_v, for solid Rb is given by the following equation [121]

$$\log P_v = 2.881 + 4.857 - \frac{4215}{T} \ , \tag{A.1}$$

and for liquid Rb is given by [121]

$$\log P_v = 2.881 + 4.312 - \frac{4040}{T} \ , \tag{A.2}$$

where T is the absolute temperature. The melting point of Rb is 39.30°C. The accuracy of the vapour pressure formulae is better than 5% in the temperature range 20 - 280°C. Using these vapour pressure formulae the number density, $\mathcal{N}$, of Rb atoms can be calculated

$$\mathcal{N} = \frac{133.323 \times P_v}{k_{\rm B} T} \ . \tag{A.3}$$

The factor 133.323 converts the vapour pressure from Torr to Pa. Figure A.1 shows the number density as a function of temperature (in °C/K) for natural

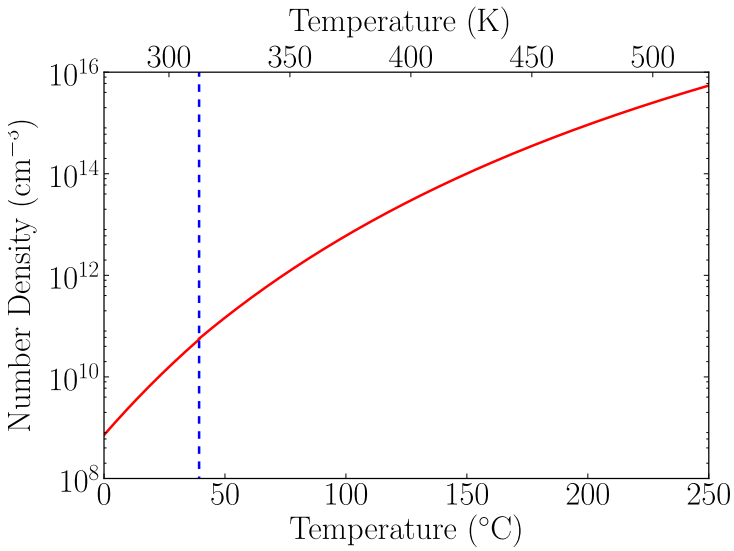

Figure A.1: The number density as a function of temperature for natural abundant Rb. The solid (red) curve corresponds to the number density for Rb. The dotted (blue) line at 39.30°C marks the transition between solid and liquid phases.

abundant Rb. As there are two isotopes present in a vapour cell, the number density of each isotope can be calculated as

$$\mathcal{N}_{85} = C_{85} \times \frac{133.323 \times P_v}{k_{\mathrm{B}} T} \,, \tag{A.4}$$

$$\mathcal{N}_{87} = C_{87} \times \frac{133.323 \times P_v}{k_{\mathrm{B}} T} \,, \tag{A.5}$$

where C_{85} and C_{87} are the relative abundances, given in tables A.1 and A.2.

A.2 Atomic data

Property	Symbol	Value
Atomic Number	Z	37 [162]
Atomic Mass	M	84.911789732(14) u [163]
Relative Natural Abundance	C_{85}	72.17(2)% [163]
Nuclear Spin	I	$\frac{5}{2}$
Groundstate Degeneracy	$2(2I+1)$	12

Table A.1: Atomic data for ^{85}Rb.

Property	Symbol	Value
Atomic Number	Z	37 [162]
Atomic Mass	M	86.909180520(15) u [163]
Relative Natural Abundance	C_{87}	27.83(2)% [163]
Nuclear Spin	I	$\frac{3}{2}$
Groundstate Degeneracy	$2(2I+1)$	8

Table A.2: Atomic data for ^{87}Rb.

A.3 Spectroscopic data

Property	Symbol	Value
Wavelength (vacuum)	λ	794.979014933(96) nm [164]
Wavevector	k	7903586.371 m^{-1}
Frequency	ν	377.107385690(46) THz [164]
Decay Rate	Γ	$2\pi \times$ 5.746 MHz [96]
Reduced Dipole Matrix Element	d	5.182 ea_0 (see section 3.3.1)

Table A.3: Spectroscopic data for D_1 line

Property	Symbol	Value
Wavelength (vacuum)	λ	780.241368271(27) nm [98]
Wavevector	k	8052873.846 m^{-1}
Frequency	ν	384.230406373(14) THz [98]
Decay Rate	Γ	$2\pi \times$ 6.065 MHz [96]
Reduced Dipole Matrix Element	d	5.177 ea_0 (see section 3.3.1)

Table A.4: Spectroscopic data for D_2 line

Appendix B

Matrix calculations

In appendix B we show calculations for the $\hat{L}\cdot\hat{S}$ and $\hat{I}\cdot\hat{J}$ matrices used in chapter 2. Here we also show the relative line-strength calculations for π transitions which are ignored in the main part of the thesis.

B.1 $\hat{L}\cdot\hat{S}$ matrix

All angular momentum operators, A, satisfy the same set of commutation rules and therefore we can derive the general result (see page 121 in [165])

$$\hat{A}_{\pm}\,|A,m_A\rangle \;=\; \sqrt{A(A+1)-m_A(m_A\pm 1)}\hbar\,|A,m_A\pm 1\rangle \;, \qquad \text{(B.1)}$$

where $\hat{A}_+ = \hat{A}_x + \mathrm{i}\hat{A}_y$. The matrix $\hat{A}_+$ is only non-zero along the upper diagonal. Note $\hat{A}_-$ is given by the transpose of $\hat{A}_+$. The $\hat{A}_x$, $\hat{A}_y$ and $\hat{A}_z$ matrices are given by (see page 523 in [166])

$$\hat{A}_x \;=\; \frac{1}{2}\left(\hat{A}_+ + \hat{A}_-\right) \;, \qquad \text{(B.2)}$$

$$\hat{A}_y \;=\; -\frac{\mathrm{i}}{2}\left(\hat{A}_+ - \hat{A}_-\right) \;, \qquad \text{(B.3)}$$

$$\hat{A}_z \;=\; \frac{1}{2}\left(\hat{A}_+\hat{A}_- - \hat{A}_-\hat{A}_+\right) \;. \qquad \text{(B.4)}$$

Using these well-known results one can construct the matrix components for any spin or angular momenta. To construct the spin-orbit interaction matrix $\hat{L}\cdot\hat{S}$ in the uncoupled basis, we introduce the total electronic angular momentum, $\hat{J} = \hat{L} + \hat{S}$, which is the sum of the spin angular momentum,

$\hat{S}$, and the orbital angular momentum, $\hat{L}$. Starting with this expression the spin-orbit interaction matrix can be written as

$$\begin{aligned} \hat{J} &= \hat{L} + \hat{S} \ , \\ \hat{J}^2 &= (\hat{L} + \hat{S})^2 \ , \\ \hat{J}^2 &= \hat{L}^2 + \hat{S}^2 + 2\hat{L} \cdot \hat{S} \ , \\ \hat{L} \cdot \hat{S} &= \frac{1}{2}\left(\hat{J}^2 - \hat{L}^2 - \hat{S}^2\right) \ , \end{aligned} \tag{B.5}$$

where we use the property that for commuting operators $\hat{L} \cdot \hat{S} = \hat{S} \cdot \hat{L}$ (see equation 4.183 in [166]). To get the form of this matrix we start by calculating the total spin angular momentum, $\hat{S}^2$. For a single electron atom the individual spin components are given by $\hat{S} = S\hat{\sigma}$, where $S = \frac{1}{2}\hbar$ and $\hat{\sigma} = (\hat{\sigma}_x, \hat{\sigma}_y, \hat{\sigma}_z)$ are the Pauli spin matrices [165]. The three components of the spin angular momentum are therefore

$$\hat{S}_x = \frac{\hbar}{2}\begin{pmatrix} 0 & 1 \\ 1 & 0 \end{pmatrix} \ \hat{S}_y = \frac{\hbar}{2}\begin{pmatrix} 0 & -\mathrm{i} \\ \mathrm{i} & 0 \end{pmatrix} \ \hat{S}_z = \frac{\hbar}{2}\begin{pmatrix} 1 & 0 \\ 0 & -1 \end{pmatrix} \ . \tag{B.6}$$

To calculate the total spin angular momentum, $\hat{S}^2$, we square the matrices to give

$$\begin{aligned} \hat{S}^2 &= \hat{S}_x \cdot \hat{S}_x + \hat{S}_y \cdot \hat{S}_y + \hat{S}_z \cdot \hat{S}_z \ , \\ &= \frac{3}{4}\hbar^2 \begin{pmatrix} 1 & 0 \\ 0 & 1 \end{pmatrix} \ . \end{aligned} \tag{B.7}$$

Here we comment that for the $5^2\mathrm{S}_{1/2}$ term where $L = 0$ there is no fine structure splitting. Consequently we chose to write the spin-orbit interaction matrix for the 5P term where $L = 1\hbar$. To calculate the total orbital angular momentum, $\hat{L}^2$, we first need to the calculate the individual components $\hat{L}_x, \hat{L}_y$ and $\hat{L}_z$ given by

$$\hat{L}_x = \sqrt{\frac{1}{2}}\hbar \begin{pmatrix} 0 & 1 & 0 \\ 1 & 0 & 1 \\ 0 & 1 & 0 \end{pmatrix} \ , \hat{L}_y = \sqrt{\frac{1}{2}}\hbar \begin{pmatrix} 0 & -\mathrm{i} & 0 \\ \mathrm{i} & 0 & -\mathrm{i} \\ 0 & \mathrm{i} & 0 \end{pmatrix} \ ,$$

$$\hat{L}_z = \hbar \begin{pmatrix} 1 & 0 & 0 \\ 0 & 0 & 0 \\ 0 & 0 & -1 \end{pmatrix} \ . \tag{B.8}$$

We then square the matrices to give

$$\begin{aligned}\hat{L}^2 &= \hat{L}_x \cdot \hat{L}_x + \hat{L}_y \cdot \hat{L}_y + \hat{L}_z \cdot \hat{L}_z \ , \\ &= 2\hbar^2 \begin{pmatrix} 1 & 0 & 0 \\ 0 & 1 & 0 \\ 0 & 0 & 1 \end{pmatrix} \ . \end{aligned} \tag{B.9}$$

To calculate $\hat{J}^2$ we once again calculate the individual components $\hat{J}_x$, $\hat{J}_y$ and $\hat{J}_z$. However now they are given by

$$\hat{J}_{x,y,z} = \hat{L}_{x,y,z} \otimes \mathbb{1}_{2S+1} + \mathbb{1}_{2L+1} \otimes \hat{S}_{x,y,z} \ , \tag{B.10}$$

here $\otimes$ is a tensor product (make copies of the second matrix with positions and prefactors given by the first) and $\mathbb{1}_{2S+1}/\mathbb{1}_{2L+1}$ are the identity matrices with dimensions $2S+1$ and $2L+1$, respectively. The components are given by

$$\hat{J}_x = \frac{1}{2}\hbar \begin{pmatrix} 0 & 1 & \sqrt{2} & 0 & 0 & 0 \\ 1 & 0 & 0 & \sqrt{2} & 0 & 0 \\ \sqrt{2} & 0 & 0 & 1 & \sqrt{2} & 0 \\ 0 & \sqrt{2} & 1 & 0 & 0 & \sqrt{2} \\ 0 & 0 & \sqrt{2} & 0 & 0 & 1 \\ 0 & 0 & 0 & \sqrt{2} & 1 & 0 \end{pmatrix} \ , \tag{B.11}$$

$$\hat{J}_y = \frac{1}{2}\hbar \begin{pmatrix} 0 & -\mathrm{i} & -\sqrt{2}\mathrm{i} & 0 & 0 & 0 \\ \mathrm{i} & 0 & 0 & -\sqrt{2}\mathrm{i} & 0 & 0 \\ \sqrt{2}\mathrm{i} & 0 & 0 & -\mathrm{i} & -\sqrt{2}\mathrm{i} & 0 \\ 0 & \sqrt{2}\mathrm{i} & \mathrm{i} & 0 & 0 & -\sqrt{2}\mathrm{i} \\ 0 & 0 & \sqrt{2}\mathrm{i} & 0 & 0 & -\mathrm{i} \\ 0 & 0 & 0 & \sqrt{2}\mathrm{i} & \mathrm{i} & 0 \end{pmatrix} \ , \tag{B.12}$$

$$\hat{J}_z = \frac{1}{2}\hbar \begin{pmatrix} 3 & 0 & 0 & 0 & 0 & 0 \\ 0 & 1 & 0 & 0 & 0 & 0 \\ 0 & 0 & 1 & 0 & 0 & 0 \\ 0 & 0 & 0 & -1 & 0 & 0 \\ 0 & 0 & 0 & 0 & -1 & 0 \\ 0 & 0 & 0 & 0 & 0 & -3 \end{pmatrix} \ . \tag{B.13}$$

Squaring the matrices gives the total electronic angular momentum to be

$$\begin{aligned}\hat{J}^2 &= \hat{J}_x \cdot \hat{J}_x + \hat{J}_y \cdot \hat{J}_y + \hat{J}_z \cdot \hat{J}_z \ , \\ &= \frac{1}{4}\hbar^2 \begin{pmatrix} 15 & 0 & 0 & 0 & 0 & 0 \\ 0 & 7 & 4\sqrt{2} & 0 & 0 & 0 \\ 0 & 4\sqrt{2} & 11 & 0 & 0 & 0 \\ 0 & 0 & 0 & 11 & 4\sqrt{2} & 0 \\ 0 & 0 & 0 & 4\sqrt{2} & 7 & 0 \\ 0 & 0 & 0 & 0 & 0 & 15 \end{pmatrix} . \end{aligned} \tag{B.14}$$

Now we have the $\hat{S}^2$, $\hat{L}^2$ and $\hat{J}^2$ matrices we can calculate the spin-orbit interaction matrix $\hat{L} \cdot \hat{S}$. First however, we need to make sure all the matrices are of the same size such that subtraction is possible. Applying $\hat{S}^2 = \hat{S}^2 \otimes \mathbb{1}_{2L+1}$ where $\mathbb{1}_{2L+1}$ is an identity matrix of dimensions $2L+1$. The total spin angular momentum can now be given by a 6×6 matrix populated with 1 along the diagonal, with eigenvalue $\frac{3}{4}\hbar^2$. Likewise we apply $\hat{L}^2 = \hat{L}^2 \otimes \mathbb{1}_{2S+1}$ where $\mathbb{1}_{2S+1}$ is an identity matrix of dimensions $2S+1$. The total orbital angular momentum can now be given by a 6×6 matrix populated with 1 along the diagonal, with eigenvalue $2\hbar^2$. The spin-orbit interaction matrix is

$$\begin{aligned}\hat{L} \cdot \hat{S} &= \frac{1}{2}\left(\hat{J}^2 - \hat{L}^2 - \hat{S}^2\right) \ , \\ &= \frac{1}{2}\hbar^2 \begin{pmatrix} 1 & 0 & 0 & 0 & 0 & 0 \\ 0 & -1 & \sqrt{8} & 0 & 0 & 0 \\ 0 & \sqrt{8} & 0 & 0 & 0 & 0 \\ 0 & 0 & 0 & 0 & \sqrt{8} & 0 \\ 0 & 0 & 0 & \sqrt{8} & -1 & 0 \\ 0 & 0 & 0 & 0 & 0 & 1 \end{pmatrix} . \end{aligned} \tag{B.15}$$

Analytic diagonlisation of this $\hat{L} \cdot \hat{S}$ matrix gives two eigenvalues with -1 and four eigenvalues with $\frac{1}{2}$. These two different values are the excited fine terms $J = \frac{1}{2}$ and $J = \frac{3}{2}$ with 2 and 4 m_J values, respectively. Note as a consequence of this fine structure splitting in section 2.4.2 we introduce an additional Hamiltonian of value $2\gamma_{\text{fs}}$ and $-\gamma_{\text{fs}}$ that allows for the centre of mass frequency of either the D_1 or D_2 lines to correspond to zero detuning, respectively. Next we calculate the $\hat{I} \cdot \hat{J}$ matrix for the $5^2S_{1/2}$ term and

unlike the spin-orbit interaction which is zero we show that for ^{87}Rb with $I = \frac{3}{2}$ hyperfine structure is present.

B.2 $\hat{I} \cdot \hat{J}$ matrix

To construct the hyperfine interaction matrix $\hat{I} \cdot \hat{J}$ in the uncoupled basis, we introduce the total angular momentum quantum number, $\hat{F} = \hat{I} + \hat{J}$, where $\hat{I}$, is the nuclear spin and $\hat{J}$, is the total electronic angular momentum. Starting with this expression the hyperfine matrix can be written as

$$\begin{aligned} \hat{F} &= \hat{I} + \hat{J} \ , \\ \hat{F}^2 &= (\hat{I} + \hat{J})^2 \ , \\ \hat{F}^2 &= \hat{I}^2 + \hat{J}^2 + 2\hat{I} \cdot \hat{J} \ , \\ \hat{I} \cdot \hat{J} &= \frac{1}{2}\left(\hat{F}^2 - \hat{I}^2 - \hat{J}^2\right) \ , \end{aligned} \tag{B.16}$$

where we use again the property $\hat{I} \cdot \hat{J} = \hat{J} \cdot \hat{I}$. In section B.1 we can write the total electronic angular momentum matrix, $\hat{J}^2$, for the $5^2S_{1/2}$ term where $L = 0$ as equation B.7. Here we introduce the ^{87}Rb isotope with nuclear spin $I = \frac{3}{2}$. In order for subtraction to be possible we again change the size of the matrix, $\hat{J}^2$. To calculate the right dimensions for this matrix we do the following $\hat{J}^2 = \hat{J}^2 \otimes \mathbb{1}_{2I+1}$, where $\mathbb{1}_{2I+1}$ is an identity matrix of dimensions $2I+1$. The total electronic angular momentum for the $5^2S_{1/2}$ term in ^{87}Rb is given by a 8×8 matrix with 1 populated along the diagonal, with eigenvalue $\frac{3}{4}\hbar^2$. Next we calculate the total nuclear spin matrix, $\hat{I}^2$. For ^{87}Rb the three components of the nuclear spin are calculated using equation B.1 together

with equations B.2, B.3 and B.4.

$$\hat{I}_x = \frac{1}{2}\hbar \begin{pmatrix} 0 & \sqrt{3} & 0 & 0 \\ \sqrt{3} & 0 & 2 & 0 \\ 0 & 2 & 0 & \sqrt{3} \\ 0 & 0 & \sqrt{3} & 0 \end{pmatrix} , \tag{B.17}$$

$$\hat{I}_y = \frac{1}{2}\hbar \begin{pmatrix} 0 & -\sqrt{3}\mathrm{i} & 0 & 0 \\ \sqrt{3}\mathrm{i} & 0 & -2\mathrm{i} & 0 \\ 0 & 2\mathrm{i} & 0 & -\sqrt{3}\mathrm{i} \\ 0 & 0 & \sqrt{3}\mathrm{i} & 0 \end{pmatrix} , \tag{B.18}$$

$$\hat{I}_z = \frac{1}{2}\hbar \begin{pmatrix} 3 & 0 & 0 & 0 \\ 0 & 1 & 0 & 0 \\ 0 & 0 & -1 & 0 \\ 0 & 0 & 0 & -3 \end{pmatrix} . \tag{B.19}$$

We then square the matrices and the total nuclear spin is given by

$$\begin{aligned} \hat{I}^2 &= \hat{I}_x \cdot \hat{I}_x + \hat{I}_y \cdot \hat{I}_y + \hat{I}_z \cdot \hat{I}_z , \\ &= \frac{15}{4}\hbar^2 \begin{pmatrix} 1 & 0 & 0 & 0 \\ 0 & 1 & 0 & 0 \\ 0 & 0 & 1 & 0 \\ 0 & 0 & 0 & 1 \end{pmatrix} . \end{aligned} \tag{B.20}$$

As before we require that the $\hat{I}^2$ matrix be of a similar size such that subtraction is possible. Applying $\hat{I}^2 = \hat{I}^2 \otimes \mathbb{1}_{2J+1}$ where $\mathbb{1}_{2J+1}$ is an identity matrix of dimensions $2J+1$. The total nuclear spin for the $5^2\mathrm{S}_{1/2}$ term in ^{87}Rb is given by a 8×8 matrix with 1 populated along the diagonal, with eigenvalue $\frac{15}{4}\hbar^2$. To calculate $\hat{F}^2$ we first need to the calculate the individual components $\hat{F}_x$, $\hat{F}_y$ and $\hat{F}_z$ given by $\hat{F}_{x,y,z} = \hat{J}_{x,y,z} \otimes \mathbb{1}_{2I+1} + \mathbb{1}_{2J+1} \otimes \hat{I}_{x,y,z}$.

The components are

$$\hat{F}_x = \frac{1}{2}\hbar \begin{pmatrix} 0 & \sqrt{3} & 0 & 0 & 1 & 0 & 0 & 0 \\ \sqrt{3} & 0 & 2 & 0 & 0 & 1 & 0 & 0 \\ 0 & 2 & 0 & \sqrt{3} & 0 & 0 & 1 & 0 \\ 0 & 0 & \sqrt{3} & 0 & 0 & 0 & 0 & 1 \\ 1 & 0 & 0 & 0 & 0 & \sqrt{3} & 0 & 0 \\ 0 & 1 & 0 & 0 & \sqrt{3} & 0 & 2 & 0 \\ 0 & 0 & 1 & 0 & 0 & 2 & 0 & \sqrt{3} \\ 0 & 0 & 0 & 1 & 0 & 0 & \sqrt{3} & 0 \end{pmatrix}, \tag{B.21}$$

$$\hat{F}_y = \frac{1}{2}\hbar \begin{pmatrix} 0 & -\sqrt{3}\mathrm{i} & 0 & 0 & -\mathrm{i} & 0 & 0 & 0 \\ \sqrt{3}\mathrm{i} & 0 & -2\mathrm{i} & 0 & 0 & -\mathrm{i} & 0 & 0 \\ 0 & 2\mathrm{i} & 0 & -\sqrt{3}\mathrm{i} & 0 & 0 & -\mathrm{i} & 0 \\ 0 & 0 & \sqrt{3}\mathrm{i} & 0 & 0 & 0 & 0 & -\mathrm{i} \\ \mathrm{i} & 0 & 0 & 0 & 0 & -\sqrt{3}\mathrm{i} & 0 & 0 \\ 0 & \mathrm{i} & 0 & 0 & \sqrt{3}\mathrm{i} & 0 & -2\mathrm{i} & 0 \\ 0 & 0 & \mathrm{i} & 0 & 0 & 2\mathrm{i} & 0 & -\sqrt{3}\mathrm{i} \\ 0 & 0 & 0 & \mathrm{i} & 0 & 0 & \sqrt{3}\mathrm{i} & 0 \end{pmatrix}, \tag{B.22}$$

$$\hat{F}_z = \hbar \begin{pmatrix} 2 & 0 & 0 & 0 & 0 & 0 & 0 & 0 \\ 0 & 1 & 0 & 0 & 0 & 0 & 0 & 0 \\ 0 & 0 & 0 & 0 & 0 & 0 & 0 & 0 \\ 0 & 0 & 0 & -1 & 0 & 0 & 0 & 0 \\ 0 & 0 & 0 & 0 & 1 & 0 & 0 & 0 \\ 0 & 0 & 0 & 0 & 0 & 0 & 0 & 0 \\ 0 & 0 & 0 & 0 & 0 & 0 & -1 & 0 \\ 0 & 0 & 0 & 0 & 0 & 0 & 0 & -2 \end{pmatrix}. \tag{B.23}$$

We then square the matrices to show

$$\begin{aligned}\hat{F}^2 &= \hat{F}_x \cdot \hat{F}_x + \hat{F}_y \cdot \hat{F}_y + \hat{F}_z \cdot \hat{F}_z \ , \\ &= \hbar^2 \begin{pmatrix} 6 & 0 & 0 & 0 & 0 & 0 & 0 & 0 \\ 0 & 5 & 0 & 0 & \sqrt{3} & 0 & 0 & 0 \\ 0 & 0 & 4 & 0 & 0 & 2 & 0 & 0 \\ 0 & 0 & 0 & 3 & 0 & 0 & \sqrt{3} & 0 \\ 0 & \sqrt{3} & 0 & 0 & 3 & 0 & 0 & 0 \\ 0 & 0 & 2 & 0 & 0 & 4 & 0 & 0 \\ 0 & 0 & 0 & \sqrt{3} & 0 & 0 & 5 & 0 \\ 0 & 0 & 0 & 0 & 0 & 0 & 0 & 6 \end{pmatrix} . \end{aligned} \tag{B.24}$$

Finally we need to calculate the hyperfine interaction matrix $\hat{I} \cdot \hat{J}$. Substituting for the 8×8 matrices $\hat{J}^2$, $\hat{I}^2$ and $\hat{F}^2$, gives the $5^2S_{1/2}$ matrix for ^{87}Rb as follows

$$\begin{aligned}\hat{I} \cdot \hat{J} &= \frac{1}{2}\left(\hat{F}^2 - \hat{I}^2 - \hat{J}^2\right) \ , \\ &= \hbar^2 \begin{pmatrix} \frac{3}{4} & 0 & 0 & 0 & 0 & 0 & 0 & 0 \\ 0 & \frac{1}{4} & 0 & 0 & \frac{\sqrt{3}}{2} & 0 & 0 & 0 \\ 0 & 0 & -\frac{1}{4} & 0 & 0 & 1 & 0 & 0 \\ 0 & 0 & 0 & -\frac{3}{4} & 0 & 0 & \frac{\sqrt{3}}{2} & 0 \\ 0 & \frac{\sqrt{3}}{2} & 0 & 0 & -\frac{3}{4} & 0 & 0 & 0 \\ 0 & 0 & 1 & 0 & 0 & -\frac{1}{4} & 0 & 0 \\ 0 & 0 & 0 & \frac{\sqrt{3}}{2} & 0 & 0 & \frac{1}{4} & 0 \\ 0 & 0 & 0 & 0 & 0 & 0 & 0 & \frac{3}{4} \end{pmatrix} . \end{aligned} \tag{B.25}$$

In chapter 2 we analytically diagonalise this matrix to give eigenvalues and eigenfunctions in terms of the uncoupled basis. These matrices are arranged in ascending order corresponding to the calculated eigenvalues. Next we show calculations for the relative line-strengths of the π transitions.

B.3 π transitions

In section 2.4.2 we showed a schematic of the eigenvalues and corresponding eigenvectors calculated from the diagonalisation of the populated 5P matrix.

Column 1 was arranged such that the first 8 and final 16 eigenvalues corresponded to the $5^2\mathrm{P}_{1/2}$ and $5^2\mathrm{P}_{3/2}$ terms, respectively. Columns $2-25$ are the eigenvectors for each hyperfine state. In the main section of the thesis we considered columns $18-25$ for the operator C_R acting on the hyperfine excited states $|F', m_{F'}\rangle$ here we chose to show the operator C_0 listed in columns $10-17$. This sub-matrix for the $5^2\mathrm{P}_{1/2}$ term is as follows

$$A_{\mathrm{hfs}}\left(\begin{array}{c:cccccccc}
-\frac{5}{4} & 0 & \sqrt{\frac{1}{12}} & 0 & 0 & \frac{1}{2} & 0 & 0 & 0 \\
-\frac{5}{4} & 0 & 0 & \sqrt{\frac{1}{6}} & 0 & 0 & \sqrt{\frac{1}{6}} & 0 & 0 \\
-\frac{5}{4} & 0 & 0 & 0 & \frac{1}{2} & 0 & 0 & \sqrt{\frac{1}{12}} & 0 \\
\hdashline
\frac{3}{4} & 0 & 0 & 0 & 0 & 0 & 0 & 0 & -\sqrt{\frac{1}{3}} \\
\frac{3}{4} & 0 & 0 & 0 & -\sqrt{\frac{1}{12}} & 0 & 0 & \frac{1}{2} & 0 \\
\frac{3}{4} & 0 & 0 & -\sqrt{\frac{1}{6}} & 0 & 0 & \sqrt{\frac{1}{6}} & 0 & 0 \\
\frac{3}{4} & 0 & \frac{1}{2} & 0 & 0 & -\sqrt{\frac{1}{12}} & 0 & 0 & 0 \\
\frac{3}{4} & -\sqrt{\frac{1}{3}} & 0 & 0 & 0 & 0 & 0 & 0 & 0
\end{array}\right), \tag{B.26}$$

For the operator C_0 acting on the $|F', m_{F'}\rangle$ states in the coupled basis, the uncoupled $|m_{L'}, m_{S'}, m_{I'}\rangle$ basis and Clebsch-Gordan coefficients can be written as

$$C_0\,|1,+1\rangle = \sqrt{\frac{1}{12}}\left|0,+\frac{1}{2},+\frac{1}{2}\right\rangle + \frac{1}{2}\left|0,-\frac{1}{2},+\frac{3}{2}\right\rangle\,, \tag{B.27}$$

$$C_0\,|1,+0\rangle = \sqrt{\frac{1}{6}}\left|0,+\frac{1}{2},-\frac{1}{2}\right\rangle + \sqrt{\frac{1}{6}}\left|0,-\frac{1}{2},+\frac{1}{2}\right\rangle\,, \tag{B.28}$$

$$C_0\,|1,-1\rangle = \frac{1}{2}\left|0,+\frac{1}{2},-\frac{3}{2}\right\rangle + \sqrt{\frac{1}{12}}\left|0,-\frac{1}{2},-\frac{1}{2}\right\rangle\,, \tag{B.29}$$

$$C_0\,|2,-2\rangle = -\sqrt{\frac{1}{3}}\left|0,-\frac{1}{2},-\frac{3}{2}\right\rangle\,, \tag{B.30}$$

$$C_0 \left|2,-1\right\rangle = -\sqrt{\frac{1}{12}}\left|0,+\frac{1}{2},-\frac{3}{2}\right\rangle + \frac{1}{2}\left|0,-\frac{1}{2},-\frac{1}{2}\right\rangle \ , \tag{B.31}$$

$$C_0 \left|2,+0\right\rangle = -\sqrt{\frac{1}{6}}\left|0,+\frac{1}{2},-\frac{1}{2}\right\rangle + \sqrt{\frac{1}{6}}\left|0,-\frac{1}{2},+\frac{1}{2}\right\rangle \ , \tag{B.32}$$

$$C_0 \left|2,+1\right\rangle = \frac{1}{2}\left|0,+\frac{1}{2},+\frac{1}{2}\right\rangle - \sqrt{\frac{1}{12}}\left|0,-\frac{1}{2},+\frac{3}{2}\right\rangle \ , \tag{B.33}$$

$$C_0 \left|2,+2\right\rangle = -\sqrt{\frac{1}{3}}\left|0,+\frac{1}{2},+\frac{3}{2}\right\rangle \ . \tag{B.34}$$

Note that for the stretched states $\left|0,-\frac{1}{2},-\frac{3}{2}\right\rangle$ and $\left|0,+\frac{1}{2},+\frac{3}{2}\right\rangle$ their Clebsch-Gordan coefficients are $-\sqrt{\frac{1}{3}}$, in section 4.3.3 we discussed the magnitude of these values in detail. In summary, the full calculation is carried out for both $5^2\mathrm{P}_{1/2}$ and $5^2\mathrm{P}_{3/2}$ terms, where the sum of their relative line-strength factors is always 2. As the D_2 line is twice as strong as the D_1 line, the Clebsch-Gordan coefficients for the D_2 line stretched states are $-\sqrt{\frac{2}{3}}$. For π transitions on the $F = 1 \rightarrow F' = 1$ line we have $m_F = -1 \rightarrow m_{F'} = -1$, $m_F = +0 \rightarrow m_{F'} = +0$ and $m_F = +1 \rightarrow m_{F'} = +1$. The calculation for total transition strength is similar to the one carried out in section 2.5.1

$$C_F^2 = \frac{1}{3}\left[\langle 1,-1|C_0|1,-1\rangle^2 + \langle 1,+0|C_0|1,+0\rangle^2 + \langle 1,+1|C_0|1,+1\rangle^2\right] \ . \tag{B.35}$$

Here $\langle 1,-1|$, $\langle 1,+0|$ and $\langle 1,+1|$ can be obtained from section 2.4.2. Substituting we have

$$\begin{aligned} C_F^2 = \quad & \frac{1}{3}\left[\left(-\sqrt{\frac{3}{4}}\left\langle 0,+\frac{1}{2},-\frac{3}{2}\right| + \frac{1}{2}\left\langle 0,-\frac{1}{2},-\frac{1}{2}\right|\right)\right. \\ & \left. C_0\left(\frac{1}{2}\left|0,+\frac{1}{2},-\frac{3}{2}\right\rangle + \sqrt{\frac{1}{12}}\left|0,-\frac{1}{2},-\frac{1}{2}\right\rangle\right)\right]^2 \\ & + \frac{1}{3}\left[\left(\sqrt{\frac{1}{2}}\left\langle 0,+\frac{1}{2},-\frac{1}{2}\right| - \sqrt{\frac{1}{2}}\left\langle 0,-\frac{1}{2},+\frac{1}{2}\right|\right)\right. \\ & \left. C_0\left(\sqrt{\frac{1}{6}}\left|0,+\frac{1}{2},-\frac{1}{2}\right\rangle + \sqrt{\frac{1}{6}}\left|0,-\frac{1}{2},+\frac{1}{2}\right\rangle\right)\right]^2 \\ & + \frac{1}{3}\left[\left(\frac{1}{2}\left\langle 0,+\frac{1}{2},+\frac{1}{2}\right| - \sqrt{\frac{3}{4}}\left\langle 0,-\frac{1}{2},+\frac{3}{2}\right|\right)\right. \\ & \left. C_0\left(\sqrt{\frac{1}{12}}\left|0,+\frac{1}{2},+\frac{1}{2}\right\rangle + \frac{1}{2}\left|0,-\frac{1}{2},+\frac{3}{2}\right\rangle\right)\right]^2 \ , \end{aligned} \tag{B.36}$$

applying the electric-dipole selection rules which were discussed in section 2.5.1 we have

$$\begin{aligned} C_F^2 = \quad & \frac{1}{3}\left[\left(-\frac{1}{2}\sqrt{\frac{3}{4}}\left\langle 0,+\frac{1}{2},-\frac{3}{2}\right| C_0 \left|0,+\frac{1}{2},-\frac{3}{2}\right\rangle\right)\right. \\ & \left.+\left(\frac{1}{2}\sqrt{\frac{1}{12}}\left\langle 0,-\frac{1}{2},-\frac{1}{2}\right| C_0 \left|0,-\frac{1}{2},-\frac{1}{2}\right\rangle\right)\right]^2 \\ & +\frac{1}{3}\left[\left(\sqrt{\frac{1}{2}}\sqrt{\frac{1}{6}}\left\langle 0,+\frac{1}{2},-\frac{1}{2}\right| C_0 \left|0,+\frac{1}{2},-\frac{1}{2}\right\rangle\right)\right. \\ & \left.+\left(-\sqrt{\frac{1}{2}}\sqrt{\frac{1}{6}}\left\langle 0,-\frac{1}{2},+\frac{1}{2}\right| C_0 \left|0,-\frac{1}{2},+\frac{1}{2}\right\rangle\right)\right]^2 \\ & +\frac{1}{3}\left[\left(\frac{1}{2}\sqrt{\frac{1}{12}}\left\langle 0,+\frac{1}{2},+\frac{1}{2}\right| C_0 \left|0,+\frac{1}{2},+\frac{1}{2}\right\rangle\right)\right. \\ & \left.+\left(-\frac{1}{2}\sqrt{\frac{3}{4}}\left\langle 0,-\frac{1}{2},+\frac{3}{2}\right| C_0 \left|0,-\frac{1}{2},+\frac{3}{2}\right\rangle\right)\right]^2 , \end{aligned} \tag{B.37}$$

substituting for equation 2.45, the total transition strength is

$$\begin{aligned} C_F^2 &= \frac{1}{3}\left[\left(-\sqrt{\frac{9}{48}}+\sqrt{\frac{1}{48}}\right)^2+\left(\sqrt{\frac{1}{12}}-\sqrt{\frac{1}{12}}\right)^2+\left(\sqrt{\frac{1}{48}}-\sqrt{\frac{9}{48}}\right)^2\right] , \\ &= \frac{1}{3}\left[\frac{1}{12}+0+\frac{1}{12}\right] , \\ &= \frac{1}{18} . \end{aligned} \tag{B.38}$$

The eletric-dipole selection rules state that for $\Delta F = 0$ i.e. $F = 1 \rightarrow F' = 1$, $m_F = 0 \rightarrow m_{F'} = 0$, the relative line-strength factor must always be zero. From equation B.38 we see that the second term in the expression is zero. In figure 2.5 we show relative line-strengths, $c^2_{m_F}$, for each π transition on the $F = 1 \rightarrow F' = 1$ line in ^{87}Rb.

Appendix C

Calibration for a single transmission plot

In appendix C we outline the method adopted to calibrate each transmission plot to ensure excellent agreement between the theoretical model and experimental measurements. For each single experiment we record three data sets: a Fabry-Perot etalon signal; a reference signal resolving the individual hyperfine peaks; and a transmission signal which we wish to compare with theory. In this appendix we outline how each set of data is used in the calibration method and state that all the detuning axes in the thesis were calculated using this technique.

C.1 Scaling the frequency axis

We start by scaling the frequency axis using the etalon and reference signals. The frequency scan is first linearised with a Fabry-Perot etalon and then calibrated by use of hyperfine/saturated absorption spectroscopy in a natural-abundant room temperature cell.

C.1.1 Fabry-Perot etalon

A Fabry-Perot etalon usually consists of two plane mirrors which are placed parallel to one another, separated by a distance d. Due to unwanted diffrac-

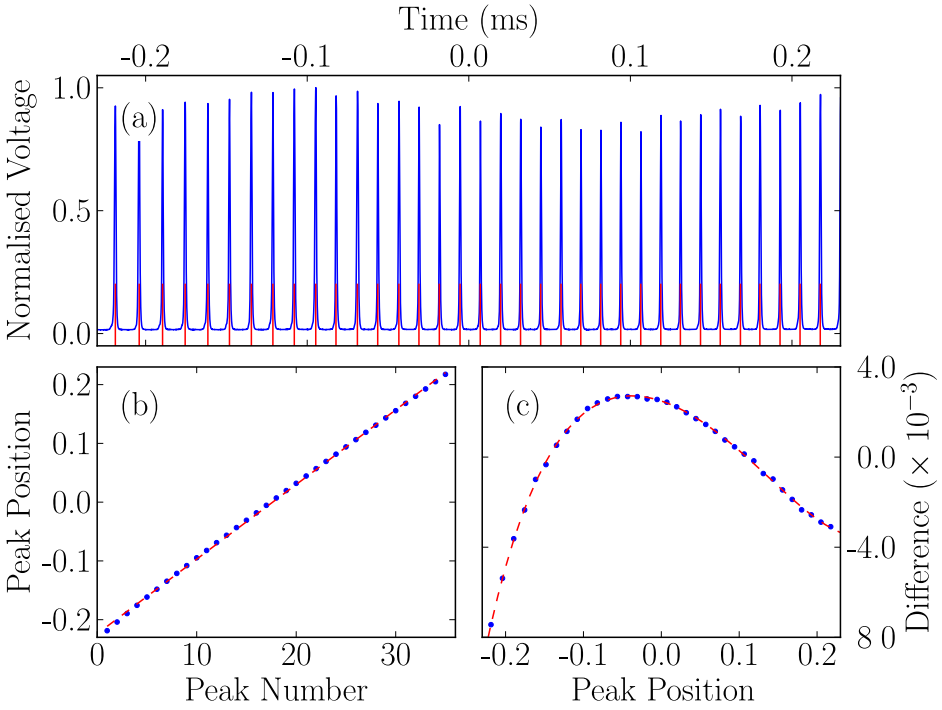

Figure C.1: Fabry-Perot etalon signal. (a) shows a typical signal as a function of the time (in ms) of a single scan. (b) shows the peak positions found in (a) measured as a function of peak number. Fitting a linear function to the data, highlights the non-linear nature of the separations. (c) shows the difference from a linear fit as a function of the peak position. A high order polynomial is fitted to these differences and corrects for the non-linearity of the scan.

tion effects which are characteristic of plane mirrors [167] we use spherical mirrors for our Fabry-Perot etalon. Figure C.1(a) shows the etalon signal for a typical experiment. Normalised voltage is plotted versus the time (in ms) of a single scan. A subroutine was created that selects all the peaks present in the trace and lists them with their exact position. In figure C.1(b) we plot the exact position of each etalon peak as a function of the number of peaks. The difference in frequency (time) between two normalised peaks, called the free spectral range (FSR) of the etalon is usually given by $FSR = c/2d$. For an interferometer with spherical mirrors the FSR is $c/4d$ rather than $c/2d$ [167]. For a cavity of length 15 cm the typical FSR for a etalon with spherical mirrors is 500 MHz. The measured peaks should be equally spaced if the response to the voltage applied across the piezo-electric transducer in the external cavity of a laser was linear. From the solid (red) line we can see

that the scan has a small non-linear contribution. It is this non-linearity that we need to remove from the scan. In figure C.1(c) we plot the difference from a linear fit as a function of the exact peak position. By fitting an n^{th} order polynomial, typically of size five, to the difference signal we get a function which we then remove from the initial etalon signal in figure C.1(a). The time axis in the etalon signal has now been linearised.

Next we take the linearised time axis and using hyperfine/saturated absorption spectroscopy we get a corresponding frequency axis.

C.1.2 Hyperfine/saturated absorption spectroscopy

Absorption spectra of hyperfine transitions in a thermal Rb vapour, are limited to the resolution of the Doppler width. Hyperfine/saturated absorption spectroscopy enables the hyperfine splittings of atomic line spectra to be measured. Spectra that resolve hyperfine structure are ideal frequency markers for locking a laser to a specific frequency [113]. A modification is seen in the absorption spectrum, when the probe and pump beams interact with atoms centred around zero velocity. When the laser beam is tuned to within a natural line-width of an atomic resonance, the probe beam detects a shortage of atoms. This is because some of the atoms have been excited by the pump beam and either reside in the excited state (saturated absorption spectroscopy) or fall into the other ground state (Hyperfine absorption spectroscopy). Hence the technique of hyperfine/saturated spectroscopy gives sub-Doppler resolution: a narrow feature centred at ω_0, within a Doppler broadened absorption spectrum.

For Rb the electric-dipole-allowed transition rules, predicts that there should be eight and twelve sub-Doppler features visible for the D_1 and D_2 lines, respectively. However, twelve and twenty-four peaks are visible in total. The majority of these features correspond to the resonant frequencies $F \rightarrow F' = F, F \pm 1$, where both probe and pump beams excite atoms with zero velocity. In addition to these resonant lines, there are four and twelve crossover features that occur at frequencies halfway between each pair of transitions [168]. Atoms in these velocity classes may be red shifted onto resonance with the probe, or blue shifted onto resonance with the pump, or

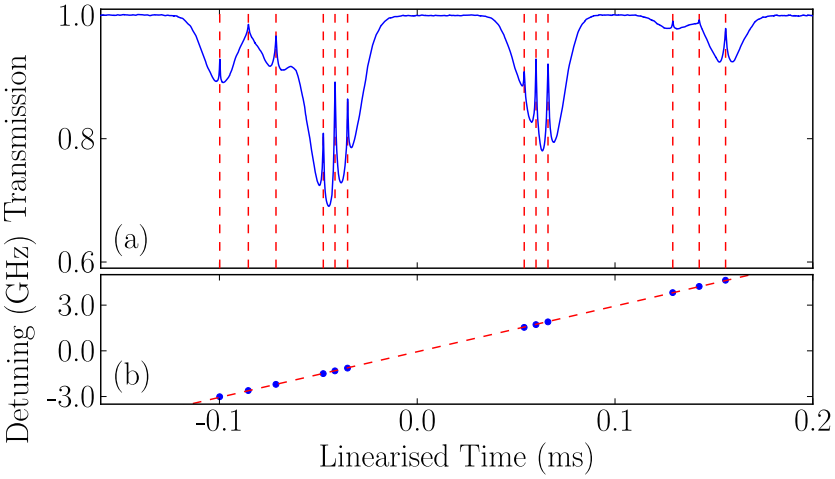

Figure C.2: (a) Typical sub-Doppler spectrum for the D_1 line through a Rb vapour of length 75 mm. All twelve features are clearly visible, with eight corresponding to the transition frequencies and the other four given by crossover resonances exactly halfway between each detuning. (b) Expected detuning values as a function of the peak position. A linear fit allows one to convert the linearised time axis into a frequency axis.

vice-versa. The crossover transitions are often more intense than the normal resonant transitions. The transition frequencies for the D_1 and D_2 lines in ^{85}Rb and ^{87}Rb are shown in table 2.3.

Here we take the example of the D_1 line in Rb, as all twelve features can be easily resolved. In the excited state manifold of the D_2 line the hyperfine intervals are smaller, therefore making them harder to resolve. Figure C.2(a) shows a typical sub-Doppler spectrum measured for the D_1 line through a Rb vapour of length 75 mm. To convert the linearised time axis into a frequency axis we use the known detunings values for these twelve peaks, which correspond to a resonant transition or a crossover. In figure C.2(b) we fit the detuning values as a function of their peak positions. A linear fit can then be used to convert the linearised time axis into a frequency axis. Note the zero of detuning is taken to be the centre-of-mass frequency of the transition.

Now we have converted the linearised time axis into a frequency axis the next step is to normalise the data.

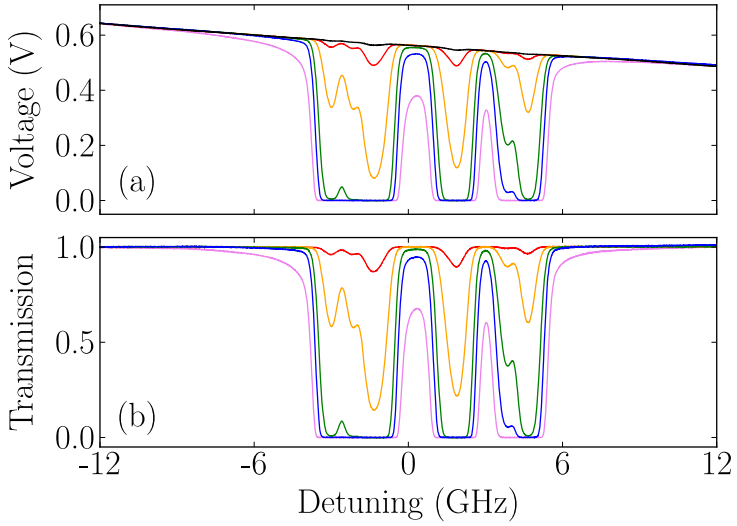

Figure C.3: Transmission signals for the D_1 line through a natural abundant Rb vapour of length 2 mm. (a) shows the raw voltage data as a function of detuning. The solid (black) line is the signal at room temperature where there are no absorption dips. The solid (coloured) lines are signals at various temperatures. Note the slope to all of these signals is very similar. (b) shows the normalised transmission signals from the simple process of dividing by the room temperature signal in plot (a). These signals are now ready to fit to theory.

C.2 Renormalising the data

To compare the transmission scan with a theoretical curve, the voltage data needs to be normalised between 0 and 1. As the power of the laser changes with frequency the slope in the data was a problem. Our first attempt at removing this background was to fit a polynomial curve and then subtract it from the raw data. However, when it came to fitting the theory code to this modified data, we encountered large residuals. Consequently this polynomial normalisation technique did not correctly adjust for the varying background signal, so another method was required.

A simpler but ultimately more effective way of normalising the data was to divide the transmission scan by a room temperature signal that had no absorption dips. As long as the power of the laser remained constant over the duration of the investigation this method was far more effective for normalising the data. The only major restriction was that we could not record any specific temperature, as the background slope would oscillate as it was

increased. We attribute these oscillations due to the fact that the cell would set-up an etalon similar to the one discussed in section C.1.1. However rather than small sharp features, what we measure is a slope with a FSR of approximately 75 GHz for a cell of length 2 mm. In the main experiments we would have to adjust the temperature until the slope of the room temperature reference and required transmission scan were as similar as possible. The most efficient way of doing this was to set the cell heater (see section 3.4.2) to a high temperature and then watch the transmission scan as the absorption increased. Every time the background slopes looked similar we would record each data set for calibration. This method would allow for five or six different readings to be taken between room temperature and 200°C.

Figure C.3(a) shows the raw voltage data for the D_1 line through a natural abundant Rb vapour of length 2 mm. At room temperature the solid (black) line has no absorption dips however highlights the varying power in the scan. It is this curve we then use to normalise data sets at higher temperatures with similar slopes. Figure C.3(b) shows the normalised transmission data between 0 and 1, which can now be used to fit to theory. Note sometimes when fitting the data, spikes appear in the residuals i.e. figure 5.2. This does not necessarily indicate disagreement between theory and experiment but rather highlights the non-linearity of the laser scanning or poor renormalisation. Next we take our normalised transmission data and consider the parameters and errors extracted from a fit to the developed theoretical model.

Appendix D

Extracting optimised parameters and their uncertainties

In appendix D we show how the optimised parameters and their uncertainties are extracted from a fit to theory. We start by considering the uncertainties associated with the voltage measured on the oscilloscope. We then discuss how the Marquardt-Levenberg algorithm is used to perform a least squares fit. Before finally defining how the errors for each parameter are obtained.

D.1 Errors from the oscilloscope

To use a least squares or chi-squared fitting algorithm we require the inclusion of uncertainties on the y-values. The uncertainties associated with the voltage values on the oscilloscope are very small. Here we introduce a method by which we average over every N data points and then take a standard error, α, from the standard deviation, σ, of these N data points, such that:

$$\alpha = \frac{\sigma}{\sqrt{N}} \, . \tag{D.1}$$

This has the advantage of significantly increasing the speed of the fitting, whilst providing an error. The main limiting factor time-wise is the speed of

iterations over all the data points, of which there can be as many as 50,000 for example. We found that the best reduced chi-squared values were obtained with around 2500 data points and binning factors of $10 - 20$.

D.2 Python fitting

In order to fit the normalised data to a theoretical curve we use the python module **scipy.optimize** and in particular a function called **leastsq()**. This function uses the Marquardt-Levenberg algorithm to perform a least squares fit. A detailed discussion of the Marquardt-Levenberg method can be found on page 90 in [123]. In summary, the optimised values are achieved via the steepest descent method with knowledge of the gradient of the error surface with respect to the free parameters. The **leastsq()** function requires a list of residuals between the measured data and theoretical curve. The theoretical curve is created for an initial set of input parameters. Note the speed of the algorithm is fastest when the initial input parameters are closest to the optimised parameters. Here we also chose to input the errors calculated from section D.1, these can be used to weight the residuals so effectively the least squared fit is now a χ^2 fit. The **leastsq()** function then returns the optimised parameters together with their uncertainties in the form of a covariance or error matrix.

D.3 Covariance matrix

The elements of the covariance matrix quantify the statistical errors on the optimised paramaters. The uncertainty in the N^{th} parameter is given by the square root of the N^{th} diagonal element of the error matrix. The off diagonal elements define the correlations. Here we chose to ignore the correlation elements and concentrate on the diagonal uncertainty elements. The uncertainty of a parameter is defined via the $\chi^2_{\text{min}} + 1$ contour along the parameter axis. That means if a parameter is set to its optimised value plus one error bar, a best fit allowing the other parameters to float freely would result in a χ^2 equal to $\chi^2_{\text{min}} + 1$. Hughes and Hase [123] provide a more in depth

discussion of computational curve fitting and error matrices. The errors produced by the **leastsq()** function are correct, however the extracted error is an underestimate of the true uncertainty. Therefore together with the errors calculated here from one scan. Errors in parameters are extracted from a statistical analysis of these repeat measurements.

Appendix E

Breit-Rabi diagrams

In appendix E we plot the Breit-Rabi diagrams for the $5^2S_{1/2}$, $5^2P_{1/2}$ and $5^2P_{3/2}$ terms in ^{85}Rb and ^{87}Rb.

E.1 Breit-Rabi diagrams for ^{85}Rb

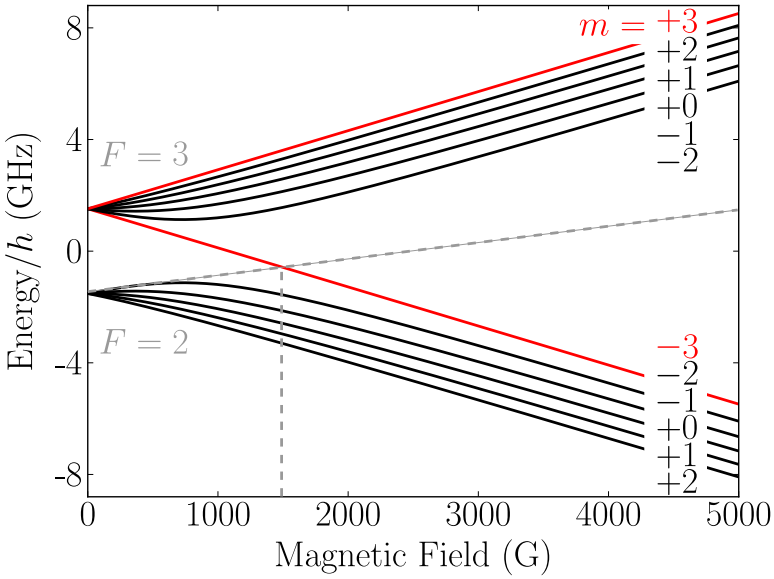

Figure E.1: Breit-Rabi diagram for the $5^2S_{1/2}$ term of ^{85}Rb.

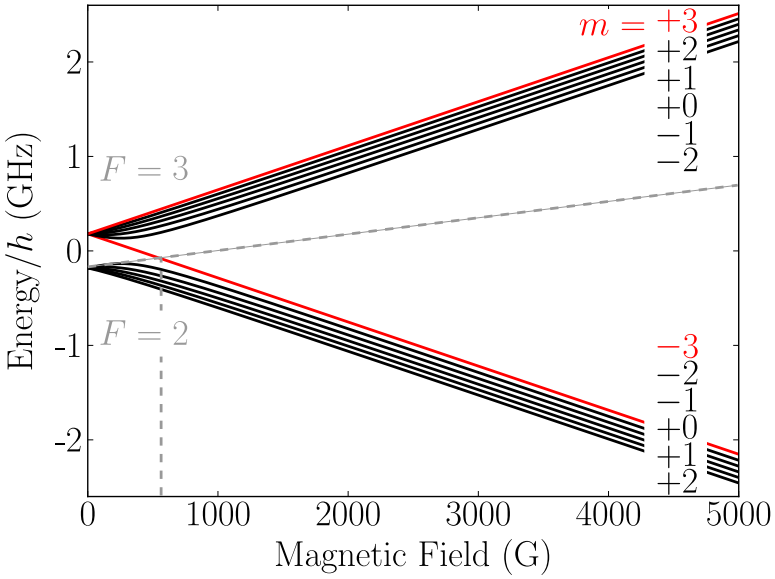

Figure E.2: Breit-Rabi diagram for the $5^2P_{1/2}$ term of ^{85}Rb.

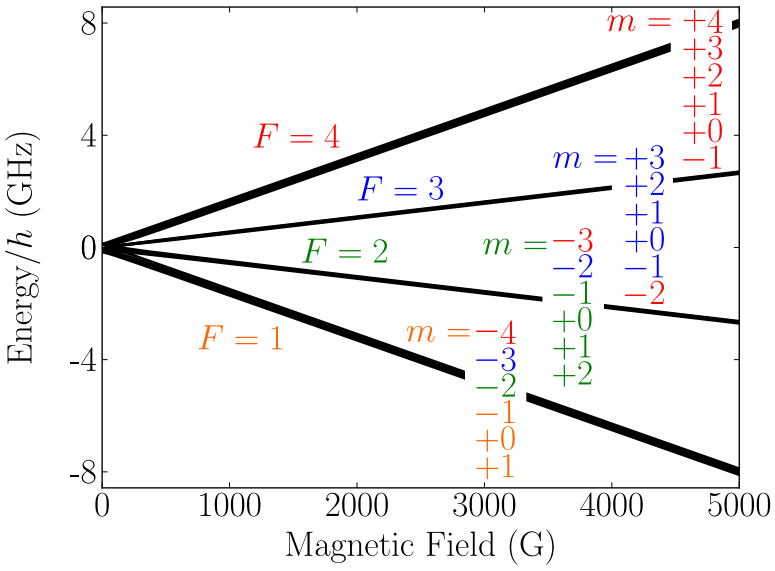

Figure E.3: Breit-Rabi diagram for the $5^2P_{3/2}$ term of ^{85}Rb.

E.2 Breit-Rabi diagrams for ^{87}Rb

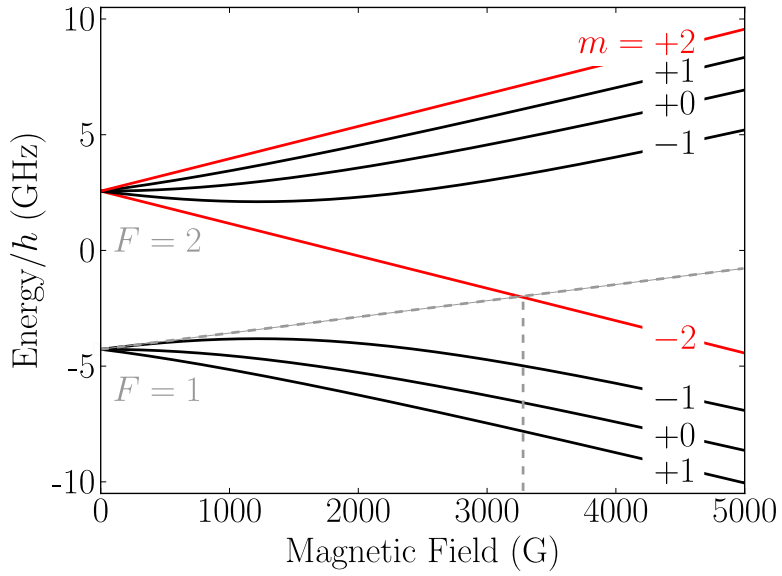

Figure E.4: Breit-Rabi diagram for the $5^2S_{1/2}$ term of ^{87}Rb.

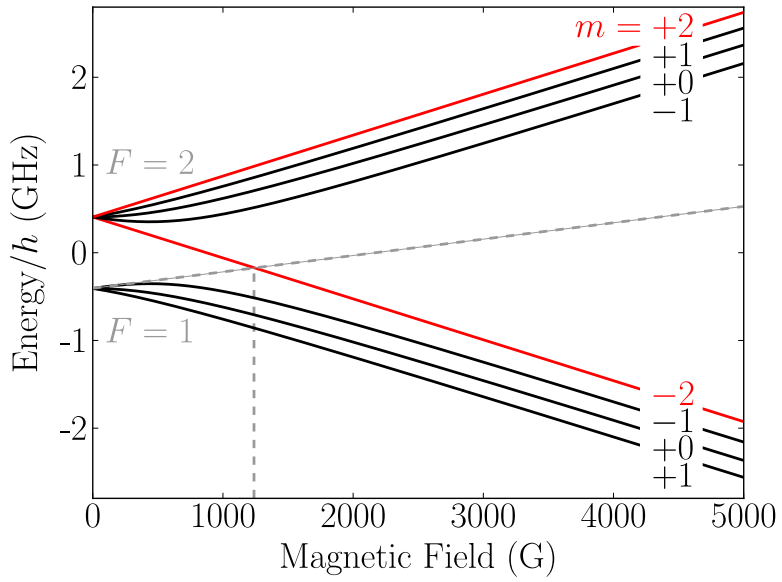

Figure E.5: Breit-Rabi diagram for the $5^2P_{1/2}$ term of ^{87}Rb.

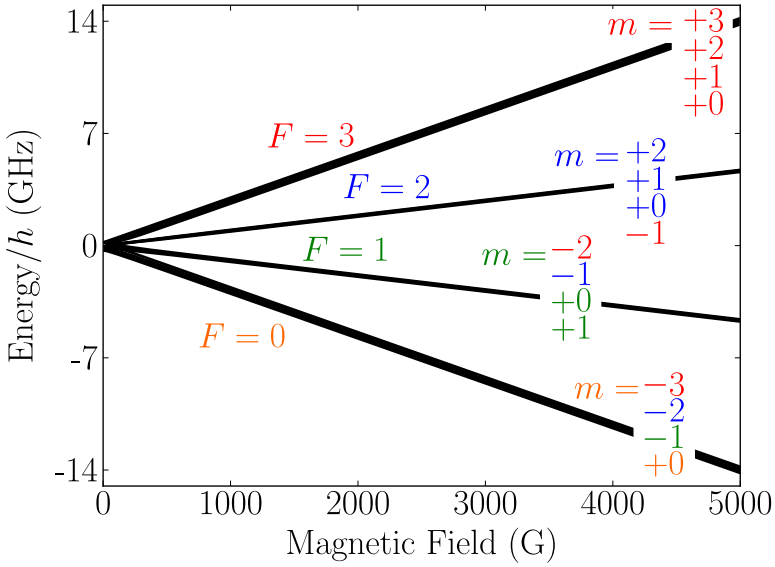

Figure E.6: Breit-Rabi diagram for the $5^2P_{3/2}$ term of ^{87}Rb.

Appendix F

Permanent neodymium magnets

In appendix F we show calculations for the magnetic field profile used in section 4.5.1. For various media of length 2 mm, analytic rotation angles are calculated for the described permanent neodymium magnet. Finally we use the analytic solution for the axial field to show ideal parameters for an optical isolator based on an atomic medium.

F.1 Magnetic field profile

The static magnetic field outside a permanent magnetic surface can be described by a scalar potential, Φ_M. The potential is related to the magnetisation, $\hat{M}(\hat{r}')$, within the material (see equation 5.100 of Jackson [169]) via:

$$\Phi_M(\hat{r}) = -\frac{1}{4\pi}\int_V \frac{\nabla' \cdot \hat{M}(\hat{r}')}{|\hat{r}-\hat{r}'|}\mathrm{d}^3r' + \frac{1}{4\pi}\int_S \frac{\hat{n}' \cdot \hat{M}(\hat{r}')}{|\hat{r}-\hat{r}'|}\mathrm{d}^2r' \ , \tag{F.1}$$

where V and S are the volume and surface of the material and $\hat{n}'$ is the normal to the surface. In figure F.1(a) we chose to consider the special case of uniform magnetisation throughout the volume where $\nabla' \cdot \hat{M}(\hat{r}') = 0$. The first term of equation F.1 vanishes and we only need to worry about the second integral, hence

$$\Phi_M(\hat{r}) = \frac{1}{4\pi}\int_S \frac{\hat{n}' \cdot \hat{M}(\hat{r}')}{|\hat{r}-\hat{r}'|}\mathrm{d}^2r' \ . \tag{F.2}$$

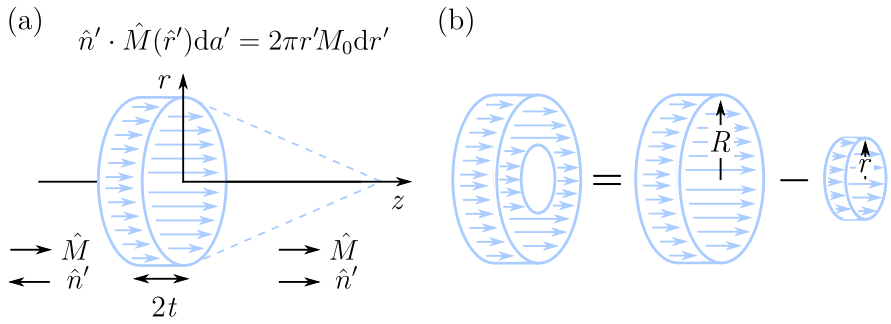

Figure F.1: (a) Schematic of a cylindrical magnet with uniform magnetisation throughout the volume. Here we also write the normal to the surface. (b) Annular magnet used in this investigation consists of a smaller magnet of radius, r, subtracted from a larger magnet of radius, R.

In figure F.1(a) we state that $\hat{n}' \cdot \hat{M}(\hat{r}')\mathrm{d}^2 r'$ is the contribution from an annulus given by $2\pi r' M_0 \mathrm{d}r'$for r' being on axis and the equation becomes

$$\Phi_M(\hat{r}) = \frac{M_0}{2} \int \frac{r'}{|\hat{r} - \hat{r}'|} \mathrm{d}r' \ . \tag{F.3}$$

Using Pythagoras $|\hat{r} - \hat{r}'| = \sqrt{r'^2 + (z-t)^2}$ and integrating between 0 and the radius of the magnet R, we get

$$\Phi_M(\hat{r}) = \frac{M_0}{2} \int_0^R \frac{r'}{\sqrt{r'^2 + (z-t)^2}} \mathrm{d}r' \ . \tag{F.4}$$

The solution to this integral is

$$\begin{aligned} \Phi_{M_{-t}} &= \frac{M_0}{2} \left[\sqrt{r'^2 + (z-t)^2} \right]_0^R \ , \\ &= \frac{M_0}{2} \left[\sqrt{R^2 + (z-t)^2} - z + t \right] \ . \end{aligned} \tag{F.5}$$

In order to calculate the whole scalar potential we also need to calculate it for the back surface. Using Pythagoras $|\hat{r} - \hat{r}'| = \sqrt{r'^2 + (z+t)^2}$ and integrating between the same limits we get

$$\begin{aligned} \Phi_{M_{+t}} &= -\frac{M_0}{2} \left[\sqrt{r'^2 + (z+t)^2} \right]_0^R \ , \\ &= -\frac{M_0}{2} \left[\sqrt{R^2 + (z+t)^2} - z - t \right] \ . \end{aligned} \tag{F.6}$$

Note $\hat{n}'$ points in the opposite direction and therefore we include a minus at the start of the expression. The total scalar potential Φ_M is

$$\begin{aligned}\Phi_M &= \Phi_{M_{-t}} + \Phi_{M_{+t}} \ , \\ &= \frac{M_0}{2}\left[\sqrt{R^2+(z-t)^2} - z + t\right] - \frac{M_0}{2}\left[\sqrt{R^2+(z+t)^2} - z - t\right] \ , \\ &= \frac{M_0}{2}\left[\sqrt{R^2+(z-t)^2} - \sqrt{R^2+(z+t)^2} + 2t\right] \ . \end{aligned} \tag{F.7}$$

Using $\hat{B} = -\mu_0 \nabla \Phi_M$ (see equations 6.88 and 6.99 in [170]), the z-component of the magnetic field is

$$\begin{aligned} B_z &= -\mu_0 \frac{\partial}{\partial z}\Phi_M \ , \\ &= -\frac{\mu_0 M_0}{2}\frac{\partial}{\partial z}\left[\sqrt{R^2+(z-t)^2} - \sqrt{R^2+(z+t)^2} + 2t\right] \ . \end{aligned} \tag{F.8}$$

If we say that the remanence of the magnetic field $B_r = \mu_0 M_0$, differentiating with respect to z gives

$$B_z = \frac{B_r}{2}\left[\frac{(z+t)}{\sqrt{R^2+(z+t)^2}} - \frac{(z-t)}{\sqrt{R^2+(z-t)^2}}\right] \ . \tag{F.9}$$

This is for an axial field with the magnet centred at $z = 0$. Here we introduce z_0 as the z-axis offset to account for the fact that the magnet is not always centred at the origin. The magnetic field expression for a cylindrical magnet of radius R with uniform magnetisation is

$$B_z = \frac{B_r}{2}\left[\frac{z+z_0+t}{\sqrt{(z+z_0+t)^2+R^2}} - \frac{z+z_0-t}{\sqrt{(z+z_0-t)^2+R^2}}\right] \ . \tag{F.10}$$

Figure F.1(b) shows a schematic of an annular magnet consisting of a cylindrical magnet of radius R with a smaller magnet of radius r removed, which is a direct analogy with the one used in this investigation. To get the final field expression for an annular magnet we simply subtract the two profiles calculated with equation F.10, to get

$$\begin{aligned} B(z) &= \frac{B_r}{2}\left(\frac{z+z_0+t}{\sqrt{(z+z_0+t)^2+R^2}} - \frac{z+z_0-t}{\sqrt{(z+z_0-t)^2+R^2}}\right) \\ &- \frac{B_r}{2}\left(\frac{z+z_0+t}{\sqrt{(z+z_0+t)^2+r^2}} - \frac{z+z_0-t}{\sqrt{(z+z_0-t)^2+r^2}}\right) \ . \end{aligned} \tag{F.11}$$

Next we calculate the analytic rotation angles for three different magneto-optic media.

F.2 Analytic rotation angle

The analytic rotation angle for a magneto-optic media of length L is

$$\theta = V \int_{-\frac{L}{2}}^{+\frac{L}{2}} B(z)\mathrm{d}z \ , \tag{F.12}$$

where V is the Verdet constant and $B(z)$ is the magnetic field profile along z. Substituting for equation F.11 we get

$$\begin{aligned}
\theta \ = \ & \frac{VB_r}{2}\left(\sqrt{\left(\frac{L}{2}+z_0+t\right)^2+R^2}-\sqrt{\left(-\frac{L}{2}+z_0+t\right)^2+R^2}\right. \\
- \ & \sqrt{\left(\frac{L}{2}+z_0-t\right)^2+R^2}+\sqrt{\left(-\frac{L}{2}+z_0-t\right)^2+R^2} \\
- \ & \sqrt{\left(\frac{L}{2}+z_0+t\right)^2+r^2}+\sqrt{\left(-\frac{L}{2}+z_0+t\right)^2+r^2} \\
+ \ & \left.\sqrt{\left(\frac{L}{2}+z_0-t\right)^2+r^2}-\sqrt{\left(-\frac{L}{2}+z_0-t\right)^2+r^2}\right) \ .
\end{aligned} \tag{F.13}$$

In section 4.5.1 we obtained the z-axis offset, $z_0 = (0.05 \pm 0.01)$ mm, inner diameter, $d = (7.98 \pm 0.10)$ mm, outer diameter, $D = (25.0 \pm 0.6)$ mm, length, $2t = (6.18 \pm 0.12)$ mm and remanence, $B_r = (1.42 \pm 0.07)$ T of a magnet from a fit to equation F.11 (see figure 4.6). If we now include the Verdet constants for the magneto-optic media TGG, YIG and Rb vapour (see table 1.1), the analytic rotation angles for a length, $L = 1$ mm, can be calculated. TGG, YIG and Rb vapour have rotation angles of -0.04 rad ($-2.47°$), -0.20 rad ($-11.46°$) and -0.74 rad ($-42.21°$), respectively. In comparison to Rb, in order to achieve a similar rotation angle for YIG we require a medium of length, $L = 4.2$ mm. For TGG we could never get enough rotation for the size of the described magnet. The maximum rotation is -0.28 rad ($-15.83°$) for a medium of length, $L = 11.5$ mm. It is important to note that if we were to require a miniaturised optical isolator, the crystal TGG would be of limited use due to its lack of rotation, and commercially we would need to look to atomic media for the solution.

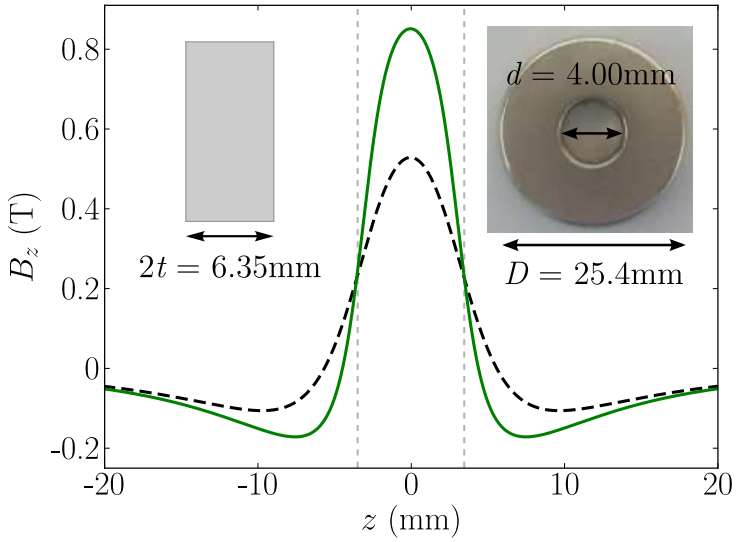

Figure F.2: Magnetic field profile for two uniformly magnetised annular magnets. The dashed (black) and solid (green) curves show the axial field profiles for magnets with dimensions described in section 4.5.1, however with inner diameters of 7.9 mm and 4.0 mm, respectively.

F.3 Ideal parameters for an optical isolator

In section 6.4.3 we showed that for an ideal optical isolator based on an atomic medium we require a magnetic field value of 0.84 T. With the current neodymium magnet used in this investigation this was not possible. As we have the analytic solution for the axial field of a uniformly magnetised annular magnet we can predict what parameters we would require in order to achieve this field value. Figure F.2 shows the magnetic field profile for two uniformly magnetised annular magnets. The dashed (black) curve describes the axial field for the magnet used in this investigation. The solid (green) curve describes the axial field for an ideal magnet with identical dimensions apart from a change in the inner diameter of 4.0 mm instead of 7.9 mm. At $z = 0$ mm the magnetic field is the required 0.84 T.

Bibliography

[1] R. W. Boyd and D. J. Gauthier, *"Slow" and "fast" light*, Prog. Optics. **43**, 497 (2002). 1

[2] M. Fleischhauer, A. Imamoglu, and J. P. Marangos, *Electromagnetically induced transparency: Optics in coherent media*, Rev. Mod. Phys. **77**, 633 (2005). 1

[3] J. Keaveney, I. G. Hughes, A. Sargsyan, D. Sarkisyan, and C. S. Adams, *Maximal refraction and superluminal propagation in a gaseous nanolayer*, Phys. Rev. Lett. **109**, 233001 (2012). 1, 35

[4] K. Hammerer, A. S. Sørensen, and E. S. Polzik, *Quantum interface between light and atomic ensembles*, Rev. Mod. Phys. **82**, 1041 (2010). 1

[5] B. Julsgaard, J. Sherson, J. I. Cirac, J. Fiurasek, and E. S. Polzik, *Experimental demonstration of quantum memory for light*, Nature **432**, 482 (2004). 1, 3

[6] P. Siddons, C. S. Adams, and I. G. Hughes, *Optical control of Faraday rotation in hot Rb vapor*, Phys. Rev. A **81**, 043838 (2010). 1

[7] A. Dawes, L. Illing, S. M. Clark, and D. J. Gauthier, *All-optical switching in rubidium vapor*, Science **308**, 672 (2005). 1

[8] R. J. Rafac and C. E. Tanner, *Measurement of the ratio of the cesium D-line transition strengths*, Phys. Rev. A **58**, 1087 (1998). 1

[9] R. Loudon, *The quantum theory of light, 3rd ed.* (OUP Oxford, 2000). 2

[10] J. Gea-Banacloche, Y. Li, S. Jin, and M. Xiao, *Electromagnetically induced transparency in ladder-type inhomogeneously broadened media: Theory and experiment*, Phys. Rev. A **51**, 576 (1995). 2

[11] A. K. Mohapatra, T. R. Jackson, and C. S. Adams, *Coherent optical detection of highly excited Rydberg states using electromagnetically induced transparency*, Phys. Rev. Lett. **98**, 113003 (2007).

[12] S. D. Badger, I. G. Hughes, and C. S. Adams, *Hyperfine effects in electromagnetically induced transparency*, J. Phys. B: At. Mol. Opt. Phys. **34**, L749 (2001). 2

[13] S. R. Shin and H. R. Noh, *Doppler spectroscopy of arbitrarily polarized light in rubidium*, Opt. Commun. **284**, 1243 (2010). 2

[14] M. R. Vanner, R. J. McLean, P. Hannaford, and A. M. Akulshin, *Broadband optical delay with a large dynamic range using atomic dispersion*, J. Phys. B: At. Mol. Opt. Phys. **41**, 051004 (2008). 2

[15] R. M. Camacho, M. V. Pack, J. C. Howell, A. Schweinsberg, and R. W. Boyd, *Wide-bandwidth, tunable, multiple-pulse-width optical delays using slow light in cesium vapor*, Phys. Rev. Lett. **98**, 153601 (2007). 2

[16] R. Zhang, J. A. Greenberg, M. C. Fischer, and D. J. Gauthier, *Controllable ultrabroadband slow light in a warm rubidium vapor*, J. Opt. Soc. Am. B **28**, 2578 (2011). 2

[17] A. Vernier, S. Franke-Arnold, E. Riis, and A. S. Arnold, *Enhanced frequency up-conversion in Rb vapor*, Opt. Express. **18**, 17020 (2010). 2, 6

[18] J. Keaveney *et al.*, *The cooperative Lamb shift in an atomic nanolayer*, Phys. Rev. Lett. **108**, 173601 (2012). 2, 6, 44, 60

[19] P. Böhi and P. Treutlein, *Simple microwave field imaging technique using hot atomic vapor cells*, Appl. Phys. Lett. **101**, 181107 (2012). 2

[20] H. R. Noh and H. S. Moon, *Calculated Hanle transmission and absorption spectra of the ^{87}Rb D_1 line with residual magnetic field for arbitrarily polarized light*, Phys. Rev. A **82**, 033407 (2010). 2

[21] G. W. Truong, E. F. May, T. M. Stace, and A. N. Luiten, *Quantitative atomic spectroscopy for primary thermometry*, Phys. Rev. A **83**, 033805 (2011). 2

[22] L. Weller, R. J. Bettles, P. Siddons, C. S. Adams, and I. G. Hughes, *Absolute absorption on the rubidium D_1 line including resonant dipole–dipole interactions*, J. Phys. B: At. Mol. Opt. Phys. **44**, 195006 (2011). 3, 7, 8, 64, 95, 98, 111, 129, 145

[23] H. J. Kimble, *The quantum internet*, Nature **453**, 1023 (2008). 3

[24] P. Zeeman and M. Bôcher, *Zeeman effect*, Nature **55**, 347 (1897). 3

[25] L. Windholz, *Zeeman-and Paschen-Back-effect of the hyperfine structure of the sodium D_1 line*, Z. Phys. A. - Hadron. Nucl. **322**, 203 (1985). 3

[26] A. Popescu, K. Schorstein, and T. Walther, *A novel approach to a Brillouin–LIDAR for remote sensing of the ocean temperature*, Appl. Phys. B. **79**, 955 (2004). 3

[27] L. Weller *et al.*, *Absolute absorption and dispersion of a rubidium vapour in the hyperfine Paschen-Back regime*, J. Phys. B: At. Mol. Opt. Phys. **45**, 215005 (2012). 3, 7, 8, 9

[28] M. Faraday, *On the magnetization of light and the illumination of magnetic lines of force*, Philos. Trans. R. Soc. London **136**, 1 (1846). 3

[29] J. F. Sherson *et al.*, *Quantum teleportation between light and matter*, Nature **443**, 557 (2006). 3

[30] S. D. Jenkins *et al.*, *In situ determination of Zeeman content of collective atomic memories*, J. Phys. B: At. Mol. Opt. Phys. **45**, 124006 (2012). 3

[31] D. Budker *et al.*, *Resonant nonlinear magneto-optical effects in atoms*, Rev. Mod. Phys. **74**, 1153 (2002). 3

[32] D. Budker and M. Romalis, *Optical magnetometry*, Nat. Phys. **3**, 227 (2007). 3

[33] A. Sargsyan *et al.*, *A novel approach to quantitative spectroscopy of atoms in a magnetic field and applications based on an atomic vapor cell with* $L = \lambda$, Appl. Phys. Lett. **93**, 021119 (2008). 4

[34] D. J. Dick and T. M. Shay, *Ultrahigh-noise rejection optical filter*, Opt. Lett. **16**, 867 (1991). 4

[35] J. A. Zieliska, F. A. Beduini, N. Godbout, and M. W. Mitchell, *Ultra-Narrow Faraday Rotation Filter at the Rb* D_1 *Line*, Opt. Lett. **37**, 524 (2012). 4, 5

[36] W. B. Lin, Z. Q. Zhou, C. F. Li, and G. C. Guo, *Proposed solid-state Faraday anomalous-dispersion optical filter*, Phys. Rev. A **84**, 055803 (2011). 4

[37] R. P. Abel, U. Krohn, P. Siddons, I. G. Hughes, and C. S. Adams, *Faraday dichroic beam splitter for Raman light using an isotopically pure alkali-metal-vapor cell*, Opt. Lett. **34**, 3071 (2009). 4, 5

[38] P. Siddons, N. C. Bell, Y. Cai, C. S. Adams, and I. G. Hughes, *A gigahertz-bandwidth atomic probe based on the slow-light Faraday effect*, Nature Photon. **3**, 225 (2009). 4

[39] A. L. Marchant *et al.*, *Off-resonance laser frequency stabilization using the Faraday effect*, Opt. Lett. **36**, 64 (2011). 4, 114

[40] S. L. Kemp, I. G. Hughes, and S. L. Cornish, *An analytical model of off-resonant Faraday rotation in hot alkali metal vapours*, J. Phys. B: At. Mol. Opt. Phys. **44**, 235004 (2011). 4, 64, 90, 111

[41] L. Weller, T. Dalton, P. Siddons, C. S. Adams, and I. G. Hughes, *Measuring the Stokes parameters for light transmitted by a high-density rubidium vapour in large magnetic fields*, J. Phys. B: At. Mol. Opt. Phys. **45**, 055001 (2012). 4, 7, 8, 111

[42] H. Dong, J. Fang, B. Zhou, J. Qin, and S. Wan, *Review of atomic MEMS: driving technologies and challenges*, Microsyst. Technol. **16**, 1683 (2010). 4

[43] J. Tatum, *VCSEL proliferation*, Proc. SPIE. **6484**, 648403 (2007). 4

[44] L. A. Liew *et al.*, *Microfabricated alkali atom vapor cells*, Appl. Phys. Lett. **84**, 2694 (2004). 4

[45] F. Benabid, F. Couny, J. C. Knight, T. A. Birks, and P. S. J. Russell, *Compact, stable and efficient all-fibre gas cells using hollow-core photonic crystal fibres*, Nature **434**, 488 (2005). 4

[46] S. Ghosh, J. E. Sharping, D. G. Ouzounov, and A. L. Gaeta, *Resonant optical interactions with molecules confined in photonic band-gap fibers*, Phys. Rev. Lett. **94**, 93902 (2005). 4

[47] S. Knappe *et al.*, *Advances in chip-scale atomic frequency references at NIST*, Proc. SPIE. **6673**, 667307 (2007). 4

[48] V. Shah, S. Knappe, P. D. D. Schwindt, and J. Kitching, *Subpicotesla atomic magnetometry with a microfabricated vapour cell*, Nat. Photon. **1**, 649 (2007). 4

[49] E. A. Donley, *Nuclear magnetic resonance gyroscopes*, in *Sensors, IEEE*, p. 17, 2010. 4

[50] S. A. Knappe, H. G. Robinson, and L. Hollberg, *Microfabricated saturated absorption laser spectrometer*, Opt. Express. **15**, 6293 (2007). 4

[51] C. Lee *et al.*, *Small-sized dichroic atomic vapor laser lock*, Rev. Sci. Instrum. **82**, 043107 (2011). 4

[52] L. Weller *et al.*, *Optical isolator using an atomic vapor in the hyperfine PaschenBack regime*, Opt. Lett. **37**, 3405 (2012). 4, 8, 9

[53] J. G. Bai, G. Q. Lu, and T. Lin, *Magneto-optical current sensing for applications in integrated power electronics modules*, Sensor. Actuat. A-Phys. **109**, 9 (2003). 5

[54] E. G. Villora *et al.*, *Faraday rotator properties of* $Tb_3[Sc_{1.95}Lu_{0.05}](Al_3)O_{12}$*, a highly transparent terbium-garnet for visible-infrared optical isolators*, Appl. Phys. Lett. **99**, 011111 (2011). 5

[55] M. F. Perutz, G. Fermi, B. Luisi, B. Shaanan, and R. C. Liddington, *Stereochemistry of cooperative mechanisms in hemoglobin*, Accounts. Chem. Res. **20**, 309 (1987). 5

[56] M. Sarovar, A. Ishizaki, G. R. Fleming, and K. B. Whaley, *Quantum entanglement in photosynthetic light-harvesting complexes*, Nat. Phys. **6**, 462 (2010). 5

[57] P. Barnes, J. L. Finney, J. D. Nicholas, and J. E. Quinn, *Cooperative effects in simulated water*, Nature. **282**, 459 (1979). 5

[58] J. D. Pritchard *et al.*, *Cooperative atom-light interaction in a blockaded Rydberg ensemble*, Phys. Rev. Lett. **105**, 193603 (2010). 6

[59] M. Viteau *et al.*, *Cooperative excitation and many-body interactions in a cold Rydberg gas*, Phys. Rev. Lett. **109**, 53002 (2012). 6

[60] T. Peyronel *et al.*, *Quantum nonlinear optics with single photons enabled by strongly interacting atoms*, Nature. **488**, 57 (2012). 6

[61] U. Vogl and M. Weitz, *Laser cooling by collisional redistribution of radiation*, Nature **461**, 70 (2009). 6

[62] R. H. Dicke, *Coherence in spontaneous radiation processes*, Phys. Rev. **93**, 99 (1954). 6

[63] T. Meijer, J. D. White, B. Smeets, M. Jeppesen, and R. E. Scholten, *Blue five-level frequency-upconversion system in rubidium*, Opt. Lett. **31**, 1002 (2006). 6

[64] A. J. Olson, E. J. Carlson, and S. K. Mayer, *Two-photon spectroscopy of rubidium using a grating-feedback diode laser*, Am. J. Phys. **74**, 218 (2006). 6

[65] A. M. Akulshin, R. J. McLean, A. I. Sidorov, and P. Hannaford, *Coherent and collimated blue light generated by four-wave mixing in Rb vapour*, Opt. Express. **17**, 22861 (2009). 6

[66] F. Shen *et al.*, *Many-body dipole-dipole interactions between excited Rb atoms probed by wave packets and parametric four-wave mixing*, Phys. Rev. Lett. **99**, 143201 (2007). 6

[67] R. T. Willis, F. E. Becerra, L. A. Orozco, and S. L. Rolston, *Correlated photon pairs generated from a warm atomic ensemble*, Phys. Rev. A. **82**, 053842 (2010). 6

[68] C. Carr, R. Ritter, K. J. Weatherill, and C. S. Adams, *Cooperative non-equilibrium phase transition in a dilute thermal atomic gas*, arXiv preprint arXiv:1302.6621 (2013). 6

[69] A. Rudolf and T. Walther, *High-transmission excited-state Faraday anomalous dispersion optical filter edge filter based on a Halbach cylinder magnetic-field configuration*, Opt. Lett. **37**, 4477 (2012). 6

[70] T. M. Wilson and J. L. Roberts, *Enhanced light-assisted-collision rate via excitation to the long-lived $5S_{1/2} \rightarrow 5D_{5/2}$ molecular potential in an ^{85}Rb magneto-optical trap*, Phys. Rev. A. **83**, 033419 (2011). 6

[71] M. Allegrini, C. Gabbanini, and L. Moi, *Energy-pooling processes in laser-excited alkali vapors: an update on experiments*, Le Journal de Physique Colloques **46**, 1 (1985). 6

[72] V. S. Kushawaha and J. J. Leventhal, *Energy pooling in Na (3p) - Na (3p) collisions*, Phys. Rev. A. **22**, 2468 (1980). 6

[73] G. H. Bearman and J. J. Leventhal, *Ionization and energy pooling in laser-excited Na vapor*, Phys. Rev. Lett. **41**, 1227 (1978). 6

[74] M. Allegrini, S. Gozzini, I. Longo, P. Savino, and P. Bicchi, *Rosonant laser excitation of potassium vapour: Experimental investigation of energy-pooling collisions and plasma production*, Il. Nuovo. Cimento. D. **1**, 49 (1982). 6

[75] R. K. Namiotka, J. Huennekens, and M. Allegrini, *Energy-pooling collisions in potassium: $4P_J + 4P_J \rightarrow 4S + (nl= 5P, 6S, 4D)$*, Phys. Rev. A. **56**, 514 (1997). 6

[76] L. Barbier and M. Cheret, *Energy pooling process in rubidium vapour*, J. Phys. B: At. Mol. Opt. Phys. **16**, 3213 (1999). 6, 135

[77] S. Yi-Fan, D. Kang, M. Bao-Xia, W. Shu-Ying, and C. Xiu-Hua, *Energy-Pooling Collisions in Rubidium: $5P_{3/2} + 5P_{3/2} \rightarrow 5S + (nl= 5D, 7S)$*, Chinese. Phys. Lett. **22**, 2805 (2005).

[78] R. H. Hill Jr., H. A. Schuessler, and B. G. Zollars, *Inelastic collisions between selectively excited rubidium atoms and ground-state rubidium atoms*, Phys. Rev. A. **25**, 834 (1982). 147

[79] L. Caiyan, A. Ekers, J. Klavins, and M. Jansons, *Studies of inelastic cross-section in Rb (7S)+ Rb (5S) collisions*, Phys. Scripta. **53**, 306 (2006).

[80] K. Orlovsky, V. Grushevsky, and A. Ekers, *Theoretical study of energy transfer in Rb (7S)+ Rb (5S) and Rb (5D)+ Rb (5S) collisions*, Eur. J. Phys. D. **12**, 133 (2000).

[81] A. E. Afanasiev, P. N. Melentiev, and V. I. Balykin, *Laser-induced quantum adsorption of atoms on a surface*, JETP. Lett. **86**, 172 (2007).

[82] M. A. Mahmoud, *Electron energy distribution function in laser-excited rubidium atoms*, J. Phys. B: At. Mol. Opt. Phys. **38**, 1545 (2005).

[83] T. Ban, D. Aumiler, R. Beuc, and G. Pichler, *Rb_2 diffuse band emission excited by diode lasers*, Eur. J. Phys. D. **30**, 57 (2004). 6, 150

[84] C. Vadla, K. Niemax, and J. Brust, *Energy pooling in cesium vapor*, Z. Phys. D. Atom. Mol. **37**, 241 (1996). 6

[85] C. Vadla, *Energy pooling in caesium vapour*, Eur. J. Phys. D. **1**, 259 (1998).

[86] Z. J. Jabbour *et al.*, *Energy-pooling collisions in cesium: $6P_J + 6P_J \rightarrow 6S + (nl= 7P, 6D, 8S, 4F)$*, Phys. Rev. A. **54**, 1372 (1996).

[87] J. M. Gagné, K. Le Bris, and M. C. Gagné, *Laser energy-pooling processes in an optically thick Cs vapor near a dissipative surface*, JOSA. B. **19**, 2852 (2002).

[88] F. De Tomasi *et al.*, *Experimental study of caesium energy pooling collisions and modelling of the excited atom density in the presence of optical pumping and radiation trapping*, J. Phys. B: At. Mol. Opt. Phys. **30**, 4991 (1999).

[89] L. Wang, J. Zhao, L. Xiao, and S. Jia, *Thermal-energy pooling collisions in cesium vapor*, Chinese. J. Lasers. **6** (2002).

[90] H. S. Kang, J. P. Kim, C. H. Oh, and P. S. Kim, *Energy-pooling collision in Cs atomic vapor*, J. Korean. Phys. Soc. **40**, 220 (2002). 6

[91] L. Weller *et al.*, *Cooperative enhancement of energy transfer in a high-density thermal vapor*, in preparation (2013). 6, 8, 9

[92] P. Siddons, C. S. Adams, C. Ge, and I. G. Hughes, *Absolute absorption on rubidium D lines: comparison between theory and experiment*, J. Phys. B: At. Mol. Opt. Phys. **41**, 155004 (2008). 7, 16, 25, 37, 47, 50, 54, 64, 90, 95, 111, 133

[93] C. J. Foot, *Atomic physics*, (2008). 13, 17

[94] C. Cohen-Tannoudji, J. Dupont-Roc, G. Grynberg, and P. Meystre, *Atom-photon interactions: Basic processes and applications*, Phys. Today. **45**, 357 (1992). 13, 14

[95] T. Berggren, *Expectation value of an operator in a resonant state*, Phys. Lett. B. **373**, 1 (1996). 15

[96] U. Volz and H. Schmoranzer, *Precision lifetime measurements on alkali atoms and on helium by beam–gas–laser spectroscopy*, Phys. Scripta. **1996**, 48 (1996). 16, 40, 56, 96, 155

[97] P. A. Tipler and G. Mosca, *Physics for scientists and engineers* (WH Freeman & Company, 2007). 18

[98] G. P. Barwood, P. Gill, and W. R. C. Rowley, *Frequency measurements on optically narrowed Rb-stabilised laser diodes at 780 nm and 795 nm*, Appl. Phys. B. Lasers. O. **53**, 142 (1991). 18, 155

[99] V. N. Fadeeva and N. M. Terent'ev, *Tables of values of the probability integral of a complex argument*, Gostekhizdat, Moscow (1954). 19

[100] B. H. Bransden and C. J. Joachain, *Quantum mechanics: second edition* (Pearson Education Limited, 2000). 20, 21, 24, 28, 65, 77

[101] A. Banerjee, D. Das, and V. Natarajan, *Absolute frequency measurements of the D_1 lines in 39 K, ^{85}Rb, and ^{87}Rb with 0.1 ppb uncertainty*, Europhys. Lett. **65**, 172 (2004). 21, 65

[102] E. Arimondo, M. Inguscio, and P. Violino, *Experimental determinations of the hyperfine structure in the alkali atoms*, Rev. Mod. Phys. **49**, 31 (1977). 21, 23, 65, 66, 80

[103] A. Corney, *Atomic and laser spectroscopy* (Clarendon Press, 1978). 21, 22, 25, 46, 47, 69, 102

[104] G. K. Woodgate, *Elementary atomic structure* (Oxford: Oxford University Press, 1983). 22, 65, 69

[105] D. J. Berkeland and M. G. Boshier, *Destabilization of dark states and optical spectroscopy in Zeeman-degenerate atomic systems*, Phys. Rev. A. **65**, 033413 (2002). 24

[106] E. Hecht, *Optics, 4th ed*, Addison-Wesley, 2003 . 24

[107] M. Weissbluth, *Atoms and molecules*. 25

[108] R. W. Boyd, *Nonlinear optics* (Academic press, 2003). 35, 37

[109] W. T. Silfvast, *Laser fundamentals* (Cambridge University Press, 2004). 36

[110] R. Eisberg and R. Resnick, *Quantum physics* (John Wiley New York, 1974). 36

[111] B. E. Sherlock and I. G. Hughes, *How weak is a weak probe in laser spectroscopy?*, Am. J. Phys. **77**, 111 (2009). 37, 54, 90, 92

[112] K. B. MacAdam, A. Steinbach, and C. Wieman, *A narrow-band tunable diode laser system with grating feedback, and a saturated absorption spectrometer for Cs and Rb*, Am. J. Phys. **60**, 1098 (1992). 39, 54, 89

[113] D. A. Smith and I. G. Hughes, *The role of hyperfine pumping in multilevel systems exhibiting saturated absorption*, Am. J. Phys. **72**, 631 (2004). 39, 54, 89, 169

[114] M. Gorris-Neveux *et al.*, *Doppler-free reflection spectroscopy of rubidium D_1 line in optically dense vapour*, Opt. Commun. **134**, 85 (1997). 44

[115] A. Thorne, U. Litzén, and S. Johansson, *Spectrophysics: principles and applications* (Springer, 1999). 47

[116] K. Niemax and G. Pichler, *New aspects in the self-broadening of alkali resonance lines*, J. Phys. B: At. Mol. Phys. **8**, 179 (1975). 47

[117] J. Huennekens and A. Gallagher, *Self-broadening of the sodium resonance lines and excitation transfer between the $3P_{3/2}$ and $3P_{1/2}$ levels*, Phys. Rev. A **27**, 1851 (1983). 49, 59

[118] E. L. Lewis, *Collisional relaxation of atomic excited states, line broadening and interatomic interactions*, Phys. Rep. **58**, 1 (1980). 49, 50, 148

[119] R. C. Hilborn, *Einstein coefficients, cross sections, f values, dipole moments, and all that*, Am. J. Phys. **50**, 982 (1982). 50

[120] E. Caliebe and K. Niemax, *Oscillator strengths of the principal series lines of Rb*, J. Phys. B: At. Mol. Opt. Phys. **12**, L45 (1979). 50

[121] C. B. Alcock, V. P. Itkin, and M. K. Horrigan, *Vapour pressure equations for the metallic elements: 2982500K*, Can. Metall. Quart. **23**, 309 (1984). 52, 53, 59, 153

[122] P. Siddons, C. S. Adams, and I. G. Hughes, *Off-resonance absorption and dispersion in vapours of hot alkali-metal atoms*, J. Phys. B: At. Mol. Opt. Phys. **42**, 175004 (2009). 52, 122

[123] I. G. Hughes and T. P. A. Hase, *Measurements and their uncertainties: A practical guide to modern error analysis* (OUP, 2010), . 57, 82, 88, 96, 174

[124] R. Kondo, S. Tojo, T. Fujimoto, and M. Hasuo, *Shift and broadening in attenuated total reflection spectra of the hyperfine-structure-resolved D_2 line of dense rubidium vapor*, Phys. Rev. A **73**, 062504 (2006). 59

[125] V. Vuletic, V. A. Sautenkov, C. Zimmermann, and T. W. Hänsch, *Measurement of cesium resonance line self-broadening and shift with Doppler-free selective reflection spectroscopy*, Opt. Commun. **99**, 185 (1993). 59, 60

[126] A. M. Akulshin *et al.*, *Collisional broadening of intra-Doppler resonances of selective reflection on the D_2 line of cesium*, JETP Lett. **36**, 303 (1982). 59

[127] J. J. Maki, M. S. Malcuit, J. E. Sipe, and R. W. Boyd, *Linear and nonlinear optical measurements of the Lorentz local field*, Phys. Rev. Lett. **67**, 972 (1991). 60

[128] V. A. Sautenkov, H. Van Kampen, E. R. Eliel, and J. P. Woerdman, *Dipole-dipole broadened line shape in a partially excited dense atomic gas*, Phys. Rev. Lett. **77**, 3327 (1996). 60

[129] L. Reggami, M. Bouledroua, A. R. Allouche, and M. Aubert-Frécon, *Self-broadening and shifting of the Li ($2s \rightarrow 2p$) and K ($4s \rightarrow 4p$) line cores*, J. Quant. Spectrosc. Ra. **110**, 72 (2009). 60

[130] T. Varzhapetyan *et al.*, *Study of atomic transition self-broadening and shift with the help of a nano-cell*, J. Phys. B: At. Mol. Opt. Phys. **41**, 185004 (2008).

[131] K. Weber and K. Niemax, *Self-broadening and shift of Doppler-free two-photon lines of Rb*, Opt. Commun. **31**, 52 (1979).

[132] R. Friedberg, S. R. Hartmann, and J. T. Manassah, *Frequency shifts in emission and absorption by resonant systems ot two-level atoms*, Phys. Rep. **7**, 101 (1973). 60

[133] H. A. Lorentz, *The theory of electrons and its applications to the phenomena of light and radiant heat* (BG Teubner, 1916). 60

[134] J. Keaveney *et al.*, *Optical transmission through a dipolar layer*, arXiv preprint arXiv:1109.3669 (2011). 61

[135] A. Sargsyan *et al.*, *Hyperfine Paschen-Back regime realized in Rb nanocell*, Opt. Lett. **37**, 1379 (2012). 64, 121, 129

[136] T. F. Gallagher, *Rydberg Atoms* (New York: Cambridge University Press, 1994). 65

[137] P. J. Mohr, B. N. Taylor, and D. B. Newell, *CODATA recommended values of the fundamental physical constants: 2010*, Rev. Mod. Phys. **84**, 1527 (2012). 66

[138] D. A. Steck, *Rubidium 85 and 87 D line data*, revision 2.1.4, 23rd December 2010. 66

[139] H. A. Bethe and E. E. Salpeter, *Quantum mechanics of one-and two-electron systems*, p. 88 (1957). 66

[140] G. Breit and I. Rabi, *Measurement of nuclear spin*, Phys. Rev. **38**, 2082 (1931). 67, 69

[141] R. Wynands, F. Diedrich, D. Meschede, and H. R. Telle, *A compact tunable 60-dB Faraday optical isolator for the near infrared*, Rev. Sci. Instrum. **63**, 5586 (1992). 81, 126

[142] S. Knappe *et al.*, *Atomic vapor cells for chip-scale atomic clocks with improved long-term frequency stability*, Opt. Lett. **30**, 2351 (2005). 87

[143] M. D. Rotondaro and G. P. Perram, *Collisional broadening and shift of the rubidium D_1 and D_2 lines ($5^2S_{1/2} \rightarrow 5^2P_{1/2}$, $5^2P_{3/2}$) by rare gases, H_2, D_2, N_2, CH_4 and CF_4*, J. Quant. Spectrosc. Ra. **57**, 497 (1997). 87

[144] S. Huard, *Polarization of Light* (Wiley New York, 1997). 89, 91, 107

[145] G. G. Stokes, *On the composition and resolution of streams of polarized light from different sources*, Trans. Cambridge Philos. Soc. **9**, 399 (1852). 103

[146] B. Schaefer, E. Collett, R. Smyth, D. Barrett, and B. Fraher, *Measuring the Stokes polarization parameters*, Am. J. Phys. **75**, 163 (2007). 103

[147] D. J. Gauthier, P. Narum, and R. W. Boyd, *Simple, compact, high-performance permanent-magnet Faraday isolator*, Opt. Lett. **11**, 623 (1986). 126

[148] A. Sargsyan, D. Sarkisyan, and A. Papoyan, *Dark-line atomic resonances in a submicron-thin Rb vapor layer*, Phys. Rev. A. **73**, 033803 (2006). 126

[149] E. Jahier *et al.*, *Temperature-tunable sapphire windows for reflection loss-free operation of vapor cells*, Appl. Phys. B. Lasers. O. **71**, 561 (2000). 126

[150] M. Minsky, *Memoir on inventing the confocal scanning microscope*, Scanning **10**, 128 (1988). 133

[151] I. V. Hertel and K. J. Ross, *Generalized oscillator strengths in the electron impact spectra of rubidium and caesium*, J. Phys. B: At. Mol. Opt. Phys. **2**, 484 (2002). 135

[152] J. E. Sansonetti, *Wavelengths, transition probabilities, and energy levels for the spectra of rubidium (Rb i through Rb xxxvii)*, J. Phys. Chem. Ref. Data **35**, 301 (2006). 135

[153] C. L. Vaillant, M. P. A. Jones, and R. M. Potvliege, *Long-range Rydberg-Rydberg interactions in calcium, strontium and ytterbium*, J. Phys. B: At. Mol. Opt. Phys. **45**, 135004 (2012). 138

[154] K. T. Tang and J. P. Toennies, *An improved simple model for the van der Waals potential based on universal damping functions for the dispersion coefficients*, J. Chem. Phys. **80**, 3726 (1984). 138

[155] S. Chandrasekhar, *Stochastic problems in physics and astronomy*, Rev. Mod. Phys. **15**, 1 (1943). 138

[156] J. D. Pritchard, *Cooperative optical non-linearity in a blockaded Rydberg ensemble*, PhD thesis, Durham University, 2011. 138

[157] S. J. Blundell and K. M. Blundell, *Concepts in thermal physics* (Oxford University Press, 2009). 139

[158] J. B. Marion and S. T. Thornton, *Classical dynamics of particles and systems*, 4th ed. (Brooks/Cole - Thompson Learning, 1995). 140

[159] L. C. Andrews and R. L. Phillips, *Mathematical techniques for engineers and scientists* (SPIE, 1000 20th Street, Bellingham, WA 98227-0010 USA, 2003). 140, 141

[160] C. Vadla, V. Horvatic, D. Veza, and K. Niemax, *Resonantly laser induced plasmas in gases: The role of energy pooling and exothermic collisions in plasma breakdown and heating*, Spectrochim. Acta. B. **65**, 33 (2010). 150

[161] A. Kölle, G. Epple, H. Kübler, R. Löw, and T. Pfau, *Four-wave mixing involving Rydberg states in thermal vapor*, Phys. Rev. A. **85**, 063821 (2012). 152

[162] R. Bunsen, *Ueber casium und rubidium (in german)*, Ann. der Chem. **119**, 107 (1861). 154, 155

[163] D. R. Lide and T. J. Bruno, *CRC handbook of chemistry and physics* (CRC PressI Llc, 2012). 154, 155

[164] J. Ye, S. Swartz, P. Jungner, and J. L. Hall, *Hyperfine structure and absolute frequency of the ^{87}Rb $5P_{3/2}$ state*, Opt. Lett. **21**, 1280 (1996). 155

[165] L. E. Ballentine, *Quantum mechanics: a modern development* (World Scientific Publishing Company, 1998). 156, 157

[166] F. S. Levin, *An introduction to quantum theory* (Cambridge University Press, 2001). 156, 157

[167] M. Hercher, *The spherical mirror Fabry-Perot interferometer*, Appl. Opt. **7**, 951 (1968). 168

[168] A. Banerjee and V. Natarajan, *Saturated-absorption spectroscopy: eliminating crossover resonances by use of copropagating beams*, Opt. Lett. **28**, 1912 (2003). 169

[169] J. D. Jackson, *Classical electrodynamics*, 3rd ed. (Wiley, 1999), . 180

[170] C. A. Brau, *Modern problems in classical electrodynamics* (Oxford University Press New York, 2004). 182